日本原子力研究開発機構

Proceedings of the 2021 Symposium on Nuclear Data

November 18-19, 2021,

On-line Connection Conference

(Eds.) Yuji YAMAGUCHI and Shin-ichiro MEIGO

J-PARC Center
Sector of Nuclear Science Research

JAEA-Conf

November 2022

Japan Atomic Energy Agency 日本原子力研究開発機構

Proceedings of the 2021 Symposium on Nuclear Data

November 18-19, 2021,

On-line Connection Conference

(Eds.) Yuji YAMAGUCHI and Shin-ichiro MEIGO

J-PARC Center, Sector of Nuclear Science Research

Japan Atomic Energy Agency

Tokai-mura, Naka-gun, Ibaraki-ken

The 2021 Symposium on Nuclear Data was held as an online connection conference on November 18-19, 2021. The symposium was organized by the Nuclear Data Division of the Atomic Energy Society of Japan (AESJ) in cooperation with the Sigma Investigative Advisory Committee of AESJ, J-PARC Center, Nuclear Science and Engineering Center of Japan Atomic Energy Agency (JAEA), and High Energy Accelerator Research Organization (KEK).

In the symposium, tutorials "New Developments in TALYS and TENDL-2021" and "Role of ADS and its Development Issues" were proposed and held. Three sessions of lectures and discussions were held: "J-PARC and JAEA Facilities", "Current Status and Future Prospects of Nuclear Data Research", and "Medical, Isotope Production, and Analysis". In addition, recent research progress on experiments, nuclear theory, evaluation, benchmark, and applications were presented in the poster session. The total number of participants was 132 participants. Each oral and poster presentation was followed by an active question and answer session. This report consists of a total of 36 papers including 14 oral and 22 poster presentations.

2021 年度核データ研究会報告集

2021 年 11 月 18 日〜19 日

オンライン開催

日本原子力研究開発機構　原子力科学研究部門 J-PARCセンター

（編）山口　雄司、明午　伸一郎

　2021 年度核データ研究会は、2021 年 11 月18 日〜19 日にオンライン形式で開催された。本研究会は、日本原子力学会核データ部会が主催し、日本原子力学会「シグマ」調査専門委員会、J-PARCセンター、日本原子力研究開発機構（原子力機構）原子力基礎工学研究センター、および高エネルギー加速器研究機構（KEK）が共催した。

　チュートリアルとして「TALYSの新展開とTENDL-2021」および「ADSの役割と開発課題」を企画し実施した。講演・議論のセッションとして、「J-PARCおよび原子力機構の施設」、「核データ研究の現状と展望」および「医療、アイソトープ生成および分析」の 3 セッションを企画し実施した。さらに、ポスターセッションでは、実験、理論、評価、ベンチマーク、応用等、幅広い研究内容について発表が行われた。参加者総数は 132 名であった。それぞれの口頭発表及びポスター発表では活発な質疑応答が行われた。本報告集は、本研究会における口頭発表 14 件、ポスター発表 22 件の合計36の論文を掲載している。

キーワード： 2021 年度核データ研究会、実験、原子核理論、核データ評価、ベンチマークテスト、核データ応用

Contents

Poster Session

目次

ポスター発表論文

1 2021 Symposium on Nuclear Data - Programme

Nov. 18–19, 2021.

Thursday, November 18

Opening Address (9:30–10:00)

Dr. Shin-ichiro Meigo (Japan Atomic Energy Agency)

Studies at J-PARC and JAEA (10:00–12:00)

Chair: Dr. Osamu Iwamoto (Japan Atomic Energy Agency)

10:00 A Plan of Proton Irradiation Facility at J-PARC and Possibilities of Application to Nuclear Data Research

Dr. Fujio Maekawa (Japan Atomic Energy Agency)

10:30 Status and Prospects on Light Sterile Neutrino Searches

Dr. Takasumi Maruyama (High Energy Accelerator Research Organization)

11:00 Research Reactor JRR-3 Restart !! – Invitation to the Various Neutron Utilization –

Dr. Hideaki Matsue (Japan Atomic Energy Agency)

11:30 Recent Activities for Nuclear Data Measurements in ANNRI

Dr. Atsushi Kimura (Japan Atomic Energy Agency)

Current Status and Prospects of Nuclear Data Study 1 (13:00–14:30)

Chair: Dr. Naoki Yamano (Tokyo Institute of Technology)

13:00 Outline of JENDL-5

Dr. Osamu Iwamoto (Japan Atomic Energy Agency)

13:30 Integral Tests of Preliminary JENDL-5 for Critical and Shielding Experiments

Dr. Yasunobu Nagaya et al. (Japan Atomic Energy Agency)

Tutorial 1 (15:00–15:40)

Chair: Prof. Satoshi Chiba (Tokyo Institute of Technology)

15:00 New Developments in TALYS and TENDL-2021

Prof. Arjan Koning (International Atomic Energy Agency)

Poster Session (16:00–18:30)

Social Gathering - Online (19:30–21:30)

Friday, November 19

Current Status and Prospects of Nuclear Data Study 2 (9:00–10:00)
Chair: Prof. Tatsuya Katabuchi (Tokyo Institute of Technology)
  9:00 **Development of FRENDY version 2**
      Dr. Kenichi Tada (Japan Atomic Energy Agency)

  9:30 **For Utilization and Promotion of Covariance Data of Nuclear Data**
      Prof. Go Chiba (Hokkaido University)

Nuclear Data Section Award in 2021 (10:30–12:00)
Chair: Dr. Nobuhiro Shigyo (Kyushu University)
  10:30 **Energy and Angular Distribution of Photoneutron for 16.6 MeV Polarized Photon on Medium-heavy Targets**
      Ms. Kim Tuyet Tran (High Energy Accelerator Research Organization)

  11:00 **Study of Thick Target Neutron Yields from Deuteron- and Triton-induced Reactions at 6.7 MeV/u**
      Mr. Hayato Takeshita (Kyushu University)

  11:30 **Neutron Beam Filter System for Fast Neutron Cross-section Measurement at the ANNRI Beamline of MLF/J-PARC**
      Dr. Gerard Rovira Leveroni (Japan Atomic Energy Agency)

Nuclear and Particle Physics (13:00–14:00)
Chair: Dr. Katsuhisa Nishio (Japan Atomic Energy Agency)
  13:00 **Study of Radii of Proton and Nuclei by Electron Scattering**
      Prof. Toshimi Suda (Tohoku University)

  13:30 **A Nuclear Periodic Table: from Elementouch to Nucletouch**
      Prof. Kouichi Hagino (Kyoto University)

Tutorial 2 (14:20–15:00)
Chair: Dr. Fujio Maekawa (Japan Atomic Energy Agency)
  14:20 **Role of ADS and its Development Issues**
      Dr. Kenji Nishihara (Japan Atomic Energy Agency)

Medical, Isotope Production, and Analysis (15:00–17:00)
Chair: Dr. Hiroki Iwamoto (Japan Atomic Energy Agency)
  15:00 **Production of At-211 Using a Cyclotron and an Import Plan of Ac-225**
      Prof. Mitsuhiro Fukuda (Osaka University)

  15:30 **Production of an Alpha-emitting Radionuclide At-211 for Medical Use at JAEA Tandem Accelerator**
      Dr. Ichiro Nishinaka (National Institutes for Quantum Science and Technology)

  16:00 **Development of the Injector for Heavy-ion Therapy Using Laser-driven Ion Acceleration**
      Dr. Hironao Sakaki (National Institutes for Quantum Science and Technology)

  16:30 **Challenging Studies by Accelerator Mass Spectrometry for the Development of Environmental Radiology**
      Dr. Maki Honda (Japan Atomic Energy Agency)

Closing Address (17:00–17:30)
Dr. Shin-ichiro Meigo (Japan Atomic Energy Agency), Dr. Tadafumi Sano (Kindai University)

2021 Symposium on Nuclear Data - Poster List

No.	Name	Title
1	Gerard Rovira Leveroni (JAEA)	^{241}Am Neutron Capture Cross Section Measurement and Resonance Analysis
2	Yosuke Iwamoto (JAEA)	Calculation of displacement damage dose of semiconductors using PHITS code
3	Kazuki Fujio (Tokyo Tech)	Estimation of fission fragment yields using random-walk models on microscopic mean-field potentials
4	Shoto Watanabe (Hokkaido U)	The Optical Potential for Neutron-nucleus Scattering Derived by Bayesian Optimization
5	Kaoru Hara (Hokkaido U)	Small-angle Scattering Measurements for Cement Paste Samples Using X-rays and Neutrons in Hokkaido University
6	Kazuki Fukui (Osaka U)	Design of a New Shadow Bar to Improve the Accuracy of Benchmark Experiments of Large angle Elastic Scattering Reaction Cross Sections by 14MeV Neutrons
7	Chikara Konno (JAEA)	Problem on Gammas Emitted in Capture Reaction of TENDL-2019 and JEFF-3.3
8	Hiroki Iwamoto (JAEA)	Measurement of 107-MeV Proton-induced Double-differential Neutron Yields for Iron for Research and Development of Accelerator-driven Systems
9	Yaoki Sato (Tokyo Tech)	TOF Measurement of Neutron Capture Cross Section of Re-185 in keV Region
10	Sota Araki (Osaka U)	Benchmark Experiment for Large Angle Scattering Cross Sections for Tungsten with 14 MeV Neutrons
11	Kazuya Shimada (Tokyo Tech)	Energy Dependence of Total Kinetic Energy of Fission Fragments for the Standard and Superlong Modes Analyzed Separately by 4D Langevin Model
12	Yoshihide Iwanaka (Osaka U)	Development of Activation Detector for Ultra-long Term DT Neutron Irradiation
13	Chikako Ishizuka (Tokyo Tech)	Semi-empirical Nuclear Fission Yield Model for Astronomical Use Based on the Four-dimensional Langevin Approach
14	Hiroya Fukuda (Kyushu U)	Development of Counter Telescopes for Light Charged Particles Emitted from Muon Nuclear Reaction on Si
15	Kenta Sugihara (Kyushu U)	Study on JQMD and INCL Models for α Particle Incident Neutron Production
16	Akira Ichihara (JAEA)	Theoretical Evaluation of Neutron Thermal Scattering Laws of Heavy Water for JENDL-5
17	Toru Yamamoto	Study of Thermal Scattering Law of Hydrogen in Water with Analysis of TCA Critical Experiments

18	Riu Nakamoto (Kansai U)	Formulation of a Shell–cluster Overlap Integral with the Gaussian Expansion Method
19	Daisuke Hatano (Osaka U)	Design of Real-time Absolute Epi-thermal Neutron Flux Intensity Monitor with LiCaF Detector
20	Ayano Makinaga (JIFS)	Measurement of $^{nat}In(\gamma, xn)$ Reaction Cross Sections with the 63 MeV Bremsstrahlung
21	Hiroki Matsuda (QST)	Shielding Design for 3 GeV Next Generation Synchrotron Radiation Facility
22	Takahiro Hirayama (Osaka U)	Design and Construction of Epi-thermal Neutron Field with an Am-Be Source for Basic Researches for BNCT
23	Naoya Furutachi (RIST)	Visualization of Nuclear Data Used in PHITS and Utilization of a Tool to Convert EXFOR to PHITS-readable Format

This is a blank page.

2   A Plan of Proton Irradiation Facility at J-PARC and Possibilities of Application to Nuclear Data Research

Fujio MAEKAWA[1*]

[1]J-PARC Center, Japan Atomic Energy Agency

2-4 Shirakata, Tokai-mura, Naka-gun, Ibaraki-ken 319-1195, Japan

[*]Email: maekawa.fujio@jaea.go.jp

The partitioning and transmutation (P-T) technology has promising potential for volume reduction and mitigation of degree of harmfulness of high-level radioactive waste. JAEA is developing the P-T technology combined with accelerator driven systems (ADSs). One of critical issues affecting the feasibility of ADS is the proton beam window (PBW) which functions as a boundary between the accelerator and the sub-critical reactor core. The PBW is damaged by a high-intensity proton beam and spallation neutrons produced in the target, and also by flowing high-temperature liquid lead bismuth eutectic alloy which is corrosive to steel materials. To study the materials damage under the ADS environment, J-PARC is proposing a plan of proton irradiation facility which equips with a liquid lead-bismuth spallation target bombarded by a 400 MeV–250 kW proton beam. The facility is also open for versatile purposes such as soft error testing of semi-conductor devises, RI production, materials irradiation for fission and fusion reactors, and so on. Application to nuclear data research with using the proton beam and spallation neutrons is also one of such versatile purposes, and we welcome unique ideas from the nuclear data community.

1. Introduction

The partitioning and transmutation (P-T) technology has promising potential for volume reduction and mitigation of degree of harmfulness of high-level radioactive waste. Japan Atomic Energy Agency (JAEA) is developing the P-T technology combined with accelerator-driven systems (ADSs). A proton beam of 30 MW and 1.5 GeV is introduced into a subcritical core of the ADS, and thermal power of 800 MW is generated by fission reactions of minor actinides (MA) and other fissile fuel [1, 2]. In the ADS, 2.5 tons of MA are loaded, and 10 % of the MA, which corresponds to the amount of MA generated in 10 units of light water reactors per year, can be transmuted per year.

To facilitate the development, JAEA has proposed Transmutation Experimental Facility (TEF) [3] since 2000 as one of experimental facilities of Japan Proton Accelerator Research Complex (J-PARC). The TEF consists of two individual facilities: ADS Target Test Facility (TEF-T) [4, 5] and Transmutation Physics Experimental Facility (TEF-P) [6]. The TEF-T equips with a spallation target in which liquid lead-bismuth eutectic (LBE) alloy flows. The LBE target is bombarded by a 400 MeV–250 kW proton beam in which ADS's candidate proton beam window (PBW) materials are irradiated to establish a

materials irradiation database. The TEF-P equips with a critical/subcritical assembly to investigate physical and dynamic properties of ADS's sub-critical cores by using a low power proton beam of 10 W at maximum. Nuclear fuel pins containing MA are loaded to the assembly. A technical design report for TEF-T [5] and a safety design report for TEF-P [6] have been published in 2017 and 2018, respectively.

In 2018, JAEA has started reorienting the concept of the experimental facility to make it more attractive and effective by introducing leading edge knowledge to its purposes and specifications [7]. The facility's primary mission stays in challenging one of the most important engineering issues in the ADS development, that is, revealing irradiation and corrosion behavior of PBW materials by proton irradiation under high-temperature LBE flowing. In this sense, the facility is a proton irradiation facility similar to TEF-T. In addition to the primary mission, the facility is also open for versatile purposes such as soft error testing of semi-conductor devises, RI production, materials irradiation for fission and fusion reactors and high-energy accelerator facilities, and so on. Application to nuclear data research with using the proton beam and spallation neutrons is also one of such versatile purposes, and we welcome unique ideas from the nuclear data community.

2. Outline of TEF-T

Since the baseline design of the proton irradiation facility takes over the design of TEF-T, this section briefly explains about TEF-T. As shown in the upper part of Figure 1, a vacuum duct is inserted vertically into an ADS's sub-critical core immersed in LBE to introduce a proton beam provided by an accelerator. The PBW is the end plate of the duct located at the bottom, and is a boundary between high vacuum in the accelerator side and LBE in the reactor core side. The PBW is exposed under very severe environment such as radiation damage due to the proton beam and spallation neutrons, high temperature around 500°C, corrosion and erosion of materials due to LBE, thermal stress and pressure difference between the high vacuum and LBE. Since engineering feasibility of the PBW is one of critical issues for the ADS development, TEF-T is proposed as a materials irradiation facility where the severe ADS environment can be simulated.
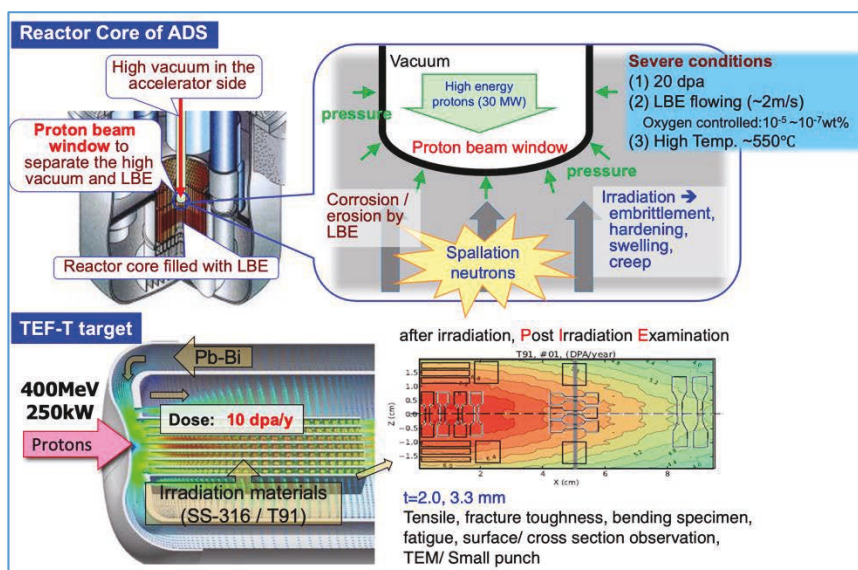
Figure 1 ADS's PBW and proton beam irradiation of the PBW materials at TEF-T

A high-power proton beam of 400 MeV–250 kW is impinged to the LBE target of TEF-T to irradiate

sample materials in the LBE target by the primary protons and spallation neutrons as shown in the lower part of Figure 1. After the irradiation, the sample materials are taken out from the target. Sample specimens are cut out from the irradiated sample materials, and transported to JAEA's PIE facilities, i.e., Reactor Fuel Examination Facility (RFEF) and/or Waste Safety Testing Facility (WASTEF). The sample specimens are then served for post-irradiation examination such as tensile tests and metallographic observation. The TEF-T equips with a hot-cell to yearly exchange the target vessel and to prepare the sample specimens.

TEF-T is a unique facility in the world because three important ADS conditions needed for the material testing can be realized; (1) irradiation dose as high as 10 dpa/y by protons and high energy neutrons, (2) maximum LBE temperature of about 550°C, (3) liquid LBE flowing with controlling oxygen concentration in LBE in a range between $10^{-5} \sim 10^{-7}$ wt% to suppress materials corrosion.

3. Concept of the proton irradiation facility

Figure 2 shows an outline of the proton irradiation facility. The proton irradiation facility takes over the main purpose of the TEF-T that is to obtain materials irradiation data in the ADS environment. Hence the baseline design of the proton irradiation facility is the design of TEF-T. Major revision points of the facility are enhancement of the idea of the multi-purpose use to meet the versatile purposes such as soft-error testing of semi-conductor devises, RI production, materials irradiation for fission and fusion reactors and accelerator facilities, and so on, and the attachment of a full-scale hot-labo.
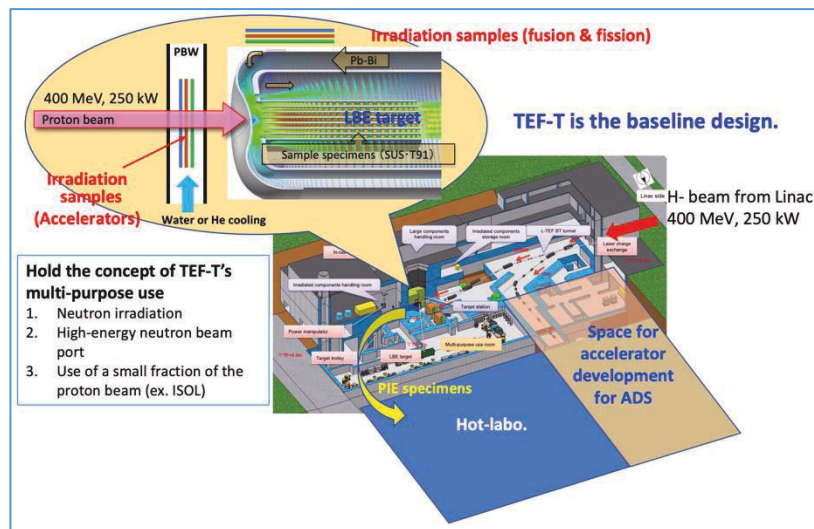
Figure 2 Outline of the proton irradiation facility

3.1. Materials irradiation for various applications

Development of "high-power targets" as well as "high-power accelerators" is of importance for high-power accelerator facilities such as J-PARC. In recent years, along with increasing accelerators' power, their targets including PBW are sometimes rate-controlling steps to increase the beam power. Radiation damage of such target materials is the most crucial factor. Hence the position in front of the LBE target is served for high-power target materials irradiation by the primary protons and spallation neutrons generated in the LBE target.

Needs for irradiation of fusion and fission reactor materials are very high whereas the number of

research reactors dedicated for materials irradiation are decreasing. Actually, it has been decided to shut down the JAEA's Japan Material Testing Reactor (JMTR) [8]. The International Fusion Materials Irradiation Facility (IFMIF) [9] is under development while it takes time to realize it. To satisfy these strong needs for materials irradiation, spaces around the LBE target where neutron flux is very high can be served. The most important parameter to characterize irradiation fields in terms of particles' energy is the ratio of He production to displacement damage (He/dpa ratio). Figure 3 illustrates a map of required irradiation parameters of the He production and displacement damage. Figure 4 shows distributions of the He/dpa ratio around the LBE target. The interior of the LBE target is suitable for high-energy accelerator materials irradiation because the He/dpa ratio is around 100. A question is how to realize the irradiation fields for fusion and fission reactors for which the He/dpa ratios of 10~15 and around 1, respectively, are required. The answer can be found in Figure 4. The He/dpa ratios outside the LBE target vary from over 10 to around 1 with changing angles with respect to the direction of the proton beam. The positions for the forward and backward angles outside the target are suitable for irradiation of fusion and fission reactor materials, respectively. Accordingly, the new facility is capable of irradiating materials for fusion and fission applications in addition to high-energy accelerator facilities including ADS.
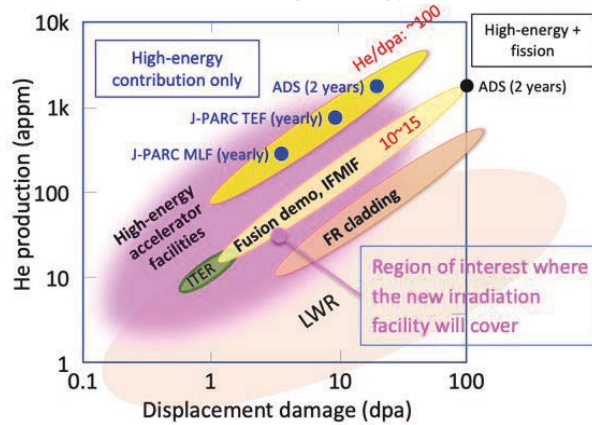
Figure 3 Map of irradiation parameters
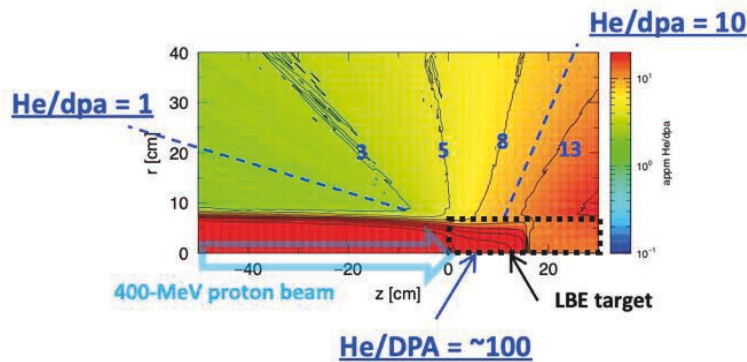
Figure 4 He/dpa ratio around the LBE target

3.2. Soft-error testing of semi-conductor devises

Semiconductor devices are key components to realize the Society 5.0 such as self-driving and IoT while cosmic-ray neutrons can induce soft-errors on semiconductor devices resulting in malfunction of the systems. It is expected that the number of semiconductor devises will increase by 60 times in 20 years. High integration of semiconductor devices enhances effects of soft-errors. However, lack of neutron

irradiation field for testing soft-errors of semiconductor devices is one of serious issues in the world. Under this situation, a neutron irradiation field suitable for the soft-error testing can be realized by using high-energy neutrons produced in the LBE target. As shown in Figure 5, the neutron flux intensity expected in the proton irradiation facility is as at least 10 times high as the existing facilities. Owing to the high flux intensity, testing time can be shortened to less than 1/10. Thus the facility can contribute to realize the Society 5.0, and strengthen the international competitiveness of semiconductor devices produced in Japan.

3.3. RI production

Many kinds of radioactive isotopes (RIs) can be produced by spallation reactions induced by high-energy protons. Needs for medical RIs, especially α-emitters such as ^{225}Ac for prostate cancer, are increasing in recent years. Production of ^{225}Ac ($T_{1/2}$ = 9.92 d) by high-energy proton reactions has been demonstrated at the TRIUMF facility in Canada [10]. They utilized the ^{232}Th(p, x)^{225}Ra reactions induced by the 438 MeV protons, and chemically extracted ^{225}Ac which was the decay product of ^{225}Ra ($T_{1/2}$ = 14.9 d). By referring the TRIUMF's result, how much ^{225}Ac can be produced in the proton irradiation facility was estimated with the following assumptions: a 10 mm thick ^{232}Th target, use of 10 % of full beam (400 MeV, 25 kW), 2 weeks irradiation for one cycle, and 12 cycles per year. As a result, it was found that about 80 GBq of ^{225}Ac could be produced per year. This amount is almost equivalent to the annual amount of ^{225}Ac currently in circulation in the world.
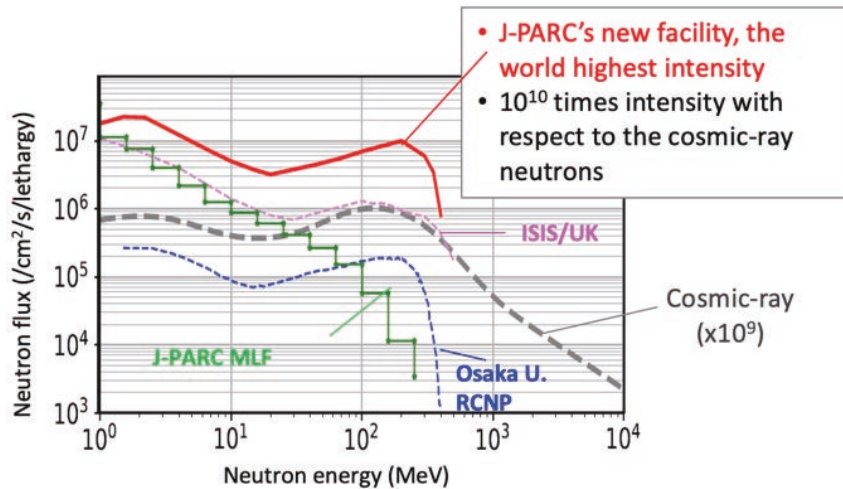
Figure 5 Comparison of neutron flux intensities
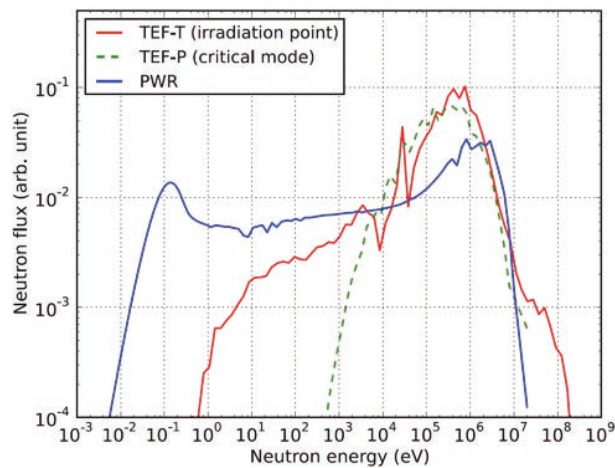
Figure 6 Neutron spectra at TEF-T and other facilities

3.4. RI beam by ISOL

The RIs are also crucial for fundamental physics research. As one of multi-purpose uses of TEF-T, a plan of heavy-ion science which would be realized by producing a radioactive beam created in the proton-induced reactions was proposed. The central framework for the RI production was based on the Isotope Separation On-Line (ISOL). The TEF-T ISOL is described in detail in the report [5].

3.5. Hot-labo

The idea of TEF-T is to irradiate sample materials with the proton beam, and once they are irradiated, the materials are transported to the JAEA's hot-labo facilities for post-irradiation examination (PIE). Although this method utilizes the existing hot-labo facilities efficiently, it is not always suitable because of the following two reasons: the transportation of irradiated samples is inefficient in time and cost, and the JAEA's hot-labo facilities are rather old as they are built more than 40 years ago. Furthermore, although there are many high-intensity accelerator facilities in the world, facilities in which PIE is possible are scarce. Hence, it is desirable to furnish the new facility with a hot-labo. The hot-labo can be used for PIE of the sample materials irradiated in the facility, and also it can accept irradiated materials from the existing J-PARC's experimental facilities, and so on. Accordingly, the new facility can contribute not only to the ADS development but also to upgrading and enhancing safety and efficient operation of the J-PARC's existing facilities.

4. Specification of the facility for the versatile needs

This section summarizes specifications of the facility for the versatile needs.

Proton beam
- Energy: 400 MeV
- Peak current: 50 mA (would be upgraded to 60 mA)
- Pulse width: 500 μs (would be upgraded to 600 μs)
  Short width pulses, several ns for example, can be separated from the 500-μs long width pulses by using the laser charge exchange method [11] but with the peak current unchanged.
- Beam power: 250 kW (would be upgraded to 360 kW)
- Repetition rate: 25 Hz

Neutron field

- High-energy neutron beam port at 8 m from the LBE target, ϕ: 2×10^7 [n/cm^2/s] (Figure 5)
- Irradiation position at 30 cm from the LBE target, ϕ_{fast}: 7×10^{12} [n/cm^2/s], $\phi_{>20\,\text{MeV}}$: 3×10^{10} [n/cm^2/s], spectrum shown in Figure 6

5. Summary

To study the materials damage under the ADS environment, J-PARC is proposing a plan of the proton irradiation facility which equips with the LBE spallation target bombarded by the 400 MeV–250 kW proton beam. The facility is also open for versatile needs such as soft-error testing of semi-conductor devises, RI production, materials irradiation for fission and fusion reactors and high-energy accelerator facilities, and so on. Application to nuclear data research with using the proton beam and spallation neutrons is also one of such versatile needs, and we welcome unique ideas from the nuclear data community.

References

1) K. Tsujimoto, et al. Neutronics Design for Lead-Bismuth Cooled Accelerator-Driven System for Transmutation of Minor Actinide, J. Nucl. Sci. Technol., 41, pp. 21-36 (2004).
2) T. Sugawara, et al. Research and development activities for accelerator-driven system in JAEA, Progress in Nuclear Energy, 106, pp. 27-33 (2018).
3) The Joint Project Team of JAERI and KEK: "The Joint Project for High-Intensity Proton Accelerators", JAERI-Tech 2000-003 (2000) (in Japanese).
4) F. Maekawa, et al. J-PARC Transmutation Experimental Facility Program, Plasma and Fusion Research, 13, 2505045 (2018).
5) Nuclear Transmutation Division of J-PARC Center, JAEA: "Technical Design Report on J-PARC Transmutation Experimental Facility - ADS Target Test Facility (TEF-T) -", JAEA-Technology 2017-003 (2017).
6) Partitioning and Transmutation Technology Division, of Nuclear Science and Engineering Center, JAEA: "Safety Design Report on J-PARC Transmutation Physics Experimental Facility (TEF-P)", JAEA-Technology 2017-033 (2018) (in Japanese).
7) F. Maekawa, A Plan of Materials Irradiation Facility at J-PARC for Development of ADS and High-power Accelerator Facilities, JPS Conf. Proc. 33, 011042 (2021).
8) JMTR Site: https://www.jaea.go.jp/04/o-arai/en/research/research_02.html (accessed 2022-1-5).
9) IFMIF Site: http://www.ifmif.org (accessed 2022-1-5).
10) Andrew K. H. Robertson, et al., ^{232}Th-Spallation-Produced ^{225}Ac with Reduced ^{227}Ac Content, Inorg. Chem. 59, pp. 12156-12165 (2020).
11) H. Takei, et al., Beam Extraction by the Laser Charge Exchange Method Using the 3-MeV LINAC in J-PARC, Plasma and Fusion Research 13, pp. 2406012-1 - 2406012-6 (2018).

Acknowledgements

This is a blank page.

3 Status and prospects on light sterile neutrino searches

Takasumi Maruyama on behalf of JSNS^2 and JSNS^2-II collaborations[1]

^{1}KEK, IPNS, 1-1 Oho, Tsukuba, Ibaraki, Japan
†Email: takasumi.maruyama@kek.jp

Abstract

The search for sterile neutrinos is one of the hottest topics in neutrino physics in this decade.

JSNS^2 (J-PARC Sterile Neutrino Search at the J-PARC Spallation Neutron Source) and the second phase of the experiment JSNS^2-II aim to search for neutrino oscillations with Δm^2 near 1 eV^2 at the J-PARC Materials and Life Science Experimental Facility (MLF). With the 1 MW of 3 GeV proton beam created by Rapid Cycling Synchrotron (RCS) and spallation neutron target, an intense neutrino beam from muon decay at rest is available. Neutrinos come predominantly from μ^+ decay: $\mu^+ \rightarrow e^+ + \bar{\nu}_\mu + \nu_e$. The oscillation searched for is $\bar{\nu}_\mu$ to $\bar{\nu}_e$, which is detected via the inverse beta decay interaction $\bar{\nu}_e + p \rightarrow e^+ + n$, followed by gammas from neutron capture of Gd. The JSNS^2 detector (and the near detector in the JSNS^2-II) with a fiducial volume of 17 tonnes is located 24 m away from the mercury target. The new far detector of the JSNS^2-II that is being newly constructed is located outside the MLF building with the baseline of 48 m. This far detector has a 32 tonnes of the fiducial volume. These experiments directly test the LSND anomaly.

Additional physics programs include the cross section measurements with neutrinos with order 10 MeV from muon decay at rest and with monochromatic 236 MeV from kaon decay at rest. These are important for the potential observation of a supernova explosion using neutrinos and nuclear physics.

JSNS^2 started data taking in 2020 and the accumulated Proton-On-Target (POT) is 1.45×10^{22}. The far detector of JSNS^2-II is under the construction. This article describes the status of these experiments.

1 Introduction

The Nobel Prize in 2015 was awarded for the discovery of neutrino oscillations in 1998 [1]. However, there are still a lot of things to be investigated in oscillation phenomena and the one of the hottest topics is to decisively confirm or refute of the existence of the sterile neutrinos with neutrino oscillations.

The existence of the sterile neutrinos was indicated by the Liquid Scintillator Neutrino Detector (LSND) experiment originally in 1998 [2]. They have no weak interaction, thus they are only sensitive to the gravity.

However, there have been no final conclusions from experiments so far, especially some other indications are shown to be in contradiction with LSND [3, 4, 5]. Many ongoing experiments have continued the search recently. For these other experiments, please refer to other references, for example [6].

JSNS^2 [7] (J-PARC Sterile Neutrino Search using J-PARC Spallation Neutron Source) will make a direct test of the LSND result. Also the new detector of the next phase of the

experiment, JSNS^2-II [8], using two detectors with different baselines, is under construction. This article briefly explains the current status of both JSNS^2 and JSNS^2-II.

2 Setup and principle of the experiments

Figure 1 shows the setup and sensitivities of the experiments. 3 GeV protons hit the mercury target and the collisions create the pure $\bar{\nu}_\mu$ via μ^+ decay-at-rest. The neutrino oscillation ($\bar{\nu}_\mu \to \bar{\nu}_e$) is studied using two liquid scintillator detectors at two short baselines: 24 m and 48 m.

The current JSNS^2 experiment has 50 tonnes of liquid scintillator detector and is located on the third floor of the MLF. This includes 17 tonnes of Gd loaded liquid scintillator (Gd-LS) inside an inner acrylic tank. JSNS^2 is taking data and it will accumulate POT, which corresponds to 1 MW (beam power) × 3 years. This detector will also be used as the near detector of JSNS^2-II after the designed JSNS^2 POT has been reached. The JSNS^2-II experiment adds 163 tonnes of liquid scintillator detector outside of the MLF building. This includes 32 tonnes of the Gd-LS inside an inner acrylic tank. JSNS^2-II aims to start data taking from 2023. Using two different
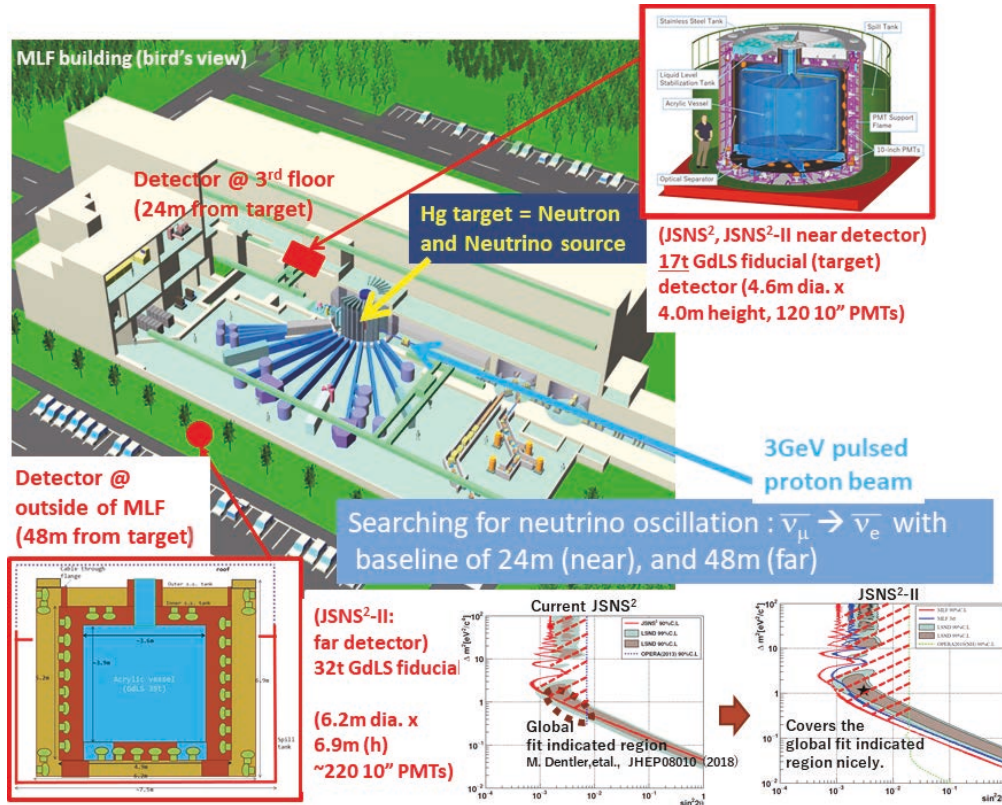
Figure 1: The setup and the sensitivities of the JSNS^2 and JSNS^2-II experiments.

baselines, the neutrino oscillation and therefore the LSND anomaly will be investigated directly. JSNS^2-II provides a better sensitivity in the low Δm^2 region than that of the current JSNS^2, as shown in the bottom two plots in Fig. 1. The new far detector therefore is essential in the investigation of the LSND anomaly.

If the $\bar{\nu}_\mu \to \bar{\nu}_e$ oscillation or conversion occurs, this will be observed via the Inverse-Bata-Decay (IBD) reaction in the Gd-LS: $\bar{\nu}_e + p \to e^+ + n$. The resulting neutron is thermalized and captured by Gd, and the coincidence with the signals between IBD prompt (e^+) and delayed

(n-Gd) can be detected. Using this coincidence eliminates most of the accidental background.

MLF has an excellent short-pulsed beam profile: two bunches with 100 ns width and separated by 600 ns. The frequency of the repetition of these two bunches is 25 Hz. To reduce the cosmic ray-induced and beam-related backgrounds, this timing structure is ideal.

Compared to the LSND experiment, the low duty factor beam and Gd-LS are strong advantages (LSND used a Linac beam with a poor duty factor and pure liquid scintillator). JSNS^2 and JSNS^2-II will have a smaller accidental background rate and therefore JSNS^2(-II) will be a direct and ultimate test for the LSND anomaly.

3 Current status

3.1 JSNS^2

JSNS^2 started data taking from 2020. The accumulated POT is 1.45×10^{22} POT, which corresponds to approximately 13% of the designed POT.

The analysis of the accumulated date is on-going. As shown in the recent paper [9], the neutron background induced by cosmic rays is the dominant background for the JSNS^2. To address this, JSNS^2 dissolved 10% Di-Isopropyl-Naphthalene (DIN) by weight into the Gd-LS in 2020-2021. DIN will improve the Pulse-Shape-Discrimination (PSD) power between neutrons and positrons and thus help to reduce any accidental coincidences due to the cosmic ray induced background.

As a result of the DIN dissolution, the neutron rejection power is 97.4±0.5%, while the positron efficiency is 94.2±2.6% in the detector central region (Fig. 2). The goal of the neutron
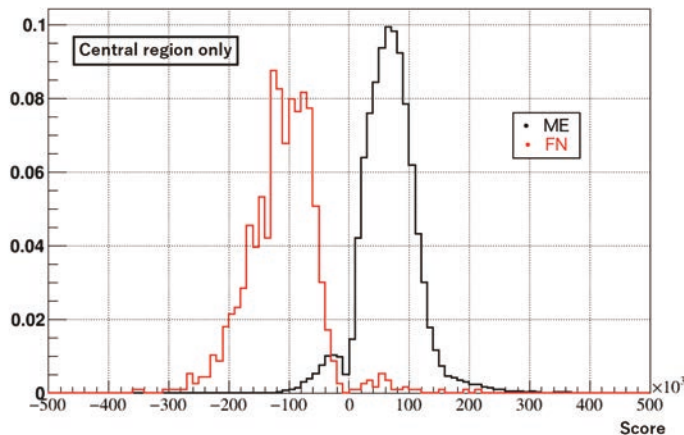
Figure 2: The Pulse Shape Discrimination (PSD) capability of the JSNS^2. The black graphs shows Michel electrons (ME) and the red shows fast neutrons (FN). The events with scores above zero correspond to "electron-like" and those below zero correspond to "neutron-like".

rejection factor is ∼100 and therefore we are achieving the good PSD capability which is near to the goal. Note that the rejection factor and the efficiency are estimated by the Michel electron made by stopped muons inside the detector and the fast neutrons control sample. Currently, the impurity inside the control samples is being estimated.

In addition to the sterile neutrino search, the events created by the monochromatic 236 MeV from kaon decay-at-rest (KDAR) are being studied. KDAR neutrinos provide quasi-elastic interactions inside the Gd-LS, resulting in a sequence of scintillation light events from the muon

and proton (the prompt signal) to the Michel electron created from the prompt muon (the delayed signal). A detailed analysis is on-going.

The next physics run will start in February 2022. The JSNS^2 collaboration is currently preparing for the data taking.

3.2 JSNS^2-II

The construction of the new far detector was started in September 2021, and being performed smoothly. Figure 3 shows the status of the construction of the stainless steel (s.s.) tank. The

Figure 3: The status of s.s. tank construction of the JSNS^2-II as of 17 December 2021. The inner s.s. tank can be seen in the back, while the base of the detector and the support structure of the outer s.s. tank can be seen in the front.

base, the support structure and the inner s.s. tank have already been produced and the outer s.s. tank for the veto region is being built at present. The construction of the s.s. tank will be completed by March 2022.

The acrylic tank will be produced in 2022. The liquid scintillator and Gd-LS were already donated by the Daya-Bay experiment [10]. Thirty Photo-Multiplier-Tubes (PMTs) will be donated from the Double-Chooz experiment [11]. The remaining ∼180 PMTs will be purchased from Hamamatsu company or donated from Double-Chooz further. The installation of the PMTs will be completed in 2022.

Most of the construction schedule follows the original schedule in the reference [8]. The data taking will start in 2023.

4 Summary

JSNS^2 is directly testing the LSND anomaly using the same neutrino source, the neutrino target and the detection principle (IBD). The JSNS^2-II will continue this test with higher precision. JSNS^2 has accumulated data corresponding to $1.45{\times}10^{22}$ POT. The data is extensively being analyzed. The new far detector of JSNS^2-II is being built at present. The construction is progressing smoothly and the data taking will start in 2023.

References

[1] Y. Fukuda et al., *Evidence for oscillation of atmospheric neutrinos, Phys. Rev. Lett.* **81** (1998) 1562.

[2] A. Aguilar et al., *Evidence for neutrino oscillations from the observation of $\bar{\nu}_e$ appearance in a $\bar{\nu}_\mu$ beam, Phys. Rev. D* **64** (2001) 112007.

[3] A. A. Aguilar-Arevalo et al., *Significant Excess of ElectronLike Events in the MiniBooNE Short-Baseline Neutrino Experiment, Phys. Rev. Lett.* **121** (2018) 221801.

[4] C. Giunti and M. Laveder, *Statistical significance of the gallium anomaly, Phys. Rev. C* **83** (2011) 065504.

[5] Th. A. Mueller et al.. *Improved predictions of reactor antineutrino spectra, Phys. Rev. C* **83** (2011) 054615.
    P. Huber, *Determination of antineutrino spectra from nuclear reactors, Phys. Rev. C* **84** (2011) 024617.

[6] M. Dentler, et al., *Updated global analysis of neutrino oscillations in the presence of eV-scale sterile neutrinos*, arXiv:1803.10661.

[7] M. Harada, et al., *Proposal: A Search for Sterile Neutrino at J-PARC Materials and Life Science Experimental Facility*, arXiv:1310.1437.
    S. Ajimura, et al., *Technical Design Report (TDR): Searching for a Sterile Neutrino at J-PARC MLF (E56, JSNS2)*, arXiv:1705.08629.
    S. Ajimura, et al., *The JSNS^2 detector, Nucl. Inst. Meth. A* **1014** (2021) 165742.

[8] A. Ajimura et al., *Proposal: JSNS^2-II*, arXiv:2012.10807.

[9] Y. Hino et al., *Characterization of the correlated background for a sterile neutrino search using the first dataset of the JSNS^2 experiment*, arXiv:2111.07482.

[10] Y. Ding et al., *A new gadolinium-loaded liquid scintillator for reactor neutrino detection, Nucl. Inst. Meth. A* **584** (2008) 238.

[11] Y. Abe et al., *Indication of Reactor $\bar{\nu}_e$ Disappearance in the Double Chooz Experiment, Phys. Rev. Lett.* **108** (2012) 131801.

Acknowledgments

This is a blank page.

4　Outline of JENDL-5

Osamu Iwamoto[*]

Nuclear Data Center, Japan Atomic Energy Agency

2-4 Shirakata, Tokai-mura, Naka-gun, Ibaraki 319-1195, Japan

[*]Email: iwamoto.osamu@jaea.go.jp

The latest version of Japanese Evaluated Nuclear Data Library, JENDL-5, was released in December 2021. JENDL-5 was developed to meet the needs of various fields including nuclear energy and accelerator application. The neuron reaction data of JENDL-5 were largely improved and increased from the previous version JENDL-4.0. In addition to the neutron data, the various data in the JENDL special purpose files were integrated into JENDL-5. In this paper, the outline of JENDL-5 is described.

1. Introduction

The first version of Japanese Evaluated Nuclear Data Library (JENDL-1)[1] aiming at fast reactor development was released in 1977. Since then, the neutron induced reaction data were continuously updated in the general-purpose files[2] to improve accuracies of neutronics calculation for nuclear reactors including thermal and fast reactors and also fusion reactors. For other applications, various kinds of data files were developed and released as special-purpose files since 1991. The release history of the JENDL general and special purpose files is shown in Fig. 1. Before 2000, the special-purpose files focused on neutron induced reaction cross sections for dosimetry and activation that were not provided by the general-purpose files. In contrast, after 2000 the files were extended to charged-particles and photon induced reactions. Those energy range including for neutron increased up to around 200 MeV for high energy accelerators. So far, may special-purpose files have been released but they sometimes arise problems in the consistencies between the general and special purpose files.

More than 10 years had already passed since the release of JENDL-4.0[3] in 2010 and large amounts of experimental data have been accumulated. The JENDL-5 project was launched to develop a new general-purpose file that covered over not only nuclear reactors but also accelerator applications by merging the special purpose files; it also targeted to update the data with reflecting current experimental and theoretical knowledge of nuclear data. In addition to the reaction data, fission yields and decay data were also newly evaluated using available experimental data with theoretical models. For the first time in the JENDL development, thermal scattering law data were originally evaluated for many materials including light and heavy water. For charged particles such as proton, deuteron, alpha-particle, and photon, the data of the special purpose files were integrated into JENDL-5 with improving the data. Since the alpha-particle induced reaction data in JENDL/AN-2005[4] contain only neutron-emission related data, the data needed for radiation transportation calculations were complemented. Regarding neutron induced reaction, in addition of the incident energy extension, the neutron cross sections were also integrated with the activation data of JENDL/AD-2017[5].
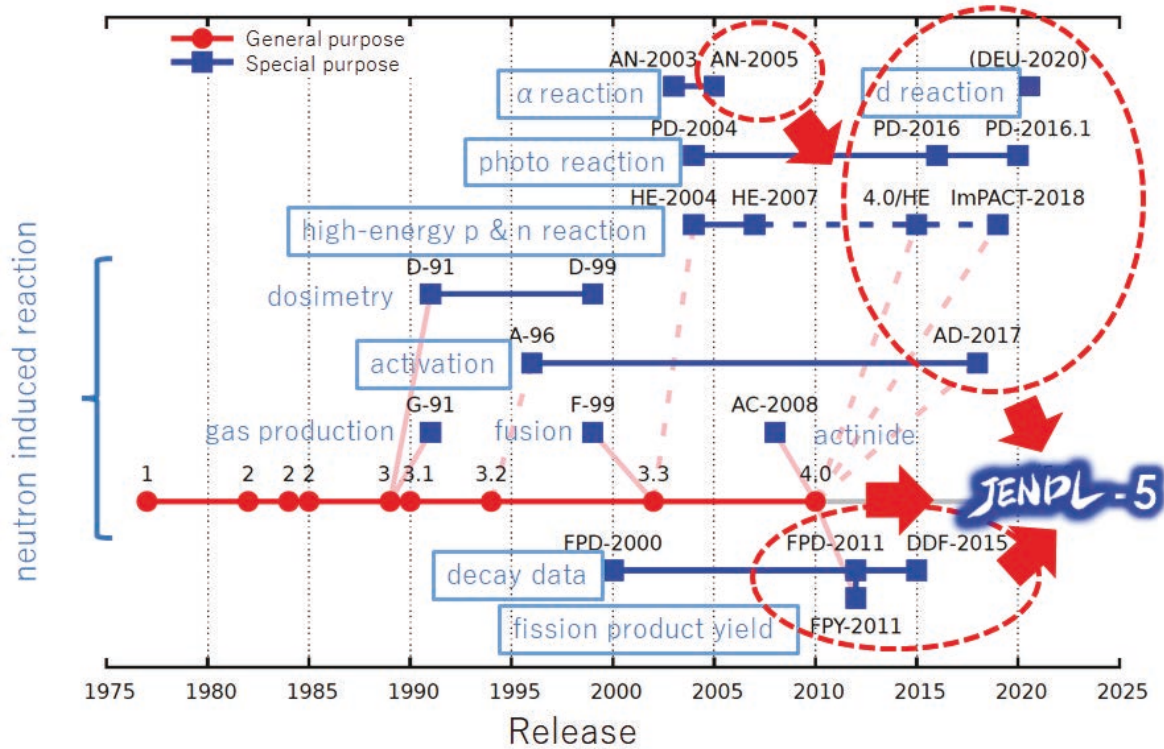
Fig. 1. Release history of the JENDL general and special purpose files. The data types are indicated by light-blue letters and the boxed ones are integrated into JENDL-5.

JENDL-5 was released in December 2021; it consists of sublibraries of neutron reaction, proton reaction, deuteron reaction, alpha-particle reaction, photo-nuclear reaction, fission product yield, decay data, thermal scattering law, photo-atomic, electro-atomic, and atomic relaxation. In this article, outline of JENDL-5 and some of the evaluated data are described.

2. Neutron reaction sublibrary

The neutron reaction sublibrary provides the data of various reactions, the secondary particle emission, and residual nucleus production for neutron induced reactions on 795 nuclides from H to Fm isotopes. The number of the nuclides became almost double of 406 as of JENDL-4.0. They include all of stable isotopes and a large number of unstable isotopes that are considered as much enough for various kinds of radiation simulations. The upper energy limit of incident energy was extended to 200 MeV (partially 20 MeV) by merge of JENDL-4.0/HE[6] and JENDL/ImPACT-2018[7] and by new evaluations. The activation related data such as isomer productions, which were provided in special purpose files so far, were also merged into JENDL-5.

The revisions of cross sections in JENDL-4.0 were carried out across from light to heavy nuclei including important data for nuclear reactors. Main points in the revision of major actinide data are listed below:

- the resolved resonance parameters of ENDF-B/VIII.0 (CIELO-1) for $^{235, 238}$U and ^{239}Pu were adopted with modifications
- fission cross sections for fast neutrons were fully updated for $^{233, 235, 238}$U, and $^{239, 240, 241}$Pu with the new SOK evaluation taking into accounts recent experimental data with extending the energy upper
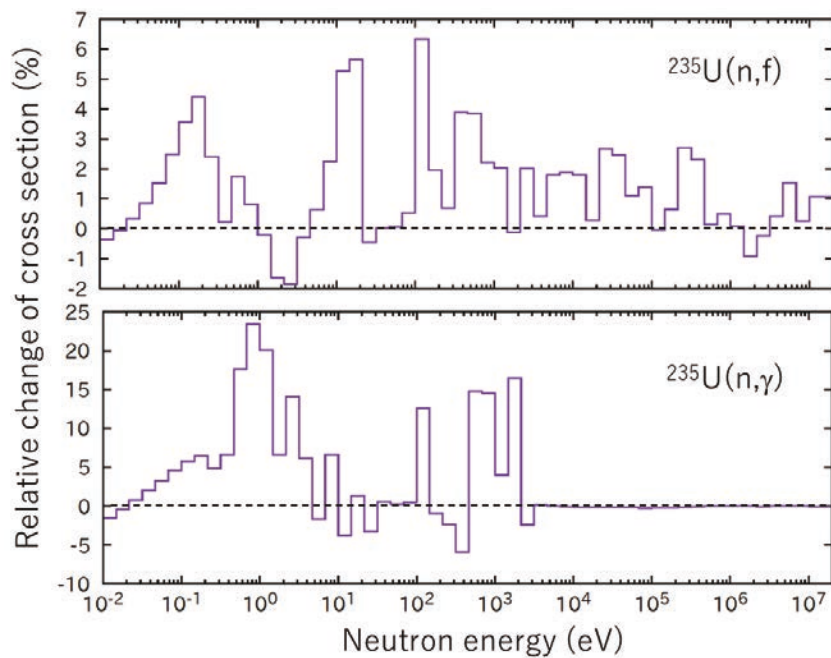
Fig. 2. Relative change of group-wise cross sections from JENDL-4.0 for fission and neutron capture

    limit to 200 MeV
- the fission neutron spectra below 5 MeV for ^{235}U were evaluated by fitting with the Los Alamos model to the experimental data
- the fission neutron multiplicities were revised taking into accounts both differential experimental data and integral benchmark testing
- the minor adjustments of fission and capture cross sections were made with the results of integral benchmark tests of fast reactors

The cross-section variations from JENDL-4.0 in group averages for ^{235}U fission and capture reactions are shown in Fig. 2. JENDL-5 adopted the resonance parameters of ENDF/B-VIII.0 which was based on the new experimental data of neutron capture cross sections. The fission cross section above 10 keV is the new evaluation by SOK. While thermal values are almost the same values as JENDL-4.0, the fission cross sections are changed by several % over wide energy region and capture cross section in resonance region also shows larger variation. After the release of JENDL-4.0, neutron capture cross sections for minor actinides were actively measured with ANNRI at J-PARC. The resonance parameters of ^{237}Np, ^{241,243}Am and ^{244,246}Cm were updated with the results of those data.

    Revisions of the data for structure materials and light nuclei were one of the main targets of JENDL-5. Many nuclides including isotopes of C, N, O, F, Na, Ne, Ti, Cr, Mn, Fe, Co, Ni, Zn, Zr, Nb, Sn, Ho, Lu, Re, Ir, Pt, Tl, Po, Rn, Pb etc. were revised or newly evaluated. The newly developed R-matrix resonance analysis code AMUR was applied to the evaluation for the light nuclei such as C, N, O, F, and Na isotopes. Above the resonance region, the nuclear reaction model code CCONE were widely used for evaluation of the various reaction cross sections and the spectrum of secondary particle emissions. JENDL-5 provides isomer production cross sections that is needed for evaluations of neutron activation of materials. Figure 3 shows the results of ^{58}Ni(n,p) reaction that were evaluated consistently for total
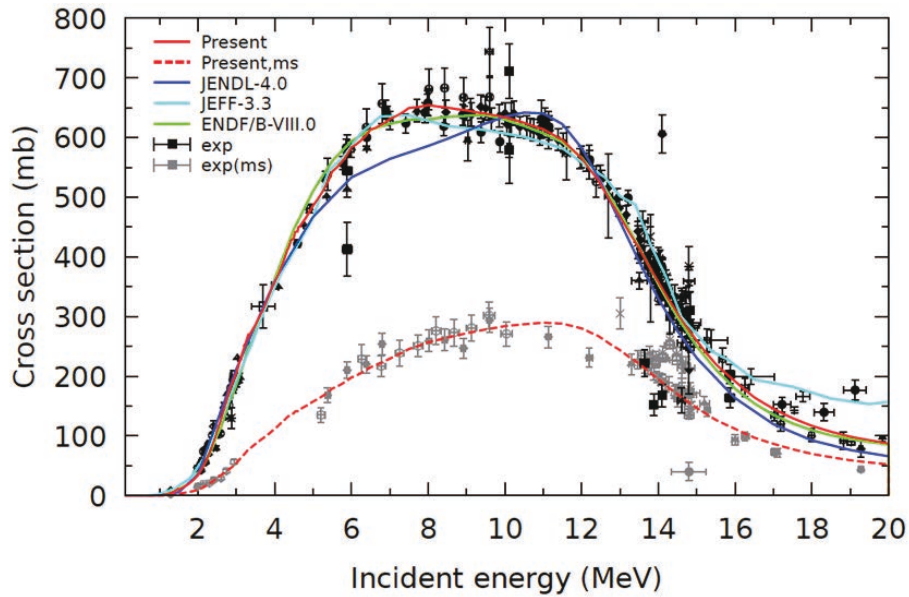
Fig. 3. Cross sections of ^{58}Ni(n,p) reaction for total reaction and isomer productions. Evaluated results of JENDL-5 are shown by red solid and dashed lines for total and isomer production, respectively.

reaction and isomer productions, showing good agreement with available experimental data.

3. Other sublibraries

Neutron thermal scattering law data are important for thermal nuclear reactors. However, original evaluations were not performed in Japan so far. For the first time in JENDL, JENDL-5 included new original evaluated data of H_2O, D_2O, methane, mesitylene, benzene, etc. that were obtained using molecular dynamics simulations[8,9]. In addition, by adopting evaluated data of ENDF/B-VIII.0 and JEFF-
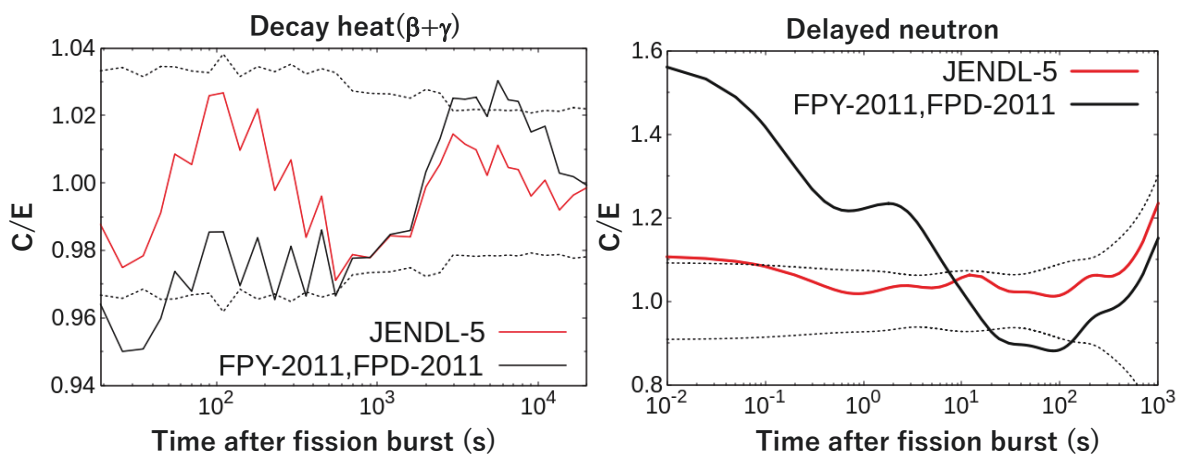
Fig. 4. Calculated results with fission yield and decay data for the decay heat for ^{235}U (left panel) and for the delayed neutron (right panel). The results are shown as ratios to the experimental data measured at YAYOI reactor for the decay heat and to the fitted value by Keepin et al. for the delayed neutron. Doted lines indicate experimental uncertainties.
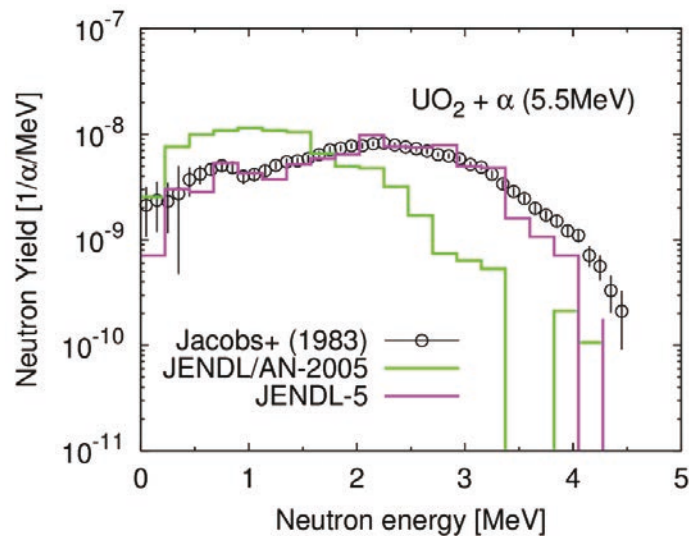
Fig. 5. Results of PHITS calculation for neutron yields form a UO_2 thick target for 5.5 MeV alpha-particle irradiation with JENDL-5 and JENDL/AN-2005.

3.3, JENDL-5 provides the data for 62 elements (37 materials) in total in the thermal scattering law sublibrary.

The fission product yield sublibary is based on the evaluation by Tsubakihara et al. They are evaluated with large amounts of the available experimental data and theoretical aspects on nuclear structure using statistical estimation with physical consistency[10]. Their covariance data were also provided as a part of JENDL-5.

The decay data sublibrary consists of 4,071 nuclides including neutron and nuclei from H-1 (Z=1) to Og (Z=118). The data were created by adopting the data of Evaluated Nuclear Structure Data File (ENSDF)[11] with complementing the total absorption gamma-ray spectroscopy (TAGS)[12] data, the theoretical model calculations, etc. Figure 4 shows the results of summation calculation of decay heat and delayed neutron with fission product yield and decay data sublibraies. While the results of delayed neutron data with JENDL/DDF-2011 and JENDL/FPY-2011 largely overestimates the data of Keepin et al.[13], which was obtained by fitting to the experimental, the result of JENDL-5 agree with it in the whole-time region with showing also good agreement for the decay heat.

JENDL-5 integrated charged particle (proton, deuteron and alpha-particle) and photon induced reaction data that were released as the special purpose files so far. The revision and addition of stored data were also made. Among the charged particle data, the alpha-particle induced reaction data, which were released as JENDL/AN-2005[4], were largely improved by adding the necessary data for particle transportation calculation and by updating emission spectrum taking into accounts new theoretical calculation with CCONE. Figure 5 shows neutron yields from a UO_2 thick target for 5.5 MeV alpha-particle irradiation. The calculated result with JENDL-5 was largely improved from JENDL/AN-2005.

4. Summary

The developed JENDL-5 has the next features: (1) increase of the number of nuclei (795) for neutron reaction data with complete isotopes in natural abundance, (2) revision of large amount of nuclear data taking into accounts up-to-date knowledge from light to heavy nuclei, (3) adoption of the first original evaluation of neutron thermal scattering law in Japan, (4) integration of special purpose files of neutron-

induced activation and high energy reactions, (5) addition of recoil spectra with newly developed method, (6) integration of the data for the proton, deuteron, alpha-particle, photon induced reactions. JENDL-5 was released in December in 2021 and the data are available at the web site of JAEA: https://wwwndc.jaea.go.jp/jendl/j5/j5.html.

References

1) Igarashi, S. et al., Japanese Evaluated Nuclear Data Library, Version-1 – JENDL-1 –, JAERI 1261, 1979, 206p.

2) Shibata, K., JENDL: Nuclear databases for science and technology, J. Nucl. Sci. Technol., vol. 50, no. 5, 2013, pp. 449-469.

3) Shibata, K., JENDL-4.0: A New Library for Nuclear Science and Engineering, J. Nucl. Sci. Technol., vol. 48, no. 1, 2013, pp. 1-30.

4) Murata, T., Matsunobu, H., Shibata, K., "Evaluation of the (α,xn) Reaction Data for JENDL/AN-2005", JAEA-Research 2006-052.

5) Shibata, K., Iwamoto, N., Kunieda, S., Minato, F., Iwamoto, O., "Activation Cross-section File for Decommissioning of LWRs" JAEA-Conf 2016-004, pp.47-52.

6) Kunieda, S. et al., "Overview of JENDL-4.0/HE and benchmark calculation" JAEA-Conf 2016-004, pp. 41-46.

7) Kunieda, S. et al., JENDL/ImPACT-2018: A New Nuclear Data Library for Innovative Studies on Transmutation of Long-lived Fission Products, J. Nucl. Sci. Technol., vol. 56, 2019, pp.1073-1091.

8) Abe, Y., Tsuboi, T., Tasaki, S., Evaluation of the neutron scattering cross-section for light water by molecular dynamics, Nucl. Instrum. Methods. Phys. Res. A, vol. 735, 2014, pp. 568-573.

9) Ichihara, A., Survey of Computational Methods of Cross Sections for Thermal Neutron Scattering by Liquids, JAEA-Review 2019-046, 2020, 36p.

10) Tsubakihara, K. et al., Evaluation of fission product yields and associated covariance matrices, J. Nucl. Sci. Technol., vol. 58, no. 2, 2021, pp. 151-165.

11) ENSDF database as of October 4, 2019 at http://www.nndc.bnl.gov/ensarchivals/.

12) Algora, A, et al., Beta-decay studies for applied and basic nuclear physics, Eur. Phys. J. A, vol. 57 2021, article no. 85.

13) Keeping, G.R., Wimett, T.F., Zeigler, R.K., "Delayed Neutrons from Fissionable Isotopes of Uranium, Plutonium, and Thorium", Rphys. Rev. vol. 107, 1957, pp. 1044-1049.

Acknowledgements

5 Integral Tests of Preliminary JENDL-5 for Critical and Shielding Experiments

Yasunobu NAGAYA[1*], Kenji YOKOYAMA[1], Kenichi TADA[1] and Chikara KONNO[1]

[1]Japan Atomic Energy Agency

2-4 Shirakata, Tokai-mura, Naka-gun, Ibaraki-ken 319-1195, Japan

[*]Email: yasunobu.nagaya@jaea.go.jp

The latest version of Japanese Evaluated Nuclear Data Library, JENDL-5, is planned to be released in 2021. To this end, we have performed integral tests of JENDL-5β3 update 1 for critical and shielding experiments. We have confirmed that JENDL-5β3 update 1 gives better than or the same prediction accuracy as JENDL-4.0 in many test cases for the critical and shielding experiments.

1. Introduction

The latest version of Japanese Evaluated Nuclear Data Library, JENDL-5, is planned to be released in 2021. To this end, we have performed integral tests of preliminary versions (4 alpha versions and 3 beta versions) of JENDL-5 since 2018. In this presentation, we show the integral test results of JENDL-5β3 update 1 (J5b3u1) for critical and shielding experiments. The test results for critical experiments include three parts: 1) small-sized fast systems and intermediate-spectrum systems, 2) middle- and large-sized fast systems, and 3) thermal-spectrum systems. The test calculations for the first and third parts were done for experiments mainly in the International Criticality Safety Benchmark Evaluation Project (ICSBEP) handbook[1] and conducted at JAEA. The test calculations for the second part were done for integral experiments used for generation of the unified cross section data set of ADJ2017.[2] The shielding benchmark tests were done mainly for FNS experiments at JAEA and OKTAVIAN experiments. We have confirmed that J5b3u1 gives better than or the same prediction accuracy as JENDL-4.0[3] (J40) in many test cases for the critical and shielding experiments.

2. Integral Tests for Critical Experiments

2.1. Small-sized Fast Systems and Intermediate-spectrum Systems

At first, we performed integral tests for small-sized fast systems and intermediate-spectrum systems to investigate the impact of major heavy nuclides of U-233, U-235, U-238, and Pu-239. Monte Carlo calculations with the MVP code[4] were performed; the total number of histories is 2.1 million, the number of histories per batch is 10,000, and the number of skipped batches is 100. Figure 1 shows the C/E values of criticality for heavy-metal loaded systems. Reflectors are natural or depleted uranium for the reflected systems except for MMF1-1 and THOR; their reflectors are high-enriched uranium and Th-232, respectively. Obviously, J5b3u1 gives the better results than J40.

2.2. Middle- and Large-sized Fast Systems

We also performed integral tests for middle- and large-sized fast systems. These test calculations were done for the experimental database of fast reactor core design, which was used for generation of the unified cross-section set ADJ2017.[2] In the database, more than 600 experimental data are included. To get the test results quickly, we adopted sensitivity analysis and selected 11 experiments from the database, which represent major and important nuclear characteristics for fast reactors. Specifically, the following experiments are selected: criticality, sodium void reactivity (SVR), and control rod worth (CRW) of MOX core (ZPPR-9 and ZPPR-10A); criticality and SVR of U-

Fig. 1 C/E values of criticality for heavy-metal loaded systems.

*Error bars show the experimental uncertainty.

enriched core (BFS-62-3A); and criticalities of core with blanket (JOYO MK-I) and core with reflector (JOYO MK-II). The sensitivity analysis was also utilized to evaluate nuclide- and reaction-wise contributions to the C/E value changes. The test results for the selected experiments were obtained by the sensitivity analysis and the reference results by MVP[4] with J40. In addition, we performed test calculations for the other experiments in the database by using the sensitivity analysis and the calculation results by a deterministic method using MARBLE[5] with UFLIB.J40.[6]

Figures 2 – 4 show the C/E values of the selected experiments. In principle, the C/E values of J5b3u1 are almost equal to those of J40. The sensitivity analysis, however, reveals that there are significant cancellations between many nuclides and reactions for criticality and SVR. For example, in the criticality of ZPPR-9, there are cancellations between the Pu-239 fission and capture, U-238 fission, and O-16 elastic scattering cross sections. In SVR, there are cancellations between the Pu-239 capture and U-238

Fig. 2 C/E values of criticality for ZPPR-9, BFS-62-3A, JOYO MK-I and -II.
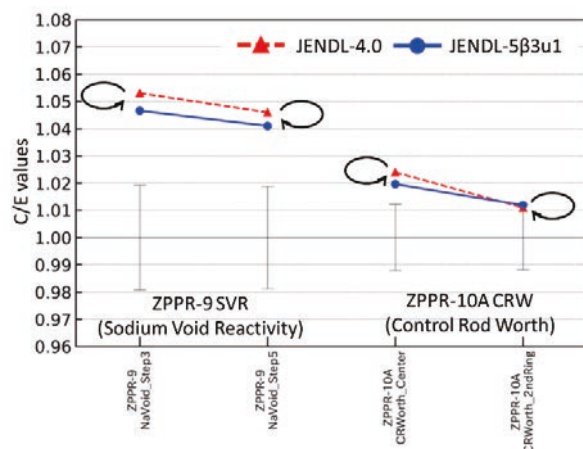
Fig. 3 C/E values of SVR and CRW for ZPPRs (MOX core).
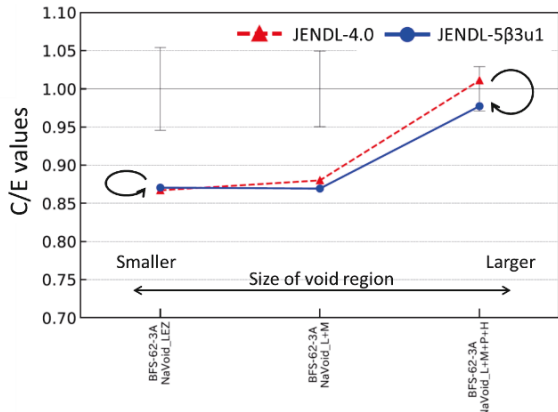
Fig. 4 C/E values of SVR for BFS-62-3A
(U-enriched core).

Table 1 Chi-squared values.

	JENDL-4.0	JENDL-5β3u1
All (11 experiments)	2.29	1.99
Criticality (keff)	2.02	1.26
Sodium void reactivity (SVR)	3.39	3.39
Control rod worth (CRW)	3.27	2.58
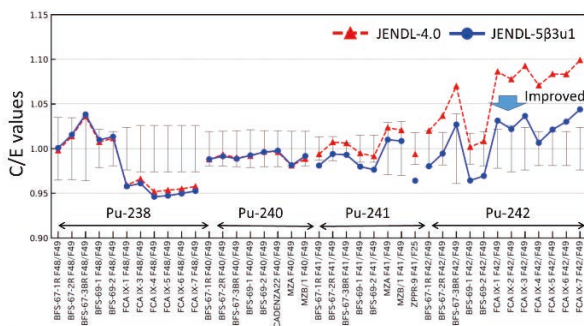
Fig. 5 C/E values of Pu fission rate ratio.
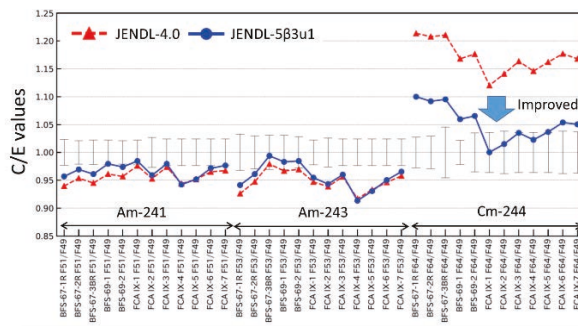
Fig. 6 C/E values of Am and Cm fission rate ratio.

inelastic scattering cross sections for ZPPR-9; and between the U-235 fission and capture for criticality, U-235 fission and capture cross sections for BFS-62-3A. Table 1 shows the chi-squared values of the selected experiments. It is seen that the chi-square values of criticality and CRW are improved. Figures 5 and 6 show the C/E values of the fission reaction rate ratio obtained by the deterministic method and the sensitivity analysis. It is seen that the C/E values of fission rate ratio related to Pu-242 and Cm-244 are significantly improved. The sensitivity analysis reveals that the improvements related to Pu-242 and Cm-244 are due to fission cross section changes of Pu-242 and Cm-244, respectively.

2.3. Thermal-spectrum Systems

The new MVP input files for the ICSBEP benchmarks are prepared to validate JENDL-5 for intermediate and thermal spectrum systems. The numbers of ICSBEP benchmark cases are shown in Table 2.

Table 3 shows the comparison of the average of C/E-1 and the chi-squared values of the ICSBEP benchmark calculations listed in Table 2 among J40, ENDF/B-VIII.0 (B80),[7] ENDF/B-VII.1 (B71) and J5b3u1. The chi-squared values of J5b3u1 are similar to those of B80 and these are smaller than those of J40 in many cases.

Table 2 The number of ICSBEP benchmark cases
for intermediate and thermal spectrum

	COMP	METAL	SOL	Total
PU	0	0	159	159
HEU	7	62	42	111
IEU	6	0	0	6
LEU	249	10	8	267
MOX	63	0	0	63
U233	9	10	147	166
Total	334	82	356	772

Table 3 Comparison of average of C/E-1 and chi-squared values of the ICSBEP benchmark calculations.

	Average of C/E-1				Chi-squared values			
	J40	B71	B80	J5b3u1	J40	B71	B80	J5b3u1
All	-0.012%	0.053%	-0.055%	-0.017%	5.35	4.90	3.87	3.95
HEU	0.046%	0.025%	0.075%	0.171%	4.72	4.88	4.20	4.24
IEU	-0.375%	-0.201%	0.038%	0.057%	3.89	1.81	0.85	1.00
LEU	-0.058%	-0.020%	0.054%	0.071%	4.31	3.19	3.00	3.71
MOX	-0.010%	-0.089%	-0.053%	-0.044%	0.58	0.45	0.90	0.97
Pu	0.610%	0.578%	0.090%	0.007%	11.10	11.13	6.24	5.80
U233	-0.550%	-0.242%	-0.457%	-0.295%	4.02	3.69	4.13	3.71
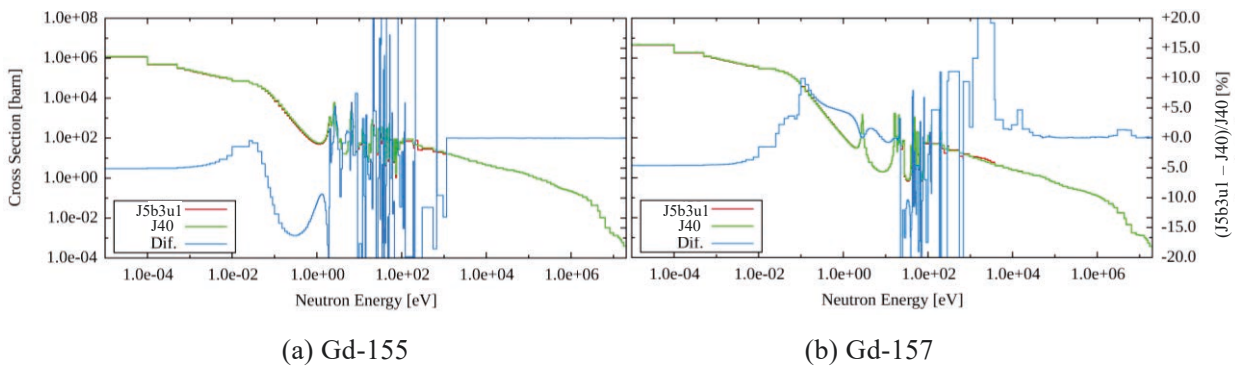
(a) Gd-155

(b) Gd-157

Fig. 7 Comparison of radiation cross sections (MT=102) of Gd-155 and -157.

The cross sections of Gd-155 and -157 for J5b3u1 are largely revised as shown in Fig. 7. To investigate the impact of the revisions on neutronics calculations, reactivity contributions of Gd-155 and -157 were calculated for benchmark cases including Gd. Figure 8 shows the contributions as a function of Gd concentration; they were obtained from the criticality difference between J40 calculations and those where only Gd-155 or -157 cross section data was replaced with J5b3u1. The reactivity contributions of Gd-155 and -157 are almost canceled out. As a result, the revisions of the Gd cross sections have no large impact on the criticality calculations. The additional investigations indicate that the contributions of Gd-155 and -157 cancel each other.
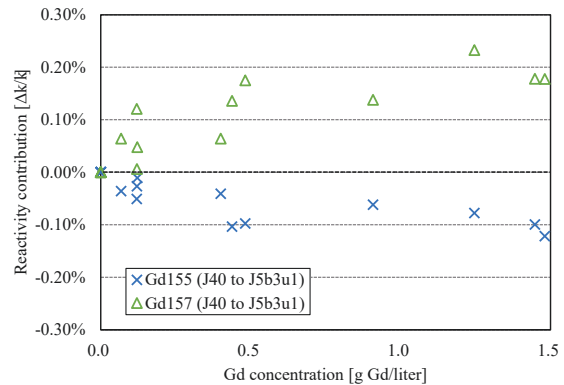
Fig. 8 Reactivity contributions of Gd-155 and -157 for benchmark cases including Gd.

3. Integral Tests for Shielding Experiments

We performed the benchmark tests for J5b3u1 with the following shielding experiments: 1) TIARA iron experiment[8] with 40 and 65 MeV neutrons, 2) FNS iron and copper experiments[8] with DT neutrons, and 3) JASPER sodium experiment[10,11] with fission neutrons. We used the MCNP6.2[12] or PHITS 3.24[13] codes and J5b3u1, J40 (or JENDL-4.0/HE[14]), B80, and JEFF-3.3.[15]

3.1. TIARA Iron Experiment

Figure 9 shows the measured and calculation results for the experiment with 65 MeV neutrons. This figure demonstrates that the calculation result with J5b3u1 agrees with the measured one the best.

(a) Neutron spectra

(b) Calculation/Experiment (C/E) of neutron flux from 60 – 70 MeV

(c) C/E of neutron flux from 10 – 60 MeV
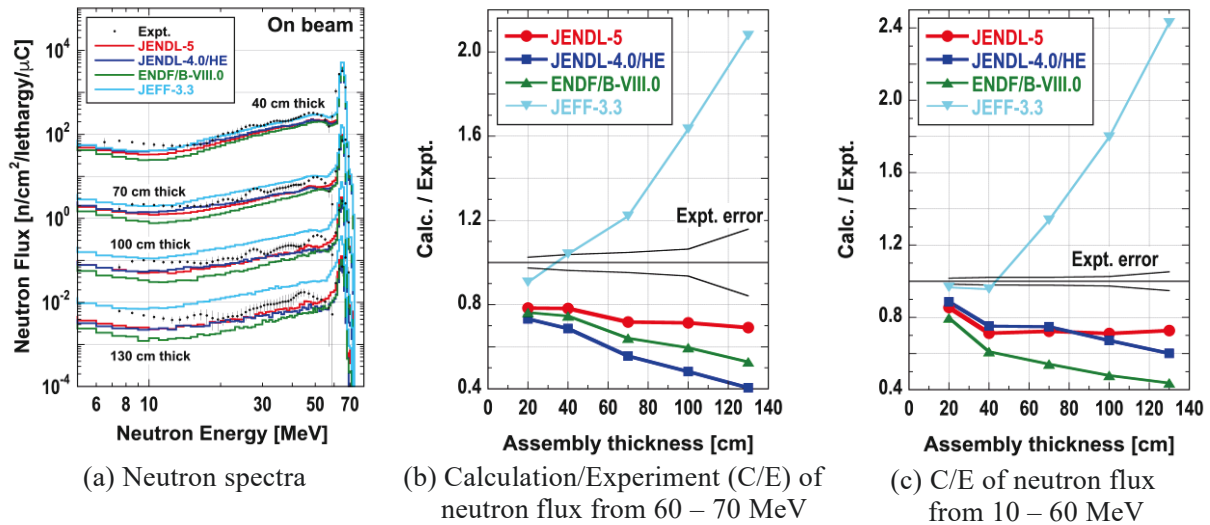
Fig. 9 Results for TIARA iron experiment with 65 MeV neutrons.

3.2. FNS Iron and Copper Experiments

The calculation result with J5b3u1 for the iron experiment was almost the same as that with J40. On the contrary, the calculation result with J5b3u1 for the copper experiment agrees with the measured one better than that with J40 as shown in Fig. 10.

(a) C/E of ^{93}Nb(n,2n)^{92m}Nb reaction rate

(b) C/E of ^{197}Au(n,γ)^{198}Au reaction rate
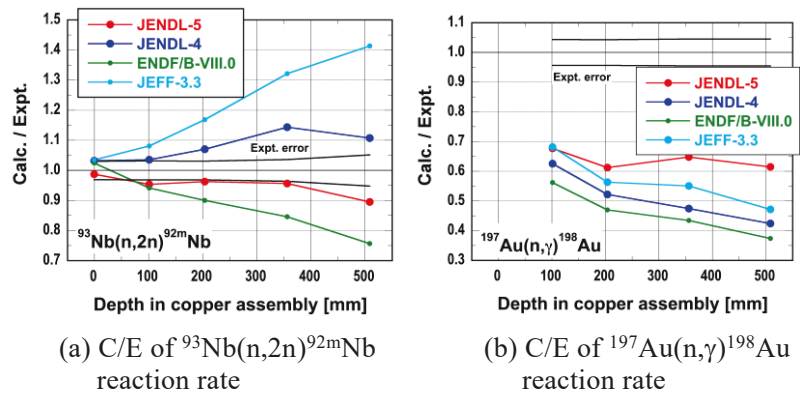
Fig. 10 Results for FNS copper experiment.

3.3. JASPER Sodium Experiment

Figure 11 shows the measured and calculated transmission neutron spectra in JASPER IHX-IB/Pb (231.5 cm sodium). The calculation result with J5b3u1 is slightly higher than that with J40, but it is almost the same as that with JEFF-3.3.
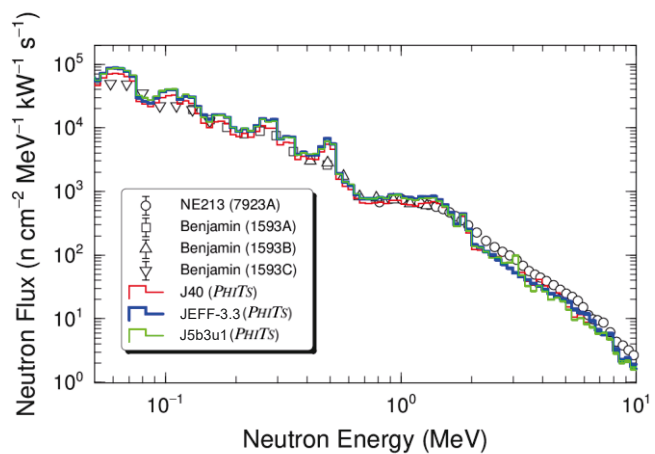
Fig. 11 Neutron spectra for JASPER IHX-IB/Pb experiment.

4. Conclusion

The integral tests of JENDL-5β3 update 1 have been performed for critical and shielding experiments. It has been confirmed that JENDL-5β3 update 1 gives better than or the same prediction accuracy as JENDL-4.0 in many test cases for the critical and shielding experiments.

References

1) NEA Nuclear Science Committee, International Handbook of Evaluated Criticality Safety Benchmark Experiments, NEA/NSC/DOC(95)03, 2019 edition (2019).

2) Yokoyama K. et al., Development of the Unified Cross-section Set ADJ2017, JAEA-Research 2018-011, 2019, 556p [in Japanese].

3) Shibata K. et al., JENDL-4.0: A New Library for Nuclear Science and Engineering, J. Nucl. Sci. Technol. 48, 2011, pp.1-30.

4) Nagaya Y. et al., MVP/GMVP Version 3: General Purpose Monte Carlo Codes for Neutron and Photon Transport Calculations Based on Continuous Energy and Multigroup Methods, JAEA-Data/Code 2016-018, 2017, 421p.

5) Yokoyama, K. et al., Development of comprehensive and versatile framework for reactor analysis, MARBLE, Ann. Nucl. Energy, vol. 66, 2014, pp.51-60.

6) Sugino, K. et al., Preparation of Fast Reactor Group Constant Sets UFLIB.J40 and JFS-3-J4.0 Based on the JENDL4.0 data, JAEA-Data/Code 2011-017, 2012, 44p [in Japanese].

7) Brown, D.A. et al., ENDF/B-VIII.0: The 8th Major Release of the Nuclear Reaction Data Library with CIELO-project Cross Sections, New Standards and Thermal Scattering Data, Nuclear Data Sheets, vol.148, 2018, pp.1-142.

8) Nakashima, H. et al., Experiments on Iron Shield Transmission of Quasi-monoenergetic Neutrons Generated by 43- and 68-MeV Protons via the ^{7}Li(n,p) Reaction, JAERI-Data/Code 96-005, 1996, 46p.

9) Maekawa, F. et al., Compilation of Benchmark Results for Fusion related Nuclear Data, JAERI-Data/Code 98-024, 1998, 174p.

10) Muckenthaler, F.J. et al., Measurements for the Jasper Program In-Vessel Fuel Storage Experiment, ORNL/TM-11989, 1992, 158p.

11) Muckenthaler, F.J. et al., Measurements for the Jasper Program Intermediate Heat Exchanger Experiment, ORNL/TM-12064, 1992, 98p.

12) Werner, C.J. (Ed.), MCNP® USER'S MANUAL Code Version 6.2, LA-UR-17-29981, 2017, 746p.

13) Sato, T. et al., Features of Particle and Heavy Ion Transport Code System (PHITS) version 3.02, J. Nucl. Sci. Technol. vol.55, 2018, pp.684-690.

14) Kunieda, S. et al., Proceedings of the 2015 Symposium on Nuclear Data, JAEA-Conf 2016-004, 2016, pp.41-46.

15) Plompen, A.J.M. et al., The joint evaluated fission and fusion nuclear data library, JEFF-3.3, Eur. Phys. J. A, vol. 56, 2020, 181.

6 New Development in TALYS - Fission Fragment Statistical Decay Model

Kazuki Fujio[†] [*1], Shin Okumura[2], and Arjan Koning[2]

[1]Laboratory for Advanced Nuclear Energy, Tokyo Institute of Technology, 2-12-1
Ookayama, Meguro-ku, Tokyo, 152-8550, Japan
[†]Email: fujio.k.aa@m.titech.ac.jp
[2]Nuclear Data Section, International Atomic Energy Agency, Vienna A-1400, Austria

Abstract

A newly developed fission fragment decay model in TALYS that adopts the Hauser-Feshbach statistical decay theory for the deexcitation by evaporating neutron and γ is explained. The fission fragment database, which consists of the list of yield Y, charge Z, mass A, excitation energy E_x, spin J, and parity Π, *i.e.* $Y_{\mathrm{ff}}(Z, A, E_x, J, \Pi)$, is prepared for TALYS' input of the fission fragment deexcitation calculation. We examine the fission fragment data for $^{235}\mathrm{U}(n, f)$ at thermal to 5 MeV incident neutron energy range produced by the GEF code. The calculated independent fission product yield $Y_{\mathrm{I}}(A)$, average prompt fission neutron emission $\bar{\nu}$, neutron multiplicity distribution $P(\nu)$, and prompt fission neutron spectra are compared with experimental and evaluated data. The database can be produced by any kind of theoretical or phenomenological model and TALYS calculates the prompt fission observables that are comparable to the experimental data.

1 Introduction

Nuclear fission is a very complex process that involves the collective motion of hundreds of nucleons in a single nucleus toward separation into two nuclei. There has been much recent interest in nuclear fission, due in part not only to engineering and applications but also to the formation of elements in the rapid neutron capture process (r-process) of nucleosynthesis in stellar environments.

The probabilities of producing fission fragments (yield) and characteristics of the emitted particles such as multiplicity and energy distribution (spectrum) of neutron and γ contain valuable information to understand pre- and post-scission physics. Many experimental and theoretical works have been made toward describing nuclear fission [1–3], while the experimental investigation in fission time scales is not generally accessible directly. In consequence, only scarce experimental data exist, limited to a few important isotopes and incident neutron energies, especially for primary fission fragments right after scission. On the theoretical side, the theoretical calculation often provides quantitative fission fragment yields in given mass and/or charge with their total kinetic energies. However, the feasibility of such theoretical calculation remains in question since it cannot be directly compared with experimental data.

In order to compare the theoretical fission calculation with experimental fission observables, the prompt neutron and γ evaporation process need to be taken into account, which is a different

---

[*]Present address: Laboratory for Advanced Nuclear Energy, Tokyo Institute of Technology, 2-12-1 Ookayama, Meguro-ku, Tokyo, 152-8550, Japan

process in terms of physics. The evaporation process is handled by nuclear reaction codes that are traditionally established on the basis of the Hauser-Feshbach statistical decay theory [4–8]. The increased interest in more unrestrictive fission observable calculations has demanded more detailed models. Various models have been developed using Monte Carlo [9–11] or deterministic [12–14] approaches associated with the Hauser-Feshbach statistical decay.

The Nuclear Data Section in the IAEA initiated the Coordination Research Project on "Updating fission product yield data for applications" [15]. The project requires enormous evaluation efforts on fission product yields in a wide incident energy range, where the past evaluations have employed phenomenological models [16, 17], and more comprehensive models are desired. In order to support its activities, we extended TALYS [6] by implementing fission fragment deexcitation by the Hauser-Feshbach statistical decay theory to calculate desired fission observables. In this report, we describe the fission fragment distribution data in TALYS and show sample cases of calculated results so that the users can produce and use their own theoretical data.

2   Methodology

The deexcitation of the fission fragments by the Hauser-Feshbach statistical decay theory is implemented in TALYS (later than version 1.96). The methodology used here is to apply the deterministic technique for primary fission fragment decay calculation similar to the HF^{3}D model [13]. In order to calculate the deexcitation of the fission fragment, input of the initial conditions is needed. Generally, the fission fragment is characterized by the yield Y_{ff}, charge Z, mass A, excitation energy E_x, spin J, and parity Π, *i.e.* $Y_{\text{ff}}(Z, A, E_x, J, \Pi)$.

Recently, Nordström et al. [18] produced such fission fragment distributions for more than 700 fissionable nuclides and 0–25 MeV incident neutron energies by the GEF code [19]. Including the GEF produced database mentioned above, TALYS incorporates three fission fragment databases produced by GEF [18, 19], HF^{3}D [13], and Scission Point Yield (SPY) [3] models, so far. The user can specify the fission fragment model in the TALYS input with `ffmodel` keyword (See TALYS manual for details).

The fission fragment distribution parameters generated by such models are stored in a tabulated format file, which is inspired by the format used in the HF^{3}D model [13] and is shown below for ^{235}U$+n_{\text{thermal}}$ reaction from the GEF model as an example.

```
# Z        =    92
# A        =   236
# Ex (MeV) = 6.55e+00
# Ntotal   =   868
# Zl  Al  Zh  Ah  Yield      TKE[MeV]    TXE[MeV]    El[MeV]     Wl[MeV]     Eh[MeV]     Wh[MeV]
  46 118  46 118  3.9358e-03  1.6387e+02  3.5404e+01  1.7702e+01  2.7264e+00  1.7702e+01  2.7264e+00
  45 117  47 119  4.4534e-03  1.6379e+02  3.4714e+01  1.5507e+01  2.2652e+00  1.9207e+01  4.0430e+00
  44 116  48 120  6.9902e-03  1.6453e+02  3.5142e+01  1.4014e+01  1.9368e+00  2.1128e+01  5.5635e+00
  43 115  49 121  1.9397e-03  1.6661e+02  3.2898e+01  1.3628e+01  2.0851e+00  1.9270e+01  6.3823e+00
  42 114  50 122  9.2456e-04  1.7326e+02  2.8813e+01  1.4316e+01  2.8689e+00  1.4496e+01  7.0989e+00
```

In this format, $Z_{l,h}$, $A_{l,h}$, and $Yield$ are the charge, mass, and yield of the complemental fission fragment pair that are supposed to be symmetric with respect to $A_{\text{CN}}/2$. Therefore,

$$Y_{\text{ff}}(Z_l, A_l) = Y_{\text{ff}}(Z_{\text{CN}} - Z_l, A_{\text{CN}} - A_l) = Y_{\text{ff}}(Z_h, A_h) \ , \tag{1}$$

where CN, l, and h denote the compound nucleus, light, and heavy fragment. TKE and TXE are the mean value of total kinetic energy and total excitation energy. In the GEF code, the TXE partitioning is determined according to a probability distribution that is given by the product of
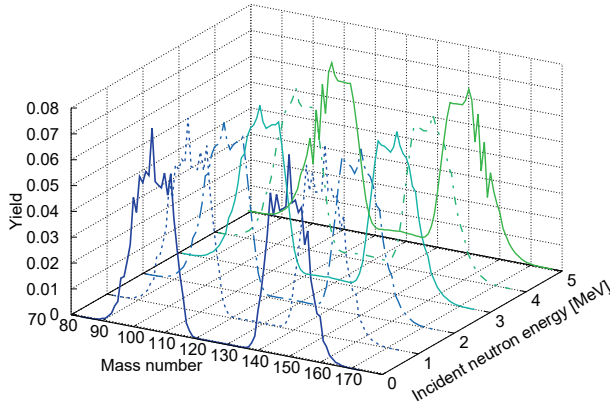
Figure 1: Primary fission fragment yield as a function of fragment mass $Y_{\mathrm{ff}}(A)$ at incident neutron energies from thermal to 5 MeV generated by GEF and stored in TALYS database[18].
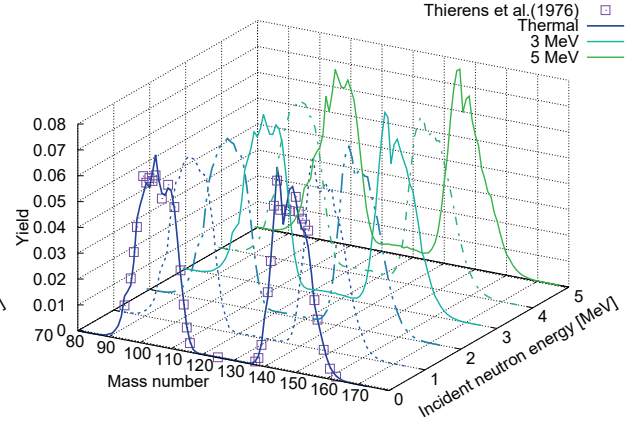
Figure 2: Calculated independent fission product yield as a function of product mass $Y_{\mathrm{I}}(A)$ using the fission fragment yields shown in Fig. 1.

the level densities of the individual fragments [20]. $E_{l,h}$ and $W_{l,h}$ are Gaussian mean and width of the partitioned TXE into two fragments. Such initial conditions of fission fragments are obtained from the MonteCarlo sampling by GEF and are reformatted by Nordström et al. [18].

TALYS reads these conditions from the file and reconstructs the excitation energy distribution $G_{l,h}(E_x)$ assuming to be a Gaussian form expressed as

$$G_{l,h}(E_x) = \frac{1}{\sqrt{2\pi}W_{l,h}} \exp\left\{ -\frac{(E_x - E_{l,h})^2}{2W_{l,h}^2} \right\}. \tag{2}$$

The spin distribution $R(J, \Pi)$, which is the probability of having the state of J and Π, is assumed to be proportional to the available spin states in the level density formula

$$R(J, \Pi) = \frac{J + 1/2}{2f^2\sigma_{l,h}^2(U)} \exp\left\{ -\frac{(J + 1/2)^2}{2f^2\sigma_{l,h}^2(U)} \right\}, \tag{3}$$

where $\sigma_{l,h}^2(U)$ is the spin cutoff parameter that can be altered by a keyword `Rspincut` and set to 1 by default, f^2 is the global adjustable constant for the spin cutoff parameter for fission fragments that can be altered by a keyword `Rspincutff` set to 9 by default following Ref. [13], and U is the excitation energy corrected by the pairing energy. After creating an initial population $P(E_x, J, \Pi) = R(J, \Pi)G_{l,h}(E_x)$ for the individual fission fragment, the Hauser-Feshbach statistical decay calculation is performed for each fission fragment.

The center-of-mass system neutron spectra $\phi_{l,h}$ from light and heavy fission fragments are calculated and normalized to the neutron multiplicity $\nu_{l,h}$ as

$$\int dE_x \sum_{J\Pi} \int d\epsilon R(J, \Pi)G(E_x)\phi_{l,h}(J, \Pi, E_x, \epsilon) = \nu_{l,h}. \tag{4}$$

The $\phi_{l,h}$ is transformed into the LAB frame using Feather's formula and the spectrum is weighted by the fission fragment yield $Y_{\mathrm{ff}}(Z_l, A_l)$. Other representative neutron quantities in TALYS outputs are listed in Table 1.
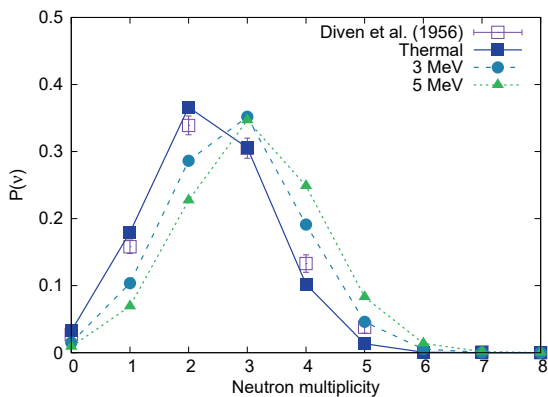
Figure 3: Neutron multiplicity distribution for ^{235}U(n, f) at thermal, 3, and 5 MeV incident neutron energies.
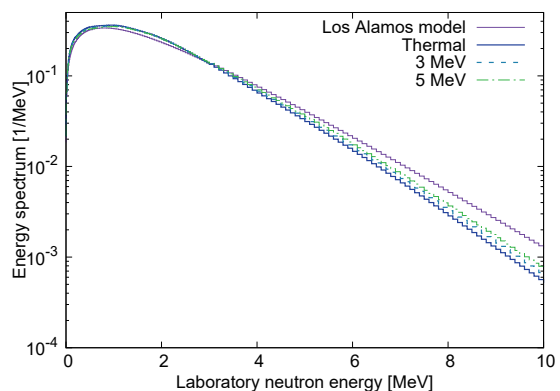
Figure 4: Neutron energy spectra for ^{235}U(n, f) reactions at thermal, 3, and 5 MeV incident neutron energies in the laboratory frame.

Table 1: Representative prompt neutron quantities in TALYS.

	Description
$Y_I(A)$, $Y_I(Z, A, M)$	Independent fission product yield
$\overline{\nu}$, $\overline{\nu}(A)$	Average number of neutrons per fission
$\langle E_n \rangle$, $\langle E_n \rangle(A)$	Average prompt neutron energy
$P(\nu)$	Neutron multiplicity distribution
$\chi(\nu)$	Prompt fission neutron energy spectrum (PFNS)

3 Calculated prompt neutron observables

We run calculations using the input attached in Appendix A by changing incident energy. Figure 1 shows $Y_{\mathrm{ff}}(A)$ of ^{235}U(n, f) reactions at incident neutron energies from thermal to 5 MeV produced by Nordström et al.[18] using GEF code. Figure 2 shows independent fission product yields $Y_I(A)$ calculated based on the fission fragments shown in Fig. 1. The calculated $Y_I(A)$ at the thermal energy well reproduced the experimental trend of fission product mass distribution.

The prompt neutron multiplicity distribution $P(\nu)$ can be deduced from the evaporation calculations, whereas the most important value, the average value $\bar{\nu} = 2.414$ (ENDF/BVIII), which is 2.30876 at thermal energy, is slightly smaller than the evaluated value. The calculated $P(\nu)$ are compared with the experimental data in Fig. 3. The calculated $P(\nu)$ reproduce the experimental trend although the dispersion is around 15%.

The prompt fission neutron spectra (PFNS) at thermal, 3, 5 MeV incident neutron energies are shown in Fig. 4 together with the Los Alamos model [16] for comparison. The PFNS from the fission fragment deexcitation seems to be in fairly good agreement with that of the Los Alamos model in a log scale. However, the TALYS calculation gives a too soft shape compared to that of the Los Alamos model at high outgoing neutron energy also quite a large deviation in the Maxwellian ratio at low outgoing neutron energy.

Note that we examined the incident energy range from thermal to 5 MeV only. We will work on further implementation including multi-chance fission.

4 Conclusion

The fission fragment deexcitation process by adopting the Hauser-Feshbach statistical decay theory to the evaporation of neutrons and γs from the excited fission fragment is implemented in TALYS (later than version 1.96). The initial conditions of the fission fragment, $Y_{\text{ff}}(Z, A, E_x, J, \Pi)$, are prepared in the tabulated format file using GEF, HF^{3}D, and SPY models.

The calculated results of ^{235}U(n, f) reactions at thermal to 5 MeV neutron energies using the fission fragments database produced by the GEF model reproduce trends in experimental or other model data for $Y_{\text{I}}(A)$, $P(\nu)$, and PFNS.

This implementation allows users to calculate prompt fission observables with TALYS using the fission fragment distribution defined by $Y_{\text{ff}}(Z, A, E_x, J, \Pi)$ from any kinds of phenomenological or microscopic model. The calculated prompt observables can be compared with available experimental data. This would be helpful for users who do theoretical fission studies that are not directly comparable to the experimental observables.

References

[1] Schunck N, Robledo LM. Microscopic theory of nuclear fission: a review. Reports on Progress in Physics. 2016 oct;79(11):116301.

[2] Andreyev AN, Nishio K, Schmidt KH. Nuclear fission: a review of experimental advances and phenomenology. Reports on Progress in Physics. 2017 nov;81(1):016301.

[3] Lemaître JF, Goriely S, Hilaire S, Sida JL. Fully microscopic scission-point model to predict fission fragment observables. Phys Rev C. 2019 Mar;99:034612.

[4] Young PG, Arthur ED, Chadwick MB. Comprehensive nuclear model calculations : introduction to the theory and use of the GNASH code. Los Alamos National Laboratory; 1992. LA-12343-MS.

[5] Kawano T. CoH$_3$: The Coupled-Channels and Hauser-Feshbach Code. Proc CNR2018: International Workshop on Compound Nucleus and Related Topics, LBNL, Berkeley, CA, USA, September 24 – 28, 2018. 2021;.

[6] Koning AJ, Hilaire S, Duijvestijn MC. TALYS: Comprehensive Nuclear Reaction Modeling. AIP Conference Proceedings. 2005;769(1):1154–1159.

[7] Herman M, Capote R, Carlson BV, Oblozinský P, Sin M, Trkov A, et al. EMPIRE: Nuclear Reaction Model Code System for Data Evaluation. Nuclear Data Sheets. 2007;108(12):2655 – 2715.

[8] Iwamoto O. Development of a Comprehensive Code for Nuclear Data Evaluation, CCONE, and Validation Using Neutron-Induced Cross Sections for Uranium Isotopes. Journal of Nuclear Science and Technology. 2007;44(5):687 – 697.

[9] Lemaire S, Talou P, Kawano T, Chadwick MB, Madland DG. Monte Carlo approach to sequential neutron emission from fission fragments. Phys Rev C. 2005 Aug;72:024601.

[10] Litaize O, Serot O. Investigation of phenomenological models for the Monte Carlo simulation of the prompt fission neutron and γ emission. Phys Rev C. 2010 Nov;82:054616.

[11] Talou P, Becker B, Kawano T, Chadwick MB, Danon Y. Advanced Monte Carlo modeling of prompt fission neutrons for thermal and fast neutron-induced fission reactions on ^{239}Pu. Phys Rev C. 2011 Jun;83:064612.

[12] Tudora A, Morillon B, Hambsch FJ, Vladuca G, Oberstedt S. A refined model for ^{235}U(n,f) prompt fission neutron multiplicity and spectrum calculation with validation in integral benchmarks. Nuclear Physics A. 2005;756(1):176–191.

[13] Okumura S, Kawano T, Jaffke P, Talou P, Chiba S. ^{235}U(n, f) Independent fission product yield and isomeric ratio calculated with the statistical Hauser–Feshbach theory. Journal of Nuclear Science and Technology. 2018;55(9):1009–1023.

[14] Okumura S, Kawano T, Lovell AE, Yoshida T. Energy dependent calculations of fission product, prompt, and delayed neutron yields for neutron induced fission on ^{235}U, ^{238}U, and ^{239}Pu. Journal of Nuclear Science and Technology. 2022;59(1):96–109.

[15] Pritychenko B, S Oberstedt OC, Vogt R, Noy RC, Okumura S, Kawano T. Updating Fission Yield Data for Applications. International Atomic Energy Agency; 2021. INDC(NDS)-0817.

[16] Madland DG, Nix JR. New Calculation of Prompt Fission Neutron Spectra and Average Prompt Neutron Multiplicities. Nuclear Science and Engineering. 1982;81(2):213–271.

[17] England TR, Rider BF. Evaluation and compilation of fission product yields. Los Alamos National Laboratory; 1994. ENDF-349, LA-UR-94-3106.

[18] Nordström F. Benchmark of the fission channels in TALYS. UPTEC ES 21016, Uppsala University. 2021;.

[19] Schmidt KH, Jurado B, Amouroux C, Schmitt C. General Description of Fission Observables: GEF Model Code. Nuclear Data Sheets. 2016;131:107 – 221. Special Issue on Nuclear Reaction Data.

[20] Jurado B, Schmidt KH. Status of the general description of fission observables by the GEF code. 2014;.

Acknowledgments

A   Example of TALYS input

```
projectile n
element    U
mass       235
energy     2.53E-8
ejectiles g n
massdis y
fymodel 4
ffmodel 1
elow 1.e-6
Rfiseps 1.E-09
outspectra y
bins 60
channels y
maxchannel 8
```

7   Development of FRENDY Version 2

Kenichi TADA[1*], Akio YAMAMOTO[2], Tomohiro ENDO[2], Go CHIBA[3], Michitaka ONO[4] and
Masayuki TOJO[4]

[1]Nuclear Data Center, Japan Atomic Energy Agency

2-4 Shirakata, Tokai-mura, Naka-gun, Ibaraki-ken 319-1195, Japan

[2]Nagoya University

Furo-cho, Chikusa-ku, Nagoya, 464-8603, Japan

[3]Hokkaido University

Kita 8, Nishi 5, Kita-ku, Sapporo, 060-0808, Japan

[4]Global Nuclear Fuel-Japan Co., Ltd.

2-3-1 Uchikawa, Yokosuka, 239-0836, Japan

[*]Email: tada.kenichi@jaea.go.jp

Many capabilities, *e.g.*, the generation of the multi-group neutron cross-section files, the modification of evaluated nuclear data files, are implemented after we released FRENDY version 1. FRENDY version 2 is developed including these new capabilities. This paper describes the overview of FRENDY version 2.

1. Introduction

FRENDY (FRom Evaluated Nuclear Data librarY to any application) [1] is a nuclear data processing code for the evaluated nuclear data libraries JENDL [2], ENDF/B [3], JEFF [4], TENDL [5], and so on. FRENDY can treat two input formats. One is the FRENDY original input format and the other is the NJOY compatible format [6]. FRENDY original input format is very simple, and it requires only the processing mode and the evaluated nuclear data file name at the minimum. Users can generate the cross-section file even if they do not have expert knowledge of the nuclear data processing method.

The first version of FRENDY was released in 2019 as an open-source software under the 2-clause BSD license. FRENDY Version 1 generates the ACE files [7] which are used for the continuous energy Monte Carlo codes such as PHITS [8], Solomon [9], Serpent [10], and MCNP [11]. Though a lot of functions are required to process the nuclear data file, the coverage of FRENDY version 1 is not yet satisfactory. New functions have been developed after the release of FRENDY version 1. The major developed capabilities are as follows:

- Multi-group neutron cross-section file generation function [12],
- Perturbation of the ACE file for the uncertainty quantification using a continuous energy Monte Carlo code [13],
- Modification of the evaluated nuclear data file.

FRENDY version 2 will be released in 2022 including these capabilities. This paper describes an overview of FRENDY and the new capabilities implemented in FRENDY version 2.

2. System Structure

The system structure of FRENDY is shown in Fig. 1. The modules with solid-lined shapes have been already implemented while the ones with dashed-lined shapes have not been developed yet. FRENDY is designed to treat not only the ENDF-6 format [14] but also other nuclear data formats, e.g., GNDS format [15]. FRENDY converts the nuclear data from each nuclear data format to NuclearDataObject. FRENDY can treat the other nuclear data formats if parser, writer, and converter modules are implemented. Each module can be easily improved, extended, and modified to satisfy future needs since each module is encapsulated and is not affected by other modules. FRENDY keeps all data on NuclearDataObject and uses NuclearDataObject for the data transfer between different processing modules, *e.g.*, the resonance reconstruction and Doppler broadening, to reduce the effect of rounding errors and overhead by file access.
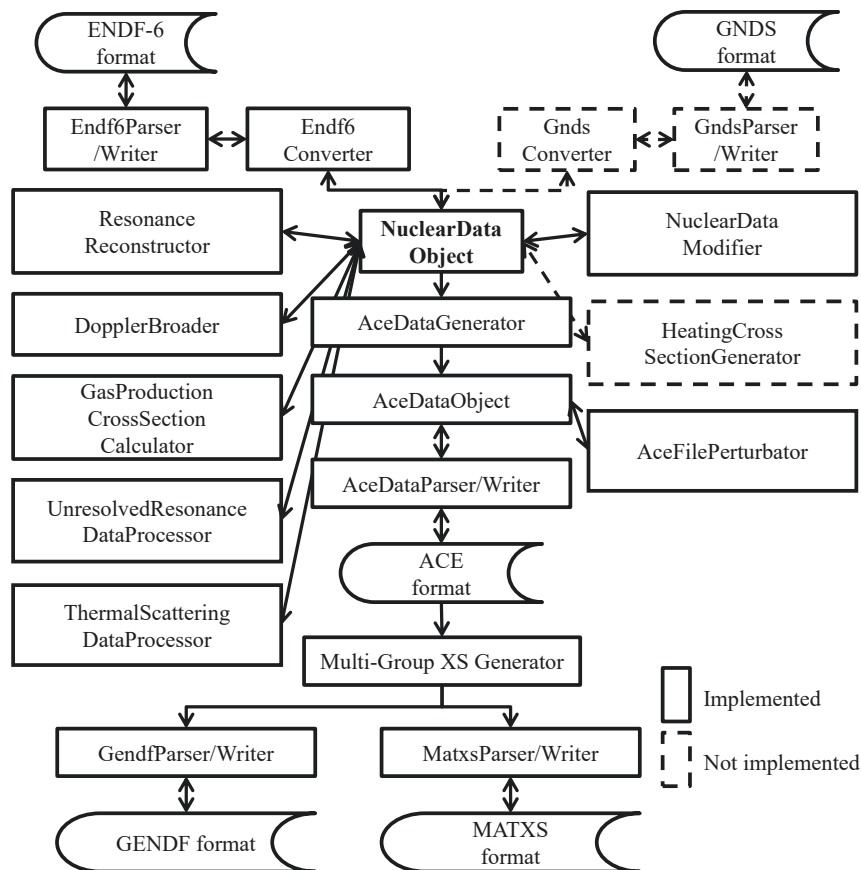
Fig. 1 The system structure of FRENDY Version 2

FRENDY has the parser and writer modules to handle the ACE file. These modules are useful for the generation and modification of the ACE file. There are some cases where users want to modify a cross-section data library by themselves to estimate the impact of the modification of the cross-section data library on the nuclear calculation results. The ACE file uses random access with pointers to the various parts of the data. If the number of energy grid points is modified, modification of the pointer data is also required. To modify the pointer data is difficult for the nuclear calculation code users who do not

know well about the ACE format. FRENDY automatically adjusts the pointer data by the ACE data writer module. Users can modify the ACE file when they write a main (control) program with the ACE data parser and writer modules in FRENDY. The ACE file perturbation tool [13] is also using these modules to handle the ACE file.

3. Input Format

As described in Sec. 1, FRENDY accepts two types of input formats, *i.e.*, FRENDY original input format and NJOY compatible input format. The original input format requires only the processing mode name and evaluated nuclear data file name at the minimum. FRENDY has the default values in the source code for the processing. Users can give the parameters in the input file if they want to change the parameters. The original input format is simple and does not require expert knowledge of nuclear data processing.

The sample input format to generate the neutron induced (fast) ACE file is as follows:

ace_file_generation_fast_mode   **// Processing mode name**
    nucl_file_name   **U235.dat**   **// Nuclear data file name**

The above sample input data generates the ACE file at a temperature of 293.6 K from the evaluated nuclear data file named "U235.dat". Note that after "//" means the comment line. FRENDY original input format accepts the C++ style comments, *i.e.*, "//" for a single line comment and "/* … */" for multi-line comments.

The sample input format to generate the multi-group neutron cross-section file is as follows:

mg_neutron_mode   **//Process mode name**
    nucl_file_name   **U235.dat**   **/Nuclear data file name**
    temp   **300.0**   **//Temperature [K]**
    mg_structure (xmas_nea-lanl_172)   **// Identical to ign=18 in GROUPR/NJOY**
    mg_weighting_spectrum (1/e)   **// Identical to iwt=3 in GROUPR/NJOY**

The above sample input data generates the multi-group neutron cross-section file at a temperature of 300.0 K from the evaluated nuclear file named "U235.dat". The energy group structure and the weighting spectrum to generate the multi-group neutron cross-section file are XMAS 172 group structure and $1/E$, respectively.

FRENDY can also accept input files for NJOY. NJOY is widely used in many laboratories and companies to generate the cross-section data library for their nuclear calculation codes. The NJOY users can easily use FRENDY without modification of their processing environment, *e.g.*, running shell scripts, input files, and post-processing programs. FRENDY has the compatible capabilities for the MODER, RECONR, BROADR, PURR, UNRESR, THERMR, ACER, GROUPR, and MATXSR modules in NJOY. Note that the UNRESR module is not prepared in FRENDY. FRENDY calculates the effective self-shielded cross-sections in the unresolved resonance region using the probability table method even if the user selects the UNRESR module. Users can easily use FRENDY without changing the input files for NJOY. They can therefore replace NJOY modules with FRENDY ones as they need. In addition, the modules of FRENDY and NJOY can be used in combination. For example, users can generate the multi-

group cross-section data library using the GROUPR module of NJOY with the PENDF file generated by FRENDY.

The input format of NJOY99 [16] is slightly different from that of NJOY2016 [6]. The "iform" option in the THERMR module and the "ismooth" option in the GROUPR module in NJOY2016 are ignored to treat both NJOY99 and NJOY2016 formats.

4. Overview of New Capabilities Implemented in FRENDY Version 2
4.1. Multi-Group Neutron Cross-Section Generation

FRENDY incorporates the multi-group neutron cross-section generation module FRENDY/MG [12] to generate the multi-group neutron cross-section file. FRENDY can generate GENDF and MATXS formatted multi-group neutron cross-section files from the ACE file. FRENDY can also create the multi-group neutron cross-section file based on the existing ACE file created by other nuclear data processing codes beforehand. The impact of the difference of the nuclear data processing on the neutronics calculation can be ignored if users use these ACE files as the cross-section files of the Monte Carlo codes.

FRENDY prepares new functions, *e.g.*, the automatic background cross-section setting with the minimum number of background cross-sections [17] and the explicit consideration of the resonance interference effect among the compound of different isotopes. These new functions are only available for the FRENDY original input format.

4.2. ACE File Perturbation

The perturbation of the cross-section, the number of neutrons per fission, fission spectrum, and so on are required for sensitivity analysis. The perturbation of these data is also used for uncertainty quantification of the nuclear characteristics due to the covariance of the nuclear data. FRENDY prepares the ACE file perturbation tool to easily perturb the cross-section, the number of neutrons per fission, and fission spectrum [13]. As shown in Fig. 2, the perturbation tool multiplies the perturbation factor f by cross-section, the number of neutrons per fission, and the fission spectrum at the arbitrary energy region. Note that this tool does not consider the continuity of the distribution. The energy boundary of the perturbation becomes discontinuous.

The ACE file contains many reaction-type data, *e.g.*, total, elastic, fission, and radiative capture reactions. The perturbation tool not only perturbs the target reaction data but also modifies the total reaction data. The energy integral of the fission spectrum must be 1.0. The perturbation tool normalizes the fission spectrum after the fission spectrum is perturbed. The perturbation tool modifies the other energy range so that the energy integral of the fission spectrum is 1.0 if users want to perturb the fission spectrum at the specified energy range.

FRENDY also prepares the ACE file editing tool. This editing tool outputs the one-dimensional data, *i.e.*, cross-section, the number of neutrons per fission, and fission spectrum. Users can plot the one-dimensional data using plotting tools such as Excel, GNUPLOT, and Matplotlib. Users can easily compare the original ACE file and the perturbed ACE file using this editing tool.

This perturbation tool was implemented in FRENDY version 1.01 and is widely used in the world [18].
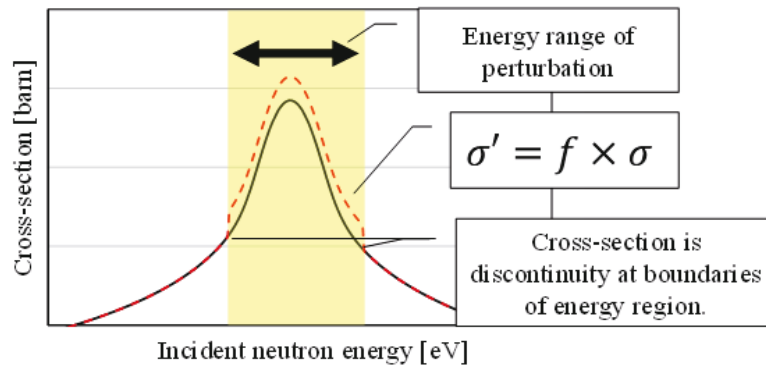
Fig. 2 Overview of ACE perturbation tool

4.3. Modification of Evaluated Nuclear Data File

Users may need the modification of the ENDF-6 formatted file when they want to add or replace the other data in the evaluated nuclear data file; *e.g.*, the covariance data is not found in the original nuclear data file or users want to investigate the impact of the neutronics calculation on the difference of evaluated nuclear data file in each reaction type. However, the modification of the ENDF-6 formatted file is difficult for beginners. FRENDY prepares the modification tool to easily modify the ENDF-6 formatted file.

As shown in Fig. 3, the ENDF modification tool removes the specified MF/MT data in the original evaluated nuclear data file and adds and replaces the specified MF/MT data from the other evaluated nuclear data file. Note that the modified evaluated nuclear data file must be checked carefully since this tool does not check the consistency of the new file.
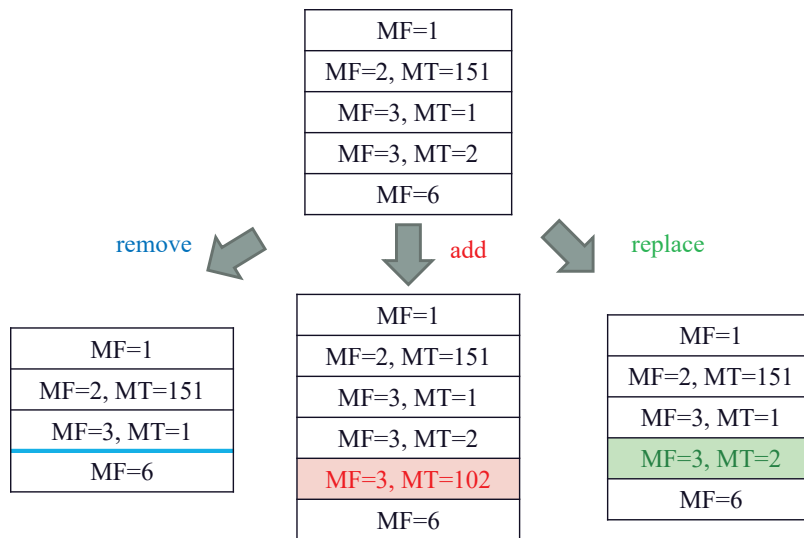
Fig. 3 Example of ENDF modification tool

5. Conclusions

Many capabilities, *e.g.*, the generation of the multi-group neutron cross-section files, the perturbation of the ACE file for the uncertainty quantification using a continuous energy Monte Carlo code, and the modification of evaluated nuclear data files, are implemented after we released FRENDY version 1. FRENDY version 2 will be released including these new capabilities in 2022.

References

1) K. Tada, Y. Nagaya, et al., "Development and verification of a new nuclear data processing system FRENDY," *J. Nucl. Sci. Technol.*, **54**, pp.806-817 (2017).

2) K. Shibata, O. Iwamoto, et al., "JENDL-4.0: A New Library for Nuclear Science and Engineering", *J. Nucl. Sci. Technol.*, **48**, pp.1-30 (2011).

3) D. A. Brown, M. B. Chadwick, et al., "ENDF/B-VIII.0: The 8th Major Release of the Nuclear Reaction Data Library with CIELO-project Cross Sections, New Standards and Thermal Scattering Data," *Nucl. Data Sheets*, **148**, pp.1-142 (2018).

4) A. Plompen, O. Cabellos, et al., "The joint evaluated fission and fusion nuclear data library, JEFF-3.3," *Eur. Phys. J. A.*, **56**, p.181 (2020).

5) A. Koning, D. Rochman, et al., "TENDL: complete nuclear data library for innovative nuclear science and technology," *Nucl Data Sheets*, **155**, pp.1-55 (2019).

6) A. C. Kahler, editors, "The NJOY nuclear data processing system, version 2016," LA-UR–17–20093, (2016).

7) J. L. Conlin, editors, "A Compact ENDF (ACE) Format Specification," LA-UR-19-29016 (2019).

8) T. Sato, Y. Iwamoto, et al., "Features of Particle and Heavy Ion Transport code System (PHITS) version 3.02," *J. Nucl. Sci. Technol.*, **55**, pp.684-690 (2018).

9) Y. Nagaya, T. Ueki, K. Tonoike, "SOLOMON: A Monte Carlo Solver for Criticality Safety Analysis," *Proc. ICNC 2019* (2019).

10) J. Leppänen, M. Pusa, et al., "The Serpent Monte Carlo code: Status, development and applications in 2013," *Ann. Nucl. Energy*, **82**, pp.142-150 (2015).

11) C. J. Werner, editors, "MCNP user's manual code version 6.2," LA-UR–17–29981 (2017).

12) A. Yamamoto, K. Tada, et al., "Multi-group neutron cross section generation capability for FRENDY nuclear data processing code," *J. Nucl. Sci. Technol.*, **59**, pp.1165-1183 (2021).

13) R. Kondo, T. Endo, et al., "Implementation of random sampling for ACE-format cross sections using FRENDY and application to uncertainty reduction," *Proc. M&C2019*, (2019).

14) A. Trkov, M. Herman, D. A. Brown, "ENDF-6 Formats Manual", Report BNL-203218-2018-INRE (2018).

15) R. E. MacFarlane, D. W. Muir, "The NJOY Nuclear Data Processing System, Version 91", LA-12740-M, Los Alamos National Laboratory (1994).

16) OECD/NEA/NSC/WPEC, "Specifications for the Generalized Nuclear Database Structure – Version 1.9", NEA No. 7519, ISBN 978-92-6490-197-1 (2020).

17) A. Yamamoto, T. Endo, K. Tada, "Adaptive setting of background cross sections for generation of effective multi-group cross sections in FRENDY nuclear data processing code," *J. Nucl. Sci. Technol.*, **59**, pp.1343-1350 (2021).

18) O. Cabellos, "P&V of JEFF-3.3 by using FRENDY code," JEFFDOC-1987 (2019).

8 For Utilization and Promotion of Covariance Data of Nuclear Data

Go CHIBA

Graduate School of Engineering, Hokkaido University

Sapporo, Hokkaido, 060-8628 Japan

e-mail: go_chiba@eng.hokudai.ac.jp

Although significant efforts have been devoted to evaluation and application of covariance data of nuclear data so far, there remain several issues which should be addressed. In Japanese nuclear data community, a new working group was established under the JENDL committee to tackle this and has ended three-year activity with the publication of a final report. This paper describes some personal comments on the covariance data utilization and promotion from one member of this working group.

1. Background

A lot of works on uncertainty quantification (UQ) of various parameters of nuclear systems have been actively carried out in recent years, and importance of covariance data of nuclear data has been recognized in the nuclear engineering community. In order to promote covariance data application to actual problems such as design studies and safety assessments of nuclear systems, the covariance data use promotion working group was established under the JENDL committee in FY2018. Information exchanges, discussions, and identification of required future works had been done among domestic experts on the nuclear data measurement/evaluation/application fields through the activities of this working group. A final report summarizing the three-year works of this working group has been published in 2021 as an official JAEA report [1]. The following are the contents of this final report.

- Reviews of fundamental information
- Evaluation of uncertainties in nuclear data measurement and current issues
- Current status and issues of uncertainty evaluation in nuclear data evaluation
- Current status and issues of uncertainty evaluation in reactor physics experiments
- Summary of theory about uncertainty quantification and data assimilation using covariance data
- How the reliability of covariance data should be assured
- How covariance data should be positioned in evaluated nuclear data file

In the present manuscript, some personal comments on the covariance data utilization and promotion will be presented by the author who joined and worked under this working group with review of the previous works related to sensitivity analysis (SA), UQ, and data assimilation (DA).

2. Is nuclear data a random variable?

Nuclear data itself is a physical constant and is not a random variable. On the other hand, evaluated nuclear data depend on some measurable quantities which are random variables. Even if most part of the evaluation is conducted with the theoretical model, used parameters in the model would be determined from measurable quantities which are random variables. Thus, evaluated nuclear data should be considered as a random variable and are represented by a specific probability density function.

Figure 1 shows an example of C/E values of the neutron multiplication factor of the several critical assemblies. The error bars represent the uncertainties in C values induced by the nuclear data and are calculated from the covariance data. When this figure is provided, do we have to say that these C/E values and their nuclear data-induced uncertainties are inconsistent with each other from the statistical point of view? If it is not assured that the covariance data of this nuclear data have been evaluated with knowledge on these reactor data, someone can say that what we should do is to update the covariance data with this "new" information. However, if nuclear data are random variables, this result cannot be practically obtained from the viewpoint of the statistics, and we have to say something like that the uncertainty of nuclear data would be "overestimated".
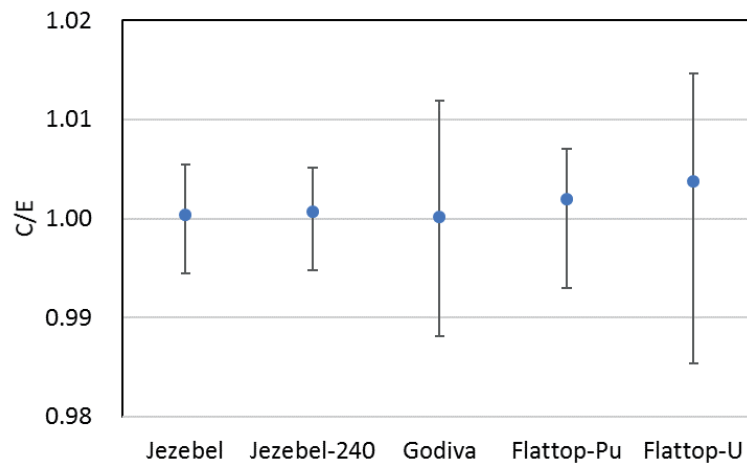
Fig.1 C/E values and nuclear data-induced uncertainties of fast critical assembly neutron multiplication factors

We must keep in mind that nuclear data evaluation is not a simple statistical and mathematical process, and it should implicitly include various professional knowledge of evaluators. If we say that covariance data of the nuclear data imply just the "degree of uncertainty" for the evaluator, evaluated nuclear data would not be random variables. If evaluated nuclear data are not random variables, further discussions and manipulations based on the statistics would be impossible. If nuclear data evaluation can be conducted with the "rigorous" statistical and mathematical process, reasonable covariance data would be obtained. The problem is how to develop evaluation method/procedure including the various professional knowledge of evaluators, which should be explicitly explained and documented.

3. Problems in very uncertain nuclear data

In uncertainty propagation calculations from nuclear data to reactor parameters, the random sampling method is generally used now. Since no detailed information on the probability distribution of nuclear data is provided in evaluated nuclear data files, the normal distributions are often assumed to nuclear data. Importance of the sensitivity of the assumed probability density function of the input nuclear data to the UQ results was recognized in the past, and several practical techniques to see that were proposed[2]. Nowadays, direct evaluation of this sensitivity becomes possible.

Sometimes relative standard deviation of over 50% is given to nuclear data. If we assume the normal distribution to this nuclear data, this means that this nuclear data can take negative values with non-negligible probability. For such nuclear data, we can insist to use other probability density functions in which positivity is assured. If the positivity should be assured, the truncated normal distribution is chosen from the maximum entropy principle[3]. Practical sampling method for the multi-variate truncated normal, however, has not yet been developed as far as the author knows. Positivity is assured also in the log-normal distribution, but possible range of the correlation coefficients between two random variables following the log-normal is limited[4].

We have to assume the probability density function for nuclear data in random sampling calculations, but it would not be meaningful to do this for very uncertain nuclear data since "very uncertain" means that there are almost no information including the probability distribution.

4. Review of sensitivity analysis, uncertainty quantification, and data assimilation

In order to identify important nuclear data for accurate predictions of reactor parameters, sensitivities of reactor parameters with respect to nuclear data are very useful quantities. Since the number of nuclear data is huge, direct numerical differentiation to calculate sensitivities is impractical. Several techniques to reduce the number of input variables had been developed in the past[2]. The perturbation theory has been developed and advanced in the field of reactor physics, and it has become possible to calculate sensitivity of various kinds of reactor parameters.

If covariance data of nuclear data are available, it becomes possible to quantify the uncertainty in reactor parameters caused by input nuclear data uncertainty with sensitivities. Uncertainty quantification calculations with covariance data and sensitivities have been conducted so far. As far as the author knows, comprehensive uncertainty quantification calculations using the evaluated nuclear data files have been initially carried out in Japan for fast reactor analyses using JENDL-3.3 since JENDL-3.3 would be the first evaluated library which contains the covariance data for a wide variety of nuclides and reactions. Nowadays, most nuclear data files contain the covariance data, and UQ calculations have been conducted everywhere.

By virtue of the rapid increase of the computer ability, sampling procedure has become practical, and for every reactor parameter which can be numerically calculated, UQ calculations become possible. The possibility of the uncertainty propagation calculations from the basic nuclear parameters to the reactor parameters was discussed before[5], and it has been realized as the well-known total Monte Carlo[6].

Use of the information on measured reactor parameters (integral data) to improve the prediction accuracy of nuclear data has been attempted. The approach can be categorized into

the following: the bias factor method, the bias operator method, and the data adjustment method[7]. The data adjustment is known as the data assimilation at present. The history of the nuclear data adjustment is very old[8]. Japanese experts also contributed to this field, and they pointed out that undetected uncertainty can result in not chi-squared distribution but non-central chi-squared distribution, and this can be utilized to identify the undetected uncertainty[9]. In recent years, the adjusted library applicable to fast reactor analyses has been developed by Japan Atomic Energy Agency known as a series of the "ADJ" libraries.

Consistency check for the original nuclear data and added integral data can be carried out by observing the chi-square/DOF of the adjusted data. Also, changes in cross section data through the adjustment can be compared with the standard deviations of the original data[7]. If the existence of undetected uncertainty is suspicious, chi-square values can be useful indicators: the integral data causing large chi-square value can be identified. Observation of the changes in cross section data is also important to identify undetected uncertainty in evaluated nuclear data[5].

The fundamental theory for radiation shielding calculations is essentially same as that for reactor calculations from a viewpoint of the particle transport, and it is possible to find works relevant to SA and UQ in the field of radiation shielding in the old literature[10]. A code dedicated for the shielding problems has been developed and advanced[11-12]. Several papers about SA and UQ have been published based on the perturbation theory[13-14], and the sampling method has been also adopted[15]. The data assimilation simultaneously using the shielding, critical and kinetics benchmark experiments has been also reported[16].

5. Summary

The final report has been published from the covariance data use promotion working group established under the JENDL committee after the three-year activity. In this manuscript, two relevant topics have been described by one of the members of this working group. In addition, reviews for SA, UA, and DA have been provided.

References

[1] Covariance Data Utilization and Promotion Working Group, JENDL Committee, "Final report of the Covariance Data Utilization and Promotion Working Group in the JENDL Committee," JAEA-Review 2021-014 (2021) [in Japanese].

[2] M. D. McKay, "Sensitivity and uncertainty analysis using a statistical sample of input values," Chap. 4, Uncertainty Analysis (Ed. Y. Ronen), CRC press (1988).

[3] S. Lahaye, "Choice of positive distribution law for nuclear data," EPJN, 4, 38 (2018).

[4] G. Zerovnik, A. Trkov, D.L. Smith, R. Capote, "Transformation of correlation coefficients between normal and lognormal distribution and implications for nuclear applications," Nucl. Inst. Methods in Phys. Res. A, 727, p.33-39 (2013).

[5] A. Gandini, "Uncertainty analysis and experimental data transposition methods based on perturbation theory," Chap. 6, Uncertainty Analysis (Ed. Y. Ronen), CRC press (1988).

[6] A.J. Koning, D. Rochman, "Towards sustainable nuclear energy: putting nuclear physics to work," Ann. Nucl. Energy., 35, p.2024-2030 (2008).

[7] Y. Ronen, "Uncertainty analysis based on sensitivity analysis," Chap. 2, Uncertainty Analysis (Ed. Y. Ronen), CRC press (1988).

[8] A. Gandini, et al., "Nuclear data and integral measurement correlation for fast reactors, part 1: statistical formulation," CNEN Rep. RT/FI(73)5, Rome, (1973).

[9] H. Mitani, H. Kuroi, "Adjustment of group cross-sections by means of integral data," J. Nucl. Sci. Technol., 9[7], p.383-394, (1972).

[10] NEA Specialist Meeting on sensitivity studies and shielding benchmarks, Paris. November 17, (1977).

[11] K. Furuta, et al., "SUSD: a computer code for cross section sensitivity and uncertainty analysis including secondary neutron energy and angular distributions," UTNL-R-0185, University of Tokyo, (1986).

[12] I. Kodeli, "A multidimensional deterministic nuclear data sensitivity and uncertainty code system: method and application," Nucl. Sci. Eng., 138, p. 45-66 (2001).

[13] I. Kodeli, "Cross-section sensitivity and uncertainty analysis of the FNG copper benchmark experiment," Fusion Eng. Design, 109-111, p. 1222-1226 (2016).

[14] G. Chiba, "Sensitivity and uncertainty analysis of fusion neutronics benchmark problem with deterministic code system CBZ," 85-90, JAEA-Conf 2017-001 (2017).

[15] D. Rochman, et al., "Exact nuclear data uncertainty propagation for fusion neutronics calculations," Fusion Eng. Design, 85, p. 669-682 (2010).

[16] I. Kodeli, L. Plevnik, "Nuclear data adjustment exercise combining information from shielding, critical and kinetics benchmark experiments ASPIS-Iron 88, Popsy and SNEAK-7A/7B," Prog. Nucl. Energy, 106, p. 215-230 (2018).

This is a blank page.

9 Study of radii of proton and nuclei by electron scattering

Toshimi Suda[†1]

[1]Research Center for Electron-Photon Science, Tohoku University, 1-2-1 Mikamine,
Sendai, 982-0826, Japan
[†]Email: suda@lns.tohoku.ac.jp

Abstract

The size of an atomic nucleus is one of the most fundamental quantities to characterize atomic nuclei. Electron scattering is known to be the best method to study their size and shape. In this report, our ongoing research activities for exploring the size of the proton and exotic nuclei by electron scattering are presented.

1 Introduction

One of the most fundamental properties of atomic nuclei is their size. The exact size provides the cornerstone in our understanding of nuclei, and is an essential input to test nuclear structure models.

The size is defined by the second moment of the nucleon density distributions, $\rho(r)$, namely

$$< r^2 > = \int r^2 \rho(r) \, \mathrm{d}^3 r. \tag{1}$$

Electromagnetic probes have played an essential role in determining the size, thanks to the fully understood nature of the electromagnetic interaction. The probes, such as electron scattering, μ X-ray, and isotope-shift, make it possible to determine the radius in the least model-dependent way. These electromagnetic probes are primarily sensitive to the proton only, as the neutron is a net-charge zero particle. The size precisely determined by the electromagnetic probes refers to the charge radius.

Among various electromagnetic probes, electron scattering has consistently played a leading role in determining the size (and shape) of the atomic nuclei. The best known historical example is the charge density distributions measured by high-energy electron scattering pioneered by the Nobel Laureate Prof. R. Hofstadter and his colleagues in the 1950s[1].

The measured charge density distributions of many stable nuclei by elastic electron scattering visualized how the charge densities and radii change as a function of mass number A[2]. Under an independent-particle picture, the charge density distribution, $\rho_c(r)$, is an incoherent sum of the wave function squared of all protons, $|\phi_i(\vec{r})|^2$ as,

$$\rho_c(\vec{r}) \;\; = \;\; \sum_{i=1}^{Z} |\phi_i(\vec{r})|^2 \quad , \tag{2}$$

where Z is the proton number. Thus it provides a direct and stringent testing ground of nuclear structure theories.

In this report, I will briefly introduce our ongoing research activities on the size of proton and nuclei including exotic ones using electron scattering.

2 Proton charge radius

After Hofstadter's work [3] which revealed that the proton is not a point particle but has a finite size, the size, especially the charge radius, has been long studied by electron scattering in addition to the intensive studies, using the higher-energy electron, of its internal structure by deep inelastic scattering followed by a discovery of the quarks.

In the 1990s, hydrogen spectroscopy started to provide the proton size as well, utilizing the fact that the orbital energy of the s-wave electron is sensitive to the finite size of the proton. Since their results were consistent with the radius determined by electron scattering, the proton charge radius has been considered to be ~ 0.88 fm[4]. In 2010, however, a new result on the proton charge radius determined by the μ-hydrogen spectroscopy appeared [5] with surprise. The radius was reported as 0.844 fm, which is not consistent with that determined by electrons.

This problem, later called the "Proton radius puzzle" [6] had a significant impact on nuclear physics as the fundamental physical quantity of the building block of atomic nuclei and on atomic physics as well. This is because the Rydberg constant being the fundamental physical constant determined so far with the greatest precision depends strongly on the proton radius. Furthermore, speculation linking this disagreement to an unknown difference in physical properties of electron and μ [7], which is beyond the Standard Model, called public attention.

Since then, experiments with state-of-art technologies have been planned and conducted worldwide, from some of which new results have been published recently [8, 9, 10, 11, 12]. Some of the recent results by electron scattering and hydrogen spectroscopy experiments were reported to be consistent with that by μ-hydrogen spectroscopy. The situation thus becomes further confused since we do not know the reason for the disagreement with the previous results.

As for the proton radius by electron scattering, possible non-negligible model dependence to extract the radius from the measured data has been pointed out[13]. It is, thus, highly desired to perform electron scattering which allows determining the radius in the least model-dependent as possible.
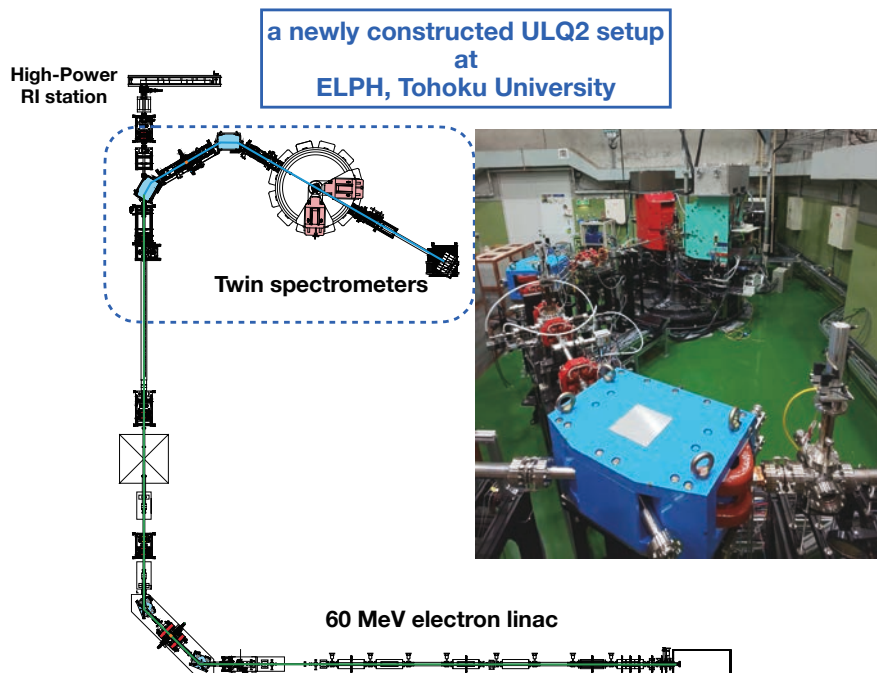
Figure 1: A newly installed ULQ2 setup at ELPH, Tohoku University aiming at determining the proton radius by low-energy electron scattering.

The proton charge radius, $< r_p >$, is defined as[14]

$$\langle r_p^2 \rangle \equiv -6 \, \frac{\mathrm{d} G_E(Q^2)}{\mathrm{d} Q^2}|_{Q^2 \to 0} \, , \qquad (3)$$

here $G_E(Q^2)$ is the proton charge form factor. Q^2 is the four-momentum transfer ,

$$Q^2 \equiv \vec{q}^2 - \omega^2 = 4 \, E_e \, E_e' \, \sin^2(\theta/2). \qquad (4)$$

ω、$\vec{q}$ are the energy and three-momentum transfer, E_e, E_e' are electron energies before and after scattering, and θ electron scattering angle, respectively.

Considering the fact that elastic cross section goes infinity at $Q^2 = 0$, it is evident from Equation 3 that the measurement of $G_E(Q^2)$ under extremely small Q^2 region as possible with great accuracy is essential.

This is why we decided to start the ULQ2 (Ultra-Low Q2) project at Tohoku, where a low-energy electron linac is still in operation. The ULQ2 project aims to measure the elastic cross section under the lowest-ever momentum transfer using the low energy electron beam, $E_e = 20 - 60$ MeV, available at the Research Center for Electron-Photon Science, Tohoku University. Using experimentally separated $G_E(Q^2)$ from the measured cross section with the Rosenbluth-separation technique, the proton charge radius will be determined in the least model-dependent way. To our knowledge, no electron-accelerator facility for nuclear physics exists today to perform such low-energy electron scattering.

The ULQ2 setup consisting of a new electron beamline and twin spectrometers, shown in Fig. 1, was completed in Dec. 2021, and their commissioning is underway. The physics run is expected to start in FY 2022.

3   Short-lived exotic nuclei

The charge radii of many exotic nuclei are available today, which were determined by isotope-shift measurements[15]. The transition-frequency difference between isotopes, measurable with super-precise technique, is directly related to their charge-radius difference. Using the charge radius of stable isotopes determined by electron scattering, one can bridge to unstable isotopes using isotope-shift measurements.

The charge radius, however, is an integrated quantity of the charge density distribution as Equation (1); thus it is not possible to discriminate different $\rho(r)$ providing the same radius. To study the internal structure in further detail, the importance of electron scattering to determine $\rho(r)$ is unquestionable.

As for the charge radius, electron scattering is also important for unstable nuclei, because it provides an absolute value of the charge radius. Note that the isotope shift provides only a relative charge radius difference between isotopes where their errors may be piled up further for those far from the stability line.

Nuclei ever studied by electron scattering strictly remained within and in the vicinity of the "valley of stability"[16]. This is simply because no thick-enough targets needed for electron scattering have been available so far for the production-hard short-lived exotic nuclei.

To apply electron scattering, the most powerful tool for structure study, to unstable exotic nuclei[17], we have constructed the world's first electron-scattering facility at the RIKEN RI Beam Factory in Japan (Fig. 2). This facility employs a novel target forming technique[18], which we invented and named as SCRIT (Self-Confining RI ion Target), to achieve the required luminosity for elastic scattering, $L \sim 10^{27}$ /cm^2/s using a pretty small number of target nuclei, $N \sim 10^{7-8}$.
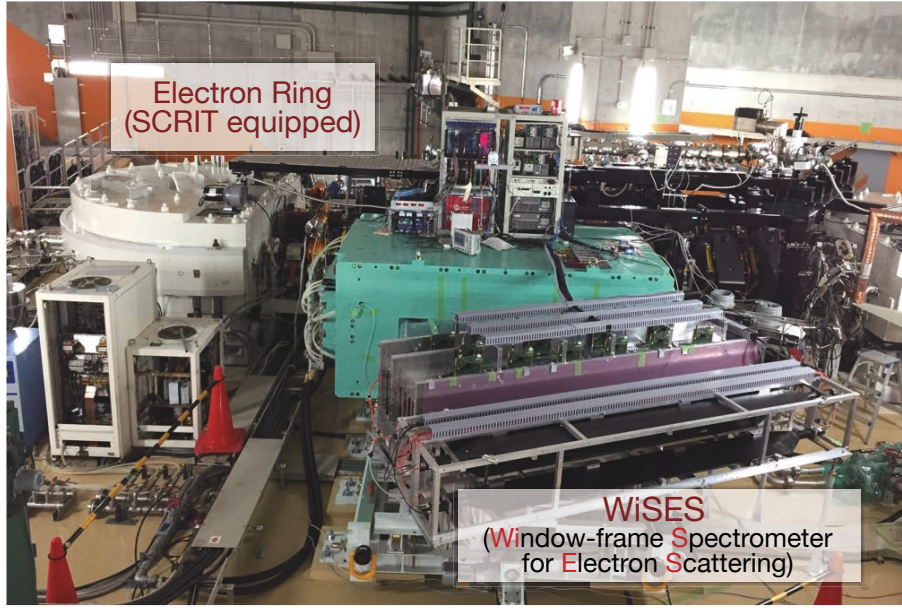
Figure 2: SCRIT electron scattering facility in RIKEN RI Beam Factory.

The performance study of the SCRIT facility using $N \sim 10^8$/s of a stable ^{132}Xe[19] successfully demonstrated that electron scattering for unstable nuclei is feasible.

The first unstable-nuclear targets for electron scattering at this facility will be ^{137}Cs and ^{138}Xe as they are relatively easy to produce and extract enough number of ions from the ISOL, ERIS (Electron-beam-driven RI separator for SCRIT), which uses the photo-fission reaction of uranium to deliver neutron-rich unstable nuclei.

4   Neutron-distribution radius of exotic nuclei

Electron scattering has revealed how the charges distribute spatially in stable nuclei. Since the proton charge mostly dominates the charge density distribution, less knowledge has been obtained so far about the neutron by electron scattering. In addition to magnetic electron scattering[20], a recent parity-violating electron scattering off ^{208}Pb at JLAB[21, 22] aiming to measure the radius of the neutron distribution is an exceptional example. Since both experiments require extremely high luminosities due to small magnetic-scattering cross section and extremely small weak-interaction effects, it is hard to imagine their application to exotic nuclei, where high-luminosity is not realistic.

Recently, one new way to access the neutron distributions by electron scattering has been proposed. Kurasawa and Suzuki have shown in their relativistic nuclear-structure models, for the first time, that the fourth moment of the nuclear charge density distribution includes the radius of the neutron distribution explicitly[23].

Here, let us start discussion about the second moment, $< r_c^2 >$, is expressed as,

$$< r_c^2 >=< R_{p(point)}^2 > +r_p^2 + \frac{N}{Z}r_n^2 + \text{rel. corr.,} \tag{5}$$

where $< R_{p(point)} >$, r_p, r_n are the radius of the point proton distribution, the proton charge radius and the neutron charge radius, respectively. The relativistic correction includes the contributions from the spin-orbit interaction. $< r_c^2 >$ is measured experimentally by electron scattering, μ-X ray, and isotope shifts, and $R_{p(point)}$ calculated theoretically.

Since the second moment corresponds to the exact (charge) size of atomic nuclei providing a strict testing ground for our understanding of the nuclear structure, they have been measured extensively, including unstable nuclei.

The fourth moment, $<r_c^4>$ is shown to include the neutron-distribution radius[23] as,

$$
\begin{aligned}
<r_c^4> = {} &<R_{p(point)}^4> + \frac{10}{3}<R_{p(point)}^2><r_p^2> \\
&+ \frac{10}{3}<R_{n(point)}^2><r_n^2>\frac{N}{Z} + (\text{rel.corr.}).
\end{aligned}
\tag{6}
$$

One finds that the neutron-distribution radius, $<R_{n(point)}>$, appears explicitly. Assuming one measures $<r_c^4>$ experimentally and knowing $<R_{p(point)}^2>, <r_p^2>$ and $<r_n^2>$, one may determine $<R_{n(point)}>$ from $<r_c^4>$ determined by elastic electron scattering.

We apply this theory to doubly-magic stable nucleus ^{208}Pb using the charge density distribution, $\rho_c(r)$, known precisely by elastic electron scattering, the neutron-distribution radius, $<R_{n(point)}>$, is determined as 5.736 ±0.013fm[24]. Extracting the (point)proton-distribution radius, 5.455±0.012 fm from the charge radius, 5.503±0.002 fm, the neutron skin thickness, defined as the difference between the proton and neutron distribution radii, is determined as 0.282±0.024 fm. This looks surprisingly consistent with the skin thickness recently determined by the parity-violating electron scattering experiment at JLAB, 0.283±0.071 fm.

The neutron skin thickness of ^{48}Ca is also estimated in the same manner as 0.219±0.013 fm[24], which will be measured at JLAB by the parity-violating electron scattering experiment.

As previously discussed, electron scattering for neutron-rich exotic nuclei will be soon started at the SCRIT electron scattering facility. Then one may ask whether it is possible to access the neutron-distribution radius of unstable nuclei also through $<r_c^4>$ at the SCRIT facility.

There are two ways to determine $<r_c^4>$ of the charge density distributions. They are 1) based on Equation (1) with $\rho_c(r)$ determined by elastic electron scattering measured covering a wide range of q, and 2) using the Taylor expansion of the charge form factor, $F_c(q)$, measured by elastic electron scattering at the low q region,

$$
F_c(q) = 1 - \frac{<r_c^2>}{3!}q^2 + \frac{<r_c^4>}{5!}q^4 + ...
\tag{7}
$$

Since elastic cross section has $1/q^4$ dependence and knowing $<R_{p(point)}^2>$ for exotic nuclei by isotope shift measurements, the method 2) may allow one to study the neutron-distribution radius through $<r_c^4>$ obtained using Equation(7) at the low-luminosity electron scattering facility for exotic nuclei. A feasibility study of this exciting opportunity at the SCRIT electron scattering facility is underway

References

[1] R. Hofstadter, Nuclear and nucleon scattering of high-energy electrons, Ann. Rev. Nucl. Sci. 7 (1957) 231.

[2] H. de Vries, C.W. de Jager, and C. de Vries, Nuclear charge-density-distribution parameters from elastic electron scattering, At. Data Nucl. Data Tables 36 (1987) 495-536.

[3] R. Hofstadter: Nobel Lecture Archive, https://www.nobelprize.org/prizes/physics/1961/hofstadter/lecture/ (accessed 2022-01-10).

[4] C. Carlson, The proton radius puzzle, Prog. Part. Nucl. Phys. **82** (2015) 59-77.

[5] R. Pohl et al., The size of the proton, Nature **466** (2010) 213-216.

[6] A. Antognini et al., Proton Structure from the Measurement of 2S-2P Transition Frequencies of Muonic Hydrogen, Science **339** (2013) 417.

[7] C. E. Carlson and B. C. Rislow, New physics and the proton radius problem, Phys. Rev. **D86** (2012) 035013.

[8] W. Xiong et al., A small proton charge radius from an electron-proton scattering experiment, Nature **575** (2019) 147-150.

[9] A. Beyer et al., The Rydberg constant and proton size from atomic hydrogen, Science **358** (2017) 79-85.

[10] H. Fleurbaey et al., New Measurement of the 1S-3S Transition Frequency of Hydrogen: Contribution to the Proton Charge Radius Puzzle, Phys. Rev. Lett. **120** (2018) 183001.

[11] N. Bezginov et al., A measurement of the atomic hydrogen Lamb shift and the proton charge radius, Science **365** (2019) 1007-1012.

[12] A. Grinin et al., Two-photon frequency comb spectroscopy of atomic hydrogen, Science **370** (2020) 1061-1066.

[13] I. Sick, Proton Charge Radius from Electron Scattering, Atoms **6** (2018) 2.

[14] G. A. Miller, Defining the proton radius: A unified treatment, Phys. Rev.**C99** (2019) 035202.

[15] P. Campbell, I.D. Moore and M.R. Pearson, Laser spectroscopy for nuclear structure physics, Prog. Part. Nucl. Phys. 86 (2016) 127-180.

[16] T. Suda and H. Simon, Prospects for electron scattering on unstable, exotic nuclei, Prog. Part. Nucl. Phys. 96 (2017) 1-31.

[17] T. Suda, Electron Scattering for Exotic Nuclei, Journal of Physics, 1643(2020) 012159.

[18] M. Wakasugi, T. Suda, Y. Yano, A new method for electron-scattering experiments using a self-confining radioactive ion target in an electron storage ring, Nucl. Instrum. Methods A 532 (2004) 216-223.

[19] K. Tsukada et al., First Elastic Electron Scattering from ^{132}Xe at the SCRIT Facility, Phys. Rev. Lett. 118 (2017) 262501.

[20] T. W. Donnelly and I. Sick, Elastic magnetic electron scattering from nuclei, Reviews of Modern Physics, 56 (1984) 461-566.

[21] S. Abrahamyan et al., Measurement of the Neutron Radius of ^{208}Pb through Parity Violation in Electron Scattering, Phys. Rev. Lett. 108, (2012) 112502.

[22] D. Adhikari et al., Accurate Determination of the Neutron Skin Thickness of ^{208}Pb through Parity-Violation in Electron Scattering, Phys. Rev. Lett. 126, (2021) 172502.

[23] H. Kurasawa and T. Suzuki, The nth-order moment of the nuclear charge density and contribution from the neutrons, Prog. Theor. Exp. Phys. 2019, (2019) 113D01.

[24] H. Kurasawa, T. Suda and T. Suzuki, The mean square radius of the neutron distribution and the skin thickness derived from electron scattering, Prog. Theor. Exp. Phys. 2021, (2021) 013D02.

Acknowledgments

10   A nuclear periodic table: from elementouch to nucletouch

Kouichi HAGINO and Yoshiteru MAENO

Department of physics, Kyoto University, Kyoto 606-8502, Japan

The magic numbers due to closures of the nucleonic shells, that correspond to noble gases in elements, have played a fundamental role in nuclear physics. We here discuss our recent invention of a periodic table for atomic nuclei, called "Nucletuch". This is in a sense an extension of the 3D periodic table for elements, "Elementouch", invented by one of the authors (Y.M.) in 2001. While the Elementouch recovers features of Mendeleev's periodic law, the "Nucletouch" provides a nice visualization of nuclear deformation. By comparing the two 3D periodic tables, we show that there is an unexpected coincidence between atoms and nuclei concerning the alignments of elements.

1. Introduction

A periodic table of chemical elements is undoubtedly one of the most important achievements in modern science. It concisely demonstrates the periodic properties of the building blocks of nature in a form of a simple table. The Mendeleev's periodic table, invented in 1869, is based on the "periodic law" in which the chemical and physical properties of elements and their compounds are periodic functions of the atomic weight [1,2]. It is in a short form consisting of eight groups, while the periodic table widely used today is in a long form consisting of 18 columns. The long form of the periodic table was first invented by Alfred Werner in 1905 [3] and then extended by Von Paul Pfeiffer in 1920 [4]. See Ref. [5] for a history of the modern periodic table.

The periodicity of the atomic properties of elements originates from the shell structure of the electron orbitals around a nucleus. In particular, the energy gap between the fully occupied shell configuration and the first unoccupied level leads to the chemically inert noble-gas elements, He, Ne, Ar, Kr, Xe (, and Og) with the atomic magic numbers 2, 10, 18, 36, 54, 86 (, and 118). We note that protons and neutrons in a nucleus also exhibit orbital shell structures similar to those of the electrons in an atom. When orbital shells are completely filled up with protons or neutrons, stable nuclei analogous to noble gas atoms are formed. The magic numbers known for stable nuclei are 2, 8, 20, 28, 50, 82, and 126. The success of the nuclear shell model was rewarded as the Nobel prize in physics in 1963 to Maria Goeppert Mayer and J. Hans D. Jensen, along with Eugene Wigner.

Since both atoms and nuclei show similar shell structures, we ask ourselves whether one can construct a periodic table of atomic nuclei, similar to the well known periodic table of elements, by arranging elements according to the nuclear shell structure. Before we address this question, however, let us first discuss in the next section a possible extension of the periodic table of elements.

2. 3D periodic table: Elementouch

Mendeleev's periodic law is embodied in his short-form periodic table [2]. In the 1871 version of periodic table, the groups forming columns represent the valence properties in forming oxides and

hydrides, as clearly indicated in his table as "R_2O" and "RO" for the groups I and II, "RH and R_2O_7" for the group VII (halogens), etc. Such valence tendencies of forming chemical compounds are no longer very explicit in the long-form table based on the electron shell structure. For instance, Ca and Cd are in the same column in the Mendeleev's table, but they are put in different columns in the long-form table. The same thing happens for Ti and Sn.

(a)   (b)   (c)
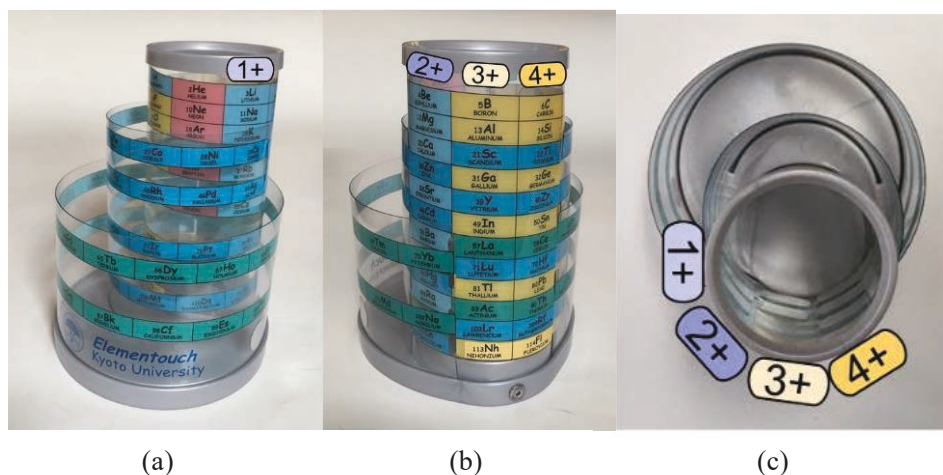
Fig. 1. The three-dimensional (3D) helical periodic table "*Elementouch*". (a) The three tubes represent *s-p* blocks, *d* block and *f* block. (b) Divalent, trivalent and tetravalent elements align in the respective columns. (c) The top view of Elementouch.

To resolve this problem, one of us (Y.M.) invented the 3D periodic table "*Elementouch*" [5,6,7], which is constructed by continuously winding a ribbon of element symbols in three-tube helix as shown in Fig. 1. In this way, all divalent, trivalent and tetravalent elements line up in the respective columns. It is thus possible to express the "periodic law" in the Mendeleev's short-form periodic table, while keeping the shell structure expressed in the modern long-form table. Mendeleev noted "Cu, Ag, and Au occupy two places – one in the first group (I) and the other in the eighth (VIII)", considering their compounds Ag_2O, CuCl and AgCl [2,8]. They were placed in the group I with parentheses. The divalent state of Cu is well known as the basis of high-temperature superconductivity of cuprates. To express such valence tendensicies, in the Elementouch, the group 11 (IB) elements are placed not exactly on the same tube as the group 1 (IA) elements as shown in Fig. 1 (a).

The Elementouch resolves other possible drawbacks of the long-form of periodic table. We here summarize the characteristic features of the Elementouch as compared with the 2D periodic table of the long-form: (1) elements with similar valence properties are arranged in the same columns, reproducing basic features of the Mendeleev's periodic law, (2) element symbols are lined up in a seamless way, without unnatural gaps between Be - B and Mg – Al, (3) the *f*-block elements are incorporated continuously and treated equally to the *d*-block elements, rather than being separated as in the long-form periodic table, and (4) from the top, an atomic model with *s/p*, *d*, and *f* orbitals can be clearly depicted as shown in Fig. 1 (c).

3. Nuclear periodic table: Nucletouch

Let us now discuss a periodic table of atomic nuclei. To this end, it should firstly be pointed out that atomic nuclei consist of two different kinds of nucleons, and thus their properties cannot be determined solely by the number of protons (or neutrons) as in the periodic table of elements. As a matter of fact, a two-dimensional map of atomic nuclei, that is, a nuclear chart [9,10], would be more useful than a one-dimensional periodic table in order to classify detailed properties of atomic nuclei. Nevertheless, it might still be useful and pedagogical to construct a nuclear periodic table e.g., in order to visualize the difference in magic numbers between nuclear systems and electronic systems. The 3D nuclear periodic table was invented with such motivation [11,12].

To construct a nuclear periodic table, we considered the shell structure of protons. Even though a similar periodic table for neutrons could be constructed, we found it much easier to consider a nuclear periodic table based on protons, as each proton magic number can be characterized by the name of a particular element. We thus first arranged the elements with the proton magic numbers in the same column. Those are: He (Z=2), O (Z=8), Ca (Z=20), Ni (Z=28), Sn (Z=50), and Pb (Z=82). Zr (Z=40) often shows behaviors similar to the magic nuclei due to the sub-shell closure at Z=40 [13], and we also included it in the same column. Though the heaviest element discovered so far is Oganessson (Z=118), the proton magic number after Z=82 is currently unknown. In our nuclear periodic table, we chose the traditional proton magic number, Z=114, for superheavy elements and arranged Fl underneath Pb.

After we set up the column for the magic and semi-magic nuclei, we next arranged other nuclei according to the known nuclear shell structure. The ordering of each single-particle level within shells depends on the number of neutrons. Moreover, for open shell nuclei, those single-particle levels are occupied only partially due to the pairing correlation. In mid-shell nuclei, nuclei may even be deformed, yielding a deformed mean-field potential. For these reasons, we considered a group of single-particle levels within each shell, instead of treating each single-particle level individually.
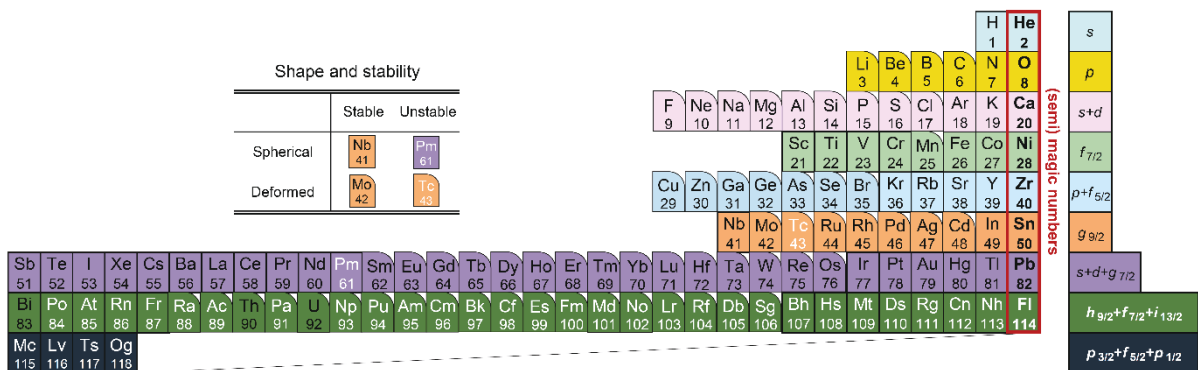
Fig. 2. A nuclear periodic table based on the proton magic numbers [11]. The rightmost column shows the elements with the proton magic and semi-magic numbers. The other elements are arranged according to the nuclear shell structure, for which the single-particle levels for the valence protons are denoted with different colors. The elements shown in round-corner boxes are those whose nucleus is substantially deformed in the ground state. Elements with black symbols have stable nuclei, while those with white symbols represent those with all the isotopes unstable.

Figure 2 shows a nuclear periodic table so constructed. We here also distinguish (nearly) spherical and deformed nuclei using different types of a box: the nuclei for the elements shown in round-corner boxes have the quadrupole deformation parameter, β_2, is larger than 0.15. To this end, we chose the most abundant nucleus for each element and estimated the deformation parameter using the theoretical calculations by Möller *et al*. [14]. For the elements lighter than N, we regarded the elements Li, Be, B, and C as deformed due to the well-known alpha-particle structure. In addition, we also distinguished between stable and unstable elements using different types of symbols: the elements with the white symbols are unstable elements, that is, elements where all the isotopes are unstable.

In the figure, one can clearly see that the elements in the vicinity of the shell closures are all spherical, while the deformation is developed in the mid-shell regions, as has been known well in nuclear physics. The former elements can be interpreted in terms of one or two protons holes outside the shell closures, and it would be meaningful to arrange them in the same columns.

The 3D version of the nuclear periodic table, Nucletouch, is shown in Fig. 3, in which the magic and the semi-magic nuclei are put in the center of the periodic table. Its paper pattern is available at a Supplemental Material page on the web site of the Japan Physics Society [15].
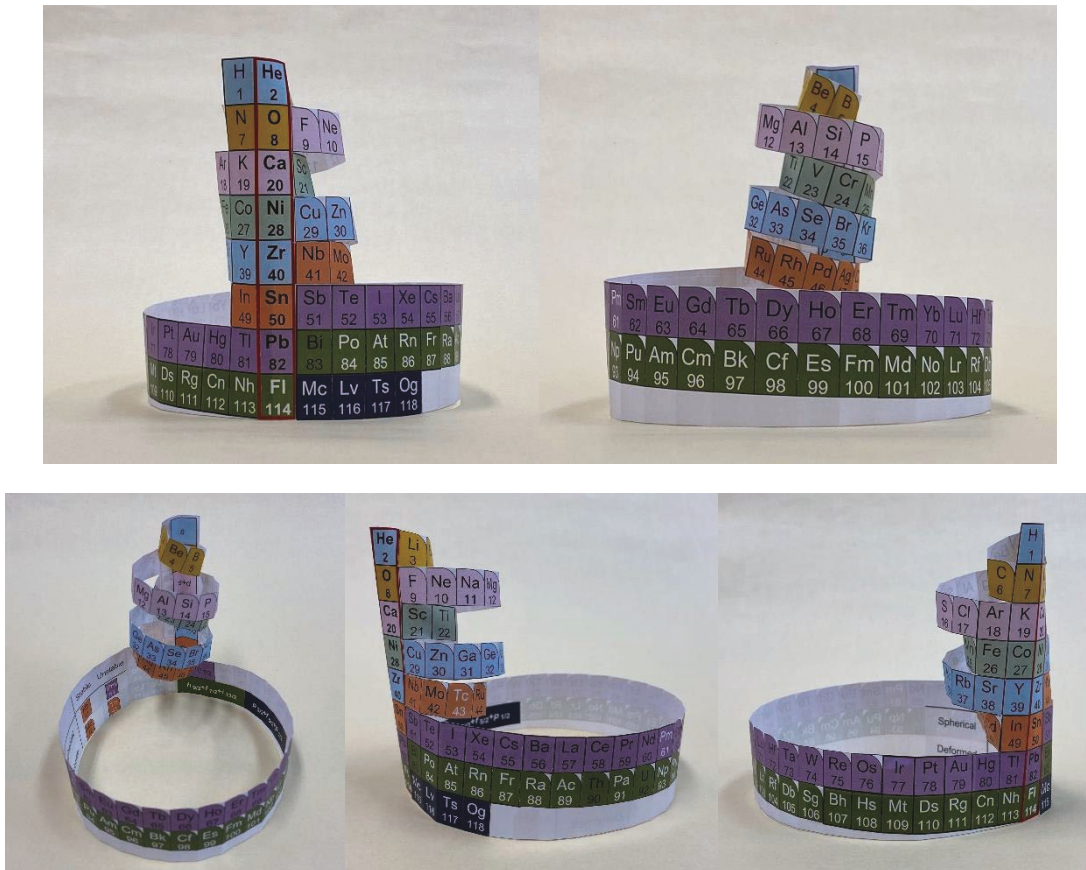
Fig. 3. The 3D nuclear periodic table, Nucletouch [11,15].

Figure 4 shows the usual periodic table of elements. It is quite amusing to notice that the magic nuclei Sn-Pb-Fl are aligned in the same column also in the ordinary "atomic" periodic table. This is merely a coincidence, but this is caused by the fact that the increment of electron numbers 32 of the noble-gas

elements from Xe (54) to Rn (86) and to Og (118) is identical to the increment of proton numbers among the magic nuclei Sn (50), Pb (82) and Fl (114). Because of this magic coincidence, the alignments of the elements in both periodic tables are very similar after Nb (41). For instance, Ag (47) is just above Au (79) and La (57) is just above Ac (89). This would not have been noticed unless the nuclear periodic table was invented.

Fig. 4. The periodic table of elements, with a highlight on the proton magic nuclei, Sn, Pb, and Fl.

4. Summary

Motivated by the 3D periodic table, Elementouch, we have constructed a similar periodic table for atomic nuclei and named it Nucletouch. This table was based on the shell structure of protons in atomic nuclei close to the stability line, in which the elements were arranged according to the known proton magic numbers. The nuclear periodic table provides a clear visualization of the well known fact that the nuclei in the vicinity of the shell closures are spherical in the ground state, while nuclei tend to be deformed as the distance from the shell closures increases. We have also pointed out a magic coincidence, for which the same sequence of elements, such as Sn-Pb-Fl, can be found both in the nuclear and in the atomic periodic tables.

The nuclear periodic table we invented has several pedagogical significances. For instance, it may provide a useful means to visualize the difference in magic numbers between nuclear and electronic systems. It may also be helpful in understanding why Ca, Pb and Bi, with which evaporation residue cross sections are enhanced for several reasons, have been used to synthesize superheavy elements up to Og.

Finally, we mention that a variety of patterns to make models of *Elementouch* and *Nucletouch* can be downloaded from: *http://www.ss.scphys.kyoto-u.ac.jp/elementouch/en/index.html*

References

[1] Mendeleev, D., On the relation of the periodic properties to the atomic weights of the elements. Zeitschr. für Chem., vol. 12, 1869, pp. 405-406.

[2] Mendeleev, D., On the periodic regularity of the chemical elements. Ann. der Chem. Pharmacie, vol. 8 (Suppl.), 1871, pp. 133-229.

[3] Werner, A., Beitrag zum Aufbau des periodischen Systems. Berichtungen der deutschen chemischen Gesellschaft, vol. 38, 1905, pp. 914-921.

[4] Pfeiffer, V. P., Die Befruchtung der Chemie durch die Roentgenstrahlenphysik. Naturwiss., vol. 8, 1920, pp. 984-991.

[5] Maeno, Y., Hagino, K., and Ishiguro, T., Three related topics on the periodic tables of elements, Found. of Chem. vol. 23, 2021, pp. 201-214.

[6] Maeno, Y., Periodic-table-of-the-elements stationery. Design No. 1149493, 2001, Japan Patent Office. https://www.j-platpat.inpit.go.jp/d0000 (accessed 2022-3-10).

[7] Maeno, Y., Three-dimensional periodic table of the elements, Butsuri, vol. 57, 2002, pp. 681-683 [in Japanese].

[8] Jensen, W.B. (ed.), Mendeleev on the periodic law: selected writings, 1869-1905, Dover, New York, 2002.

[9] Koura, H., Katakura, J., Tachibana, T., Minato, F.. Chart of the nuclides, Japan Atomic Energy Agency, 2018. https://wwwndc.jaea.go.jp/CN14/sp/ (accessed 2022-3-10).

[10] Magill, J., Dreher, R., Sóti, Zs., Karlsruher Nuklidkarte/Chart of the Nuclides, 10th edition, Nucleonica GmbH, Karlsruhe, 2018.

[11] Hagino, K. and Maeno, Y., A nuclear periodic table, Found. of Chem. vol. 22, 2020, pp. 267-273.

[12] Maeno, Y. and Hagino, K., Nuclear periodic table: magical relation, Butsuri, vol. 75, 2020, pp. 761-765 [in Japanese].

[13] Garcia-Ramos, J.D., Heyde, K., Quest of shape coexistence in Zr isotopes, Phys. Rev. C, vol. 100, 2019, 044315.

[14] Möller, P., Sierk, A.J., Ichikawa, T., Sagawa, H., Nuclear ground-state masses and deformations: FRDM(2012), Atomic Data and Nucl. Data Tables, vol. 109-110, 2016, 1.

[15] https://www.jps.or.jp/members/books/suppl.php (accessed 2022-3-10).

Acknowledgements

11　Role of ADS and its development issues

Kenji NISHIHARA[1*]

[1] Japan Atomic Energy Agency

2-4 Shirakata, Tokai-mura, Naka-gun, Ibaraki-ken 319-1195, Japan

*Email: nishihara.kenji@jaea.go.jp

This tutorial contains a role of accelerator-driven system (ADS) in the nuclear fuel cycle and necessity of nuclear data to realize the ADS. After an overview of the Japanese nuclear fuel cycle and government direction, the geological disposal concept of high-level waste (HLW) will be described. By partitioning problematic elements from the HLW and transmuting, utilizing or storing them, geological disposal can be changed. ADS plays a role of transmuting minor actinide (MA) separated from HLW to fission product (FP), which are less radio-toxic than MA. The principle of ADS will be introduced with technological issues, and finally utilization of nuclear data for R&D on ADS will be introduced.

1. Role of ADS and Partitioning & Transmutation (P&T) technology in the nuclear fuel cycle

1.1. Background

The tutorial begins with our nation's current and near-future nuclear fuel cycle. In 2020, nuclear power plants and nuclear fuel cycle restarts after shock of Fukushima Daiichi Nuclear Power Plant accident. Nuclear power plants gradually restart after meeting new regulatory standards. Rokkasho Reprocessing Plant will soon start operation. A literature survey on geological disposal of radioactive waste begins.

Prime Minister Kan declared aiming for a carbon-neutral, decarbonized society by 2050 in Oct., 2020. Then, the sixth Basic Energy Plan was approved by the Cabinet in Oct., 2021. In the plan, Nuclear Power Plant (NPP) will supply 20-22% of electricity in 2030, and 30-40% in 2050 including thermal power with CO_2 capture as a reference value for further discussion. Toward 2050, utilization of NPP is very ambiguous, so nuclear fuel cycle as well. However, nuclear spent fuel accumulated past and near-future must be managed in any future scenario. Partitioning and transmutation technology is being developed for this purpose.

1.2. Origin of radioactive waste

Radioactive materials occur in two passes in NPP. One is the fission process of uranium-235, which is a heat source in the core of NPP. When nucleus of uranium-235 is hit by a neutron, it fissions in certain probability, then divided into two FPs. Because this process is stochastic, various kind of FPs is produced and some of them are radioactive. Another origin is the capture process of uranium-235 and uranium-238. When the nucleus of uranium is hit by a neutron again, it can capture neutron instead of fission and

becomes another isotope with increased mass. The capture process is repeated sometimes and the isotope becomes heavier in nuclear fuel. Finally, the fuel contains plutonium and minor actinide (MA: neptunium, americium, and curium) in addition to uranium. Plutonium is used as fuel after reprocessing, but MA is regarded as radioactive wastes.

After two kinds of the process several hundreds of isotopes are produced in the fuel, but only 7 FPs and 4 MAs are categorized as long-lived isotopes, as listed in Fig.1. Americium-241 and curium-244 decay rather early, but daughters (neptunium-237 and plutonium-240, respectively) possess a long half-life. Half-life of these 11 isotopes is in order of 1 million years. Four MAs and iodine-129 must be paid attention, because they affect human when they are ingested as represented by dose coefficients in Fig.1. MAs emit alpha particle in decay process, which damages organs and iodine-129 deposits in the thyroid. Strontium-90 and cesium-137 decay fast in around 30 years but are listed because of their importance in handling waste and designing the repository.

Nuclide	Half-life (Year)	Dose coefficient (μSv/kBq)	Amount (/tHM)
U-235	0.7B	47	10 kg
U-238	4.5B	45	930 kg
Pu-238	87.7	230	0.3 kg
Pu-239	24.11M	250	6 kg
Pu-240	65.61M	250	3 kg
Pu-241	14.29	4.8	1 kg
Np-237	2.144M	110	0.6 kg
Am-241	432.6	200	0.4 kg
Am-243	7.370K	200	0.2 kg
Cm-244	18.11	120	60 g

Nuclide	Half-life	Dose coefficient (μSv/kBq)	Amount (/tHM)
Se-79	0.295M	2.9	6 g
Zr-93	1.61M	1.1	1 kg
Tc-99	0.211M	0.64	1 kg
Pd-107	6.5M	0.037	0.3 kg
Sn-126	0.23M	4.7	30 g
I-129	15.7M	110	0.2 kg
Cs-135	2.3M	2.0	0.5 kg
Sr-90	28.79	28	0.6 kg
Cs-137	30.08	13	1.5 kg

Dose coefficient= dose(Sv)/radioactivity(Bq).
An indicator of the dose by ingestion

Fig. 1   List of long-lived FP and MA

1.3. Underground disposal

Radioactive and stable isotopes produced in the nuclear fuel are vitrified in glass waste in the current technology adopted in the Rokkasho reprocessing plant. The glass waste is packed in the iron overpack with the thickness of 200 mm that can stand for corrosion for 1,000 years. In the underground repository deeper than 300 m, the overpack is placed in buffer material (compacted cray) that delays transport of radioactive isotope to groundwater. Glass, iron overpack, and cray are called "engineering barriers." Another "natural barrier" is the bedrock that delays the migration of ground water to the underground waterway.

The current repository design is affected by the strength of radioactivity in many aspects. Long-lived radioactivity from MA and FP determines the function of engineering and natural barriers, such as the necessity of buffer material and distance from the ground surface. Heat from strontium, cesium and americium dictates layout, i.e., the density of glass wastes in the repository. Gamma ray from glass waste affects the thickness of overpack as to protect workers during the handling of wastes. Partitioning and transmutation is a technology with a purpose to decrease the radioactivity and ease the difficulty of underground disposal.

1.4. Impact of partitioning and transmutation on underground disposal

Figure 2 depicts the radioactive dose contained in glass wastes originating from the spent fuel of 1 ton. After 1,000 years, when the overpack loses function, MA, uranium, plutonium and long-lived FPs remain. To reduce the long-term dose, the transmutation of these isotopes is effective. Note that the dose is "potential," that is, normally confined in the four barriers and does not contact to our life zone. From Fig.2, MA looks dominant and prior transmutation target, but it actually depends on the degree of migration to the environment in normal and unexpected conditions. Such deeper investigation is an unresolved issue.

Figure 3 shows a radioactive heat source in glass waste. Strontium and cesium are dominant in the first 150 years, then americium-241 takes place for several hundreds of years. Both heat source is important for layout design of repository. Partitioning and "storage" strategy is effective for strontium and cesium because half-life of 30 years is rather short. If they are stocked at the surface facility for 300 years, heat becomes 1/1000 and very compact repository can be realized. As to americium-241, the same strategy cannot be adopted because half-life is as long as 432 years. By partitioning and transmutation of americium to FP, the heat of americium becomes negligibly small.

Figure 4 illustrates "full-spec." partitioning and transmutation containing transmutation of MAs and long-lived FPs, storage of strontium and cesium and recycling of platinum group metals. If this scheme is realized, the long-term dose can be reduced by one or two orders of magnitudes and the repository scale can be minimized by two orders of magnitudes.
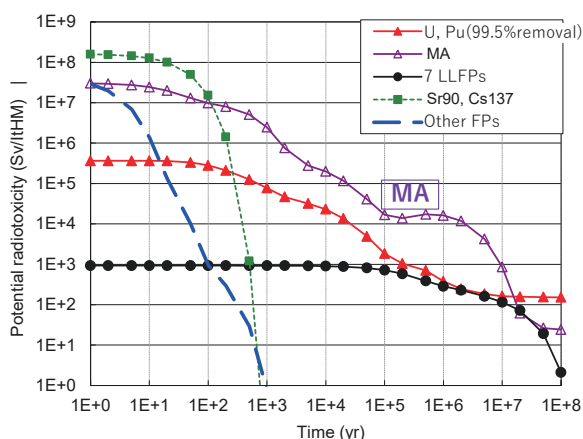
Fig. 2 Radioactive dose in glass waste normalized to spent fuel of 1 ton
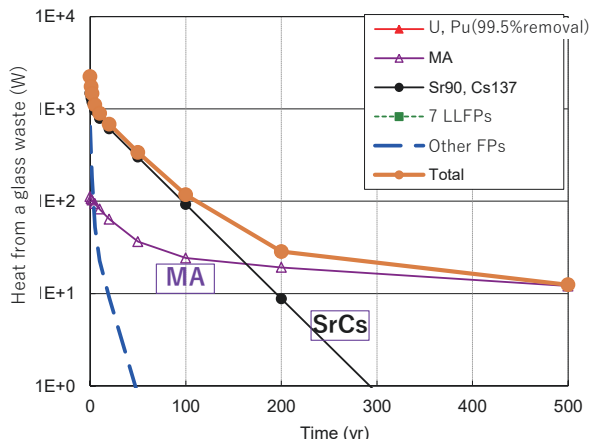
Fig. 3 Radioactive heat in glass waste
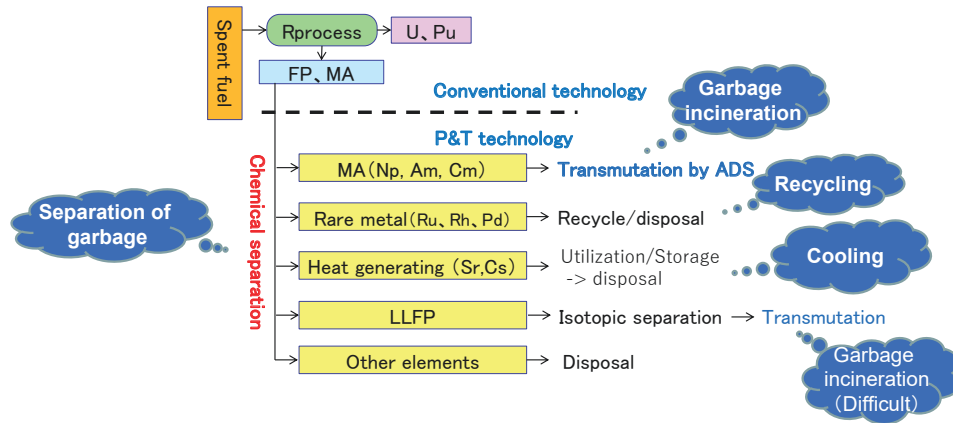
Fig.4　Full-spec partitioning and transmutation

2. Principle of ADS for MA transmutation

Accelerator-driven system (ADS) is devoted to transmutation of MA using fission reaction. Neptunium-237 and americium-241 that are main component of MA are not fissile isotope, so that fission probability is much less than capture probability when a slow neutron is absorbed to the nucleus. However, all actinide has a larger chance to fission for fast neutron with energy around 1 MeV. In ADS, fast neutrons are utilized by eliminating water from the core and using lead-bismuth eutectics as coolant.

After the fission reaction of actinides, a very small fraction of FPs releases delayed neutrons that play an important role in controlling the critical nuclear plant. However, the fraction of delayed neutron from MA fission reaction is smaller than that of uranium and the control becomes difficult. This is why ADS is considered. As illustrated in Fig. 5, the number of neutrons is kept in the critical as a result of a balance between fission versus capture and escape. On the contrary, neutron supplied by proton accelerator and fission neutron is balanced to capture and escape in the subcritical core. When accelerator operation is terminated in the accidental situation, the number of neutrons decreases very rapidly and the chain reaction stops.

R&D issues for ADS is summarized in Fig. 6. There are 5 issues: accelerator, structure, fuel, spallation target and material in lead-bismuth eutectics, and reactor physics. Nuclear data is especially relating to spallation target and reactor physics.
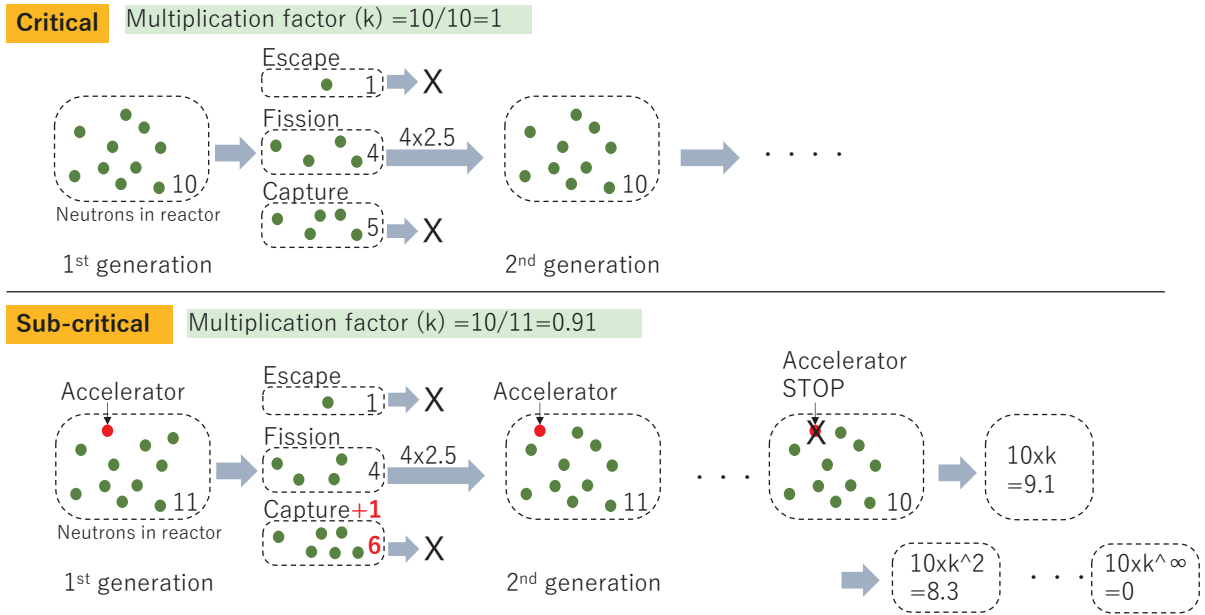
Fig.5 Critical versus sub-critical
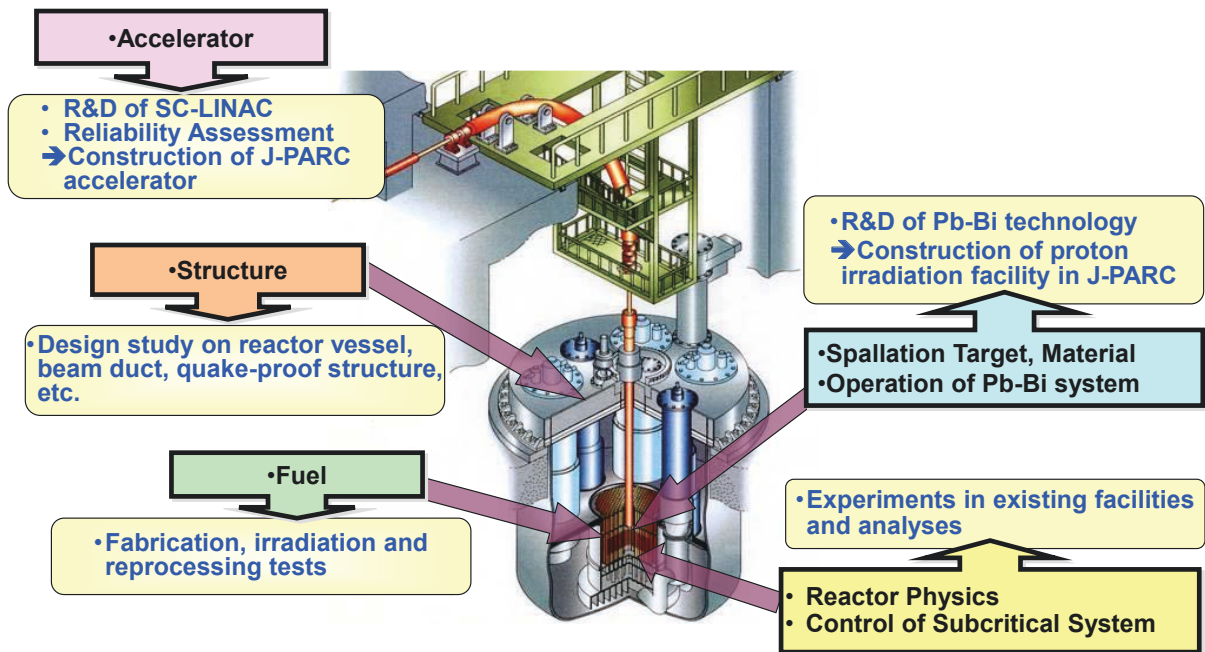
Fig. 6   R&D issues of ADS

3. Nuclear data in ADS design

Many kinds of nuclear data are used in ADS design as shown in Fig. 7, where the proton beam is accelerated and induced into lead-bismuth liquid target through the beam window, then, makes spallation neutrons.

At first, the number and energy of spallation neutron per proton is essential nuclear data that determines necessary proton beam current according to predefined total core power. Currently, the uncertainty of nuclear data is estimated as 10% in the number of spallation neutrons. Because this uncertainty is directly affecting the accelerator and target design, and current accuracy is not enough.

Fig. 7 Nuclear reactions in ADS

The second important value deduced from the nuclear data and nuclear model is heat generation in the target that is removed by the flow of liquid metal, as shown in Fig.7. For reliable designs of flow path and shape of the beam window, accurate estimation of heat distribution is important.

The third one is radiation damage on the beam window made of stainless steel. When protons or neutrons pass the steel, they bounce atoms in the lattice. Most of the atoms return to each original position, but the flaw remains. The DPA, displacement per atom, is an index of this damage. Recently, measurement of DPA in J-PARC revealed that the DPA model should be modified. High energy proton also produces hydrogen and helium nucleus in the steel and they induce embrittlement. Measurement and evaluation of production cross section are also of importance.

The forth one is production of radioactive isotopes in lead-bismuth generated by spallation reaction that causes dose on the operator and becomes waste. Estimation of isotopes with a mass far from targe nucleus possesses high uncertainty, so measurement and modification of nuclear model are desirable.

The last nuclear data is nuclear data of novel materials for neutron in the range of fission neutron energy. MA, lead-bismuth and nitrogen-15 have not been used in conventional reactors and uncertainty caused by nuclear data is large. One of the most important core parameters for ADS is multiplication factor as well as the critical reactor. The uncertainty of the factor is desired to be less than 1%, but a difference of estimator or version of evaluated nuclear library brings discrepancy of around 3%. More effort to measure and verify the uncertain nuclear data is necessary.

4. Summary

Management of spent fuel and radioactive waste from light water reactors is an important issue for Japanese nuclear power utilization. Partitioning and technology is being developed to reduce long-term radiotoxicity and heat in the underground repository. For transmutation of MA, ADS operated in sub-critical condition is considered because critical reactor with MA fuel is difficult to control. To develop the ADS, many kinds of nuclear data for a wide range of energy are necessary, especially data relating to spallation reaction and reactions of low energy neutron to unfamiliar isotopes (MA, lead, bismuth…).
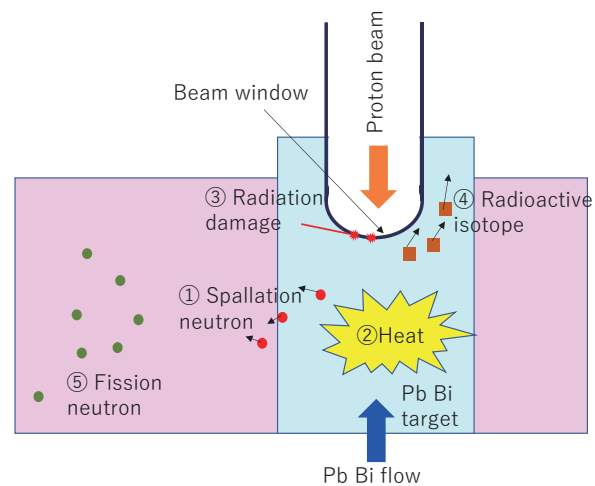
12 Production of At-211 using a cyclotron and an import plan of Ac-225

Mitsuhiro FUKUDA[1*], Atsushi TOYOSHIMA[2], Atsushi SHINOHARA[2], Hiroki KANDA[1],

Tetsuhiko YORITA[1], Yuusuke YASUDA[1], Takashi NAKANO[1] and Paul SCHAFFER[3]

[1]Research Center for Nuclear Physics(RCNP), Osaka University

10-1 Mihogaoka, Ibaraki, Osaka 567-0047, Japan

[2]Institute for Radiation Sciences, Osaka University

2-4 Yamadaoka, Suita, Osaka 565-0871, Japan

[3]TRIUMF

4004 Wesbrook Mall, Vancouver BC V6T 2A3, Canada

*Email: mhfukuda@rcnp.osaka-u.ac.jp

Targeted alpha-particle therapy (TAT), using short-lived alpha emitters such as At-211, Ac-225 and Ra-223, is one of remarkable cancer treatment methods especially for refractory cancer. At-211 with a half-life of 7.2 hours is produced by the nuclear reaction of $^{209}Bi(^4He,2n)^{211}At$. At-211 of several hundred MBq can be obtained by irradiation of a few μA 29 MeV $^4He^{2+}$ ion beam. Small amounts of At-211 are now available only for academic studies, provided from "Supply Platform for Short-lived RI" called RI-PF. Ac-225 with a half-life of 10 days is also one of the most powerful alpha emitters for TAT, commonly obtained from the parent nucleus Ra-225 by a milking method. In recent years, an accelerator-based Ac-225 production technique using an around 500 MeV proton beam has been developed at TRIUMF in Canada. A Th-232 target placed at the beam dump was used for production of RIs such as Ac-225 and Ra-225 by the spallation reaction of $^{232}Th(p,x)$. We have a plan to import the generator Th-229 or Ra-225 for milking Ac-225 in near future.

1. Introduction

Targeted particle therapy using beta-ray or alpha-ray emitters is expected to be one of the most effective treatments of refractory cancer such as metastatic cancer and invasive cancer. Especially targeted alpha-particle therapy (TAT) has a great advantage of dose concentration in a cancer cell, resulting from the large energy loss and short range of the alpha particles[1]. The energy and range of the alpha-emitting radionuclides such as At-211, Ac-225 and Ra-223 are around 7 MeV and 50 μm, respectively. Target medicine labeled with alpha emitting RIs is intravenously injected, selectively delivered to tumor tissues, and spontaneously accumulated in cancer cells. The cancer cell intaking the target medicine is severely damaged due to DNA double strand break caused by the energy loss of the emitted alpha particle or chemical reaction with free radicals generated by alpha induced ionization.

In recent years, demand for supply of the alpha emitting RIs is growing[2]. Property of At-211, Ra-223 and Ac-225 are listed in Table 1. Astatine is a radioactive halogenic element without any stable natural nuclei. At-211 with a short half-life of 7.2 hours emits two alpha particles with a mean energy of

6.8 MeV in a sequential decay. At-211 is easily produced by the nuclear reaction of ^{209}Bi(^{4}He,2n)^{211}At using a ^{4}He^{2+} ion beam accelerated by a cyclotron. The energy of ^{4}He^{2+} ions should be tuned to 29 MeV or less to avoid production of At-210 which decays to a toxic element of Po-210. A chemical compound of At-211 can be produced by replacing a halogenic element of chlorine and iodine, for example NaCl-like NaAt and MIBG-like MABG. Ac-225 with a half-life of 10 days provides five alpha particles with a mean energy of 6.9 MeV in a sequential decay. Ac-225 can be obtained by milking from the decay of the parent nucleus Ra-225. Accelerator-based Ac-225 production methods are now being developed by using nuclear reactions of ^{226}Ra(p,2n)^{225}Ac and ^{226}Ra(γ,n)^{225}Ra. A new project of Ac-225 mass production using a high energy proton beam was started at TRIUMF cyclotron facility in Canada. They proposed an alternative production method using a proton-induced spallation reaction ^{232}Th(p,x)^{225}Ac. RCNP collaborates with TRIUMF for importing the proper amount of Ac-225 from Canada. We have a plan of the first Ac-225 import from TRIUMF in 2022.

Table 1 Properties of alpha-particle emitters for TAT.

RI	Half life	Daughter nucleus	Number of emitted alpha particles	Mean energy of alpha particles（MeV）	Production method
^{211}At	7.21 hours	^{211}Po	2	6.8	^{209}Bi(^{4}He,2n)^{211}At
^{223}Ra	11.4 days	^{219}Rn ^{215}Po ^{211}Bi ^{211}Po	5	6.7	^{226}Ra(n,γ)^{227}Ra → ^{227}Th → ^{223}Ra
^{225}Ac	10.0 days	^{221}Fr ^{217}At ^{213}Bi ^{213}Po	5	6.9	[Reactor] ^{229}Th → ^{225}Ra → ^{225}Ac [Accelerator] ^{226}Ra(p,2n)^{225}Ac ^{226}Ra(γ,n)^{225}Ra ^{232}Th(p,x)^{225}Ac

2. Supply of short-lived RIs

A short-lived radioisotope (RI) is widely utilized as a highly sensitive probe for investigating properties of materials and imaging invisible conditions. In recent years, there is a growing need for supplying short-lived RIs for academic use, especially for the research on diagnosis and therapy in nuclear medicine. In Japan, the short-lived RI supply platform (RI-PF)[3] was organized in 2016 in cooperation among the following accelerator facilities; 1) Research Center for Nuclear Physics (RCNP), Osaka University, 2) Radioactive Isotope Beam Factory (RIBF), RIKEN, 3) Cyclotron and Radioisotope Center (CYRIC), Tohoku University, 4) Research Center for Electron Photon Science (ELPH), Tohoku University, 5) National Institute of Radiological Sciences (NIRS), National Institutes for Quantum and Radiological Science and Technology (QST), 6) Takasaki Advanced radiation Research Institute, QST. The RI-PF is supported by MEXT/JSPS KAKENHI for supplying short-lived RIs to basic and applied research in a variety of academic fields regularly and stably. Technical assistance is also given to research beginners for safe RI treatment. One of the most popular short-lived RIs supplied from the platform is At-211 mainly used for basic research of TAT, investigator-initiated clinical trials, development of At-

211 labeled medicine and an imaging system for At-211 accumulation.

3. Production of At-211 at RCNP cyclotron facility

RCNP was founded in 1971 at Osaka University to promote nuclear physics research using a variable-energy, multi-particle AVF cyclotron with a K-value of 140 MeV. Construction of the AVF cyclotron facility was finished in 1973 and nuclear physics experiments started from 1976[4]. A ring cyclotron with a K-value of 400 MeV was completed in 1991 mainly for pioneering precision nuclear physics experiment by increasing the maximum energy of proton and heavy ion beams up to 420 MeV and 100 MeV/nucleon, respectively. The AVF cyclotron in a standalone operation mode is mainly used for RI production using proton and helium ion beams with energies from 10 to 30 MeV. The bird eye view of the RCNP cyclotron facility is shown in Fig. 1. The upgrade program of the AVF cyclotron was started in 2019 to provide not only an intense light ion beam for RI mass production but also a high-quality intense beam for nuclear physics precision experiments. Most of equipment besides the AVF cyclotron main magnet was replaced by new one. A new coaxial-type resonator was designed to cover a frequency range from 16 to 36 MHz for acceleration of various kinds of particles using acceleration harmonic mode of h=2 to maximize the energy gain per turn. The commissioning of the AVF cyclotron has started and we will have a new beam in 2022.
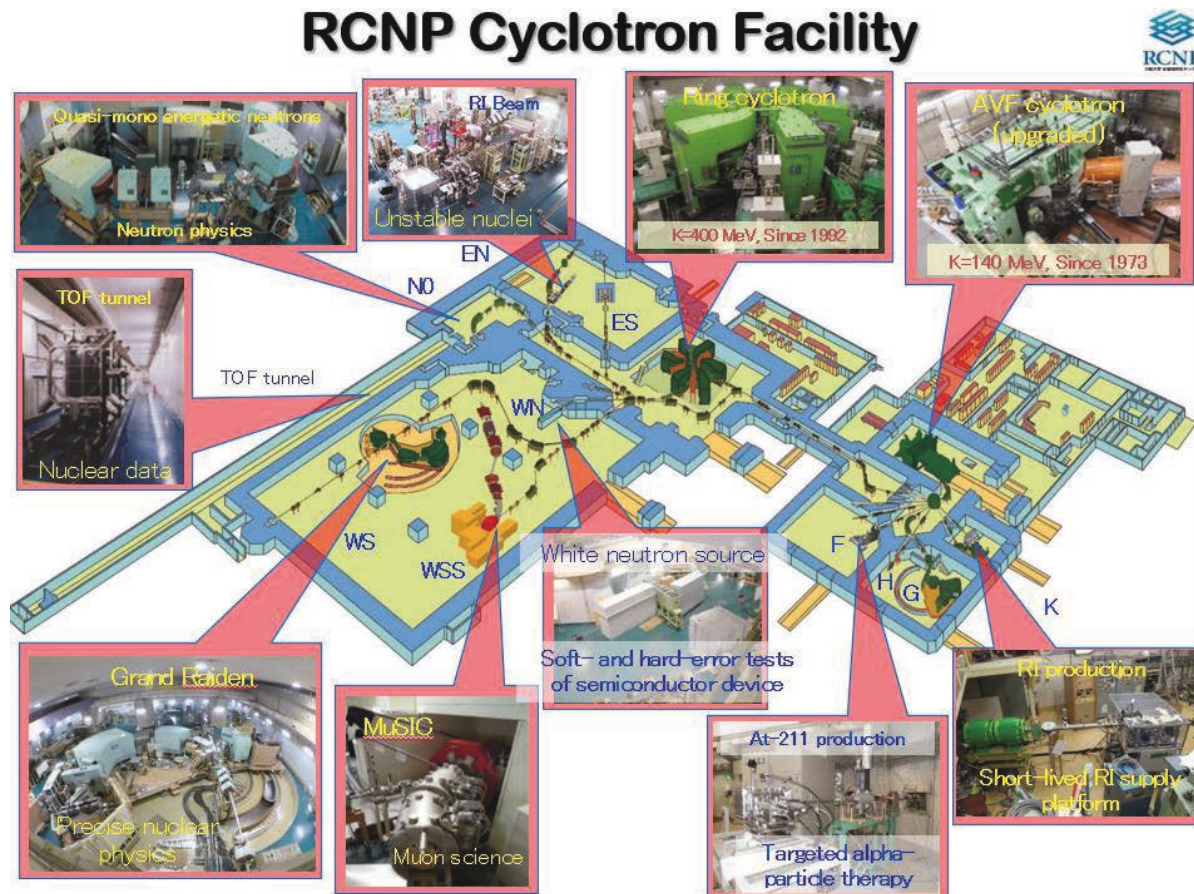
Fig. 1 Bird eye view of the RCNP cyclotron facility

The beam line K-course placed in S Experimental Room is used for production of any kinds of RIs except for At-211, especially for supply short-lived RIs through the RI-PF program. Semiautomatic irradiation equipment was installed at the end of the beamline. The irradiated target is transferred directly to a hot cell in the RI Building by pneumatic tube equipment. The target chamber for At-211 production is located at the end of F-course in M Experimental Room. A thin bismuth target is formed on the surface of an aluminum backing plate with cooling water behind the plate and a helium gas is additionally blown on the surface of the bismuth target to cool down the heated target. A 29 MeV, 2 or 3 μA ^{4}He^{2+} ion beam was focused on the target with a beam spot size of 10 mm in diameter. At-211 with several hundred MBq was produced by several hour irradiation. The At-211 production beam time was scheduled once or twice a month. The annual beam time for RI production at the RCNP cyclotron facility increased year by year and reached more than 600 hours a year. The beam current will be increased to 30 μA after upgrading the AVF cyclotron to increase the At-211 activity to more than 1 GBq, required for investigator-initiated clinical trials at Osaka University Hospital. The target system will be also upgraded to improve the performance for higher beam power irradiation. A beam scanning system will be installed to avoid localization of heat on the target. The target cooling performance will be reinforced as well.

4. Import of Ac-225 from TRIUMF

The TRIUMF cyclotron facility is equipped with a large-scale ring cyclotron to accelerate a H⁻ ion beam up to 500 MeV and several compact H⁻ cyclotrons for RI production. Th-229 of a few GBq, the parent nucleus of Ac-225 and Ra-225, was produced by irradiating a Th-232 target, placed at the beam dump of the IPF beam line, with 70 μA, 480 MeV proton beam[5]. The beam current will be increased to more than 350 μA within several years. The decay scheme of the neptunium series is shown in Fig. 2. The spallation reaction of ^{232}Th(p,x) produces two different Ac-225 products, i.e. generator-produced Ac-225 and directly-produced Ac-227,225. The Ra-225 generator with a half-life of 14.9 days may contain small amounts of Ra-228 with a half-life of 5.8 years. Ac-227 with a half-life of 22 years may be contained as a by-product in the directly produced Ac-225. The separation of the by-product isotopes will be key issue to be resolved for purification of Ac-255. We have negotiated with TRIUMF about the import of the Ra-225 generator. Small amounts of Ra-225 generator will be imported to Japan in 2022.
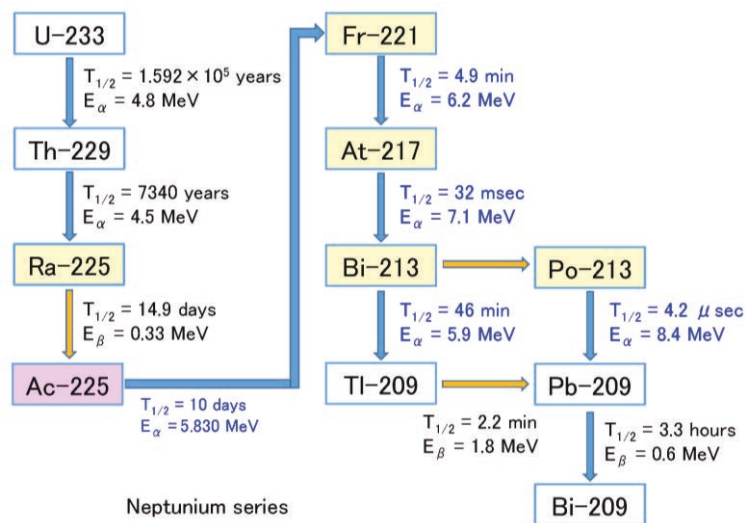
Fig. 2 Decay scheme of the neptunium series including the Th-229 and Ra-225 generators.

References

1) Matthews, H.S., Lave, L.B., Applications of Environmental Valuation for Determining Externality Costs, Environ. Sci. Technol., vol.34, no.8, 2000, pp.1390-1395.

2) Haba, H., Fukuda, M., Kobayashi, N., Nagatsu, K., Nishi, K., Hatano, K., Magata, Y., Yamada, T., Washiyama, K., Watabe, H., Survey Report of RI Production and Application in 2019, RADIOISOTOPES, vol. 70, pp. 251-260, 2021, (in Japanese).

3) Fukuda, M., Nakano, T., Haba, H., Sakemi, Y., Watabe, H., Kikunaga, H., Yorita, T., Supply Platform of Short-lived Radioisotopes for Fundamental Research, J. Particle Accelerator Society of Japan, vol.14, No.2, 2017, pp.81-86 (in Japanese).

4) Kondo, M., AVF Cyclotron, RCNP Annual Report, 1976, pp.1-5.

5) Radchenko, V., Schaffer, P., et. al., Journal of Nuclear Medicine, vol.62, No.11, 2021, pp.1495-1503.

Acknowledgements

This is a blank page.

13　Production of an α-emitting radionuclide At-211 for medical use

at JAEA tandem accelerator

Ichiro NISHINAKA[1]

[1]Tokai Quantum Beam Science Center, Takasaki Advanced Radiation Research Institute, Quantum Beam Science Research Directorate, National Institutes for Quantum Science and Technology

2-4 Shirakata, Tokai-mura, Naka-gun, Ibaraki-ken 319-1106, Japan

[*]Email: nishinaka.ichiro@qst.go.jp

Experimental studies concerning the production of a medical α-emitting radionuclide ^{211}At have been conducted at the JAEA tandem accelerator under a research project of the development of a ^{211}Rn–^{211}At generator system since 2011. Some results of the research project as well as related research subjects are reported.

1. Introduction

In general, the ^{211}At nuclide, a prospective candidate for targeted alpha radiotherapy (TAT), has been produced through the ^{209}Bi(α,2n)^{211}At reaction [1]. In contrast, our project focused on the production of the ^{209}Bi(^{7}Li,5n)^{211}At reaction using the Japan Atomic Energy Agency (JAEA) tandem accelerator [2,3]. This enables us to supply ^{211}At in a ^{211}Rn–^{211}At generator system. The daughter ^{211}At of 7.2 h in half-life ($T_{1/2}$) is generated through EC decay of the parent ^{211}Rn of $T_{1/2}$=14.7 h, expanding time-frame for transportation and use of ^{211}At. In this project, chemical procedures based on dry- and wet-chemistry have been studied to develop the ^{211}Rn–^{211}At generator system. In addition, research subjects related to the development of the ^{211}Rn–^{211}At generator system, namely, production of astatine and iodine radioisotopes [4, 5], astatine chemistry [6, 7, 8] as well as the analytical method of ^{211}At using an α-scintillation camera and thin-layer chromatography (TLC) [9] have been studied using the JAEA tandem accelerator.

Some experimental results of the project and related research subjects, e.g., production of astatine and iodine radioisotopes [3, 4, 5], the chemical procedure based on dry-chemistry for the ^{211}Rn–^{211}At generator system, astatine chemistry [6, 7], and the analytical method of ^{211}At using an α-scintillation camera and TLC [9] are presented.

2. Production of astatine, iodine and radon radioisotopes

Production cross sections are fundamental physical quantities to produce radioisotopes in nuclear reactions using ion beams. Therefore, we measured the excitation functions of radon and astatine isotopes in the ^{7}Li-induced reactions with ^{209}Bi for the development of a ^{211}Rn–^{211}At generator [3]. In addition, the production cross sections of astatine and iodine radioisotopes were measured in ^{7}Li-induced reactions

with [nat]Pb [4] and [nat]Sn [5], respectively, for fundamental chemical studies of non-carrier-added astatine and iodine.

Production cross sections were determined with the so-called activation method. The thin targets of bismuth, lead or tin of 1.2-1.5 mg/cm^2 in thickness were prepared by vacuum evaporation of bismuth, lead or tin metal on a 10 or 20-μm foil backing of aluminum. As a typical case, five targets were thus prepared, covered with a 10 or 20-μm aluminum foil, arranged in a stack, and irradiated with 60 MeV [7]Li ions of 80-200 nA current at the beam course of the JAEA tandem accelerator. After the irradiation, the radioactivity of products was determined using a Ge detector via γ-ray spectrometry [3–5]. The α-radioactivity of [211]At was determined by a chemical procedure based on the dry-distillation method and α-ray spectrometry [4]. The production cross section was calculated from the relation of the numbers of target and product atoms, and the beam flux with corrections of the change of the beam flux and the decay of the product [3–5].

The excitation functions of products in the [7]Li + [209]Bi [3], [7]Li + [nat]Pb [4] and [7]Li + [nat]Sn [5] reactions are shown in Figs. 1(a)–(c), respectively. Experimental data are plotted with solid lines calculated by the HIVAP code [10,11]. The calculations rather well reproduced experimental data. However, the considerably small experimental cross section of [211]Rn and [209,210]At compared with the statistical calculations were clearly observed in [7]Li + [209]Bi and [7]Li + [nat]Pb, respectively. This indicates that the effects of breakup reaction of weakly bound nuclei of [7]Li play a crucial role in the reactions with [209]Bi and [nat]Pb [3,4]. Incomplete fusion including breakup reaction is not taken into consideration in the HIVAP code. Generally, the statistical model calculations predict only complete fusion cross sections. Thus, the missing complete fusion cross sections observed as suppression are found in yields of incomplete fusion including breakup reaction.
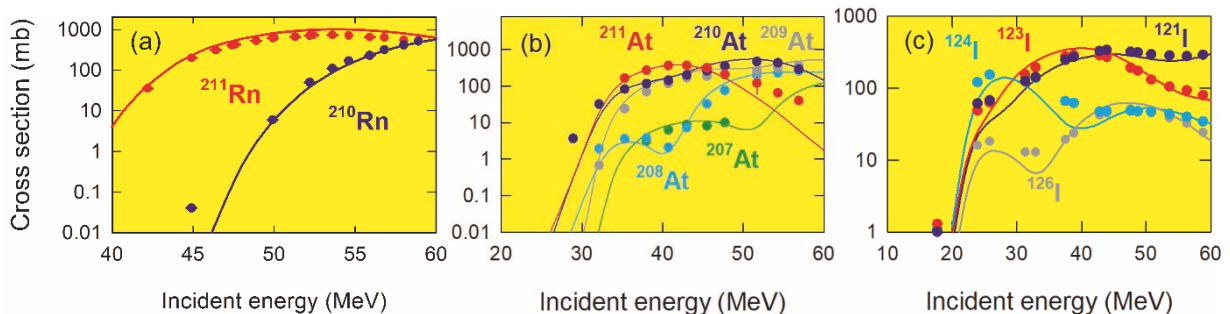
Fig. 1 Excitation functions of ^{209}Bi(^{7}Li, xn)^{210,211}Rn (a), ^{nat}Pb(^{7}Li, xn)$^{207–210}$At (b) and ^{nat}Sn(^{7}Li, xn)$^{121–126}$I (c).

3. Chemical procedure based on dry chemistry for ^{211}Rn–^{211}At generator system

The concept of the [211]Rn–[211]At generator was proposed by Lambrecht and Mizadeh 37 years ago [12]. Several projects for the development of the [211]Rn–[211]At generator have recently been independently conducted in Japan [2], the United States of America [13] and Canada [14,15]. In Japan, our research project has been studying a chemical procedure based on dry-chemistry as well as that based on wet-chemistry [2] to develop the [211]Rn–[211]At generator system using the JAEA tandem accelerator. Preliminary results of the chemical procedure based on dry-chemistry are presented.

Radon-211 was produced in the irradiation of a thin bismuth target of approximately 1 mg/cm^2 on an aluminum backing sheet with 60 MeV [7]Li^{3+} beams from the JAEA tandem accelerator via the ^{209}Bi(^{7}Li, 5n)^{211}Rn reaction. After the irradiation, the [211]Rn was separated from the target and purified in a chemical

procedure based on dry-chemistry using an apparatus for the ^{211}Rn–^{211}At generator system. The bismuth target placed in a test tube which is a part of the apparatus was heated up to a temperature 520 °C by an electric furnace to melt the bismuth target. Radon-211 escaped from the melted bismuth target was transported to a steel tube, cooled to the temperature of liquid nitrogen, by helium gas stream which circulates through the apparatus. The ^{211}Rn trapped in the steel tube was allowed to stand for over half a day to generate ^{211}At. After removing the helium gas including ^{211}Rn from the steel tube, no-carrier-added ^{211}At deposited on the wall of the steel tube was recovered by rinsing the tube with flowing ethanol. Eluted ethanol was successively collected in three glass vials of 2 mL. Radioactivity of ^{211}At was measured by α-ray spectrometry to determine recovery yields. The no-carrier-added ^{211}At solution included some amounts of ^{207}Po ($T_{1/2}$=5.8 h), produced by α-decay of ^{211}Rn with 27% decay branch, as a by-product.

The dry-chemical process, namely, the separation and collection of ^{211}Rn in the apparatus for the ^{211}Rn–^{211}At generator system was accomplished within 15 min. The overall recovery yields of ^{211}At generated from ^{211}Rn (n=3) were approximately 35% in the first fraction of the eluted ethanol of 2mL, 8 % in the second and 1 % in the third. Ethanol easily removes a large portion of astatine generated through EC decay of ^{211}Rn from the steel tube. The results demonstrate that the chemical procedure based on dry-chemistry as well as that based on wet-chemistry [2] would provide the unique ability of the ^{211}Rn–^{211}At generator.

4. Astatine chemistry

Astatine belongs to halogen, therefore, knowledge and experience of proven radiopharmaceuticals labeled with its homologue iodine are expected to be adaptable for utilization of astatine in TAT. However, astatine shows some different chemical behaviors in comparison with homologue iodine. This becomes problematic in the repeatability of yields in the chemical and radiolabeling reactions. The understanding basic chemical properties of astatine has been required to develop ^{211}At-labeled radiopharmaceuticals in TAT [16]. Although a large number of analytical methods have been applied to study astatine chemistry but the speciation of astatine and its basic chemical properties are still unknown. The difficulty in astatine chemistry comes from the lack of stable or long-lived isotopes as well as the low amounts of astatine produced by using an accelerator.

In our studies, the speciation of dissolved astatine chemical species of astatide (At$^-$), astatate (AtO$_3^-$) and perastatate (AtO$_4^-$) was confirmed by thin layer chromatography (TLC) on silica gel with an ethanol/water solution [6]. Additionally, the chemical properties of dissolved and volatile astatine species were studied [7].

Astatine and iodine radionuclides were produced in the ^{7}Li+^{nat}Pb [4] and ^{7}Li+^{nat}Sn [5] reactions at the JAEA tandem accelerator, respectively, as described in Sec. 2. No-carrier-added astatine ^{208,209,210,211}At or iodine ^{120,121,123}I were separated by a dry distillation method and recovered in ethanol or distilled water as a solvent [8]. Astatine in the aqueous solution was reacted with an oxidizing (KIO$_4$) or a reducing reagent (Na$_2$SO$_3$, N$_2$H$_4$). The speciation of astatine and iodine was conducted by TLC on silica gel with an ethanol/water solution (1:1, v/v). The distributions of radioactivity on the TLC plates were measured by imaging plates (IPs) and visualized by Bioimaging Analyzer System (BAS) [6,7].

The results of TLC for radioactive astatine and iodine, as shown in Fig. 2, reveals that astatine is successfully separated and identified as At$^-$, AtO$_3^-$, AtO$_4^-$, while iodine is I$^-$. The identification was carried out by comparing retardation factor (R_f) with those of standard iodine species, I$^-$, IO$_3^-$, IO$_4^-$ [6].

Besides dependence of relative amounts of the astatine anions on the solution, as shown in Fig. 2b-f, strongly supports that the three oxidation states of astatine are assigned to $At^-(-I)$, $AtO_3^-(V)$ and AtO_4^- (VII). The oxidizing and reducing reagents reasonably control the relative yields of $At^-(-I)$, $AtO_3^-(V)$ and $AtO_4^-(VII)$.
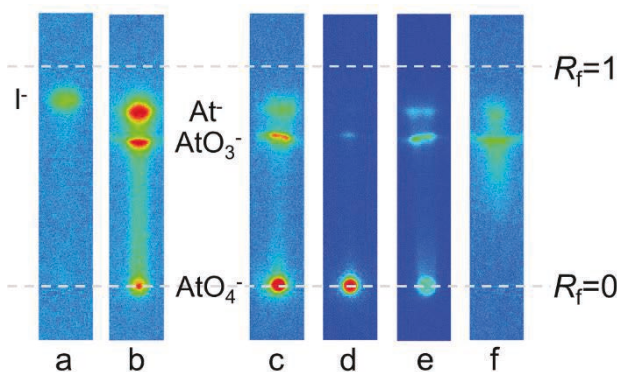
Fig. 2 Results of TLC experiments visualized by BAS: **a** iodine ethanol solution, **b** astatine ethanol solution, **c** astatine aqueous solution, **d** astatine aqueous solution + KIO_4, **e** astatine aqueous solution + Na_2SO_3, **f** astatine aqueous solution + N_2H_4.
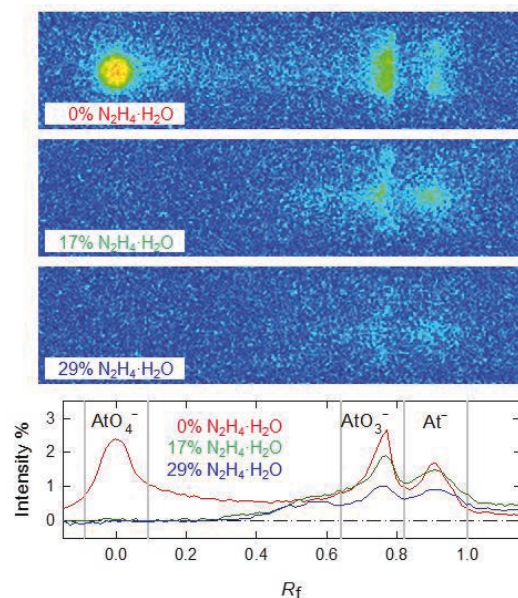
Fig. 3 Typical TLC images and chromatograms for N_2H_4 aqueous solution of astatine.

Figure 3 shows typical TLC images and chromatograms for N_2H_4 aqueous solution of astatine. An increase in the concentration of hydrazine hydrate $N_2H_4 \cdot H_2O$ enhances the relative amounts of At^- and AtO_3^- compared with that of AtO_4^-, however, intensities of At^- and AtO_3^- decrease. This behavior is reasonably taken into account as follows. The reduction of $AtO_4^-(VII)$ enhances the amounts of $At^-(-I)$ and $AtO_3^-(V)$. This facilitates the formation of the volatile species $At^0(0)$ through the oxidation-reduction reactions between $At^-(-I)$ and $AtO_3^-(V)$ in dynamical equilibria due to both effects of the oxidation on silica gels and the reduction with N_2H_4, leading to the volatilization of $At^0(0)$ from TLC plates. The volatilization of At^0 (0) subsequently leads to a decrease in the amounts of $At^-(-I)$ and $AtO_3^-(V)$ on the TLC plates.

In these studies [6,7], some basic chemical characteristics of astatine are elucidated: these astatine anions, At^-, AtO_3^- and AtO_4^-, are stable but readily oxidized and/or reduced between them in dynamical equilibria owing to the more electropositive character of astatine than iodine. In addition, the volatile astatine At^0 is formed via the oxidation-reduction reaction between At^- and AtO_3^-.

5. Analytical method of ^{211}At using an α-scintillation camera and thin-layer chromatography

A rapid method analyzing both the radioactivity and all chemical forms of medical radioisotopes ^{211}At ($T_{1/2}$=7.2 h) was required for related fundamental researches. We provided a new analytical method of ^{211}At in a short time with constructing an α-scintillation-camera system capable of imaging α-rays using TLC as samples (Fig. 4). The experiments were conducted to evaluate the performance of the

developed system for the radioactivity and chemical forms utilizing ^{211}At produced by ^{211}Rn–^{211}At generator [9].

^{211}At and ^{207}Po, used as α- and X-ray emitters, were obtained by ^{211}Rn–^{211}At generator, as described in Sec. 3. The radioactivity of 56–672 Bq for ^{211}At was measured in a short time of 100 s and was successfully quantitatively determined within an uncertainly of 5%. The sensitivities of the developed system were estimated to be ~200 times higher than those of the conventional IPs method. As shown in Fig. 5, the separation performance of the chemical forms was verified by visualizing the TLC images for ^{211}At and comparing the results for the developed system to those for the IPs. The developed system enabled the visualization of ^{211}AtO$_4^-$, which could not be quantitated with IPs because of the large number of background X-rays emitted from ^{207}Po, without chemical separation and purification. These results revealed that the use of the developed system provided the rapid method to analyze both of the radioactivity and all chemical forms of ^{211}At.

The proposed method would be a useful tool for the labeling yield analysis of radiopharmaceutical at the administrated place and related researches of TAT in the future.
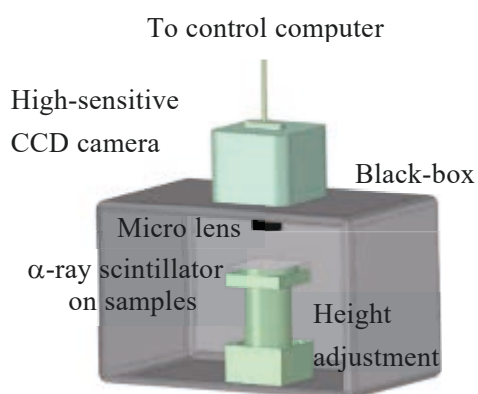
Fig. 4 Schematic of the developed system.
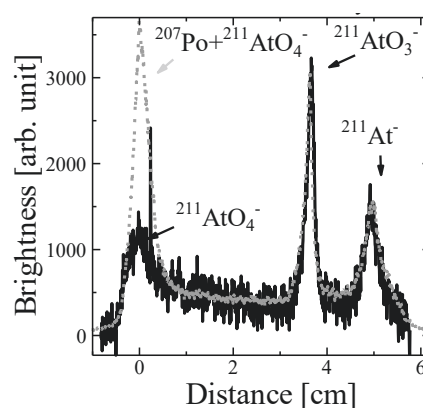
Fig. 5 Chromatograms measured with IPs (gray dashed line) and the developed system (solid line).

References

[1] Y. T. Feng and M. R. Zalutsky, Production, purification and availability of At-211: Near term steps towards global access., Nucl. Med. Bio. vol.100, 2021, pp.12–23.

[2] E. Maeda et al., Extraction of astatine isotopes for development of radiopharmaceuticals using a ^{211}Rn-^{211}At generator, J. Radioanal. Nucl. Chem. vol.303, 2015, pp.1465–1468.

[3] E. Maeda et al., Measurements of the excitation functions of radon and astatine isotopes from ^{7}Li-induced reactions with ^{209}Bi for development of a ^{211}Rn-^{211}At generator, J. Radioanal. Nucl. Chem. vol.323, 2020, pp. 921–926.

[4] I. Nishinaka et al., Production and separation of astatine isotopes in the ^{7}Li+^{nat}Pb reaction, J. Radioanal. Nucl. Chem. vol.304, 2015, pp.1077–1083.

[5] I. Nishinaka et al., Production of iodine radionuclides using ^{7}Li ion beams, J. Radioanal. Nucl. Chem. vol.314, 2017, pp.1947–1965.

[6] I. Nishinaka et al., Thin layer chromatography for astatine and iodine in solutions prepared by dry distillation, J. Radioanal. Nucl. Chem. vol.318, 2018, pp.897–905.

[7] I. Nishinaka et al., Speciation of astatine reacted with oxidizing and reducing reagents by thin layer chromatography: formation of volatile astatine, J. Radioanal. Nucl. Chem. vol.322, 2019, pp.2003–2009.

[8] I. Nishinaka et al., Separation of astatine from irradiated lead targets based on dry distillation in a glass test tube, J. Radioanal. Nucl. Chem. vol.327, 2021, pp.869–875.

[9] M. Segawa et al., Analytical method for the determination of ^{211}At using an α-scintillation camera system and thin-layer chromatography, J. Radioanal. Nucl. Chem. vol.326, 2020, pp.773–778.

[10] K. Nishio et al., Fusion of deformed nuclei in the reactions of ^{76}Ge+^{150}Nd and ^{28}Si+^{198}Pt at the Coulomb barrier region, Phys. Rev. C vol.62, 2000, pp.014602–1–12.

[11] W. Reisdorf and M. Schädel, How well do we understand the synthesis of heavy elements by heavy-ion induced fusion?, Z. Phys. A vol.343, 1992, pp.47–57.

[12] R. M. Lambrecht and S. Mirzadeh, Cyclotron isotopes and radiopharmaceuticals–XXXV Astatine-211, Int. J. Appl. Radiat. Isot. vol.36, 1985, pp.443–450.

[13] J. P. Greene et al., Nickel-backed Bi targets for the production of ^{211}At, J. Radioanal. Nucl. Chem. vol.305, 2015, pp.943–946.

[14] J. R. Crawford et al., Development of a preclinical ^{211}Rn/^{211}At generator system for targeted alpha therapy research with ^{211}At, Nucl. Med. Bio. Vol.48, 2017, pp.31–35.

[15] J. R. Crawford et al., ^{211}Rn/^{211}At and ^{209}At production with intense mass separated Fr ion beams for preclinical ^{211}At-based α-therapy research, Appl. Radiat. Isot. vol.122, 2017, pp.222–228.

[16] D. S. Wilbur, Enigmatic astatine, Nat. Chem. vol.5, 2013, p.246.

Acknowledgments

14   Development of the injector for heavy-ion therapy
using laser-driven ion acceleration

Hironao SAKAKI

National Institutes for Quantum Science and Technology

8-1-7 Umemidai, Kizugawa, Kyoto 619-0215, Japan
*Email: sakaki.hironao@qst.go.jp

Heavy-ion therapy is widely used at domestic and foreign due to provide a high therapeutic effect with the least invasiveness. However, there are one of issues that the treatment cost becomes high, because of the high construction and operation cost of the therapy system. In National Institutes for Quantum Science and Technology (QST), for the treatment cost down, the development of a compact hadron therapy system, that's called "Quantum scalpel (using laser-driven ion acceleration as an injector to the superconducting synchrotron)" using the laser-driven ion acceleration method is underway. We are shown the features of the laser acceleration method and the challenges for the performance required as injector for Quantum scalpel.

1. Introduction

Heavy-ion therapy, the accelerated carbon beam to a maximum energy of 400 MeV/nucleon with a synchrotron is irradiated to cancer, provides a high therapeutic effect without surgical operation. Since this treatment has few side effects, it can be used in combination with other treatments such as molecular targeted drug therapy and immunoregulatory therapy, and we can expect further therapeutic effects. But, heavy-ion therapy is the huge facility size, high operating cost are reflected in the personal treatment cost. So, only 11 facilities (6 facilities in Japan) are widespread worldwide. Therefore, it is essential to overcome each of the issues that contribute to the cost of treatment and to develop an ultra-miniaturized next-generation heavy-ion therapy system. We call the next-generation treatment system "Quantum scalpel"[1,2], since heavy-ion therapy has the potential to replace surgical operation depending on the affected area. Quantum scalpel plans to be composed of the superconducting magnet technology and laser-driven ion acceleration technology of QST to reduce the size of the current synchrotron (diameter about 20 meters) and injector (length about 15 meters with acceleration and beam transport system) to about half size. Figure 1 shows a schematic drawing of Quantum scalpel. The footprint of the system is designed to be 20meters x 10meters in area size. The laser-driven ion injector will be placed at a size that can be installed inside the synchrotron. Quantum scalpels also include super conductivity synchrotron and an advanced treatment technology called "Irradiation of multiple nuclides", but in this paper, we describe only the features of laser-driven ion acceleration technology that contributes to the miniaturization of the ion injector.
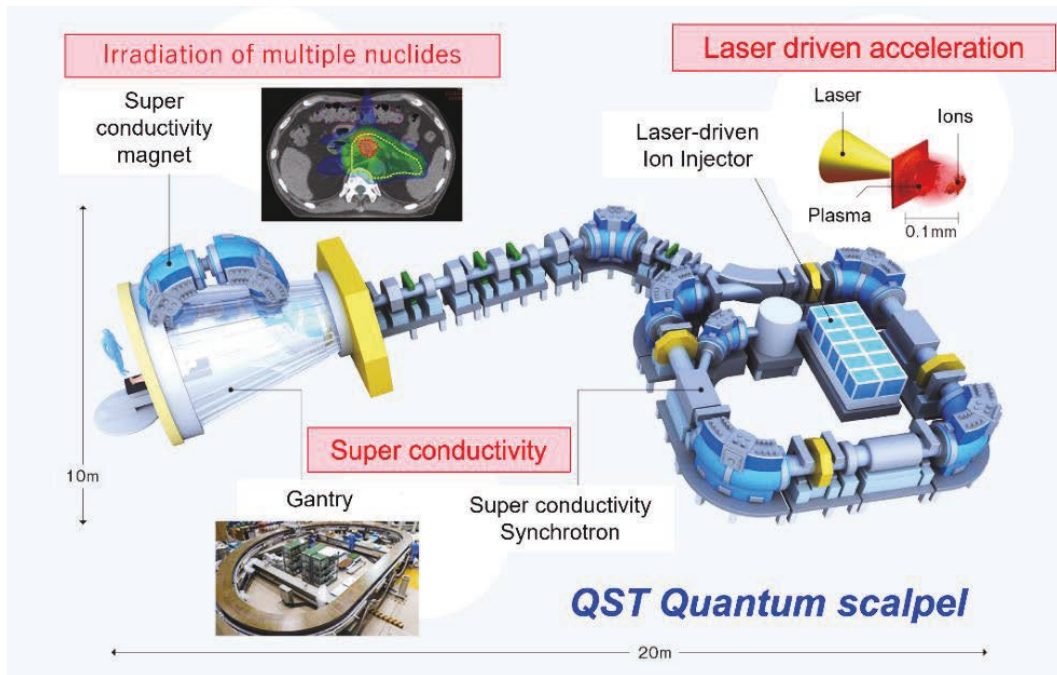
Figure 1: A schematic drawing of QST Quantum scalpel

2. Miniaturization of ion injector

2.1. Limits of ion-accelerated field gradient

In a general RF-type particle injector, high power electric-field generator (a resonance cavity) that changes periodically positive and negative electric-field polarities, is used for particle acceleration. It is known that the resonance cavity has a discharge limit determined by the operation frequency according to Kilpatrick's law[3], and the discharge limit decreases as the operation frequency of the resonance cavity decreases. The beam quality is improved when the beam is extracted high energy from the ion source, generally. Therefore, we design to extract the beam with a strong electric field using an electrode or a resonant cavity, but the electric field of the ion source is limited by Kilpatrick's law, and only an acceleration gradient of several MeV/m or less can be obtained to avoid discharge. For this reason, with the current RF-type injector, the length of the injector is 15 meters to ion acceleration and transport carbon with the energy of 4 MeV/nucleon, and it is difficult to compose it smaller than this length. Quantum scalpel uses superconducting technology to reduce the diameter of the synchrotron from the current size 20 meters to 8 meters. Therefore, the significant progress in miniaturization of the injector is required, and it is necessary to break through the limit of miniaturization of the injector by the acceleration technology different from the RF-type injector.
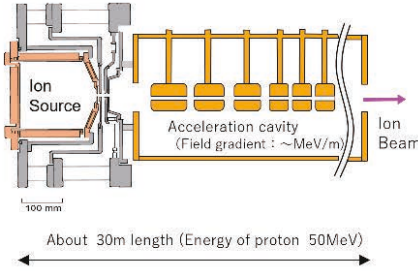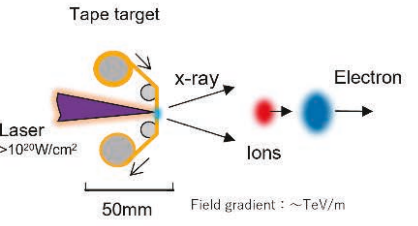
2.2. Laser-driven ion acceleration

Around 2000, with the progress of high-intensity lasers, a novel ion acceleration phenomenon was discovered, this ion acceleration is used an accelerated field gradient that reaches ~ TV/m created by high-intensity lasers[4,5]. Basic research using the phenomenon as a downsizing technology for RF-type accelerators have started in many countries around the world[6]. This acceleration is carried out by the laser light that is emitted by a laser material doped with titanium in sapphire. The laser light is narrowed down spatially and temporally to reach the level of 10^{20} W/cm^2 and irradiates a tape target. It is a method of accelerating carbon ions to the energy of MeV region by converting laser-energy into an ion-accelerated

electric field. Table 1 is a characteristic table that compares laser-driven injector to the RF-type injector. While laser acceleration has an advantage of being compact size, it also has disadvantages of having large energy dispersion and simultaneous acceleration of many ion nuclides. These will be solved by the development of the tape target materials and the beam energy selection devices at beam transport system.

Table 1: Characteristic table that compares laser-driven injector to the RF-type injector

	Ion source, Acceleration parts	Characteristics of Ion beam	
RF-type injector		Field gradient	~ MeV/m
		Length (for 50MeV p+)	~ 30m
		Particles (1 bunch)	Depend on Ion source value
		Bunch length	DC~nano sec (with beam chopper)
		Energy width	Monochromatic
		Beam divergence	< 1 degree
		Emittance	transverse ~1 [π mm · mrad] longitudinal ~5 [eV · s] (exp. J-PARC)
		Charge	Low charge at ion sources
Laser-driven ion Injector		Field gradient	~ TeV/m
		Length (for 50MeV p+)	< μ m
		Particles (1 bunch)	~10^{13} proton and other nuclide
		Bunch length	< pico sec at target
		Energy width	Broad
		Beam divergence	~ 10 degrees
		Emittance	transverse ~10^{-4} [π mm · mrad]
		Charge	High charge ion (e.g. ~Ag^{+42})

3. Summary

Around 2016, Quantum scalpel was proposed in QST, the laser-driven ion acceleration was at the level of a basic study. So, we will proceed with the demonstration of stable acceleration of high-purity carbon ions by a high-intensity laser at the short schedule. When research and development for practical use proceed as planned, it is expected that an injector prototype using laser-driven ion acceleration technology will be made around 2030.

References

1) Koji Noda, REVIEW OF ION THERAPY MACHINE AND FUTURE PERSPECTIVE, 10th Int. Particle Accelerator Conf., 2019, pp. 3391-3395.
2) QST Innovation Project, https://www.qst.go.jp/site/innovative-project-english/quantum-scalpel.html (accessed 2022-3-10).
3) W. D. KILPATRICK, Criterion for Vacuum Sparking Designed to Include Both rf and dc, Review of Scientific Inst. 28, 1957, pp. 824-826.
4) S. Hatchett, et al., Electron, photon, and ion beams from the relativistic interaction of Petawatt laser pulses with solid targets, Phys. Plasmas 7, 2000, pp.2076-2082.
5) E. Clark, et al., Measurements of Energetic Proton Transport through Magnetized Plasma from Intense Laser Interactions with Solids, Phys. Rev. Lett. 84, 2000, pp. 670-673.
6) S. V. Bulanov, V. S. Khoroshkov, Feasibility of using laser ion accelerators in proton therapy,

Plasma Physics Reports volume 28, 2002, pp. 453-456.

15　Challenging studies by accelerator mass spectrometry for the development of environmental radiology

-Status report on the analysis of ^{90}Sr and ^{135}Cs by AMS-

Maki HONDA[1a*], Martin MARTSCHINI[1], Alexander WIESER[1], Oscar MARCHHART[1], Johannes LACHNER[1b], Alfred PRILLER[1], Peter STEIER[1], Robin GOLSER[1], and Aya SAKAGUCHI[2]

[1]University of Vienna, Faculty of Physics, Isotope Physics

Währinger Street 17, Vienna 1090, Austria

[2]Center for Research in Isotopes and Environmental Dynamics, University of Tsukuba

1-1-1 Tennodai, Tsukuba, Ibaraki 305-8577, Japan

[*]Email: honda.maki@jaea.go.jp

Inventive techniques for the determination of ^{90}Sr and ^{135}Cs by accelerator mass spectrometry (AMS) were developed to promote environmental radiology. For this study ^{90}Sr and ^{135}Cs have been measured in environmental samples using the ILIAMS system at the VERA Laboratory (University of Vienna). This novel method removes isobaric anions via selective laser photodetachment much more efficiently than any conventional AMS technique. The limit of detection for ^{90}Sr at VERA is <0.08 mBq, which is lower than that for β-ray spectrometry. The new ^{90}Sr analytical technique will be applied to field studies on a trial basis. Although there are still several significant issues in ^{135}Cs AMS, such as Ba separation in chemical processing and cross-contamination in the negative ion source, AMS also achieved a suitable ^{135}Cs measurement performance for environmental samples.

1. Introduction

The fission products ^{90}Sr ($t_{1/2}$ = 28.79 years) and ^{135}Cs ($t_{1/2}$ = 2.6×10^6 years) have been released into the environment by past atmospheric nuclear tests and nuclear power plant accidents and are still released from nuclear fuel reprocessing plants [1, 2]. Strontium-90 is one of the most concerning nuclides in the assessment of internal exposure of residents because it can accumulate in bones and teeth and cause health problems [1]. Cesium-135 is a long-lived radionuclide that is assessed as an influential contributor to the long-term radiological risk associated with deep geological disposal of radioactive waste [2]. As both radionuclides are pure beta emitters, other beta emitters such as Ra isotopes, ^{210}Pb, ^{90}Y and ^{137}Cs in environmental samples must be removed entirely. While this is obviously impossible for conventional β-

---

ray spectrometry of ^{135}Cs, it does work for ^{90}Sr but requires a large volume of the sample due to the low concentrations of ^{90}Sr in general environmental samples. Therefore, the chemical separation of the target nuclides is time-consuming. This study addresses the limitations by applying accelerator mass spectrometry (AMS) to the highly-sensitive analysis of ^{90}Sr and ^{135}Cs in environmental samples. The isobaric interferences of ^{90}Zr and ^{135}Ba, respectively, are the most significant concern in AMS of ^{90}Sr and ^{135}Cs. With conventional AMS, the separation from isobars becomes more difficult as the atomic number Z of the analyte increases because $\Delta Z/Z_{isobar}$ becomes low ($\Delta Z = |Z_{isobar} - Z_{analyte}|$). In our case, the $\Delta Z/Z$ of $_{38}$Sr and $_{40}$Zr is 5% and the $\Delta Z/Z$ of $_{55}$Cs and $_{56}$Ba is a mere 1.8%. The atomic electron affinities of these elements are Sr 0.0521, Zr 0.427, Cs 0.472, and Ba 0.1459 eV [3], and thus both isobars have non-negligible ionization yields in the ion source with Zr even being favored over Sr [4, 5]. Therefore, preceding studies all used molecular ion beams such as $SrFn^-$, $ZrFn^-$, $CsFn^-$, $BaFn^-$ (n ≥ 1) for beam extraction from the ion source [5-8]. Specific molecular ions like SrF_3^- and CsF_2^- are especially suited as the formation of their isobaric counterparts (ZrF_3^- for SrF_3^-, BaF_2^- for CsF_2^-) is suppressed by several orders of magnitude [4-6,8].

Pioneering work demonstrated the feasibility of ^{90}Sr detection with conventional AMS and reached a limit of detection (LOD) of 3 mBq, which is comparable to that of β-ray spectrometry, but with a more straightforward chemical separation [8, 9]. Sasa et al. even reported the successful detection of ^{90}Sr in tap water (IAEA-TEL-2015-03) by AMS [8]. However, in these pioneering studies the LOD depended critically on the intensity of the Zr-interference. The 3 MV AMS system at the Vienna Environmental Research Accelerator (VERA), the University of Vienna, is coupled with a novel, powerful isobaric removal system (ILIAMS: Ion Laser InterAction MasSpectrometry) [6, 7]. The ILIAMS system removes isobaric anions via selective laser photodetachment much more efficiently than any conventional AMS technique and thus should achieve better detection limits. This paper reports the results of ^{90}Sr and ^{135}Cs analyses in environmental samples towards the practical application of ILIAMS.

2. Experiment
2.1. Sample Preparation

One gram of environmental samples with known ^{90}Sr concentrations was analyzed by ILIAMS to assess the validity of the chemical treatment and the AMS measurement in this study. The analyzed environmental samples were moss soil (IAEA-447, 5.0±0.3 Bq/kg, 15 November 2009), animal bone (IAEA-A-12, $54.8^{+4.4}_{-8.5}$ Bq/kg, 15 December 1981) and Syrian soil (IAEA-TEL-2015-03 sample 5, 36.2±2.7 Bq/kg, 1 January 2015). These dry environmental samples were ashed in a muffle oven at 450°C for 4 hours. Strontium in the ashen samples was purified according to Figure 1(A). The Sr resin® column was a pre-packed column (50-100 μm, 2 mL) from Eichrom Technologies. The Anion exchange column was prepared by filling 2 mL of MCl Gel CA08P (120 μm, Mitsubishi Chemicals) into a polypropylene column (φ6.5-8.5 mm, Muromach Chemicals). The chemical treatment took ~2 days. The naturally dried precipitate (strontium fluoride) was mixed with PbF_2 powder in a weight ratio of 1: 8 (SrF_2: PbF_2). The mixture was pressed into a copper cathode, and measured by AMS. The AMS results of the environmental samples were normalized to an inhouse standard material (^{90}Sr/Sr = (4.93±0.10) × 10^{-12}, 5 March 2019) prepared from a ^{90}Sr radioactivity standard solution (1.99±0.4 kBq/mL, 4 December 2018).

For the analysis of ^{135}Cs, one dry gram of grass (IAEA-372, 11320±360 Bq/kg, 1 July 2006) was ashed in the same manner as for ^{90}Sr. Cesium in the grass sample was purified according to Figure 1(B) procedure. The column was AG 1 × 8 (100-200 mm mesh, Bio-Rad) filled with 2 mL in a polypropylene

column (φ 6.5-8.5 mm, Muromachi Chemicals). The cation exchange column was prepared by packing 10 mL of Dowex 50W × 8 (100-200 mm mesh, Alfa Aesar) in a PTFE column (φ9.5 mm, Bohlender GmbH). The chemical treatment took ~2 days as with Sr. The dry material was mixed with PbF_2 and copper powders (Cs: F: Cu atomic ratio = 1: 4: 1), pressed into copper cathodes, and subjected to AMS for measurement of $^{135}Cs/^{137}Cs$.

Regarding stable elements of Sr, Zr, Cs, and Ba, the concentrations in the environmental samples and the recoveries in the chemical treatment were determined by ICP-MS (Agilent 7700, single quadrupole, Agilent 8800, MS/MS mode, He collision) and the standard solution of XSTC-622 (35 elements, 10 mg/L each, SPEX).

(A)

Ashen environmental sample
- 1 mg Sr carrier
- 20 mL conc. HNO_3
- acid leaching (4 hours at 230°C)
- filtration (0.45 μm PTFE filter)

Solution
- dry up at 230 °C
- 2 mL 8M HNO_3 and dry up × 3 times
- 10 mL 8M HNO_3

Sr resin® column
bed volume: 2 mL   10 mL 8M HNO_3 / 40 mL 0.01M HNO_3

Solution
- dry up at 230 °C
- 2 mL conc. HCl and dry up × 3 times
- 10 mL conc. HCl

Anion exchange column
bed volume: 2 mL   10 mL conc. HCl

Solution
- dry up at 230 °C
- 2 mL 3M HNO_3 and dry up × 3 times
- 1 mL 0.3M (2%) HNO_3
- 1 mL 48% HF
- allow to stand for 12 hours

Precipitation
- centrifugation (5 min. at 3500 rpm)
- 1 mL ethanol and centrifugation × 3 times
- dry naturally

Precipitation

(B)

Ashen environmental sample
- 1 mg Cs carrier
- 20 mL conc. HNO_3
- acid leaching (4 hours at 230°C)
- filtration (0.45 μm PTFE filter)

Solution
- dry up at 230 °C
- 5-10 mL 3M HNO_3
- 35 mg AMP
- stir for 1 hour

Residue (Cs-AMP)
- filtration (0.45 μm PTFE filter)
- 10 mL 4M NH_4OH
- 10 mL water

Anion exchange column
bed volume: 2 mL   10 mL 1.5M NH_4OH

Cation exchange column
bed volume: 10 mL   20 mL 1.5M NH_4OH / 20 mL water / 110 mL 1 M HNO_3

Solution
(50-110 mL portion of the eluate)
- dry up at 300 °C
- 10 μL 0.2M H_2SO_4 and dry up × 3 times

Residue

Figure. 1 Schematic chart of chemical separation for ^{90}Sr AMS (A) and ^{135}Cs AMS (B). Each of these procedures takes ~2 days.

2.2. AMS measurement at VERA

In the AMS measurements of ^{90}Sr, various molecular ions such as $SrFn^-$ and $ZrFn^-$ (n ≥ 1) were extracted from the ion source and accelerated to 30 keV. The typical current of SrF_3^- from the ion source was ~300 nA. The molecular ions with specific mass-to-charge ratios m/q (e.g., $^{90}SrF_3^-$, $^{90}ZrF_3^-$ for m/q 147) were selected by a 90°bending magnet and injected into the RFQ ion guide in the ILAMS system. The molecular ions are electrostatically decelerated to ~30 eV on a high voltage platform before being injected into the RFQ [6]. Inside the RFQ (ion cooler), collisions with a buffer gas mixture of He and O_2 gas further reduce the ion energy to <1 eV. In addition, the O_2 gas produces oxide ions such as $O-ZrF_3$

and separates Zr (exothermic reaction between O_2 gas and Zr, endothermic reaction between O_2 gas and Sr) [4, 9]. Here, a 12 W laser (VERDI, Coherent Inc., 532 nm (2.33 eV)) overlaps collinearly with the ion beam. ZrF_3^-, which has a lower electron affinity than the laser's photon energy of 2.33 eV, is neutralized by photodetachment [6], while SrF_3^- has an electron affinity above 2.33 eV and is therefore not affected by the laser light. After passing through the ion cooler, $^{90}SrF_3^-$ was re-accelerated to 30 keV and injected into the terminal of the accelerator, where it was subjected to charge conversion and molecular ion destruction (terminal voltage 3.00 MV, charge state 3+, total ion energy 10.85 MeV), and finally detected in a split-anode gas-ionization (ΔE-E) detector. Trace amounts of $^{90}Zr^{3+}$ that still reach the ΔE-E detector were separated from $^{90}Sr^{3+}$ by the difference in energy loss characteristics in the gas. The overall Sr detection efficiency in this system is evaluated to be 0.4‰, and the Zr is suppressed by $>10^{12}$ with respect to Sr [6].

For ^{135}Cs-AMS, the molecular ions ($^{135}CsF_2^-$ and $^{135}BaF_2^-$) with m/q = 173 were injected into the ion cooler filled with He buffer gas. The BaF_2^- is separated by photodetachment with the 532 nm laser in the ion cooler [6]. After passing through the ion cooler, CsF_2^- was guided to the accelerator, accelerated at a terminal voltage of 2.65 MV and finally injected into the ΔE-E detector (total ion energy 10.04 MeV). The CsF_2^- current extracted from the negative ion source was ~50-100 nA and Ba is suppressed by $>10^7$ with respect to Cs [6]. With ILIAMS, presently 10% of negative ions are detected in the ionization chamber, however the ionization efficiency in the ion source has not yet been assessed.

3. Results and Discussion

The Sr recoveries (amount of Sr in the solution passing through the anion exchange column against 1 mg Sr carrier added) were 96% (moss soil), 83% (animal bone), and 80% (Syrian soil). The atomic ratio of Zr/Sr in the target was estimated to be 2×10^{-7} based on the recoveries of Zr and Sr, and the $^{90}Zr/^{88}Sr$ atomic ratio was calculated to be $(0.9-1.0) \times 10^{-7}$. This is more than sufficient since VERA provides a suppression of Zr with the ILIAMS system of $>10^{12}$ reducing the isobaric contribution to background to $^{90}Zr/^{88}Sr \sim 10^{-19}$. The chemical treatment will be improved to achieve better Sr recovery. The limit of detection (LOD), which is determined by the ^{90}Sr purity of the chemicals and cross contamination in the lab and the ion source was <0.08 mBq (^{90}Sr/Sr atomic ratio $<1\times10^{-14}$) based on the results of a blank sample (Sr carrier treated as in Figure 1(A)). This LOD is about 30 times lower than that of 3 mBq [8, 9], which is the LOD for conventional AMS measurements as well as for β-ray spectrometry. The concentrations of ^{90}Sr in the environmental samples (Figure 2) were calculated from the AMS results (^{90}Sr/Sr atomic ratio) and Sr concentration in the environmental samples. The ^{90}Sr concentrations obtained by AMS are in good agreement with the nominal values of the IAEA reference materials within the uncertainties, indicating that the chemical treatment and the AMS measurement are reliable. Therefore, AMS can apply a new sensitive ^{90}Sr analysis method to environmental samples.

The recoveries of Cs (amount of Cs in the solution passing through the cation exchange column against 1 mg Cs carrier) and Ba were 84% and <0.01% (10^{12} atoms), respectively. The Ba/Cs atomic ratio and $^{135}Ba/^{133}Cs$ atomic ratio in the target were estimated to be $<3\times10^{-7}$ and 2×10^{-8}, respectively, based on the recoveries of Cs and Ba carriers. Since the total suppression factor of Ba at VERA is $>10^7$ [6], further Ba reduction by both chemical separation and possibly Ba suppression in the ILIAMS system is not crucial but still desirable to minimize possible interference of ^{135}Ba in AMS. Chemically, this might be achieved by changing the separation conditions (column capacity and elution conditions) of Cs and Ba by cation exchange. With ILIAMS, blank values on samples containing 1 mg of stable Cs carrier of

^{135}Cs/^{133}Cs=6×10^{-12} and ^{137}Cs/^{133}Cs=3×10^{-12} have been reported [6]. This corresponds to a LOD (=Blank + 3·ΔBlank) of ~0.4 µBq for ^{135}Cs and ~18 mBq for ^{137}Cs. With this, the abundance sensitivity (^{135}Cs/Cs atomic ratio) of AMS is the highest among mass spectrometry methods: TIMS 10^{-10}, SF-ICP-MS 10^{-6}, ICP-MS/MS <10^{-8} [2, 11]. The LOD of ^{137}Cs with ILIAMS is about one order of magnitude higher than the 2.5 mBq (20 L seawater, 661 keV) reported for ultra-low background Ge-detectors [12]. Further development of our method with respect to cross contamination in the ion source will hopefully allow us to improve these values in the near future and achieve a detection limit comparable to that of γ-ray spectrometry also for ^{137}Cs.

The analysis of ^{135}Cs in IAEA-372 (soil) by AMS was complicated by low ion source output of < 1 nA on this sample. We collected 218 counts of ^{135}Cs on this sample in total. The obtained result of ^{135}Cs/^{137}Cs = 0.69 ± 0.11 is in reasonable agreement with a previous reported value of ^{135}Cs/^{137}Cs atomic ratio = 0.612 ± 0.008 using TIMS (the decay correction date for both values is 1 January 2018) [13]. However, it has to be noted that the VERA results are normalized only to an in-house reference material that is not yet cross-calibrated, due to the lack of a certified ^{135}Cs/^{137}Cs reference material. Therefore, producing a ^{135}Cs reference material is an urgent issue for us. Furthermore, developments towards an efficient negative ionization and producing intense, stable ion currents from the source are also important issues.
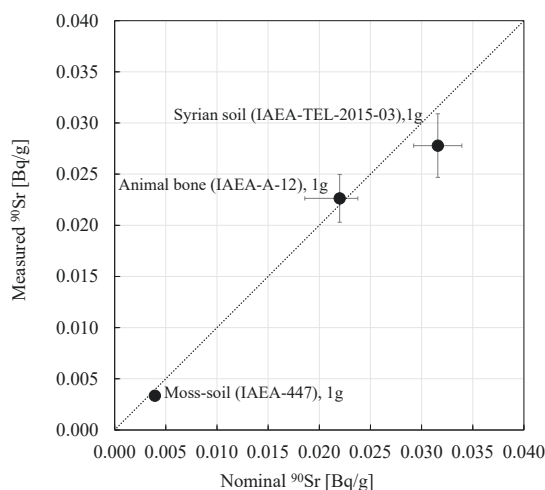
Figure 2 Summary of ^{90}Sr analysis results by AMS. Stated uncertainties are 1 sigma. Reference dates are 11 Dec. 2019 (IAEA-447), 15 Nov. 2019 (IAEA-A-12) and 2 Sep. 2020 (IAEA-TEL-2015-03).

4. Conclusion

First AMS measurements of ^{90}Sr in environmental reference samples with ILIAMS have confirmed the excellent performance of this novel technique. The good agreement between the ^{90}Sr AMS results and the nominal value of the IAEA reference materials within the margin of error indicates that the new sensitive ^{90}Sr analysis is accurate. The new ^{90}Sr analysis will be conducted to research the distribution of ^{90}Sr in a selected area. ^{135}Cs AMS still has several issues, such as Ba separation in chemical treatment, cross-contamination between samples in AMS measurement, low ion source output and the lack of a proper ^{135}Cs reference material. However, first AMS-results on IAEA-372 soil match the value reported by TIMS within 1 sigma. This study demonstrated that ^{135}Cs AMS has the potential to be adapted for environmental radiology.

Acknowledgements

References

[1] Tazoe, H. et al., Determination of strontium-90 from direct separation of yttrium-90 by solid phase extraction using DGA Resin for seawater monitoring, Talanta, vol. 152, 2016, pp. 219-227.

[2] Russell, B. C. et al., Determination of ^{135}Cs and ^{137}Cs in environmental samples: a review, Anal. Chim. Acta, vol. 890, 2015, pp. 7-20.

[3] Rienstra-Kiracofe, J. C. et al., Atomic and molecular electron affinities: photoelectron experiments and theoretical computations, Chem. Rev., vol. 102(1), 2002, pp. 231-282.

[4] Eliades, J. A., et al., Negative ion-gas reaction studies using ion guides and accelerator mass spectrometry I: SrF_3^-, YF_3^-, ZrF_3^-, YF_4^- and ZrF_5^- in NO_2, Nucl. Instrum. Methods Phys. Res. B, vol. 361, 2015, pp. 294-299.

[5] Lachner, J. et al., Developments towards detection of ^{135}Cs at VERA, Nucl. Instrum. Methods Phys. Res. B, vol. 361, 2015, pp. 440-444.

[6] Martschini, M. et al., 5 YEARS OF ION-LASER INTERACTION MASS SPECTROMETRY-STATUS AND PROSPECTS OF ISOBAR SUPPRESSION IN AMS BY LASERS, Radiocarbon, 2021, pp. 1-14.

[7] Martschini, M., et al., The ILIAMS project–An RFQ ion beam cooler for selective laser photodetachment at VERA, Nucl. Instrum. Methods Phys. Res. B, vol. 456, 2019, pp. 213-217.

[8] Sasa, K. et al., A sensitive method for Sr-90 analysis by accelerator mass spectrometry, J. Nucl. Sci. Technol., vol. 58(1), 2021, pp. 72-79.

[9] Tumey, S.J. et al., Further development of accelerator mass spectrometry for the measurement of ^{90}Sr at Lawrence Livermore National Laboratory, J. Radioanal. Nucl. Chem., vol. 282, 2009, pp. 821-824.

[10] Amr, M. A, The collision/reaction cell and its application in inductively coupled plasma mass spectrometry for the determination of radioisotopes: A literature review, Adv. Appl. Sci. Res., vol. 3(4), 2012, pp. 2179-2191.

[11] Zheng, J., et al., Determination of ^{135}Cs and ^{135}Cs/^{137}Cs atom ratio in environmental samples by combining AMP selective Cs adsorption and ion-exchange chromatographic separation to triple quadrupole inductively coupled plasma mass spectrometry, Anal. Chem., vol. 86, 2014, pp. 7103-7110.

[12] Kumamoto, Y. et al., Radiocesium in the western subarctic area of the North Pacific Ocean, Bering Sea, and Arctic Ocean in 2013 and 2014, Appl. Radiat. Isot., vol. 126, 2017, pp. 88-92.

[13] Bu, W. et al., Ultra-trace determination of the ^{135}Cs/^{137}Cs isotopic ratio by thermal ionization mass spectrometry with application to Fukushima marine sediment samples, J. Anal. At. Spectrom., vol. 34(2), 2019, pp. 301-309.

16 ^{241}Am Neutron Capture Cross Section Measurement and Resonance Analysis

Gerard ROVIRA$^{\dagger 1}$, Atsushi KIMURA^{1}, Shoji NAKAMURA^{1}, Shunsuke ENDO^{1},
Osamu IWAMOTO^{1}, Nobuyuki IWAMOTO^{1}, Tatsuya KATABUCHI^{2}, Yu KODAMA^{2},
Hideto NAKANO^{2}, and Yaoki SATO^{2}

^{1}Nuclear Science and Engineering Center, Japan Atomic Energy Agency, 2-4 Shirakata,
Tokai-mura, Naka-gun, Ibaraki 319-1195, Japan
^{2}Laboratory for Zero-Carbon Energy, Institute of Innovative Research, Tokyo Institute
of Technology, Ookayama 2-12-1-N1-26, Meguro-ku, Tokyo 152-8550, Japan
†Email: gerard.rovira@jaea.go.jp

Abstract

Neutron capture cross section measurements for ^{241}Am have been conducted using the NaI(Tl) spectrometer of the Accurate Neutron Nucleus Reaction Measurement Instrument (ANNRI) at the Materials and Life Science Facility (MLF) of the Japan Proton Accelerator Research Complex (J-PARC). Neutron time-of-flight experiments were performed to determine the cross section from 10 meV to 100 eV. Moreover, neutron filter experiments involving the use of a 20-cm-thick ^{nat}Fe filter were also carried out to measure the capture cross section at the energy of 23.5 keV. Together with the cross section measurement, the preliminary results of a resonance analysis using the REFIT program are also presented.

1 Introduction

Accurate nuclear data for minor actinides (MAs) is of utmost importance for the design of advanced nuclear systems since MAs are set to be included as fuel material in many of the upcoming generation of nuclear facilities [1]. One of such facilities is Accelerator-Driven Systems (ADS), a proposed sub-critical nuclear facility aimed at diminishing the environmental burden of the accumulated amount of MAs by means of nuclear transmutation. Recent studies have pinpointed the effects of the current nuclear data in the criticality designs of ADS, setting accuracy targets not only for the fission cross section, which is how the nuclear transmutation of MAs is achieved, but also for the neutron capture cross section as it is the main reaction channel open in most of the keV region [2]. ^{241}Am (t$_{1/2}$ = 432.2 yr) is one of the most abundant MAs in spent nuclear fuel. A preliminary ADS nuclear transmutation study has been performed assuming the MA isotope concentration of 20.72% for ^{241}Am in the core, the second highest after ^{237}Np [3]. The present JENDL-4.0 uncertainties for the neutron capture cross section of ^{241}Am that range from 3% to as high as 40%, much larger than the requirements of below 5% in the energy range from 0.454 keV to 1.35 MeV [4]. Thus, a precise determination of the neutron capture cross section is essential for the design of advanced nuclear systems.

Neutron capture cross section measurements for ^{241}Am were performed in the Accurate Neutron Nucleus Reaction Measurement Instrument (ANNRI) at the Materials and Life Science Facility (MLF) of the Japan Proton Accelerator Research Complex (J-PARC). The time-of-flight (TOF) method was applied in a non-filter condition experiment to determine the neutron

capture cross section from thermal to about 100 eV. In addition, neutron filter experiments were performed using a 20-cm-thick ^{nat}Fe neutron filter to obtain the neutron capture cross section at the energy of 23.5 keV [5].

A sample of ^{241}Am with a mass of 7.5 mg was used for the measurements with an activity of 950 MBq. In the non-filter condition experiment, the energy dependence of the incident neutron spectrum was derived using the 478 keV gamma-rays from the ^{10}B(n, $\alpha\gamma$)^{7}Li reaction with a boron sample containing enriched ^{10}B up to 90%.

In this study, preliminary results of the ^{241}Am neutron capture cross section from 10 meV to about 100 eV determined in TOF experiments and at 23.5 keV from Fe filter experiments are presented. Moreover, early-stage results of a resonance analysis of the ^{241}Am capture resonances are also presented.

2   Experimental Setup

The experiments were performed at the ANNRI beamline of the MLF facility in J-PARC. Pulsed neutrons were generated by the Japanese Spallation Neutron Source (JSNS) in the MLF using the 3 GeV proton beam of the J-PARC facility. The proton pulses were shot in double-bunch mode at the Hg spallation target every 40 ms, with a beam power of about 600 kW. Time-of-flight and neuton filter experiments were conducted to determine the neutron capture cross section of ^{241}Am from 10 meV to around 100 eV; and at 23.5 keV, respectively. In both experiments, prompt capture γ-rays were detected using a NaI(Tl) detector installed in the experimental area 2 of the ANNRI beamline. The NaI(Tl) detector was situated at a 90° angle with respect to the neutron beam axis and a neutron flight path of 27.9 m from the spallation chamber.

A 7.5 mg (950 MBq) ^{241}Am sample with a diameter of 10 mm diameter and 0.5 mm thickness was employed in this experiment. The sample was encapsulated in an Al casing in order to comply with the MLF regulations. A replica of the Al container was used to derive the sample-dependent background induced by the Al case. At the same time, the sample-dependent backgrounds due to scattered neutrons for both the boron and ^{241}Am samples were determined by using a carbon sample.

2.1   Time-of-flight Experiments

The neutron capture cross section of ^{241}Am was determined from 10 meV to 100 eV in time-of-flight experiments by applying the pulse-height weighting technique [6, 7]. This technique allows for the determination of the ^{241}Am neutron capture yield using a weighting function that takes into account the sample characteristics and detector efficiencies. In the present analysis, the weighting function for the ^{241}Am sample was obtained with Monte-Carlo simulations with the SG code [8]. The energy-dependence of the incident neutron spectrum was derived by a boron sample enriched with ^{10}B up to 90% with a diameter of 10 mm and a thickness of 0.5 mm. The ^{10}B(n, α)^{7}Li reaction emits only one γ-ray with the energy of 478 keV. Hence, events from this reaction are easy to isolate. Further information about the ANNRI NaI(Tl) detector time-of-flight experimental setup can be found here [9].

2.2   Neutron Filter Experiments

The neutron filtering technique has been recently proven to be a successful approach in order to bypass the double-bunch structure of the incident neutron flux of ANNRI [5, 10]. In the present experiments, 20 cm of ^{nat}Fe were introduced into the rotary collimator of the ANNRI beamline to mold the incident neutron flux into a quasi mono-chromatic peak with an average neutron energy of 23.5 keV. Alongside the measurements of the ^{241}Am, Al dummy and carbon samples;

a Au sample was also measured to determine the ^{241}Am neutron capture cross section relative to the ^{197}Au neutron capture yield.

3   Data Analysis

3.1   Neutron flux

The time distribution of the incident neutron flux was obtained by measuring the emitted 478 keV γ-rays from the ^{10}B(n,α)^{7}Li reaction in the measurement of the boron sample. The net TOF spectrum was attained by subtracting the sample-dependent and sample-independent backgrounds derived from a carbon sample measurement and a measurement with no sample, respectively. Finally, the incident neutron flux was determined by dividing the net TOF spectrum by the reaction rate calculated from Monte-Carlo simulations with the PHITS code [11]. This reaction rate takes account for the self-shielding and multiple scattering effects within the sample can be formulated as:

$$R(E_n) = \frac{\sigma_{^{10}\text{B},\alpha}}{\sigma_{tot}} \left(1 - e^{-\sigma_{tot}t}\right) \tag{1}$$

with $\sigma_{^{10}\text{B},\alpha}$ as the cross-section for the ^{10}B (n,$\alpha\gamma$)^{7}Li reaction obtained from the PHITS simulation, t as the boron sample area density in "at/b" and σ_{tot} as the sample total cross-section which was calculated in terms of the sample enrichment using the σ_{tot} values from JENDL-4.0.

3.2   Cross section Calculation

The energy dependence of the neutron capture cross section of ^{241}Am was determined from 10 meV to 100 eV by dividing the neutron capture yield, which was corrected by self-shielding and multiple scattering effects using PHITS, by the time distribution of the incident neutron flux derived from the boron sample measurement. The data were normalized using the saturated resonance method. This technique hinges on the use of a sample thick enough for a resonance, where $\Gamma_\gamma \gg \Gamma_n$, to be completely saturated, meaning that, all incident neutrons are expected to interact with the sample. This process is explained in more detail in the following reference [12]. This process can be summarized as:

$$\sigma_{Am}(E_n) = N_{sat} \frac{Y_{Am}(E_n)C(E_n)}{\phi_n(E_n)S_{Am}} \tag{2}$$

where $\sigma_{Am}(E_n)$ means the neutron capture cross section of ^{241}Am. $Y_{Am}(E_n)$, $C(E_n)$, $\phi_n(E_n)$, S_{Am} and N_{sat} stand for the ^{241}Am neutron capture yield, the correction factor for self-shielding and multiple scattering, the incident neutron flux, the area density of the ^{241}Am sample, and the normalization factor, respectively.

In the neutron filter experiments, the absolute value for the neutron capture cross section of ^{241}Am was obtained relative to the ^{197}Au capture yield and the JENDL-4.0 ^{197}Au(n, γ) cross section at the energy of 23.5 keV as follows:

$$\sigma_{Am} = \frac{Y_{Am}}{Y_{Au}} \cdot \frac{S_{Au}}{S_{Am}} \cdot \frac{P_{Au}}{P_{Am}} \cdot \sigma_{Au} \tag{3}$$

being σ_x, Y_x, S_x and P_x, the neutron capture cross section at 23.5 keV, the neutron capture yield, the area density of the sample in at/b and the proton shots during the experiment for both ^{241}Am and ^{197}Au. More information about the cross section calculation in the keV region using the neutron filtering system is provided here [13].

4 Resonance Analysis

The REFIT fitting program [14] was used to analyze the ^{241}Am resonances below 20 eV. This process is still on-going and only preliminary results are presented in this paper. The present preliminary results provide better agreement with the evaluated data from JEFF-3.3 [15] rather than JENDL-4.0 as can be seen in Fig. 1

(a) 0 to 5 eV

(b) 5 to 10 eV
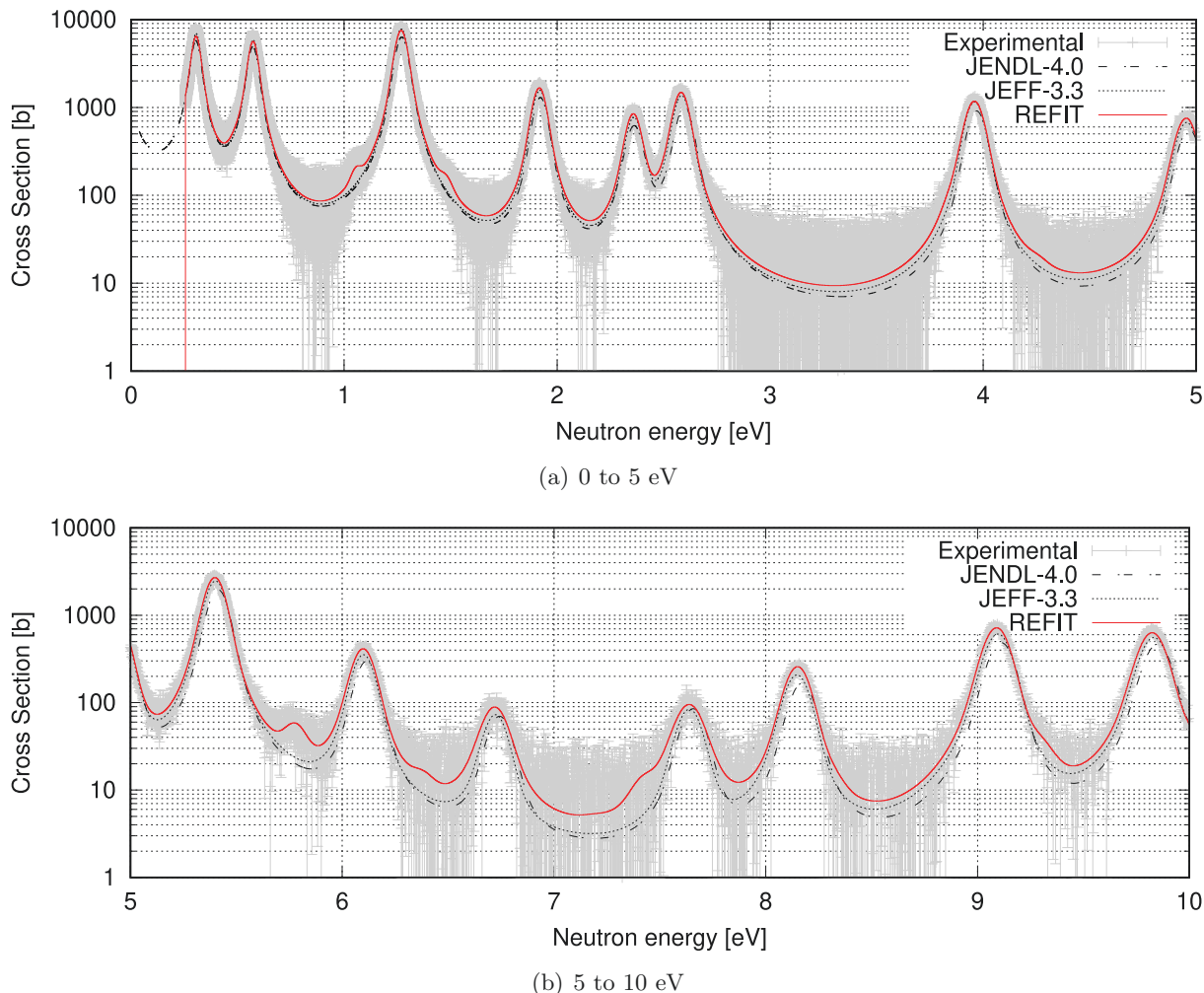
Figure 1: Preliminary ^{241}Am resonance fitting results using REFIT compared to the evaluated data from JENDL-4.0 and JEFF-3.3

5 Cross section Results

The neutron capture cross section of ^{241}Am was determined from 10 meV to 100 eV in time-of-flight experiments and at 23.5 keV by means of the neutron filtering technique involving the use of a 20-cm-thick ^{nat}Fe neutron filter using the formulations explained in Sec. 3.2. The present preliminary results for the ^{241}Am neutron capture cross section are shown in Figs. 2 and 3 together with the evaluated nuclear data from JENDL-4.0 and JEFF-3.3. In the thermal region, JENDL-4.0 seems to better reproduce the present preliminary results as JEFF-3.3 slightly overestimates the present experimental data. In the resonance region, as was discussed in the resonance analysis (see Sec. 4), the present results offer better agreement with the evaluation

from JEFF-3.3 in terms of both resonance area and resonance energy. JENDL-4.0 displays on average lower values for the cross section areas in the resonance region as well as higher values for the resonance energies. In the keV region, the preliminary result with the neutron filtering technique for the ^{241}Am(n,γ) cross section provides agreement within uncertainties with both JENDL-4.0 and JEFF-3.3.
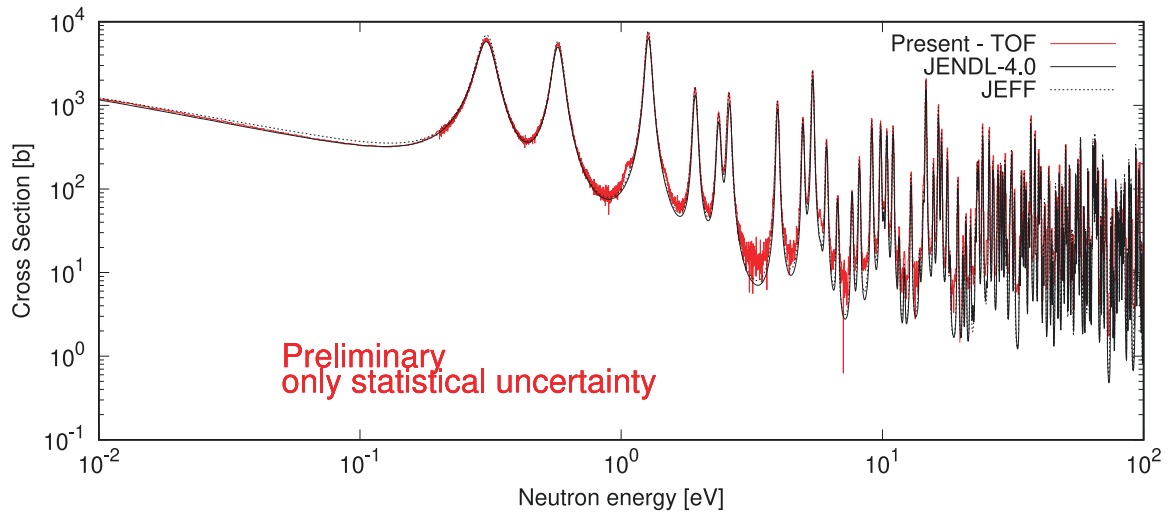
Figure 2: Preliminary results for the ^{241}Am(n,γ) cross section compared to the evaluated data from JENDL-4.0 and JEFF-3.3
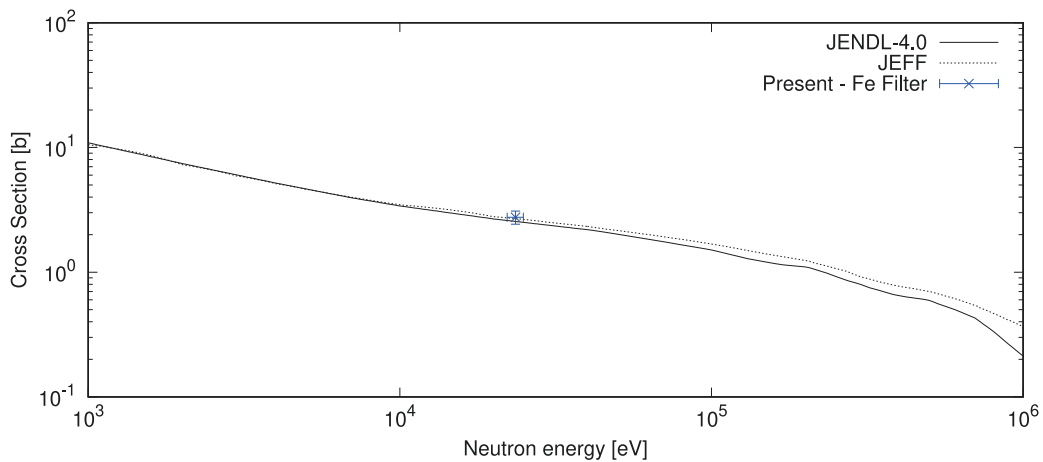
Figure 3: Preliminary results for the ^{241}Am(n,γ) cross section compared to the evaluated data from JENDL-4.0 and JEFF-3.3

6 Conclusions

The neutron capture cross-section of ^{241}Am was measured from 10 meV to 100 eV in TOF experiments and at 23.5 keV using neutron filter experiments at the ANNRI beamline at J-PARC. Preliminary cross section results offer better agreement in the thermal region with the evaluated data from JENDL-4.0 rather than the recommended values from JEFF-3.3. A resonance analysis with the REFIT code was performed below 20 eV and the present experimental data provides similar values for the resonance cross section areas and energy to those from JEFF-3.3.

In the keV region, the results obtained using a 20-cm-thick ^{nat}Fe filter yield agreement within the statistical uncertainty with both JENDL-4.0 and JEFF-3.3.

References

[1] Annual Report 2020. [Internet]. GEN-IV International Forum; [Released in June 2021; cited 20 December 2021]. Available from: https://www.gen-4.org/gif/jcms/c_178290/gif-2020-annual-report

[2] Salvatores M et al., Uncertainty and Target Accuracy Assessment for Innovative Systems Using Recent Covariance Data Evaluations. vol. 26, no. NEA/WPEC-26. 2008.

[3] Iwamoto H et al., Sensitivity and uncertainty analysis for a minor-actinide transmuter with JENDL-4.0. Nuclear Data Sheets, 2014; 118:519-522.

[4] Shibata K et al., JENDL-4.0: a new library for nuclear science and engineering. J. Nucl. Sci. Technol, 2011. 48:1–30

[5] Rovira G et al., eutron beam filter system for fast neutron cross-section measurement at the ANNRI beamline of MLF/J-PARC. Nucl. Inst. Meth. Phys. 2021; 1003:165318.

[6] Moxon MC et al., A gamma-ray detector for neutron capture cross-section measurements. Nucl. Inst. and Meth., 1963. 24:445-455.

[7] Macklin RL et al., Capture-cross-section studies for 30-220 keV neutrons using a new technique. Phys. Rev. 1967; 159:1007-1015.

[8] Ohsaki T et al., An NaI(Tl) spectrometer system for keV neutron radiative-capture reactions. Nuc. Ins. and Meth. in Phys., A 1999; 425:302-319.

[9] Rovira G et al., Neutron capture cross-section measurement and resolved resonance analysis of ^{237}Np. J. Nucl. Sci. Technol. 2020; 57:24-39.

[10] Rovira G et al., KeV-neutron capture cross-section measurement of 197Au with a Cr-filtered neutron beam at the ANNRI beamline of MLF/J-PARC J. Nucl. Sci. Technol. 2021.

[11] Sato T et al., Features of Particle and Heavy Ion Transport Code System PHITS Version 3.02, J. Nucl. Sci. Technol. 2018; 55:684-690.

[12] Rovira G et al., KeV-region analysis of the neutron capture cross-section of ^{237}Np. J. Nucl. Sci. Technol. 2021.

[13] Kodama Y et al., Measurements of the neutron capture cross section of ^{243}Am around 23.5 keV. J. Nucl. Sci. Technol. 2021; 11:1159-1164.

[14] Moxon MC et al., REFIT-2009 A Least-Square Fitting Program for Resonance Analysis of Neutron Transmission, Capture, Fission and Scattering Data Users' Guide for REFIT-2009-10 (UKNSF(2010)P243, April 2010).

[15] Kellet MA et al., The Decay Data Evaluation Project (DDEP) and the JEFF-3.3 radioactive decay data library: Combining international collaborative efforts of evaluated decay data. EPJ Web of Conf. 2017;146:2009.

Acknowledgments

17　Calculation of displacement damage dose of semiconductors using PHITS code

Yosuke IWAMOTO[1][*]

[1]Nuclear Science and Engineering Center, Japan Atomic Energy Agency

2-4 Shirakata, Tokai-mura, Naka-gun, Ibaraki-ken 319-1195, Japan

[*]Email: iwamoto.yosuke@jaea.go.jp

In the space environment, radiations irradiate the semiconductors of the devices, and the atomic displacement caused by these radiations degrades the electrical performance of the devices. The atomic displacement of the semiconductor is proportional to the displacement damage dose (DDD), which is expressed by the non-ionizing energy loss (NIEL). In order to calculate the DDD of semiconductors for various radiation in space, we have developed a method for calculating the DDD in the PHITS code. When silicon was irradiated with protons, neutrons, and electrons, the results of the NIEL calculations by PHITS agreed with the numerical data obtained by the NIEL web calculator for semiconductors. The defect production efficiencies obtained from the recent molecular dynamic simulations for SiC, InAs, GaAs, and GaN were also implemented in PHITS. The results show that InAs and GaAs are the most sensitive to displacement damage and SiC is the most resistant to damage when irradiated with 10 MeV protons.

1. Introduction

As humans advance into space, the use of general-purpose devices in space will increase. Semiconductors such as GaAs, InAs, and GaN are used in general-purpose devices, and there is a concern about the degradation of these semiconductors due to atomic displacement by space radiation. The displacement damage dose (DDD), which is the integration of the non-ionizing energy loss (NIEL) and particle fluence, is used as an index to determine the replacement frequency of equipment in space radiation environment. Monte Carlo particle transport codes such as GEANT4[1], and FLUKA[2] can calculate DDD using NIEL and particle fluence in space. The NIEL data can be obtained from the Screened Relativistic (SR) Nuclear and Electronic Stopping Power Calculator on the web site[3]. This SR-NIEL web calculator can produce the NIEL data of semiconductors for neutrons, electrons, protons, heavy-ions with Coulomb interaction for charged particles and hadronic cascade contributions.

On the other hand, Gao et al. reported the defect production efficiency of compound semiconductors such as SiC[4], GaAs[5], GaN[6], and InAs[7] calculated by molecular dynamics (MD) simulations. According to the papers[4-7], defect production efficiencies change with damage energy in semiconductors. Therefore, it is important to calculate the effective NIEL of semiconductors with considering these defect production efficiencies. We had developed the calculation method of displacement per atoms (dpa) cross sections of metals for all particles in the particle and heavy-ion

transport code (PHITS) [8-10] based on the NRT model[11] and the athermal corrected (arc) model[12]. The defect production efficiencies obtained by MD simulation were implemented in PHITS to calculate the arc-dpa cross sections. Based on this dpa calculation method, it is possible to calculate the effective NIEL and DDD of semiconductors for all particles.

In this work, the calculation method of NIEL and DDD for semiconductors were developed based on the dpa calculation method in PHITS. The defect production efficiencies of SiC, GaAs, InAs, and GaN were implemented in PHITS to calculate the effective NIEL. The original NIEL were compared with the effective NIEL of these semiconductors for neutrons and protons.

2. Methods

The calculation model of DDD with Monte Carlo method has been developed in PHITS, which simulates particle transport in three-dimensional space. The calculation method of DDD is similar with the dpa calculation of hadron, electron and gamma irradiation implemented in PHITS. The present study for DDD of semiconductors is based on them.

2.1. DDD calculation method

The DDD in each region mesh is expressed with NIEL related to the displacement damage of materials as:

$$DDD = NIEL\phi = NIEL\frac{l}{v} \tag{1}$$

where ϕ is a fluence in a mesh, l is a track length of the particle, and v is the volume of a mesh. Based on the Kinchin-Peace (KP) model[11], NIEL of the particle related to the displacement damage of materials is written as:

$$NIEL = \rho \int_{E_d}^{T_{max}} T \frac{d\sigma}{dT} G(T) \, dT \tag{2}$$

where ρ is the atomic density, T is the kinetic energy of recoils, $d\sigma/dT$ is the differential interaction cross section, $G(T)$ is the energy-partition function related to the energy transferred to the lattice atoms along with the KP model, and E_d is the displacement threshold energy. For DDD calculations in a region, the average value of T in a region is used. T_{max} is the maximum energy that can be transferred to a recoil nucleus by an incident particle.

$$T_{max} = \frac{4M_1M_2}{(M_1+M_2)^2}T \tag{3}$$

where M_1 and M_2 are the mass of incident particles and target material, respectively.

The differential scattering cross section $d\sigma/dt$ of charged particles is described with classical scattering theory using the screening functions $f(t^{1/2})$. A universal one-parameter differential scattering cross section equation in reduced notation is expressed by Lindhard et al. [13] as:

$$\frac{d\sigma}{dt} = \frac{\pi a_U^2}{2} \frac{f(t^{1/2})}{t^{3/2}} \tag{4}$$

where $t = \varepsilon^2 T/T_{max}$ is a dimensionless collision parameter related to recoil energy T. The screening function, $f(t^{1/2})$, can be generalized to provide a one parameter universal differential scattering cross section equation for interatomic potentials such as screened and unscreened Coulomb potentials. The general form is:

$$f(t^{1/2}) = \lambda t^{1/2-m}[1 + (2\lambda t^{1-m})^q]^{-1/q} \tag{5}$$

where λ, m, and q are fitting parameters. In this study, λ =5.01, m=0.203, and q=0.413 related to Ziegler-Briersack-Littmark (ZBL) screen potential[14] are adopted. For the Coulomb scattering cross section of electrons, the relativistic and quantum mechanical cross section derived by McKinley and Feshbach[15] is used. For the PHITS calculation, NIEL is calculated in each region event-by-event using the analytic formula. Therefore, PHITS can calculate DDDs for all incident particles and target materials not only silicon but also other materials without NIEL data.

Figure 1 shows NIELs for proton, neutron and electron irradiation on silicon calculated by PHITS and comparison with numerical data obtained from the SR Nuclear and Electronic Stopping Power Calculator [3]. Since NIELs calculated by PHITS agree well with the data obtained from SR-calculator, DDD calculation in three-dimensional materials is also reliable using PHITS.
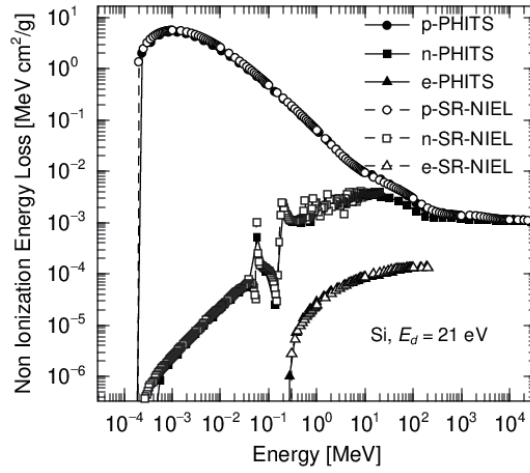
Figure 1: NIELs for proton, neutron and electron irradiation on silicon calculated by PHITS and numerical data obtained from the SR Nuclear and Electronic Stopping Power Calculator (version 7.7.3)[3].

2.2. Implementation of defect production efficiencies

The model in Equation (2) can be estimated by the Kinchin-Pease model. The number of defects produced by a PKA is linearly proportional to the recoil energy, which means that the NIEL becomes to the number of defects produced by the irradiation. However, it has been recognized that the NIEL is not proportional to the number of defects, due to non-linear processes that take place in semiconductors, related with the formation of multiple disordered regions or amorphous pockets[4-7]. A MD method was applied to study defect production in semiconductors. The defect production efficiency is expressed by the ratio of the number of defects calculated by MD simulation, N_F, and the number of defects by the NRT model, N_{NRT}, as follows:

$$\kappa = \frac{N_F}{N_{NRT}} = \frac{E_{MD}}{T_d} \tag{6}$$

where E_{MD} is the damage energy in MD simulation and T_d is the damage energy which is equal to $TG(T)$ in Equation (2).

Figure 2 shows defect production efficiencies calculated by MD simulations as a function of cascade damage energy for SiC[4], GaAs[5], GaN[6], and InAs[7], respectively. In this study, these data were fitted by the following formula based on the arc model[12].

$$\kappa = \frac{(a_{MD} - c_{MD})}{(2.5E_d)^{b_{MD}}} T_d^{b_{MD}} + c_{MD} \tag{7}$$

where E_d is the threshold displacement energy and a_{MD}, b_{MD}, and c_{MD} are the fitting parameters listed in Table 1. The effective NIELs for SiC, InAs, GaAs, and GaN were calculated by the integral of NIEL in Equation (2) and the defect production efficiency in Equation (7). It is evident that GaAs and InAs share the same trend, but GaN and SiC exhibit opposite one. The surviving probabilities for GaAs and InAs increase with damage energy. For damage energy range from 1 keV to 20 keV, they increase with nonlinear. According to the MD results[4-7], nonlinear behavior can be explained by the direct-impact amorphization because the formation of these disordered regions will be exaggerated at higher energies for both InAs and GaAs. However, defect production efficiency decreases with damage energy for GaN and SiC once recombination becomes significant.
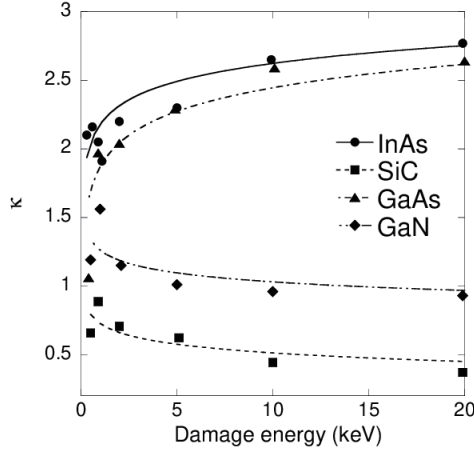
Figure 2: Defect production efficiencies as a function of cascade damage energy for SiC[4], GaAs[5] and GaN[6], InAs[7], respectively. The numerical data were fitted by the function in Equation (7).

Table 1: Material constants for damage production. E_d for SiC[4], GaAs[5], GaN[6], and InAs[7] was obtained from the literature, respectively.

	SiC	InAs	GaAs	GaN
E_d (eV)	25	15	14	50
a_{MD}	1.0	1.5	1.0	1.5
b_{MD}	-0.023	-0.023	-0.011	-0.067
c_{MD}	-3.46	10.7	25.5	-0.35

3. Results

Calculated NIELs of SiC, InAs, GaAs and GaN for proton and neutron irradiation are plotted in Figure 3. The energy range of neutron is from 10^{-11} MeV to 10 GeV and that of proton is from 10^{-4} MeV to 10 GeV, respectively. For the comparison of neutron NIELs among materials the energy range below 10^{-4}, NIEL of GaN is larger than NIELs of GaAs and InAs by a factor of 10 and NIEL of SiC by a factor of 10^3. In this energy range, secondary particles produced by the neutron capture reaction are dominant for GaAs, InAs and SiC. On the other hand, 30 keV ^{14}C and 0.58 MeV proton produced by the ^{14}N(n,p)^{14}C nuclear reaction are dominant for GaN. With the consideration of particle transport in 0.1μm thick GaN, 99.8 % DDD in total is obtained by 30 keV C. From this result, semiconductors with nitrogen are not recommended to be set under low-energy neutron irradiation due to high displacement damage.
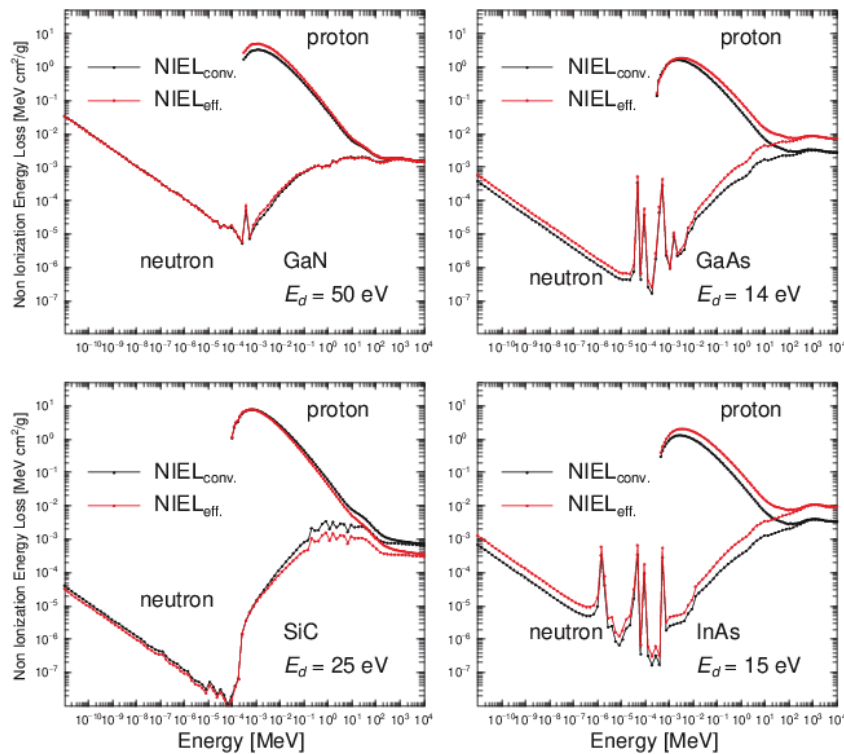
Figure 3: NEIL$_{eff}$ and NEIL$_{conv}$ for the proton and neutron irradiation of GaN, GaAs, SiC, and InAs calculated by the PHITS code.

For neuron irradiation with energies over 10^{-4} MeV, charged particles produced by neutron elastic and inelastic reactions contribute to NIELs. For proton irradiation, Coulomb scattering between incident proton and target is dominant to the radiation damage below 10 MeV and secondary particles produced by nuclear reactions are dominant in high-energy range above 10 MeV.

Figure 3 also shows the effective NIELs (NEIL$_{eff}$) under proton and neutron irradiation. Except for SiC, the ratio of effective NIEL to conventional NIEL (NEIL$_{conv}$) is higher than 1 in the whole energy range of proton and neutron because the defect production efficiencies to the damage energy is higher than 1 as shown in Figure 2. For SiC and GaN under proton irradiation, this ratio decreases with proton energy. On the other hand, for InAs and GaAs, this ratio increases with proton energy up to 100 MeV and it reaches constant value because the defect production efficiency over 20 keV of damage energy is set to be same with that at 20 keV. When irradiated with 10 MeV protons, the results show that InAs and GaAs are the most sensitive to displacement damage and SiC is the most resistant to damage.

4. Summary

In order to calculate the DDD of semiconductors for various radiation, we have developed a method for calculating the NIEL and DDD in the PHITS code. When silicon was irradiated with protons, neutrons, and electrons, the results of the NIEL calculated by PHITS agreed with the numerical data obtained by the NIEL computer for semiconductors. The defect production efficiencies obtained from the recent molecular dynamic simulations for SiC, InAs, GaAs, and GaN semiconductors were also implemented in PHITS. The results show that InAs and GaAs are the most sensitive to displacement damage and SiC is the most resistant to damage when irradiated with 10 MeV protons.

References

1) Allison J., et al., Recent developments in Geant4, Nucl. Instrum. Meth. A, vol.835, 2016, pp.186-225.

2) Battistoni G., et al., Overview of the FLUKA code, Annals of Nuclear Energy, vol.82, 2015, pp.10–18.

3) Boschini, M., Rancoita, P. & Tacconi, M. Sr-niel calculator: Screened relativistic (sr) treatment for calculating the displacement damage and nuclear stopping powers for electrons, protons, light- and heavy- ions in materials (version 7.7.3). [Online] available at INFN sez. Milano-Bicocca, Italy DOI: http://www.sr-niel.org/ (accessed 2022-03-20).

4) Gao, F., Weber, W., Devanathan, R. Atomistic simulation of displacement damage and amorphization in β -SiC, Nucl. Instrum. Meth. B, vol.180, 2001, pp.176-186.

5) Gao, F., Chen, N., Hernandez-Rivera, E., Huang, D., LeVan, P. D., Displacement Damage and Predicted Nonionizing Energy Loss in GaAs, J. Appl. Phys., vol.121, 2017, 095104.

6) Chen, N., Rasch, E., Huang, D., Heller, E. R., Gao, F., Atomic-Scale Simulation for Pseudometallic Defect-Generation Kinetics and Effective NIEL in GaN, IEEE Transactions on Nuclear Science, vol.65, 2018, pp.1108–1118.

7) Chen, N., Huang, D., Heller, E. R., Cardimona, D. A., Gao, F., Atomistic simulation of displacement damage and effective nonionizing energy loss in InAs, Phys. Rev. Mater., vol.5, 2021, 033603.

8) Sato, T. et al., Features of Particle and Heavy Ion Transport Code System (PHITS) Version 3.02, J. Nucl. Sci. Technol., vol.55, 2018, pp.684–690.

9) Iwamoto, Y., Niita, K., Sawai, T., Ronningen, R., Baumann, T., Improvement of Radiation Damage Calculation in PHITS and Tests for Copper and Tungsten Irradiated with Protons and Heavy-Ions over a Wide Energy Range, Nucl. Instruments Methods Phys. Res. B, vol.274, 2012, pp.57–64.

10) Iwamoto, Y., Meigo, S., Hashimoto, S., Estimation of Reliable Displacements-Per-Atom Based on Athermal Recombination-Corrected Model in Radiation Environments at Nuclear Fission, Fusion, and Accelerator Facilities. J. Nucl. Mater,. vol.538, 2020, 152261.

11) Norgett, M.J., Robinson, M.T., Torrens, I.M., A Proposed Method of Calculating Displacement Dose Rates, Nucl. Eng. Des. Vol.33, 1975, pp.50-54.

12) Nordlund, K. et al., Primary Radiation Damage: A Review of Current Understanding and Models. J. Nucl. Mater., vol.512, 2018, pp.450–479.

13) Lindhard, J., Scharff, M., Schiøtt, H.E., Range Concepts and Heavy Ion Ranges (Notes on Atomic Collisions, II), Mat. Fys. Medd. Dan. Vid. Selsk., vol.33 (14), 1963, pp.1-44.

14) Ziegler J.F., Biersack J.P., The Stopping and Range of Ions in Matter. In: Bromley D.A. (eds) Treatise on Heavy-Ion Science. Springer, Boston, MA.

15) William A., Mckinley, JR., The Coulomb Scattering of Relativistic Electrons by Nuclei, Physical Review, vol.74, 1948, pp.1759-1763.

Acknowledgements

18 The optical potential for neutron-nucleus scattering derived by Bayesian optimization

Shoto WATANABE[†1], Futoshi MINATO[2], Masaaki KIMURA[1,3,4], and Nobuyuki IWAMOTO[2,3]

[1]Department of Physics, Hokkaido University, Sapporo 060-0810, Japan
[2]Nuclear Data Center, Japan Atomic Energy Agency, Tokai, Ibaraki 319-1195, Japan
[3]Nuclear Reaction Data Centre, Hokkaido University, Sapporo 060-0810, Japan
[4]RIKEN Nishina Center, Wako, Saitama 351-0198, Japan
[†]Email: shoto@nucl.sci.hokudai.ac.jp

Abstract

To produce the nuclear data efficiently, we considered a new method that combines the nuclear reaction models with the Gaussian process regression. Within this framework, we first optimized the parameters of the optical potential using experimental data of neutron elastic scattering. We then calculated angular distributions at various neutron energies with the optimized parameters, and found that the calculated results reasonably reproduced the experimental data.

1 Introduction

The nuclear data are used in various fields such as design of nuclear reactors, nucleosynthesis in stellar objects, and production of radioisotopes. In general, the production of nuclear data requires a large amount of human and time resources. In this respect, we pay attention to the data science and machine learning, which are recently developed with increasing computational resources and provide a lot of benefits to many social fields.

The use of machine learning has already been attempted to produce nuclear data. Gaussian process regression was applied to predicting the nuclear data, based on available experimental data [1]. Their methodology is helpful to estimate cross sections in the region where many experimental data are present. In contrast, the predictive power becomes weak if experimental data are sparse or not present. This is because their methodology is not built on a physical background.

To efficiently and effectively produce the nuclear data, we come up with the idea that combines nuclear reaction models with the machine learning technique. As a first attempt, we developed a system that consists of the Gaussian process regression and the nuclear reaction model code CCONE [2]. Using the system, we optimized nuclear reaction model parameters that are used for the nuclear data evaluation, and calculated nucleon-nucleus scattering cross sections. We present in this paper our results that were calculated at various incident energies and were compared with existing experimental data.

2 Framework

2.1 Nuclear reaction model

We used the CCONE code [2], which is based on the optical model and the Hauser-Feshbach statistical model, to calculate the cross sections and angular distributions for neutron-nucleus scattering. In this work, the following functional form of the optical model potential V was adopted [3]:

$$
\begin{aligned}
V(r) =& K \left[-V_R U_R(r) + i \left(4W_D a_D \frac{d}{dr} U_D(r) - W_V U_V(r) \right) \right] \\
& + \left(\frac{\hbar}{m_\pi c} \right)^2 (V_{SO} + iW_{SO}) \frac{1}{r} \frac{d}{dr} U_{SO}(r) \boldsymbol{L} \cdot \boldsymbol{\sigma},
\end{aligned} \tag{1}
$$

$$
U_i(r) = \frac{1}{1 + \exp\{(r - R_i)/a_i\}}, \quad i = R, D, V, SO, \tag{2}
$$

$$
R_i = r_i A^{1/3} \left(1 + \sum_{l=2,4,\cdots} \beta_l Y_{l0}(\hat{r}) \right), \quad i = R, D, V, SO, \tag{3}
$$

where R_i, r_i, and a_i are the potential radius, radius and diffuseness parameters, respectively. The symbols R, D, V, SO stands for the real volume, imaginary surface, imaginary volume, and spin-orbit terms, respectively. The mass and deformation parameter are denoted by A and β_l, respectively, and Y_{l0} stands for the spherical harmonics with the multipolarity l. The forms of real volume and imaginary surface terms are as follows:

$$
V_R(E) = (V_R^0 + V_R^{DISP} e^{-\lambda_R E}) \times \left[1 - \frac{1}{V_R^0 + V_R^{DISP}} C_{viso} \frac{N - Z}{A} \right], \tag{4}
$$

$$
W_D(E) = \left[W_D^{DISP} - C_{wiso} \frac{N - Z}{A} \right] e^{-\lambda_D E} \frac{E^2}{E^2 + WID_D^2}, \tag{5}
$$

$$
\tag{6}
$$

where E is the neutron energy relative to the Fermi energy, and N and Z are the neutron and atomic numbers of the target, respectively. The parameters V_R^0, V_R^{DISP}, r_R, a_R, W_D^{DISP} and λ_D were optimized in this work. The other parameters were fixed to the same values as Table 4 of Ref. [3].

2.2 Evaluation function

In order to obtain optimum parameters, we defined an evaluation function that quantifies the difference between the cross sections calculated within the CCONE and the experimental data. In this work, we used the following evaluation function:

$$
f(x) = \frac{1}{N_D} \sum_i^{N_D} \left(\frac{\sigma_{exp}^{(i)}}{\Delta\sigma_{exp}^{(i)}} \log_{10} \frac{\sigma_{th}^{(i)}(x)}{\sigma_{exp}^{(i)}} \right)^2, \tag{7}
$$

where σ_{th} and σ_{exp} are the calculated and experimental cross sections, respectively, N_D is the number of experimental data, and x represents the parameters introduced in Section 2.1. Experimental uncertainty is denoted by $\Delta\sigma_{exp}$. The superscript i corresponds to data point of the experiments.

We considered that the parameter set that minimizes the evaluation function of Equation (7) is the likelihood one. Since we did not know the exact form of $f(x)$ at the beginning, we needed to calculate the cross sections by various parameter sets, and to obtain $f(x)$ as a function of the parameter set. However, this approach usually requires a number of human resource and time. For this reason, we applied the Bayesian optimization based on the Gaussian process regression in this work to finding the minimum of $f(x)$ effectively.

2.3 Gaussian process regression and Bayesian optimization

The Gaussian process regression is one of the algorithms for solving regression problems. Supposed that we have several data points, e.g. input x and output y. There exists a function given by $y = f(x)$ that transform input x to output y, however, we do not know $f(x)$ for many cases. The Gaussian process predicts the function $y = f(x)$ that represents the relation between input and output from existing data points, including the uncertainty.

Given output $y = f(x)$ for an input x, the Gaussian process assumes that the conditional probability distribution of the output at an arbitrary input x^* besides x is expressed as follows:

$$p(\boldsymbol{y}^*|\boldsymbol{y}) = \mathcal{N}(\boldsymbol{K}_*^T \boldsymbol{K}^{-1} \boldsymbol{y}, \boldsymbol{K}_{**} - \boldsymbol{K}_*^T \boldsymbol{K}^{-1} \boldsymbol{K}_*) \equiv \mathcal{N}(\boldsymbol{M}(\boldsymbol{x}^*), \boldsymbol{\Sigma}^*), \tag{8}$$

where $\mathcal{N}$ denotes the multivariate Gaussian distribution, and $\boldsymbol{K}$, $\boldsymbol{K}_*$, $\boldsymbol{K}_{**}$ are the kernel functions for the set of inputs (x, x), (x^*, x), and (x^*, x^*), respectively. We defined the mean and covariance matrix as $\boldsymbol{M}(x^*) = \boldsymbol{K}_*^T \boldsymbol{K}^{-1} \boldsymbol{y}$ and $\boldsymbol{\Sigma}^* = \boldsymbol{K}_{**} - \boldsymbol{K}_*^T \boldsymbol{K}^{-1} \mathbf{K}_*$, respectively.

In this work, we use the RBF kernel function for $\boldsymbol{K}, \boldsymbol{K}_*$, and $\boldsymbol{K}_{**}$, which is given by

$$\boldsymbol{K}(x_i, x_j) = \exp\left\{-\frac{1}{2}\|x_i - x_j\|^2\right\}. \tag{9}$$

From Equation (8), we can predict $f(x)$ for an arbitrary input x^*, however we cannot usually determine the minimum of $f(x)$ only with the limited number of input and output data point of (x, y). In the case, we need to increase the data point by appropriately choosing a new input denoted as x_{new} in addition to x. The selection of x_{new} is carried out within the so-called lower confidence bound (LCB) acquisition function:

$$x_{new} = \operatorname{argmin}_{k=n+1,\ldots,n+m}(M(x_k^*) - 2\sigma_k^*), \tag{10}$$

where σ_k^* is the value of the estimation uncertainty, which is calculated by $\sigma_k^* = 1/\sqrt{(\boldsymbol{\Sigma}^*)_{kk}}$. This LCB acquisition function chooses x_{new}, where $y = f(x)$ is small including the uncertainty. New output y is, then, calculated from x_{new}, increasing the number of data point by 1. The conditional probability distribution of Equation (8) is updated, using the new data points. We repeat this operation until we obtain $f(x)$ that is enough to determine the minimum. When optimizing six parameters, this operation was repeated until the minimum value was not updated more than 200 times in a row.

3 Results

3.1 Optimization process of parameters

In this section we will explain the search process for optimal parameters. We selected the angular distributions of elastic scattering on ^{54}Fe at neutron energy of 7 MeV. The calculated result is
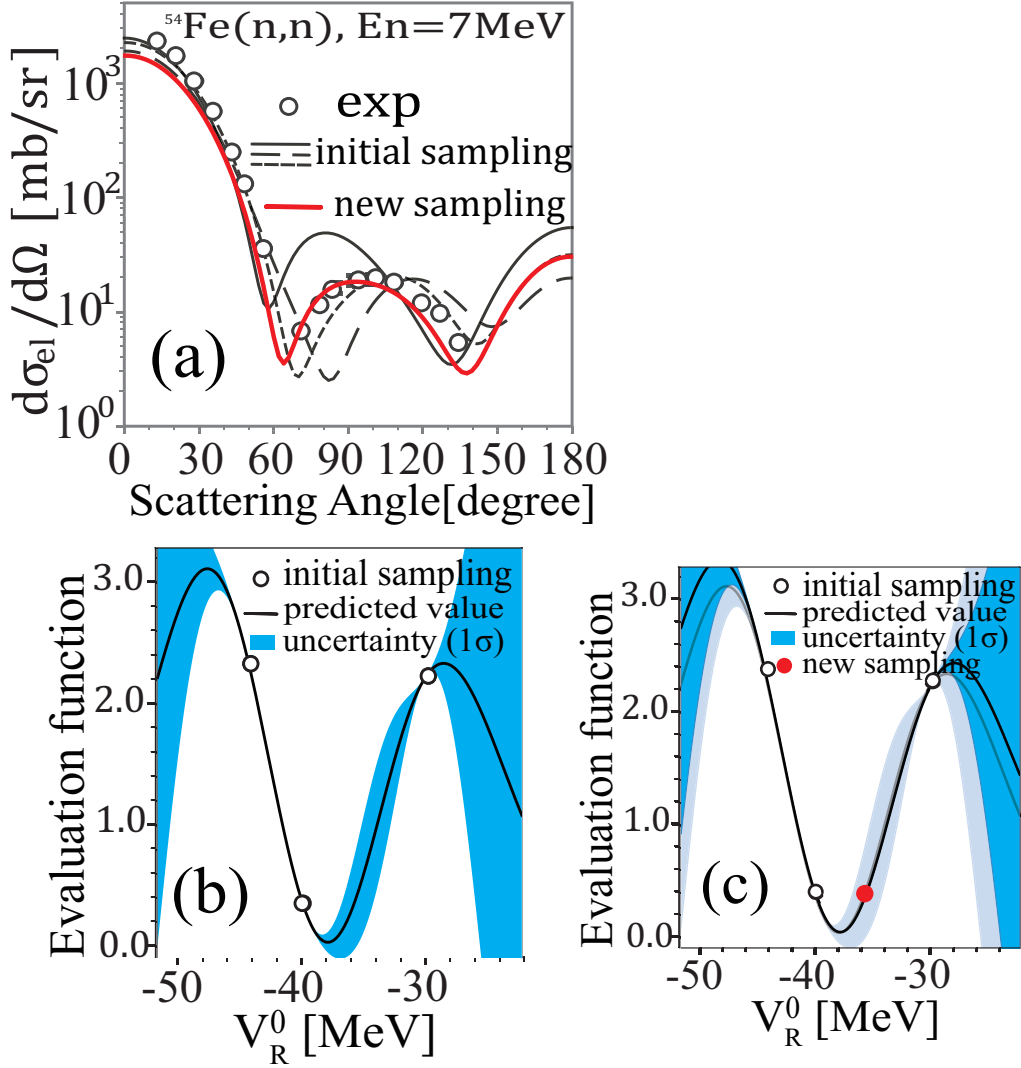
Figure 1: Example of the optimization process. (a) Angular distributions of elastic scattering on ^{54}Fe calculated by CCONE, using the initial and new samplings of V_R^0 (black solid, long-dashed, long-dashed and red solid lines). (b) Evaluation function of the initial samplings (open circles) and predicted value (solid line) computed by the Gaussian process regression. (c) Same as (b), but the result after adding the new sampling point (red filled circle). The prior predicted result shown in (b) is shown with the light blue color.

shown in Figure 1. Firstly, we took three V_R^0 randomly and calculated the angular distributions, which are drawn with the black solid, dashed, and long-dashed lines in Figure 1(a). Then, we computed the evaluation functions at each initial sampling point of V_R^0 as illustrated with the open circles in Figure 1(b). Next, the sampling points were used as the training data of the Gaussian process regression, and the evaluation function at points other than the initial samples is predicted, which is shown by the solid line in Figure 1(b) together with the prediction uncertainty. With the condition of Equation (10), the new input x_{new} was determined and the differential cross section and the evaluation function were calculated again. The angular distribution calculated by the new input is shown by the red solid line in Figure 1(a) and the evaluation function is shown by the red filled circle in Figure 1(c). Now we had four data points to be used as the training data of the Gaussian process regression. The evaluation function was

again predicted with the newly sampled results, and the result is shown in Figure 1(c). We can find that the prediction uncertainty becomes small, especially in $-40 \leq V_R^0 \leq -30$ MeV after adding the new data point. By updating sampling points iteratively, we can obtain V_R^0 that made the evaluation function the smallest.

3.2 Prediction of angular distributions at arbitrary energies

We present in this section how our method predicts the angular distributions at arbitrary energies from the known experimental data. Table 1 lists the experimental data of ^{54}Fe (neutron total section σ_{tot}, elastic scattering cross sections σ_{ela}, angular distributions of the neutron elastic scattering $\mathrm{d}\sigma_{ela}/\mathrm{d}\Omega$, and angular distributions of the neutron inelastic scatterings to the first excited state $\mathrm{d}\sigma_{inel}/\mathrm{d}\Omega$). The upper five rows list the data used for the optimization of the potential parameters V_R^0, V_R^{DISP}, W_D^{DISP}, λ_D, r_R and a_R, whereas the lower two rows are the data used to check the predicted angular distributions. Here, we note that the parameters V_R^{DISP} and λ_D are related to the energy dependent terms of the optical potential given by Equation. 1

Table 1: Experimental data of ^{54}Fe used for optimization of parameters (upper five rows) and for check of predicted angular distributions (lower two rows). We used experimental data, Carton et al. [4], Korzh et al. [5], El-Kadi et al. [6], Cornelis et al. [7], Mellema et al. [8], Kinney et al. [9].

Energy (MeV)	σ_{tot}	σ_{ela}	$\mathrm{d}\sigma_{ela}/\mathrm{d}\Omega$	$\mathrm{d}\sigma_{inel}/\mathrm{d}\Omega$
7	[4]	[5]	[5]	[5]
7.96	[4]	[6]	[6]	[6]
9.94	[7]	[6]	[6]	[6]
11	[7]	—	[8]	[8]
11.93	[7]	[6]	[6]	[6]
8.5	—	—	[9]	[9]
24	—	—	[8]	[8]

Figure 2 shows that the angular distributions at 7 and 12 MeV calculated with the optimized parameters (blue lines) are compared with the experimental data. We can see that the calculated results reproduce the experimental data reasonably. This indicates that the optimization of parameters successfully works within our framework.

Using the optical potential derived with the obtained parameters, we predicted the angular distributions at 8.5 and 24 MeV which are shown by the red lines in Figure 2. We can see that the experimental data at 8.5 and 24 MeV are well reproduced. This fact clarifies that we were able to obtain the optimal optical potential from a set of experimental data.

4 Summary

In the present study, we combined the nuclear reaction model with the Gaussian process regression, and optimized the parameters representing the optical potential. We showed that the angular distributions calculated by our framework were predicted with sufficient reproducibility. In the future, we plan to lead our research to the goal of directly predicting the optimal parameters at arbitrary energies.
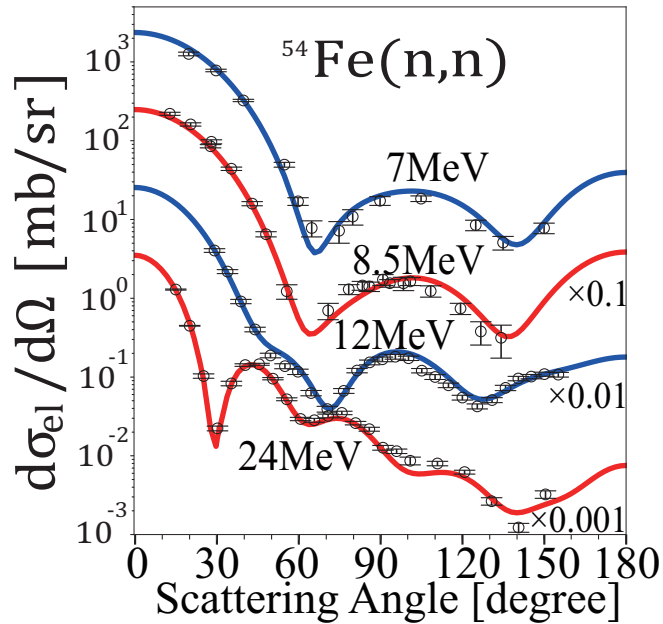
Figure 2: Angular distributions of neutron elastic scattering on ^{54}Fe predicted using optical potentials optimized so as to reproduce experimental data at energies of 7 and 11.93 MeV (blue lines) plus 7.96, 9.94 and 11 MeV and using the optical potential derived with the obtained parameters at 8.5 and 24 MeV (red lines).

References

[1] Iwamoto H. Generation of nuclear data using Gaussian process regression. J. Nucl. Sci. Technol. 2020;57(8):932–938.

[2] Iwamoto O, Iwamoto N, Kunieda S, et al. The CCONE code system and its application to nuclear data evaluation for fission and other reactions. Nuclear Data Sheets. 2016;131:259–288.

[3] Kunieda S, Chiba S, Shibata K, et al. Coupled-channels optical model analyses of nucleon-induced reactions for medium and heavy nuclei in the energy region from 1 keV to 200 MeV. J. Nucl. Sci. Technol. 2007;44(6):838–852.

[4] Carlton RF, Harvey JA, Castel B. Single particle strength in ^{55}Fe. Bull. Am. Phys. Soc. 1985.

[5] Korzh IA, Mishchenko VA, Pravdivyi NM. Fast neutron elastic and inelastic scattering cross sections of ^{54}Fe. Soviet Atomic Energy. 1987;62(6):487–492.

[6] El-Kadi S, Nelson C, Purser F, et al. Elastic and inelastic scattering of neutrons from ^{54,56}Fe and ^{63,65}Cu. Nucl. Phys. A. 1982;390(3):509–540.

[7] Cornelis E, Mewissen L, Poortmans F. Total neutron cross section of Fe-54 and Fe-56 in the energy range 500 keV to 19 MeV. Int. Conf. Nucl. Data for Sci. and Technol., Antwerp, 1982, 135

[8] Mellema S, Finlay RW, Dietrich FS, et al. Microscopic and conventional optical model analysis of fast neutron scattering from ^{54,56}Fe. Phys. Rev. C. 1983;28(6):2267–2277.

[9] Kinney WE, Perey FG. ^{54}Fe neutron elastic and inelastic scattering cross sections from 5.50 to 8.50 MeV. Oak Ridge National Laboratory, ORNL-4907, 1974.

19 Small-angle scattering measurements for cement paste samples using X-rays and neutrons in Hokkaido University

Kaoru Y. HARA[1*], Yuka MORINAGA[1], Yuya YODA[2] and Masato OHNUMA[1]

[1]Faculty of Engineering, Hokkaido University

Kita 13 Nishi 8, Kita-ku, Sapporo 060-8628, Japan

[2]Institute of Technology, Shimizu Corporation

3-4-17 Etchujima, Koto-ku, Tokyo 135-8530, Japan

[*]Email: hara.kaoru@eng.hokudai.ac.jp

An in-situ SAXS measurement for a cement paste sample was demonstrated using a laboratory-based SAXS instrument in Hokkaido University. The time-evolution of nanostructure under the cement hydration process was obtained at 20℃ in the age from 4 h to 14 d. The SAXS for a hardened cement paste sample was also measured at the age of 1 y. As a complementary approach, in addition, a SANS experiment has been prepared at an accelerator-driven neutron source facility in Hokkaido University.

1. Introduction

Small-angle scattering (SAS) technique with X-rays or neutrons is a good method to characterize a nanoscale structure of material. In the previous work, the SAS technique had been applied to investigate the nanostructure of cement paste such as size, shape, and surface area [1–5].

We have conducted small-angle X-ray scattering (SAXS) measurements for cement paste samples to obtain the time-evolution of nanostructure under the cement hydration process [6]. Our purpose is to research an effect of initial curing temperature on cement paste nanostructure and their relationship between compressive strength and nanostructure. For the measurements, it is important to avoid drying the cement paste sample. By combining a sample cell, a laboratory-based SAXS instrument in Hokkaido University allowed us to do an in-situ SAXS measurement of cement paste in the curing time from initial- to long-term. Though some in-situ SAXS measurements, we have attended on a fine structure in a size order of about 1 nm that has emerged in the SAXS profiles for the cement paste sample.

On the other hand, we have prepared a small-angle neutron scattering (SANS) measurement with a heavy-water cement paste sample [7] at an accelerator-driven neutron source facility in Hokkaido University [8]. As a complementary approach, we are planning to estimate the composition of nanostructure of cement paste by utilizing the difference between the electron and neutron scattering length.

In this paper, a part of SAXS data and the experimental procedures using X-rays are reported to introduce our ongoing activities in Hokkaido University. In addition, the plan of SANS experiment is described briefly.

2. Experimental procedure

2.1. In-situ SAXS measurement for a cement paste sample under the hydration process

Ordinary Portland cement paste was prepared with water-to-cement ratio (w/c) of 0.4 and sealed into a sample cell. As shown in Fig. 1, the sample cell which was composed of O-rings and cover glasses was fixed to acrylic plate holders by screws. To obtain the time evolution of SAXS profiles, the SAXS measurements were successively performed using the cement paste sample in the age from 4 to 24 h. In addition, the SAXS measurements were performed at the age of 1, 3, 7, and 14 d. The measurement time was 0.5 h for each datum. The laboratory-based SAXS instrument which was composed of a NANO-viewer SAXS system (Rigaku Corporation, Japan) with a Mo-Kα X-ray source and a PILUTUS 100K detector (Dectris Ltd, Switzerland) was used, where the wavelength of X-ray beam λ was 0.071 nm. During the measurements, the cement paste sample which was set on the X-ray beam line in a vacuum scattering chamber was cured at 20℃. Between the measurements, the cement paste sample was stored in a thermostatic chamber at the curing temperature of 20℃.

2.2. SAXS measurement for a hardened cement paste sample at the long age

Ordinary Portland cement paste was prepared with w/c of 0.4 and sealed into a plastic bottle. The cement paste was cured in a thermostatic chamber at 20℃ until the age of 1 y. To check the drying effect on a SAXS profile, the measurements for a hardened cement paste sample were performed with three step procedures: (1) The hardened cement paste was demolded from the plastic bottle and sliced to a thin piece (1 mm in thickness). And then the thin piece of hardened cement paste was sealed into a sample cell as shown in Fig. 2. The SAXS for the hardened cement paste sample was measured as the first step. (2) Next, the change of the SAXS profile for the hardened cement paste sample was successively measured by 0.5 h under the vacuum drying condition. Here, the O-ring of the sample cell was intendedly cut as shown in the inset of Fig. 2. The hardened cement paste sample was gradually dried in the vacuum scattering chamber since the broken O-ring could not seal. In the measurements, the pressure of beam course was approximately 10^2 Pa. (3) After drying, the hardened cement paste sample was soaked in water for 10 hours. The hardened cement paste was sealed into the sample cell again while the broken O-ring was replaced to a new one. The SAXS for the rewet sample was measured finally. The measurement time was 0.5 h for each datum.
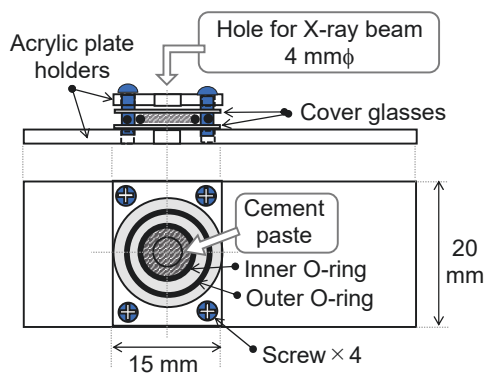

Figure 1: Sample cell holder for the cement paste sample. The line diameter of O-rings is 1 mm. The cement paste sample was sandwiched within the O-rings between two cover glasses.
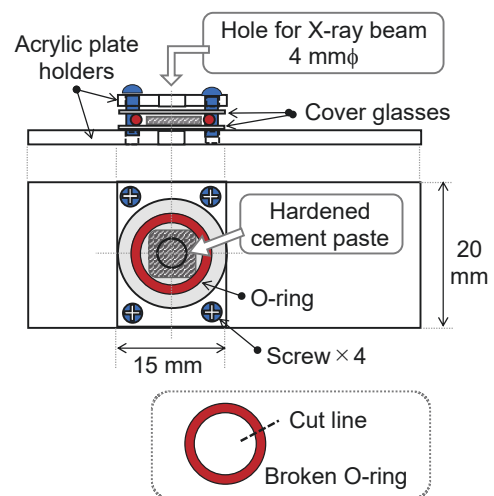
Figure 2: Sample cell holder for the hardened cement paste sample. The line diameter of O-ring is 1.9 mm.

3. Results and discussion

3.1. SAXS profiles measured with the cement paste sample

The measured SAXS profiles for the cement paste sample under the cement hydration process are shown in Fig. 3, where q (= $4\pi \sin \theta / \lambda$) is a magnitude of scattering vector and θ is the scattering angle. The SAXS profiles are plotted by the solid and dashed lines at representative ages. The value in legend stands for the average age of cement paste sample over the interval of measurement time. As shown in Fig. 3, the intensity is increased as a function of the age of cement paste sample. A shoulder, which corresponds to a fine structure, is subsequently observed at around $q = 3$ nm^{-1}.
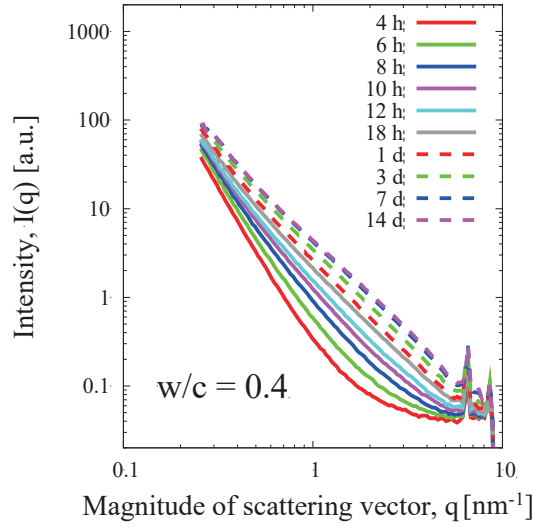
Figure 3: Measured SAXS profiles with the cement paste sample

3.2. Time-evolution of nanostructure in the cement paste sample

The least-square fitting analysis were performed to the SAXS profiles in order to find the time-evolution of nanostructure in the cement paste sample. The following equation was applied to the fitting function.

$$I(q) = I_1(q) + I_2(q) + aq^{-4} + b , \qquad (1)$$

where $I_1(q)$ and $I_2(q)$ are scattering intensity terms for fine and medium nanoparticles, respectively, $aq^{-4} + b$ is a background term. For convenience of classification, the components of nanostructure were roughly divided into two q ranges as the fine and medium nanoparticles. Each of the function of scattering intensity $I_i(q)$ is defined by

$$I_i(q) = N_i \Delta\rho_i^2 \int f_i(R) V_i^2(R) F^2(q, R) dR , \qquad (2)$$

where N_i is the number of nanoparticles, $\Delta\rho_i$ is the difference in scattering length densities between matrix and nanoparticle, $f_i(R)$ is the size distribution of nanoparticles, $V_i(R)$ is the particle volume, $F(q, R) = 3$ $(\sin(qR)$-$qR \cos(qR))/(qR)^3$ is the particle shape factor. The shape of all nanoparticles is assumed as spherical. The R corresponds to the radius of particle. The log-normal distribution function is used for the size distribution. For example, the fitting results in the q range of 0.3−6 nm^{-1} are shown by the solid lines in Fig. 4(a). The measured SAXS profiles are also shown by the open circles in Fig. 4(a).

The time-evolution of nanostructure in the cement paste sample were deduced from the parameters of fitting results. Figures 4(b) and 4(c) correspond to the integrated volume of nanoparticles having the

size distribution and the representative particle size (weighed average diameter), respectively. The fine and medium particles are involved in the integrated volume and the representative particle size. The integrated volume increased with the age while the representative particle size remained approximately 1 nm.
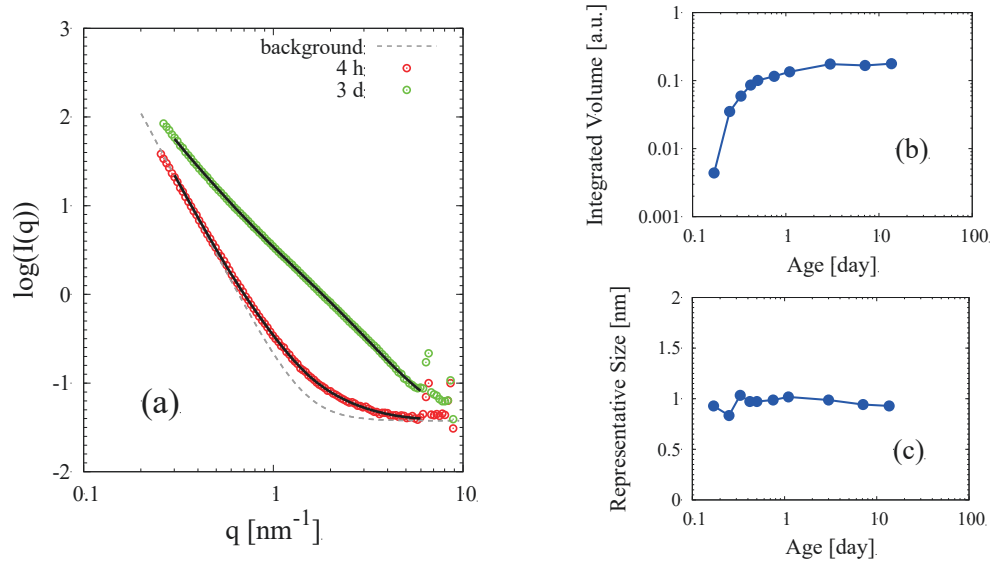
Figure 4: Fitting analysis of SAXS profiles (a) and the time-evolution of nanostructure (b)(c)

3.3. SAXS profiles measured with the hardened cement paste sample

The measured SAXS profiles for the hardened cement paste sample are shown in Fig. 5. The number in legend is labeled in order of increasing the elapsed time. The solid line stands for the original SAXS profile (1). Due to the vacuum drying process from (2) to (7), a significant increase in intensity of SAXS profile is observed at $q < 3$ nm^{-1} as shown by the dashed lines in the figure. By contrast, the SAXS profile for the rewet sample (8) (dot-dashed line) is almost same to the original (1) (solid line). In particular, the shoulder at around $q = 3$ nm^{-1} agrees with each other.

Additionally, the SAXS profile for the cell without sample is shown by the dotted line as a baseline.
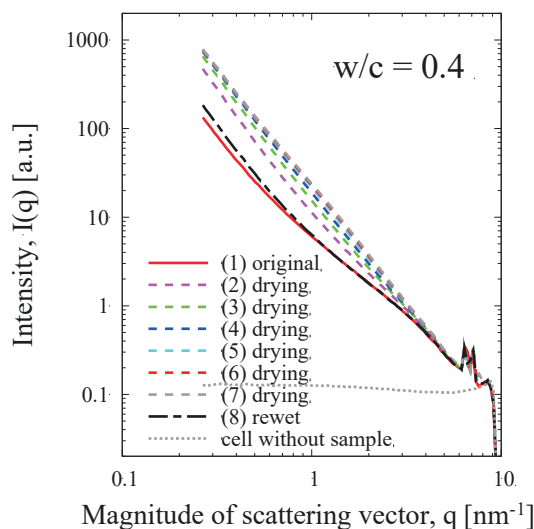
Figure 5: Measured SAXS profiles with the hardened cement paste sample

3.4. Discussion

It is important to avoid drying the cement paste sample especially at the initial age because the drying leads to an inhibition of the cement hydration. In addition, the SAXS profiles of the hardened cement sample drastically changed due to drying as presented in Sec. 3.3. Owing to the sample cell (Fig. 1), the SAXS profiles of cement paste sample was successfully measured under the hydration process in the age from 4 h to 14 d (Fig. 3). In the deduced time-evolution of nanostructure (Fig. 4), the nanostructure formed in the size order of about 1 nm on the cement paste sample and the integrated volume increased with the age of cement paste sample. From the results, we expected that the amount of the integrated volume corresponded to the degree of cement hydration. To gain further information of the nanostructure, currently, three in-situ SAXS measurements for cement paste samples have been conducted in the age from initial- and long-term at the initial curing temperature of 5℃, 20℃, and 50℃ [6].

4. Preparation of a SANS measurement

As a complementary approach, a SANS measurement has been prepared a with a heavy-water cement paste sample at the accelerator-driven neutron source facility in Hokkaido University. For the sample preparation, two in-situ SAXS measurements with light-water (H_2O) and heavy-water (D_2O) cement paste samples was conducted at the age before 3 d [7]. The same nanostructures in a size order of about 1 nm were formed on the H_2O and D_2O cement paste samples although the formation speed of the nanostructure in D_2O cement paste was slow. Based on the results, we expected that the nanostructure in the D_2O cement paste becomes gradually close to the one in the H_2O cement paste at the age of 1 month. Accordingly, we have considered a SANS measurement with a D_2O cement paste sample in a middle-term age.

5. Conclusion

The in-situ SAXS measurement for the cement paste sample was demonstrated using the sample cell and the laboratory-based SAXS instrument in Hokkaido University. The cement paste was prepared with w/c = 0.4. By the fitting analysis to the SAXS profiles, the time-evolution of nanostructure in the cement paste sample under the hydration process was obtained at 20℃ in the age of 4 h−14 d. The integrated volume of nanoparticles increased with the age while the representative particle size remained approximately 1 nm. To check the dying effect on the SAXS profile, in addition, the SAXS for the hardened cement paste sample was measured at the age of 1 y. The hardened cement paste was prepared with w/c = 0.4. In consequence of the low vacuum drying, the significant increase in the intensity of SAXS profile was observed at $q < 3$ nm^{-1}. On the other hand, as a complementary approach, a SANS experiment has been planned with the D_2O cement paste sample in Hokkaido University.

References

1) Winslow DN, Diamond S. Specific surface of hardened Portland cement paste as determined by small-angle X-ray scattering, J. Am. Ceram. Soc. 1974;57:193−197.
2) Maruyama I, Sakamoto N, Matsui K, Igarashi G. Microstructural changes in white Portland cement paste under the first drying process evaluated by WAXS, SAXS, and USAXS, Cem. Concr. Res. 2017;91:24−32.
3) Bogner A, Link J, Baum M, et al. Early hydration and microstructure formation of Portland

cement paste studied by oscillation rheology, iso thermal calorimetry, ^{1}H NMR relaxometry, conductance and SAXS, Cem. Concr. Res. 2020;130:105977.

4) Allen AJ, Thomas JJ, Jennings HM. Composition and density of nanoscale calcium-silicate-hydrate in cement, Nat. Mater. 2007;6:311−316.

5) Chiang W-S, Fratini E, Baglioni P, Liu D, Chen S-H. Microstructure determination of Calcium-Silicate-Hydrate globules by small-angle neutron scattering, J. Phys. Chem. C 2012;116:5055−5061.

6) Hara KY, Morinaga Y, Yoda Y, Tsujino M, Nishida A, Ohnuma M. Effect of initial curing temperature on cement nanostructure, AESJ 2020 Fall Meeting, 3L11; 2020 Sep 16−18; Online Meeting [in Japanese].

7) Hara KY, Morinaga Y, Yoda Y, Ohnuma M. Measurements of small-angle X-ray scattering for cement paste samples with light water and heavy water, IEEE 2021 NSS-MIC, N-28-064; 2021 Oct. 16−23; Online Conference.

8) Ishida T, Ohnuma M, Seong BS, Furusaka M. Intermediate-angle neutron scattering instrument for quantitative and non-destructive characterization of nanostructures in steels and other alloys, ISIJ Int 2017;57:1831–1837.

Acknowledgements

20　Design of a new shadow bar to improve the accuracy of benchmark experiments of large angle elastic scattering reaction cross sections by 14MeV neutrons

Kazuki FUKUI[1], Sota ARAKI[1], Indah Rosidah MAEMUNAH[1], Rio MIYAZAWA[1],

Shingo TAMAKI[1], Sachie KUSAKA[1], Isao MURATA[1]*

[1]*Graduate school of Engineering, Osaka University*

Yamada-oka 2-1, Suita, Osaka 565-0871, Japan

e-mail: fukui@qr.see.eng.osaka-u.ac.jp

When the energy of incident neutrons is high, the elastic scattering reaction cross section data is generally smaller at the backward angle than that of the forward angle. Neutron benchmark experiments using a DT neutron source focusing on backscattering phenomena such as gap streaming experiments have reported differences between experimental and calculated values. To solve this problem, the author's group developed a benchmark method for large-angle scattering cross sections using two types of shadow bars with different thicknesses, and has been performing experiments on iron samples for the past few years.

When we conducted the experiments, we used to irradiate with D^+ beam locally to a disk-shaped tritium target to ensure necessary intensity of DT neutrons, however we found that we could not obtain correct results if the position of the plane source was random in each experimental system out of four required for the present benchmark experiments. Therefore, it was decided to irradiate the D^+ beam uniformly on the tritium target instead of locally, however it was found that using the current thin shadow bar would allow neutrons to enter directly into the Nb activation detector due to a small installation error during the preparation of the experiment, resulting in an overestimation of the reaction rate.

In order to solve this problem, we have designed a new thin shadow bar that prevents neutrons from direct incidence on the Nb foil under a uniform neutron source condition on the disk-shaped tritium target.

As a result of the calculation design, the bottom of the thin shadow bar was changed from 3 cm to 4 cm. In the future, we will carry out other experiments for fusion structural materials using the newly designed shadow bar.

1.　Introduction

Since the large-angle elastic scattering reaction cross section is much smaller than the forward scattering reaction cross section, especially when the incident neutron energy is as high as that of fusion neutrons, the backscattering reaction cross section data is usually not regarded as important in fusion reactor design. However, in a high neutron flux field such as a fusion reactor, the backscattering reaction cross section will have a non-negligible effect on the calculation results. In the past, neutron benchmark experiments using a DT neutron source focusing on backscattering phenomena were reported showing differences observed between experimental and calculated values [1]. The FNS experiment by Ohnishi et al. reported possibility of a problem in the backscattering cross section of iron from the gap streaming experiment. In fact, as shown in Figure 1, the reaction cross section

of elastic scattering of ^{56}Fe, the most important fusion material, at 14 MeV is different among nuclear data libraries, especially in large angle elastic scattering [2 - 4]. Experimentally, Takahashi et al. measured double-differential neutron emission reaction cross sections (DDX) at 14 MeV [5 - 8]. From the result, the angle-differential cross section (ADX) can be obtained. However, this measurement is technically difficult and very time-consuming. In addition, as shown in Figure 1, the large-angle elastic scattering reaction cross section is very small, resulting in large errors, making it difficult to evaluate cross sections in backward angles. In fact, few experimental approaches have been reported directly measuring or benchmarking the large-angle neutron scattering cross sections. To solve this problem, the author's group developed a method to benchmark the large-angle elastic scattering cross section using shadow bars [9].
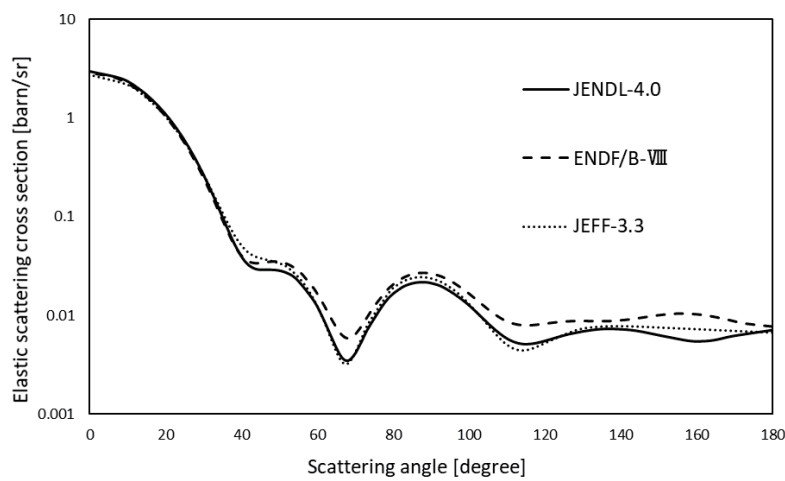
Figure 1 Angle-differential elastic scattering cross section of ^{56}Fe at 14 MeV.

First we briefly explain the present benchmark method, which is detailed in Hayashi's paper [9]. Four kinds of experiments （S_{1TC}, S_{2TC}, S_{1C}, S_{2C}）are performed using a thin shadow bar S1 with a bottom diameter of 3 cm and a thick shadow bar S2 with a bottom diameter of 15 cm, and for TC with the target and C without it as shown in Figure 2(b). In the benchmark experiment, there are three possible elements for neutrons to pass through, i.e., the shadow bar, the wall and the target. So seven paths in total (=$_3C_1+_3C_2+_3C_3$) are possible for neutrons to pass through during the transport, as shown in Figure 2(a). Out of the seven paths, path ③ is the one we want to measure, which is the path of neutrons correctly scattered by the target at a large angle. The contribution of path ③ only appears in the experimental system of S_{1TC}. However, S_{1TC} contains other contributions, which need to be removed. The basic principle of the present benchmark method is to perform the four types of experiments shown in Figure 2(b) to estimate and eliminate the contribution of neutron paths other than path ③. Specifically, by substituting the reaction rates of the four experiments into Equation (1), the contributions of neutrons other than path ③ will be canceled out. Reaction rates of paths ①, ④ and ⑥ do not change irrespective of existence of the sample, hence $S_{1TC}=S_{1C}$ and $S_{2TC}=S_{2C}$ hold and are canceled out with each other as shown in Figure 2(b). Similarly, ⑤ can be canceled out considering the presence of the shadow bar. Finally, although the term （②$_{S_{1Tc}}$ + ⑦$_{S_{1Tc}}$ − ⑦$_{S_{2TC}}$ − ⑦$_{S_{1c}}$ + ⑦$_{S_{2c}}$）remains as an error, only the contribution of path ③ can be extracted. Fortunately, it is known

that the contributions of path ② and ⑦ are very small compared to ③, so that ② + ⑦ is regarded as the evaluation error [9]. In the last few years, we have conducted experiments with an iron sample. Consequently, the benchmark method was successfully established on the basis of the Nb foil activation, which has a large activation cross section around 14 MeV.

$$S_{1TC} - S_{2TC} - (S_{1C} - S_{2C}) = ③ + (②_{S_{1Tc}} + ⑦_{S_{1Tc}} - ⑦_{S_{2TC}} - ⑦_{S_{1c}} + ⑦_{S_{2c}}) \tag{1}$$
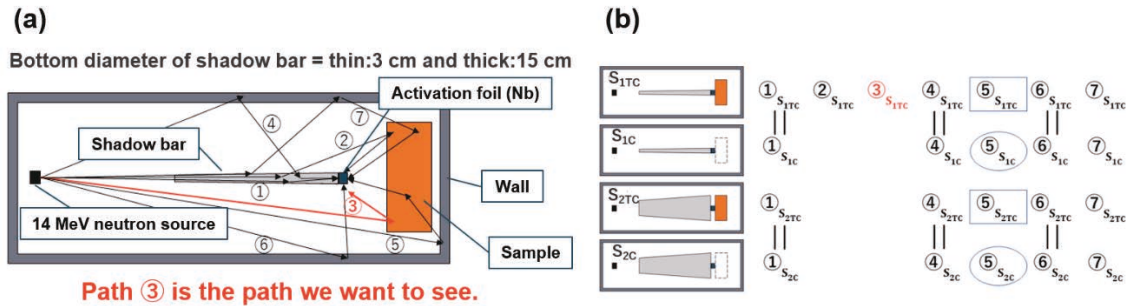
Figure 2 Overview of the benchmark experimental method
(a) path diagram (b) four systems and path pairs

Table 1 shows the summary of the results for iron. The experimental results are compared with the calculations using the nuclear data libraries for the total reaction rates (summing up all the 7 paths) and their subtracted values by Equation (1) [9]. The nuclear data used were JENDL-4.0, ENDF/B-VII, and JEFF-3.3. From the results four reaction rates show a similar trend, i.e., $S_{1TC} > S_{1C} > S_{2C} > S_{2TC}$ for all calculated and experimental values. However, when comparing each of four experimental systems, we can recognize that all the calculated and experimental values are very different. This tendency is similarly seen for targets other than the iron targets, and the reason for this was not yet known. Therefore, in this study, we investigate the experimental system and calculation conditions especially concentrating on the shadow bars in order to solve the abovementioned problem.

Table 1 Simulation and experimental results using three nuclear data libraries for iron.

[10^{-9} reaction rate/cm^3/source neutron] [9]

	S_{1TC}		S_{2TC}		S_{1C}		S_{2C}		$S_{1TC}-S_{2TC}-(S_{1C}-S_{2C})$	
JENDL-4.0	4.20	±0.10	1.18	±0.08	2.87	±0.11	2.32	±0.09	2.47	±0.19
ENDF/B-VII	5.58	±0.10	1.21	±0.08	2.87	±0.11	2.32	±0.09	3.82	±0.19
JEFF-3.3	4.08	±0.10	1.20	±0.08	2.87	±0.11	2.32	±0.09	2.34	±0.19
Experiment	8.31	±0.06	1.68	±0.06	5.01	±0.14	3.83	±0.03	5.45	±0.17
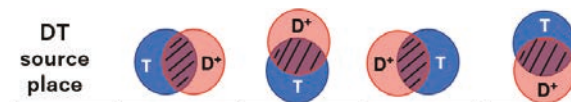
2. Problems and Objectives

First of all, we have investigated the calculation model to solve the problem described in chapter 1. As a result, it was found that the modeling of the DT neutron source was different between the experiment and calculation. Specifically, in the simulation, the DT neutron source was treated as a point source. This is because in the previous operation of the accelerator, the beam was narrowed down to hit the center of the tritium target as much as possible. However, due to the difficulty in obtaining the target, the D^+ beam was irradiated in a locally small region (not a point) on the disk-shaped tritium target in order to keep an enough strong DT neutron intensity for as long as

possible. This means that the neutron source is actually a surface source, and the position of the surface source is varying in each of S_{1TC} - S_{2C}. Therefore, we simulated the local plane source with MCNP5. The results are shown in Table 2. The table shows source position for each case simulating that the position of the source is random. As a result, the subtraction of the total reaction rates does not agree to the reaction rate of path ③, showing that the subtraction is not correctly carried out. Of course, we confirm that if the source position is fixed for all the four systems, the above two values (③ and the subtracted value) are found to be almost identical. Therefore, it was decided to irradiate the tritium target with the D^+ beam after totally blurring the beam so as to irradiate uniformly on the tritium target.

This is the current status. However, if the current thin shadow bar is continuously used, indicating that the diameter of the bottom of the shadow bar of 3 cm is quite close to 2.5 cm of the tritium target diameter, a small installation error in the experimental preparation may allow neutrons to directly enter the Nb foil and overestimate the reaction rate. To solve this problem, we design a new thin shadow bar to prevent neutrons from direct incidence on the Nb foil for a disk-shaped surface source. We expect that this countermeasure may eventually solve the discrepancy between experiment and calculation.

Table 2 Reaction rates and subtraction results for each pathway of each system at locally positioned sources using JENDL-4.0. [10^{-9} reaction rate/cm³/source neutron]

DT source place					
PATH	S_{1TC}	S_{2TC}	S_{1C}	S_{2C}	S_{1TC}-S_{2TC}-(S_{1C}-S_{2C})
①	0.72	0.09	0.70	0.09	0.02
②	0.06	0.00	0	0	0.06
③	**2.49**	0	0	0	2.49
④	0.66	0.54	0.64	0.47	-0.05
⑤	0.78	0.60	1.96	1.94	0.16
⑥	0.52	0.13	0.49	0.15	0.06
⑦	0.00	0.01	0.01	0.03	0.01
TOTAL	5.23±0.11	1.36±0.09	3.81±0.12	2.68±0.11	**2.75±0.22**

3. Examination Method

For the design of the shadow bar, we utilize the evaluation index R based on the previous studies [9]. R is expressed as in Equation (2).

$$R = \frac{R_n(= ③)}{R_f(= ① + ②)}, \tag{2}$$

where R_n is the reaction rate due to neutrons entering the Nb foil without passing through the shadow bar, and R_f is the reaction rate due to neutrons entering the Nb foil through the shadow bar. In other words, R_n is the path ③, and R_f is the neutron contribution from paths ① and ② in Figure 2(a). Since the neutron path we want to see is ③, the larger R is, the more dominant the activation of the Nb foil is by neutrons scattered at large angles by the sample, and the more optimal the shadow bar is.

This time, since we only change the source from a point source to a disk-shaped source, we decided to examine

only the diameter of the thin shadow bar. Using MCNP5, we determine the diameter at which the Nb detection foil is sufficiently activated and the evaluated value R shows the maximum value, even if the diameter of the thin shadow bar is increased.

4. Result

The relationship between the amount of Nb foil activation and the respective R value, which were calculated by MCNP5, is shown in Figure 3 as a function of the diameter of the bottom of the thin shadow bar. It can be seen that the radioactivity decreases linearly with increase of the diameter from the current value of 3.0 cm. This is because the thicker the shadow bar is, the more neutrons are shielded by the shadow bar, and as the result the amount of neutrons incident on the Nb foil decreases. The R value increases rapidly as the diameter increases from 3.0 cm, and saturates around 16 after 4.0 cm. This means that the existing 3.0 cm shadow bars could not shield neutrons sufficiently and thus the R_f becomes large. Consequently, the diameter of the thin shadow bar was decided to be 4.0 cm, which has a sufficiently small R_f showing the maximum R value of 16, and at the same time can secure an enough radioactivity.
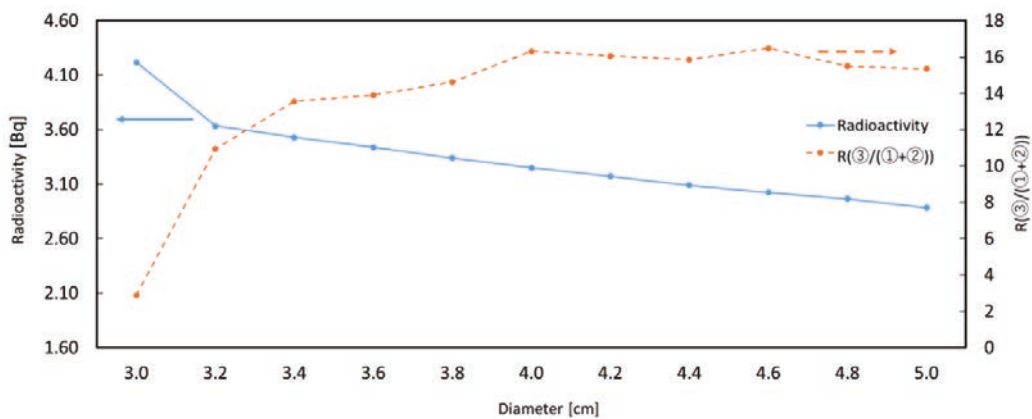
Figure 3 Amount of Nb foil activation and R value for the diameter of the bottom of the thin shadow bar.

Finally, we confirm whether the benchmark could be performed correctly for the newly determined thin shadow bar of 4.0 cm with a disk-shaped neutron source. Four different experimental systems were modeled with MCNP5, under the condition that the same thick shadow bar was used as before. The calculated results are shown in Table 3. It can be seen from the table that the total reaction rate obtained by subtraction with Equation (1), 2.12±0.23 x 10^{-9} reaction rate/cm³/source neutron, and the reaction rate by path ③, 2.07, are almost identical. These results show that our benchmark method can work properly with the newly designed shadow bar. In addition, from the present design the upper bottom of the narrow shadow bar becomes 2.7 cm in diameter. Since the disk-shaped neutron source is 2.5 cm in diameter, the direct incidence can be completely eliminated if the installation error is suppressed within about 1 mm.

Table 3 Reaction rates and subtraction results for each path of the system in the thin shadow bar with a

bottom diameter of 4.0 cm and a disk-shaped neutron source

(JENDL-4.0) [10^{-9} reaction rate/cm^3/source neutron]

PATH	S_{1TC}	S_{2TC}	S_{1C}	S_{2C}	S_{1TC}-S_{2TC}-(S_{1C}-S_{2C})
①	0.06	0.09	0.06	0.09	0.00
②	0.06	0.00	0	0	0.06
③	**2.07**	0	0	0	2.07
④	0.76	0.46	0.76	0.46	0.00
⑤	0.67	0.66	1.89	1.86	-0.03
⑥	0.43	0.20	0.43	0.20	0.00
⑦	0.01	0.01	0.01	0.03	0.01
TOTAL	4.06±0.11	1.43±0.10	3.16±0.13	2.64±0.12	**2.12**±0.23

5. Conclusion

In this study, we investigated the design of a new thin shadow bar to prevent neutrons from directly entering the Nb foil using MCNP5. As a result, the diameter of the bottom of the thin shadow bar was determined to be 4.0 cm. This can ensure sufficient radioactivity for γ-ray measurement and a large R value so as to improve the accuracy of the benchmark experiment. In the future, we will manufacture the designed shadow bar and test it by comparing the experimental and calculated results. We will also conduct benchmark experiments using samples of medium and heavy nuclides such as iron and tungsten, and light nuclides such as lithium and oxygen.

References

[1] Ohnishi S., Kondo K., Azuma T., Sato S., Ochiai K., Takakura K., Murata I., Konno C. New integral experiments for large-angle scattering cross section data benchmarking with DT neutron beam at JAEA/FNS. Fusion Engineering and Design, 2012; 87: 695-699.

[2] Shibata K., Iwamoto O., Nakagawa T., Iwamoto N., Ichihara A., Kunieda S., Chiba S., Furutaka K., Otuka N., Ohsawa T., Murata T., Matsunobu H., Zukeran A., Kamada S., and Katakura J.: "JENDL-4.0: A New Library for Nuclear Science and Engineering," J. Nucl. Sci. Technol. 48(1), 1-30 (2011).

[3] Brown D.A., Chadwick M.B., Capote R., et al., "ENDF/B-VIII.0: The 8th Major Release of the Nuclear Reaction Data Library with CIELO-project Cross Sections, New Standards and Thermal Scattering Data", Nuclear Data Sheets, 148: pp. 1-142 (2018).

[4] NEA, " JEFF-3.3", https://www.oecd-nea.org/dbdata/jeff/jeff33/index.html, (accessed 2020-02-01).

[5] Takahashi A., Ichimura E., Sasaki Y. and Sugimoto H. Measurements of double differential neutron emission cross sections for incident neutrons of 14 MeV. J. Nucl. Sci. Technol, 1988; 25: 215-232.

[6] Takahashi A. Measurements of double differential cross sections at OKTAVIAN. J. Nucl. Sci. Technol., 1989; 26: 15-20.

[7] Takahashi A., Ichimura E., Sasaki Y., Sugimoto H. Double and Single Differential Neutron Emission Cross Sections at 14.1 MeV: Vol. 1. OKTAVIAN Report, 1987; A-87-03 385.

[8] Takahashi A., Gotoh M., Sasaki Y., Sugimoto H. Double and Single Differential Neutron Emission Cross Sections at 14.1 MeV: Vol. 2. OKTAVIAN Report 1992; A-92-01 577.

[9] Hayashi N., Ohnishi S., Fujiwara Y., Kusaka S., Sato F., Murata I. Optimization of Experimental System Design for Benchmarking of Large-Angle Scattering Reaction Cross Section at 14MeV Using Two Shadow Bars. Plasma and Fusion Research, 2018; 13: 2405002, 4.

This is a blank page.

21　Problem on Gammas Emitted in Capture Reaction

of TENDL-2019 and JEFF-3.3

Chikara KONNO[1*] and Saerom KWON[2]

[1]Japan Atomic Energy Agency

2-4 Shirakata, Tokai-mura, Naka-gun, Ibaraki-ken 319-1195, Japan

[2]National Institutes for Quantum Science and Technology

2-166 Oaza-Obuchi-Aza-Omotedate, Rokkasho-mura, Kamikita-gun, Aomori-ken 039-3212, Japan

[*]Email: konno.chikara@jaea.go.jp

Previously we had pointed that energy distribution data for secondary gammas from the capture reaction of a lot of nuclei in TENDL-2017 had no high-energy gamma peaks. Here we examined whether secondary gamma energy distribution data of the capture reaction in the latest nuclear data libraries had high-energy gamma peaks or not. As a result, we found that a lot of nuclei in TENDL-2019 still did not have high-energy gamma peaks in secondary gamma spectra from the capture reaction and several nuclei in JEFF-3.3 also did not, while other nuclear data libraries such as JENDL-4.0 and ENDF/B-VIII.0 had those peaks. This problem causes not only drastically small damage energy production cross sections for radiation damage calculations at incident neutron energies below a few keV but also smaller gamma productions in shielding calculations. The problematic energy distribution data for secondary gammas in TENDL-2019 and JEFF-3.3 should be revised.

1. Introduction

We reported that energy distribution data for secondary gammas from the capture reaction of a lot of nuclei in TENDL-2017 [1] had no high-energy gamma peaks, which other nuclear libraries had, at the IAEA FENDL meeting in 2018 [2, 3]. Figure 1 shows secondary gamma spectra of the capture reaction of ^{184}W at incident neutron energy of 10^{-5} eV in JENDL-4.0 [4], ENDF/B-VII.1 [5], JEFF-3.2 [6] and TENDL-2017. TENDL-2017 has no high-energy gamma peaks above 5 MeV which the other nuclear data libraries have.

In the process of JENDL development we examined whether the latest TENDL, TENDL-2019 [7], and the major nuclear data libraries (JENDL-4.0, JEFF-3.3 [8] and ENDF/B-VIII.0 [9]) had this issue or not. We also investigated effects of no high-energy gamma peaks in the capture reaction in detail. Here we describe the results.
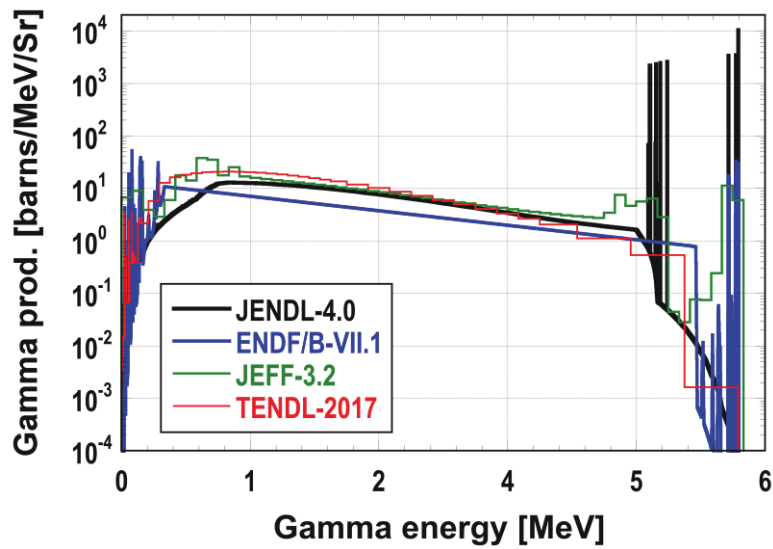
Fig. 1 Secondary gamma spectra of capture reaction of ^{184}W at incident neutron energy of 10^{-5} eV.

2. Method

It is not so easy to obtain secondary gamma energy distribution data directly from ENDF-6 files. Thus we extracted secondary gamma energy distribution data of the capture reaction for all the nuclei from the official ACE files of JENDL-4.0 [10], JEFF-3.3 [11], ENDF/B-VIII.0 [12] and TENDL-2019 [7] with a simple program and automatically checked whether they had high-energy gamma peaks or not.

3. Results

It was found that most of the nuclei in TENDL-2019 and several nuclei in JEFF-3.3 had no high-energy gamma peaks above 5 MeV in secondary gamma spectra from the capture reaction (see Figs. 2 and 3), while JENDL-4.0 and ENDF/B-VIII.0 had those ones. Note that JEFF-3.3 has only discrete gammas in Fig. 2 and TENDL-2019 and JEFF-3.3 are the same in Fig. 3.

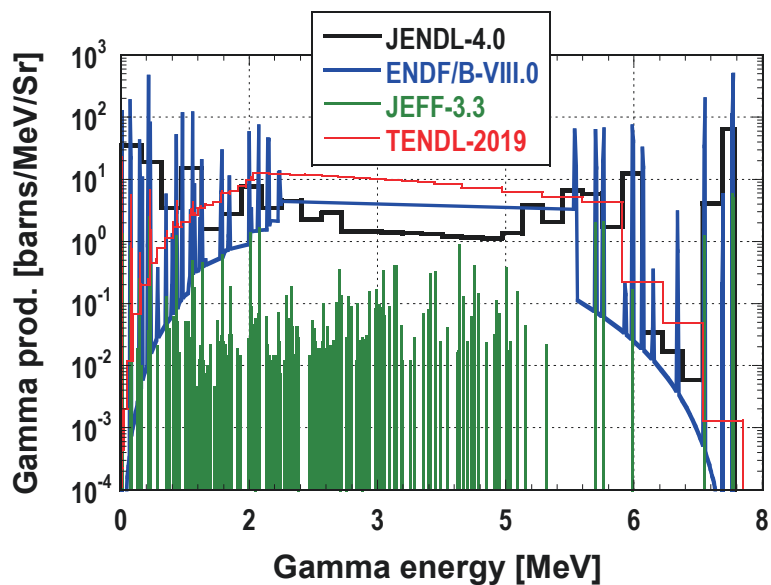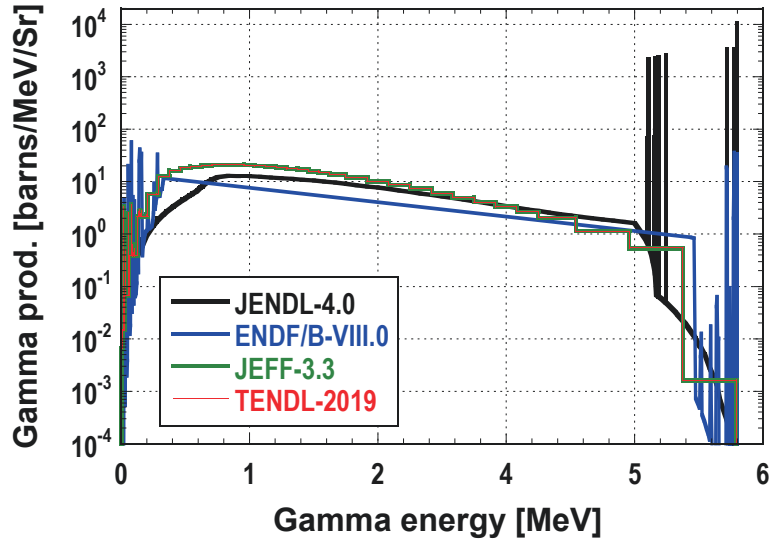Fig. 2 Secondary gamma spectra of capture reaction of ^{56}Fe in neutron energy of 10^{-5} eV.

Fig. 3 Secondary gamma spectra of capture reaction of ^{184}W in neutron energy of 10^{-5} eV.

4. Effects of No High-energy Gamma Peaks

4.1. DPA cross section

The problem of no high-energy gamma peaks in the capture reaction may cause much smaller displacement per atom (DPA) cross sections below ~ a few keV for nuclei with a larger displacement energy such as tungsten (displacement energy: 90 eV) than those of other nuclear data libraries. This is explained as follows. Only the capture reaction contributes the DPA cross section below a few keV. The energy E_R of nucleus recoiled by the capture reaction is described as

$$E_R = \frac{E}{A+1} + \frac{E_\gamma^2}{2(A+1)mc^2},$$ (1)

where E is the incident neutron energy, A is the mass of the target nucleus, mc^2 is the neutron mass energy and E_γ is the gamma energy. When E is negligibly small, e.g. 10^{-5} eV,

$$E_R = \frac{E_\gamma^2}{2(A+1)mc^2}.$$ (2)

If E_R is more than the displacement energy E_d, the neutron contributes DPA. Conversely only gammas above the following threshold gamma energy $E_{\gamma,thresh}$ contribute DPA,

$$E_{\gamma,thresh} = \sqrt{2(A+1)mc^2 E_d}.$$ (3)

$E_{\gamma,thresh}$ is 5.59 MeV for ^{184}W. Thus only gamma above 5.59 MeV contribute DPA.

Figure 4 shows the DPA cross sections of ^{184}W extracted from the official ACE files of JENDL-4.0, JEFF-3.3, ENDF/B-VIII.0 and TENDL-2019 with a simple program. It is noted that the DPA cross sections of TENDL-2019 and JEFF-3.3 are by four orders smaller than those of JENDL-4.0 and ENDF/B-VIII.0.

On the other hand, the DPA cross sections of nuclei with smaller displacement energy do not have such a serious effect by the problem of no high-energy gamma peaks in the capture reaction. Figure 5 shows the DPA cross sections of ^{56}Fe, the displacement energy of which is 40 eV. In this case $E_{\gamma,thresh}$ is 2.07 MeV. The DPA cross section of TENDL-2019 is not so different from those of the other nuclear data libraries.
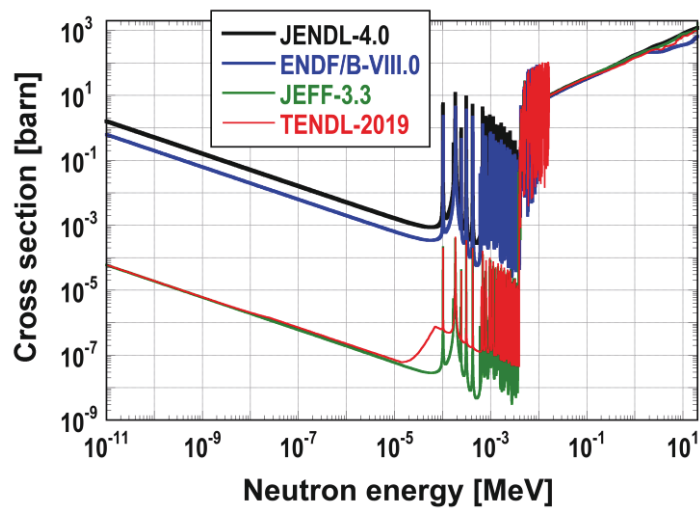
Fig. 4 DPA cross-sections of ^{184}W in official ACE files.
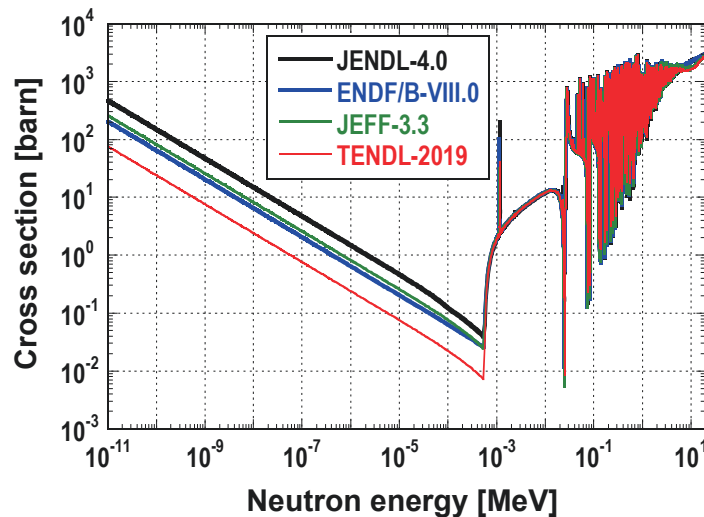
Fig. 5 DPA cross-sections of ^{56}Fe in official ACE files.

4.2. Gamma spectra in shielding calculations

This issue causes smaller gamma fluxes in coupled neutron-gamma calculations. In order to demonstrate this effect, gamma spectra inside a tungsten sphere of 1 m in radius with an isotropic neutron source of 20 MeV at the sphere center were calculated with the MCNP6.2 [13] code by using JENDL-4.0, ENDF/B-VIII.0, JEFF-3.3 and TENDL-2019. Figures 6 and 7 show the calculated neutron and gamma spectra at 60 cm from the tungsten sphere center, respectively. Though the neutron spectra are different below 100 keV among the nuclear data libraries, the calculated gamma spectra with TENDL-2019 and JEFF-3.3 are much smaller than those with the other libraries and are shifted to lower gamma energy.
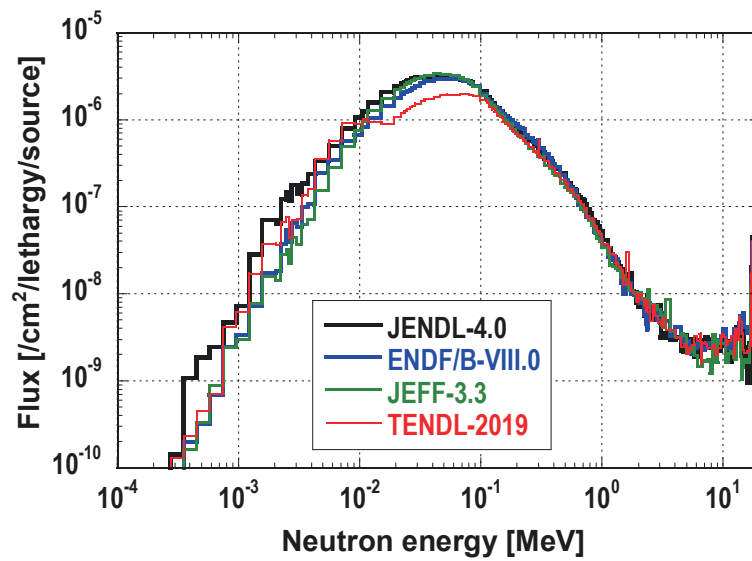
Fig. 6 Neutron spectra at 60 cm from tungsten sphere center.
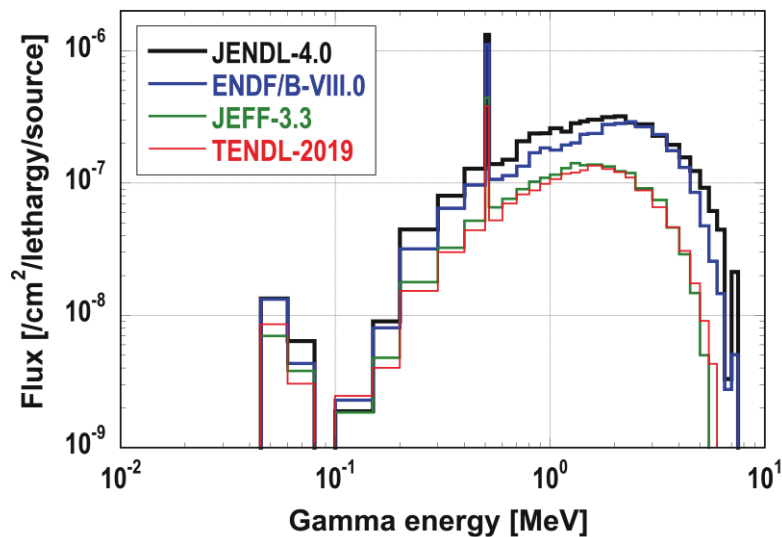
Fig. 7 Gamma spectra at 60 cm from tungsten sphere center.

5. Conclusion

We found that secondary gamma spectra from the capture reaction of a lot of nuclei in TENDL-2019 and several nuclei in JEFF-3.3 had no high-energy gamma peaks. This problem causes much smaller DPA cross-section data below a few keV for nuclei with a larger displacement energy such as tungsten (displacement energy: 90 eV) than those of other nuclear data libraries. It also causes smaller gamma fluxes in coupled neutron-gamma calculations than those with other nuclear data libraries. The problematic energy distribution data for secondary gammas in TENDL-2019 and JEFF-3.3 should be revised.

References

1) TENDL-2017 TALYS-based evaluated nuclear data library, https://tendl.web.psi.ch/tendl_2017/tendl2017.html (accessed 2022-1-5).

2) Packer, L., Trkov, A. (Ed.), FENDL Library for Fusion Neutronics Calculations Summary Report from the Consultants' Meeting, INDC(NDS)-0769, pp.9-11.

3) Konno, C., New comments on data below 20 MeV in FENDL-3.1d, https://www-nds.iaea.org/index-meeting-crp/CM-FENDL-2018/docs/Konno_FENDL_r7_2017.pdf (accessed 2022-1-5).

4) Shibata, K. et al., JENDL-4.0: a new library for nuclear science and engineering, J Nucl. Sci. Technol., vol.48, 2011, pp.1-30.

5) Chadwick, M.B. et al., ENDF/B-VII.1 Nuclear Data for Science and Technology: Cross Sections, Covariances, Fission Product Yields and Decay Data, Nucl. Data Sheets, vol.112, 2011, pp.2887–2996.

6) JEFF-3.2 evaluated data library – Neutron data, https://www.oecd-nea.org/dbforms/data/eva/evatapes/jeff_32/ (accessed 2022-1-5).

7) TENDL-2019 TALYS-based evaluated nuclear data library, https://tendl.web.psi.ch/tendl_2019/tendl2019.html (accessed 2022-1-5).

8) Brown, D.A. et al., ENDF/B-VIII.0: The 8th Major Release of the Nuclear Reaction Data Library with CIELO-project Cross Sections, New Standards and Thermal Scattering Data, Nucl. Data Sheets, vol.148, 2018, pp.1-142.

9) Plompen, A.J.M. et al., The joint evaluated fission and fusion nuclear data library, JEFF-3.3, Eur. Phys. J. A, vol. 56, 2020, 181.

10) PRODAS, https://prodas.jaea.go.jp/?AceLibJ40 (accessed 2022-1-5) [in Japanese].

11) JEFF-3.3, https://www.oecd-nea.org/dbdata/jeff/jeff33/index.html (accessed 2022-1-5).

12) Lib80x-Library based on ENDF/B-VIII.0, https://nucleardata.lanl.gov/ace/lib80x/ (accessed 2022-1-5).

13) Werner, C.J. (Ed.), MCNP® USER'S MANUAL Code Version 6.2, LA-UR-17-29981, 2017.

22 Measurement of 107-MeV proton-induced double-differential neutron yields for iron for research and development of accelerator-driven systems

Hiroki IWAMOTO[1,2], Keita NAKANO[1], Shin-ichiro MEIGO[1], Daiki SATOH[2], Yosuke IWAMOTO[2], Yoshihiro ISHI[3], Tomonori UESUGI[3], Yasutoshi KURIYAMA[3], Hiroshi YASHIMA[3], Katsuhisa NISHIO[4], Kentaro HIROSE[4], Hiroyuki MAKII[4], Kota OKABE[1], Fumi SUZAKI[4], Akito OIZUMI[2], Riccardo ORLANDI[4], Kazuaki TSUKADA[4], Fujio MAEKAWA[1], and Yoshiharu MORI[3]

[1]J-PARC Center, Japan Atomic Energy Agency
[2]Nuclear Science and Engineering Center, Japan Atomic Energy Agency
[3]Institute for Integrated Radiation and Nuclear Science, Kyoto University
[4]Advanced Science Research Center, Japan Atomic Energy Agency
[†]E-mail: iwamoto.hiroki@jaea.go.jp

Abstract

The 107-MeV proton-induced double-differential thick-target neutron-yields (TTNYs) and cross-sections (DDXs) were measured for iron using the fixed field alternating gradient accelerator at Kyoto university by the time-of-flight method. So far, the experimental TTNY data for the detector angle of 5° have been determined via the data analysis process. Future work will focus on detailed analyses of the rest of the measured TTNY and DDX data for iron, and the next step measurement of the experimental program, i.e. TTNY and DDX measurements for lead and bismuth targets, will be conducted.

1 Introduction

For accurate prediction of neutronic characteristics for accelerator-driven systems (ADS) [1, 2], we have launched an experimental program to measure nuclear data on ADS using the Fixed Field Alternating Gradient (FFAG) accelerator at Kyoto University. As part of this program, the proton-induced double-differential thick-target neutron-yields (TTNYs) and cross-sections (DDXs) for iron have been measured. These data will also be useful for source term calculation of spallation neutrons for reactor physics experiments for the ADS at Kyoto University Critical Assembly (KUCA) [3, 4, 5, 6, 7].

2 Experiment

Figures 1 and 2 show shematic drawings of experimental setup for the TTNY and DDX measurements, respectively. In this experiment, 30-mm-thick and 2-mm-thick iron targets were used for the TTNY and DDX measurement, respectively; they were installed in vacuum chambers indicated in Figs 1 and 2. The proton beams were accelerated to 107 MeV with 30-Hz repetition by the FFAG accelerator, and the iron target installed in each measurement was bombarded with the 107-MeV proton beam. In each measurement, spallation neutrons produced from the
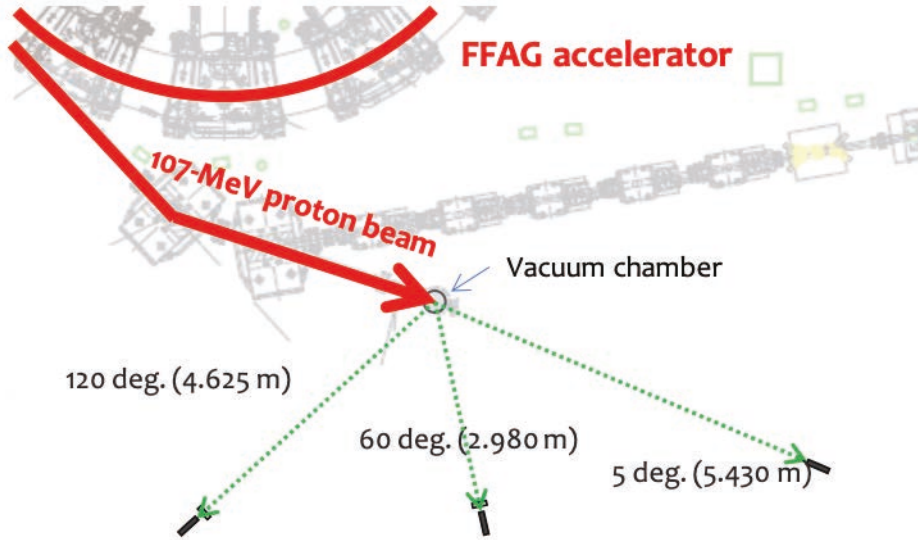
Figure 1: Schematic of horizontal plane view of the experimental setup for the TTNY measurement.
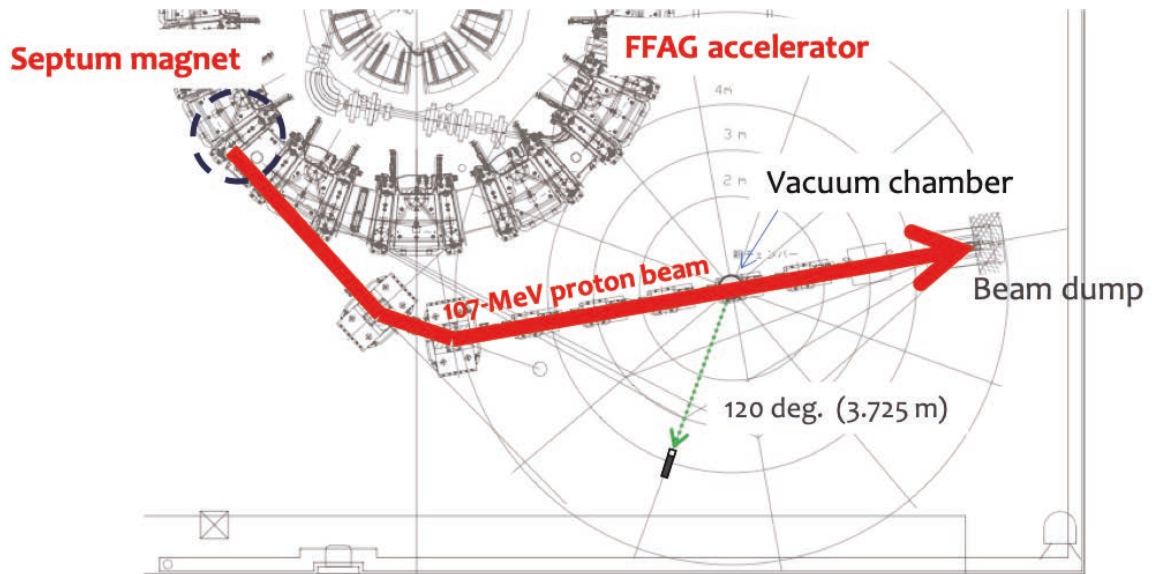

Figure 2: Schematic of horizontal plane view of the experimental setup for the DDX measurement.

iron target were detected with a neutron detector system positioned at about 3–6 m distance from the target, and the time-of-flight (TOF) of neutrons between the target and the neutron detector system was measured, where a high-frequency signal of the 30-Hz was used as the start signal. The neutron detector system is composed of eight neutron detectors consisted of a small-sized NE213 liquid organic scintillator (8 mm in diameter and 20 mm in thickness) and a photomultiplier tube. The proton beam current was monitored by a beam-profile monitor located upstream from the target during the measurements, and the values were calibrated to the number of incident protons using the data taken by a Faraday cup.

The background neutrons were measured using a shadow bar made of stainless steel (1 m in length) and subtracted from measurement results without the shadow bar. Hereafter, the measurements with and without the shadow bar are referred to as background (BG) and foreground (FG) measurements, respectively. The measurements were conducted at angles of 5°, 60°, and 120° from the incident beam direction for TTNY and 120° for DDX. The measurement conditions are summarized in Table 1.

Table 1: Measurement conditions for the TTNY and DDX measurements.

	Detector angle (°)	Beam current (pA)	Measurement time (s) FG	BG
TTNY	5	50	6334	7252
TTNY	60	50	7929	3617
TTNY	120	20	9041	4838
DDX	120	40	3317	1602

3 Data analysis

The neutron detectors were connected to a data acquisition (DAQ) system via signal cables. For the DAQ system, a 16-channel digitizer mounted with a field-programmable gate array was used. The neutron and gamma-ray events were discriminated based on their pulse shapes. The neutron TOF spectrum was obtained by summing for each TOF bin, and the neutron energy spectrum was obtained from the TOF spectrum using the following formula:

$$E_n = m_n c^2 \left(\frac{1}{\sqrt{1 - \beta^2}} - 1 \right), \tag{1}$$

where m_n is the neutron rest mass, c is the speed of light, and β is the ratio of velocity to c, which is written as

$$\beta = \frac{L}{L + c\Delta t}. \tag{2}$$

Here, L is the flight path and Δt is time difference between neutrons and gamma rays.

The TTNYs and DDXs were obtained by the following equations:

$$\frac{\mathrm{d}^2 Y}{\mathrm{d}E\mathrm{d}\Omega} = \frac{N_n(E_n, \theta)}{\Delta E_n \Delta \Omega} \frac{1}{N_p \, \varepsilon(E_n) \, \eta(E_n)} \qquad \text{(for TTNYs)} \tag{3}$$

and

$$\frac{\mathrm{d}^2 \sigma}{\mathrm{d}E\mathrm{d}\Omega} = \frac{N_n(E_n, \theta)}{\Delta E_n \Delta \Omega} \frac{1}{N_p N_t \, \varepsilon(E_n) \, \eta(E_n)} \qquad \text{(for DDXs)}, \tag{4}$$

where E_n is the neutron energy, θ is the emission angle, Ω is the solid angle, N_n is the number of detected neutrons, N_p is the number of incident protons, N_t is the target area density, ε is the neutron detection efficiency, and η is the neutron attenuation. In these equations, ε and η were obtained by the neutron efficiency calculation code SCINFUL-R [8] and the Monte Carlo particle transport simulation code PHITS [9], respectively.

4 Results

As an example, Figure 3 shows the obtained TTNY at 5° compared with the PHITS simulation result with the nuclear reaction model of the Liège intranuclear cascade model version 4.6, INCL4.6 [10] coupled to the generalized evaporation model, GEM [11], (INCL4.6/GEM) and the PHITS simulation result with the evaluated high-energy nuclear data library, JENDL-4.0/HE [12]. Here, experimental data measured by Meier et al. [13] are also plotted as a reference, while incident proton energy and detector angle is slightly different (incident proton energy: 113 MeV, detector angle: 7.5°). From this figure, we obtained the following findings:

- The obtained spectral shape and quasi-free peak position (60–70 MeV) are similar to Meier's data, but a peak observed at energies around 3 MeV for Meier's data was not observed.

- Both JENDL-4.0/HE and INCL4.6/GEM do not agree with the experimental data at energies above 30 MeV; INCL4.6/GEM does not reproduce the spectral shape; JENDL-4.0/HE agrees with the quasi-free peak position (60–70 MeV) but underestimates the energy spectrum around it.
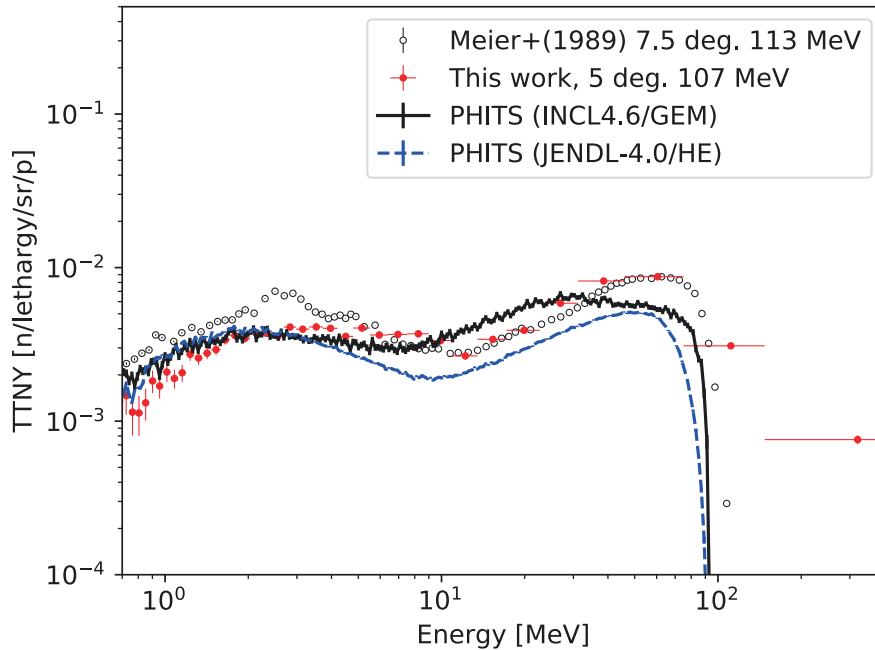

Figure 3: Measured TTNY energy spectrum at 5° compared with the PHITS simulation results with INCL4.6/GEM and JENDL-4.0/HE.

5   Summary and future work

We have measured the 107-MeV proton-induced double-differential TTNYs and DDXs for iron using the FFAG accelerator at Kyoto University, and so far the experimental TTNY data for the detector angle of 5° have been determined via the data analysis process. Future work will focus on detailed analyses of the rest of the measured TTNY and DDX data for iron, and the next step measurement of the experimental program, i.e. TTNY and DDX measurements for lead and bismuth targets, will be conducted.

References

[1] Iwamoto H., et al., Impact of PHITS spallation models on the neutronics design of an accelerator-driven system, J. Nucl. Sci. Technol., vol.53, no.10, 2016, pp.1585-1594.

[2] Sugawara T., et al., Development of three-dimensional reactor analysis code system for accelerator-driven system, ADS3D and its application with subcriticality adjustment mechanism, J. Nucl. Sci. Technol., vol.53, no.12, 2016, pp.2018-2027.

[3] Pyeon C.H., et al., Preliminary experiments on accelerator-driven subcritical reactor with pulsed neutron generator in Kyoto University Critical Assembly, J. Nucl. Sci. Technol., vol.44, no.11, 2007, pp.1368-1378.

[4] Yamanaka M., et al., Effective delayed neutron fraction by Rossi-α method in accelerator-driven system experiments with 100 MeV protons at kyoto university critical assembly, J. Nucl. Sci. Technol., vol.54, no.3, 2017, pp.293-300.

[5] Iwamoto H., et al., On-line subcriticality measurement using a pulsed spallation neutron source, J. Nucl. Sci. Technol., vol.54, no.4, 2017, pp.432-443.

[6] Pyeon C.H., et al., Reacgtion rate analyses of accelerator-driven system experiments with 100 MeV protons at Kyoto University Critical Assembly, J. Nucl. Sci. Technol., vol.55, no.2, 2017, pp.190-198.

[7] Endo T. and Yamamoto A., Data assimilation using subcritical measurement of prompt neutron decay constant, Nucl. Sci. Eng., vol.194, no.11, 2020, pp.1089-1104.

[8] Meigo S., Measurements of the response function and the detection efficiency of an NE213 scintillatior for neutrons between 20 and 65 MeV, Nucl. Instrum. Methods Phys. Res. A, vol.401, 1997, pp.365-378.

[9] Sato T., et al., Features of Particle and Heavy Ion Transport code System (PHITS) version 3.02, J. Nucl. Sci. Technol., vol.55, no.6, 2018, pp.684-690.

[10] Boudard A. et al., New potentialities of the Liège intranuclear cascade model for reactions inducedby nucleons and light charged particles, Phys. Rev. C, vol.87, 2013, 014606.

[11] Furihata S., Statistical analysis of light fragment production from medium energy proton-induced reactions, Nucl. Instrum. Methods Phys. Res. B, vol.171, 2000, pp.251-258.

[12] Kunieda S., et al., Overview of JENDL-4.0/HE and benchmark calculations, JAEA-Conf 2016-004, 2016, pp.41-46.

[13] Meier M.M., et al., Differential neutron production cross sections and neutron yields from stopping-length targets for 113-MeV protons, Nucl. Sci. Eng., vol.102, 1989, pp.310-321.

Acknowledgments

This is a blank page.

23 TOF measurement of neutron capture cross section of Re-185 in keV region

Y. Sato[1*], T. Katabuchi[1], K. Takebe[1], N. Iwamoto[2]

1) Laboratory for Advanced Nuclear Energy, Tokyo Institute of Technology
2) Japan Atomic Energy Agency
e-mail: sato.y.ca@m.titech.ac.jp

Abstract

The neutron capture cross section of ^{185}Re in the keV region is important in the various fields such as astrophysics and nuclear data. There are limited number of experimental data currently available, most of which are with large uncertainties. In this work, time-of-flight measurement of neutron capture cross sections of ^{185}Re was carried out by using a 3MV Pelletron accelerator at the Laboratory for Advanced Nuclear Energy of the Tokyo institute of technology. Using the pulse height weighting technique, the cross sections in the keV neutron energy region were measured.

I. Introduction

Rhenium has been utilized in various sectors of nuclear science and engineering. For example, alloys containing Re are one of the attractive candidates for reactor uses such as space reactors [1] and fusion reactors [2]. For isotope usage, ^{186}Re and ^{188}Re are utilized as a component of radiopharmaceutical [3]. Also, ^{187}Re-^{187}Os pair is considered to be one of the candidates of cosmo-chronometers [4].

Although there are various usages, limited number of neutron capture cross section measurements of ^{185}Re in the keV region have been performed. Most of them were conducted using the activation method and there is only one time-of-flight (TOF) measurement. The consistency of the experimental data is questionable since there are large discrepancy in trend of capture cross section, which up to 19% in the keV region.

Since an accurate cross section data in the keV region is needed, especially in the field of astrophysics [5], precise measurements are required.

II. Experiment and analysis

Experiments and analysis are described briefly. Details of the experimental method and analysis can be found elsewhere [6].

The experiment was conducted by using a 3 MV Pelletron accelerator at the Tokyo institute of technology. ^{7}Li(p,n)^{7}Be reaction was used as a neutron source. The prompt gamma rays from the neutron capture reaction were detected with an anti-Compton NaI(Tl) detector, placed at 125 degree with respect to the neutron beam axis. Neutron energy spectrum were obtained by a Li glass detector.

Three types of target were used, sample of rhenium, sample of gold and blank. The samples were irradiated in cyclic manner. The capture cross section data of ^{197}Au in ENDF/B-VII was used as a standard. The cross section of ^{185}Re was determined relative to the standard cross section.

The TOF spectra of neutron was measured with the Li glass detector. From TOF data, neutron energy spectra was determined, as shown in Fig.1. In this work, energy range from 15 keV to 90 keV was analyzed. The energy range was divided into four region called "Gate". The average neutron cross sections of each gates were determined. Details of each gates were listed in Table 1.

The capture cross section is obtained by pulse height weighting method. The net pulse height spectra after background subtraction is shown in Fig.2.

Table 1: *Gate information*

Gate No.	Energy range(keV)	Average energy(keV)
Gate1	15.0-25.0	20.1
Gate2	25.0-35.0	29.9
Gate3	35.0-55.0	44.0
Gate4	55.0-90.0	66.9
Total	15.0-90.0	45.4
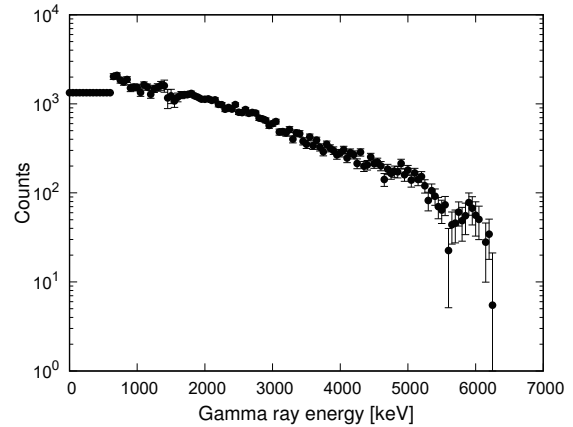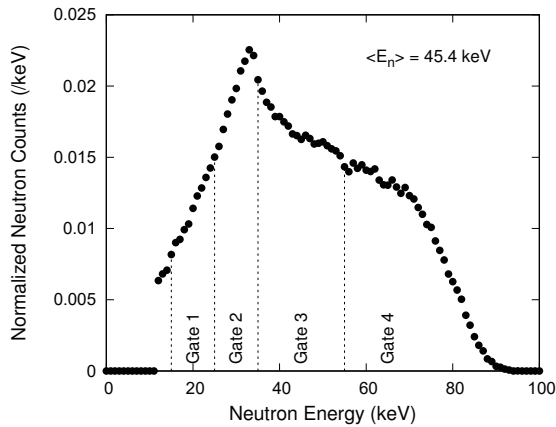
Figure 1: *Neutron energy spectra obtained from TOF spectra*

Figure 2: *Net pulse height spectra of capture reaction*

III. RESULTS AND DISCUSSION

The result of neutron capture cross sections measurement of ^{185}Re is shown in Fig.3, compared with past measurements. The uncertainties range from 4.6% to 5.4%, which are smaller than those of the past measurements. The cross sections of ENDF/B-VII.0 and the Joint Evaluated Fission and Fusion (JEFF-3.3) are also shown. The major components of uncertainties are the cross section data of ^{197}Au, and statistical errors. The results of Bergman *et al.* [7] agree with the present results, however the uncertainties are not provided for all energy points of their data. The results of Friesenhahn *et al.* [8] also agree with the present results. However other experimental data disagree with the present data. ENDF/B-VII.0 follows the trend of the present data while JEFF-3.3 disagree.

IV. SUMMARY

Neutron capture cross sections of ^{185}Re in keV region were measured by using the TOF method. The cross sections were obtained relative to the standard cross section, neutron capture cross section of ^{197}Au. The uncertainties range from 4.6% to 5.4% which are smaller than past measurements in keV region. Since the accuracy of Re-Os cosmochronometers [5] can be improved together with the cross section of ^{185}Re n, γ ^{186m}Re, further experimental study is anticipated.

REFERENCES

[1] Busby JT, Leonard KJ, Zinkle SJ. Radiation-damage in molybdenum rhenium alloys for space reactor applications. J Nucl Mater, 2007, 366(3):388–406,
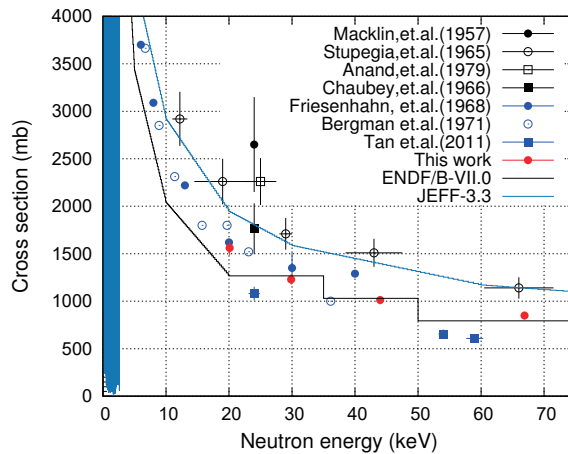
Figure 3: *Measured neutron capture cross sections of ^{185}Re and evaluated data in linear scale*

[2] Guan W, Nogami S, Fukuda M, et al. Tensile and fatigue properties of potassium doped and rhenium containing tungsten rods for fusion reactor applications. Fusion Eng Des, 2016,109-111:1538–1542.

[3] Blower P. Towards molecular imaging and treatment of disease with radionuclides: the role of inorganic chemistry. Dalton Trans, 2006, 14:1705–1711.

[4] Clayton DD. Cosmoradiogenic Chronologies on Nucleosynthesis. Astrophys J, 1964, 139.

[5] Hayakawa T, Shizuma T, Kajino T, et al. New s-Process Path and Its Implications for a ^{187}Re-^{187}Os Nucleo-Cosmochronometer. Astrophys J, 2005, 628(1):533.

[6] Nishiyama J, Igashira M, Ohsaki T, et al. Measurements of keV-Neutron Capture Cross Sections and Capture Gamma-Ray Spectra of ^{117,119}Sn. J Nucl Sci Technol, 2008, 45(4):352-360.

[7] Bergman AA, Kaipov DK, Konks VA, et al. Radiative capture of neutrons by rhenium isotopes. Proceedings of Neutron Physics Conference;1971 May 24-28; Kiev; Naukova Dumka; 1971. 144–149.

[8] Friesenhahn SJ, Gibbs DA, Haddad E, et al. Neutron capture cross sections and resonance parameters of rhenium from 0.01 eV to 30 keV. J Nucl Energy, 1968, 22(4):191–210.

This is a blank page.

24   Benchmark Experiment for Large Angle Scattering Cross Sections for Tungsten with 14 MeV Neutrons

Sota Araki[*], Kazuki Fukui, Indah Rosidah Maemunah, Rio Miyazawa,

Shingo Tamaki, Sachie Kusaka, Isao Murata

Graduate school of Engineering, Osaka University

Yamada-oka 2-1, Suita, Osaka 565-0871, Japan

[*]*e-mail: araki21@qr.see.eng.osaka-u.ac.jp*

Cross sections of large angle scattering reaction in nuclear data are commonly smaller than those of forward scattering reaction when energy of an incident neutron is high. However, in a high intensity neutron field, such as fusion reactor, contribution of cross sections of large angle scattering reaction is not negligible on calculation results. Actually, in the past difference between experimental and calculated values in benchmark experiments for large angle scattering reaction cross sections was reported for iron. In the previous research, the author's group thus developed a benchmark method for large angle scattering reaction cross sections and carried out experiments with an iron target.

In this study, we carried out benchmark experiments for large angle scattering reaction cross section for tungsten and compared with neutron transport calculation results with Monte Carlo code, MCNP5. By comparing the experimental values with calculated results, we discussed accuracy of large angle scattering reaction cross sections of ENDF/B-VIII, JEFF-3.3 and JENDL-4.0. As a result, we found that all the three cross section data underestimated large angle scattering reaction cross section of tungsten largely. However, JENDL-4.0 and JEFF-3.3 most agreed with the experimental values.

1. Introduction

Large angle scattering reaction cross section is commonly smaller than forward scattering reaction cross section by 2 or 3 order magnitude when incident neutron energy is high. However, in high energy and high intensity neutron field like fusion reactor, large angle scattering reaction has non-negligible effects on neutron transport calculation through gap streaming phenomenon. It was pointed out that large angle scattering reaction in such as gap streaming phenomenon causes low prediction accuracy of neutron transport calculation in fusion reactor[1]. Figure 1 shows angular distribution of elastic scattering reaction cross section of ^{184}W, which is the most abundant nuclide of tungsten [2-4]. Tungsten is an important fusion reactor constituent element to be planned to use in the divertor, the first wall and so on in fusion reactor. As shown in Fig.1, elastic scattering reaction cross section data vary among nuclear data libraries especially in large angles. To improve the accuracy of design calculation in such a gap streaming phenomenon in fusion reactor, experimental approaches to get rid of this uncertainty of large angle scattering reaction cross section are required. Elastic scattering reaction cross section can be benchmarked directly by measuring double-differential cross section. However, in large angle range, this method is quite difficult and time-consuming, in addition it may have large experimental uncertainties because large angle scattering cross section is very

small. To solve this problem, our group developed a benchmark experiment method for large angle scattering cross section[5,6]. In this study, we performed benchmark experiments for large angle scattering cross section of tungsten with the developed benchmark method.
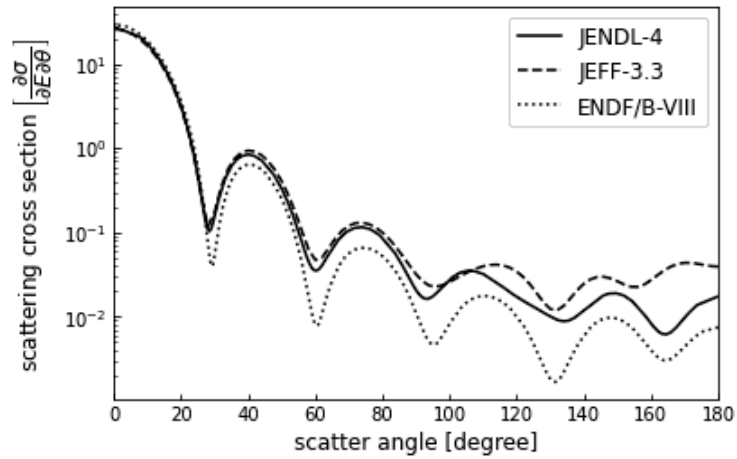
Fig.1   14 MeV neutron elastic scattering cross section angular distribution of ^{184}W.

2. Method

Figure 2 shows outline of the benchmark experimental system. The benchmark experimental system consists of a DT neutron source, niobium activation foil, iron shadow bar, tungsten sample and wall of irradiation room. The shadow bar is an iron trapezoidal conical bar and set up to shield direct incident neutrons. In the experiments, we use two types of shadow bar, thin and thick ones. The tungsten sample is a cylinder with a thickness of 6 cm, which is twice the mean free path of tungsten. By using a sample with a thickness equal to twice the mean free path, an effect of multiple scattering neutron can be reduced. In this study, in addition to the two experimental systems shown in Fig.2, we performed two experiments with systems in which the tungsten sample is removed from each experimental system. In total, four experiments
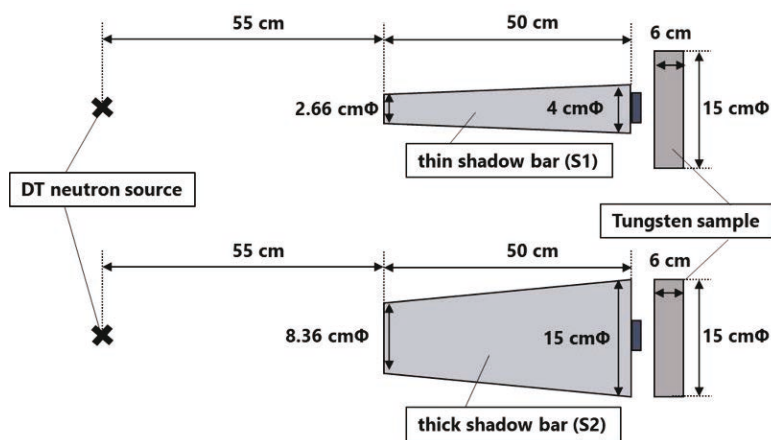
Fig.2   Two types of experimental system for benchmark.

are carried out in one sample. The four experimental systems are named as follows: S1T and S1 are experimental systems using thin shadow bar with and without sample, respectively. S2T and S2 are experimental systems using thick shadow bar with and without tungsten sample, respectively.

The whole experimental system including a wall in the irradiation room has three elements: shadow bar, tungsten sample and wall, in addition to DT neutron source and activation foil. Therefore, there are seven combination of elements ($= {_3}C_1 + {_3}C_2 + {_3}C_3$) that are assigned as paths which an incident neutron passes through before entering the activation foil. In this study, we distinguished these seven types of neutron transport paths contributing to the activation of niobium foil. Figure 3 shows each path. Neutrons which pass though path ③ are scattered only with the sample, so the nuclear data of tungsten can be benchmarked by comparing the contribution of neutrons through this path in calculations and experiments [5]. Each experimental system does not contain all the seven paths, that is, possible paths in each experimental system are limited and different with each other. Figure 4 shows possible paths in each experimental system.

① (Shadow Bar)
② (Shadow Bar, Sample)
③ **(Sample)**
④ (Shadow Bar, Wall)
⑤ (Sample, Wall)
⑥ (Wall)
⑦ (Shadow Bar, Sample, Wall)

Fig.3　Possible paths in the benchmark experimental system. List on the right shows the elements which neutron passes through on each path.

Fig.4　Possible paths in each experimental system.

Since neutrons entering the niobium foil can be assumed to pass through one of the paths shown in Fig.4, the contribution of path 3 can be estimated from reaction rates of the four activation foils by the following equation.

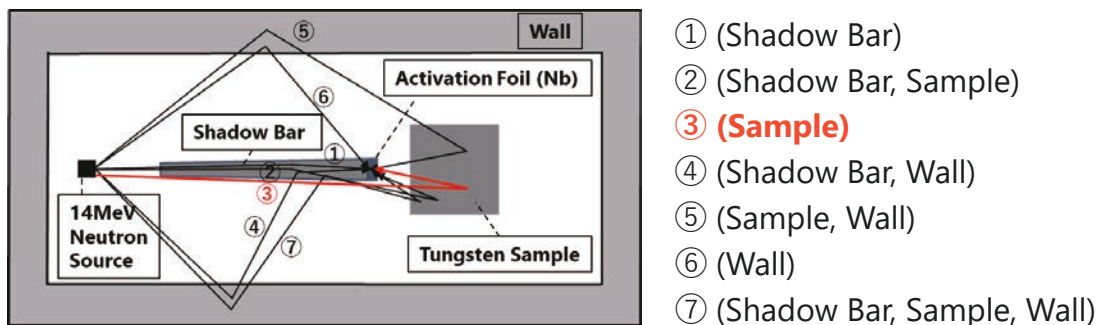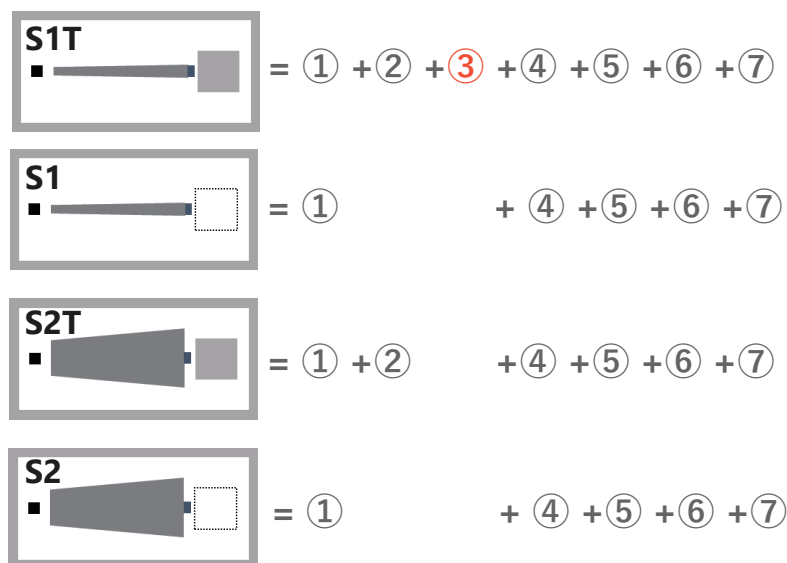$$(R_{S1T} - R_{S1}) - (R_{S2T} - R_{S2}) = N_a \int_E \sigma\{(\phi_{S1T} - \phi_{S1}) - (\phi_{S2T} - \phi_{S2})\}dE$$

$$= N_a \int_E \sigma\{(\phi_1 + \phi_2 + \phi_3 + \phi_4 + \phi_5 + \phi_6 + \phi_7)_{S1T} - (\phi_1 + \phi_4 + \phi_6)_{S1}$$

$$- (\phi_1 + \phi_2 + \phi_4 + \phi_5 + \phi_6 + \phi_7)_{S2T} + (\phi_1 + \phi_4 + \phi_6)_{S2}\}dE$$

$$= N_a \int_E \sigma\phi_{3,S1T}dE, \tag{1}$$

where N_a is number of niobium atoms, σ is activation cross section of niobium, $\phi_i(i = 1,2\cdots 7)$ is neutron flux passing through path i.

In Equation (1), we assume a relation expressed in Equation (2).

$$(\phi_{S1T} - \phi_{S1}) - (\phi_{S2T} - \phi_{S2}) = \phi_{3,S1T} \tag{2}$$

This is because, we found from physical consideration that contributions of neutrons through paths ①, ④, ⑤ and ⑥ can be canceled out, and those of paths ② and ⑦ remain, however, they are small and regarded as the estimation error of the present benchmark method. To verify this hypothesis, we calculated both physical quantities of Equation 2 by Monte Carlo code, MCNP5 [6]. Table 1 shows the calculated reaction rate by each path and $(\phi_{S1T} - \phi_{S1}) - (\phi_{S2T} - \phi_{S2})$. As shown in Table 1, reaction rate of $\phi_{3,S1T}$ is expressed well by reaction rate of $(\phi_{S1T} - \phi_{S1}) - (\phi_{S2T} - \phi_{S2})$. We performed experiments using the benchmark method descried above, and the results are presented in section 3.

Table 1   Neutron flux of path 3 calculated by MCNP5 [s^{-1}].

	S1TC	S2TC	S1C	S2C	S1TC-S2TC-(S1C-S2C)
①	1.5E-11	1.2E-10	1.5E-11	1.2E-10	-1.0E-14
②	6.1E-11	1.6E-12	0	0	6.0E-11
③	**2.5E-09**	0	0	0	2.5E-09
④	1.0E-09	5.6E-10	1.0E-09	5.6E-10	1.0E-14
⑤	1.2E-09	1.2E-09	3.0E-09	3.0E-09	-2.0E-11
⑥	7.5E-10	2.3E-10	7.5E-10	2.3E-10	-1.0E-14
⑦	2.0E-11	2.7E-11	2.4E-11	5.4E-11	2.4E-11
Total	5.6E-09	2.1E-09	4.8E-09	3.9E-09	**2.6E-09**

3. Result

We performed benchmark experiments for tungsten sample and measured four reaction rates of niobium foils. We also calculated the reaction rates in JENDL-4.0 [2], ENDF/B-VIII [3], JEFF-3.3 [4] using MCNP5 code with the calculation model shown in Fig. 3. The experimental results were compared with calculated values. The results are shown in Table 2.

Table 2　Result of experiment and calculation [s⁻¹].

	S1TC	S2TC	S1C	S2C	S1TC-S1C-(S2TC-S2C)	C/E
Experimental Result	8.37±0.18	2.07±0.04	5.01±0.14	3.83±0.03	5.12±0.16	
JENDL-4.0	4.69	1.29	2.87	2.32	2.85	0.56
ENDF-B/VIII	3.36	1.25	2.87	2.32	1.55	0.30
JEFF-3.3	4.75	1.25	2.87	2.32	2.95	0.58

In Table 2, calculated reaction rates in the four experimental systems are largely different from their experimental results. This is thought to be due to omission of some elements such as the accelerator itself, structural materials and surrounding other massive objects in the irradiation room in the calculation. However as shown in section 2, we can cancel out contributions of neutrons passing through other paths than path ③. As shown in the table, the C/E values are 0.3-0.5 for all the three nuclear data. Practically, all the calculated values are smaller than the experimental values. This is caused by underestimation of the amount of large angle scattering neutrons through path ③, and it may indicate underestimation of large angle elastic scattering cross sections in all the nuclear data libraries. It can also be concluded that JEFF-3.3 and JENDL-4.0 reproduced experimental values better among the three nuclear data in this study.

4. Conclusion

In this study, we performed benchmark experiments for large angle elastic scattering cross sections for tungsten by the benchmark experimental method developed by the authors' group previously. As a result, it was found that all three nuclear data, JENDL-4.0, ENDF/B-VIII, and JEFF-3.3, underestimated the large angle scattering cross sections. Among them, JEFF-3.3 and JENDL-4.0 were found to reproduce the experimental results better.

In the future, we will perform benchmark experiments for light nuclides such as lithium and oxygen. We will also develop a method to feed back the results of the present integral experiments to the angular distribution of the evaluated nuclear data.

Reference

[1] Ohnishi, S., Keitaro, K., Tetsushi, A., et al., New integral experiments for large angle scattering cross section data benchmarking with DT neutron beam at JAEA/FNS, Fusion Eng. Des., vol.87, 2012, pp. 695-699.

[2]   Shibata, K., Iwamoto O., Nakagawa T., et al., JENDL-4.0: A New Library for Nuclear Science and Engineering, J. Nucl. Sci. Technol., vol 48, no.1, 2011, pp.1-30.

[3]   Brown, D.A., Chadwick, M.B., Capote, R., et al., ENDF/B-VIII.0: The 8th Major Release of the Nuclear Reaction Data Library with CIELO-project Cross Sections, New Standards and Thermal Scattering Data, Nucl. Data Sheets, vol.148, 2018, pp.1-142.

[4]   NEA, JEFF-3.3, https://www.oecd-nea.org/dbdata/jeff/jeff33/index.html (accessed 2022-02-13).

[5]   Hayashi, N., Ohnishi, S., Fujiwara, Y., et al., Optimization of Experimental System Design for Benchmarking of Large Angle Scattering Reaction Cross Section at 14 MeV Using Two Shadow Bars, Plasma Fusion Res., vol.13, 2018, 2405002

[6]   Brown, F.B., MCNP-A General Monte Carlo N-Particle Transport Code, Oak Ridge(US): Los Alamos National Laboratory; 2003.

25   Energy dependence of total kinetic energy of fission fragments

for the standard and superlong modes analyzed separately

by 4D Langevin model

Kazuya SHIMADA[1*], Chikako ISHIZUKA[1], and Satoshi CHIBA[1]

[1]Nuclear Engineering Course, Transdisciplinary Science and Engineering, School of Environment and Society, Tokyo Institute of Technology, Tokyo, 152-8550 Japan

*Email: Shimada.k.af@m.titech.ac.jp

Our previous study has shown that the decrease of average total kinetic energy (TKE) with increasing excitation energy is due to change of the deformation of the heavy fission fragments from spherical to ellipsoidal shape. However, decrease of the average TKE has been understand in the fission community as an increase of the fraction of symmetric (superlong) mode, which has smaller average TKE compared to the asymmetric (standard) mode. In this study, the average TKE for the asymmetric and symmetric fission modes were deduced separately in neutron-induced fission of ^{235}U based on 4-dimensional Langevin calculation.   It was found that the energy dependence of the overall TKE was primarily governed by the decrease of TKE of the standard mode.

1. Introduction

TKE is the sum of kinetic energies of 2 fission fragments, which account for most of the energy released by nuclear fission. Therefore, accurate and quantitative evaluation of TKE is desired from the viewpoint of nuclear energy utilization and basic research. Figure 1 shows the average TKE of fission fragments when neutrons are incident on ^{235}U. Both experimental data [1-4] and our calculation (blue and orange lines) show decrease of TKE as the incident neutron energy increases. In addition, good reproducibility was obtained as a result of considering multichance fission (orange line). The multichance fission is a phenomenon in which nuclear fission takes place after emitting a couple of neutrons. The calculation of the multichance fission is basically a superposition of TKE of first chance fission for a series of nuclei having different number of neutrons. Therefore, reason of the energy dependence of the first chance fission is investigated in this work.

Our previous study has made it clear that the decrease of average TKE with increasing incident neutron energy is due to change of deformation of the heavy fragments [5]. Figure 2 shows the average quadrupole deformation parameter Q_{20} of fission fragments as a function of the fragment mass number and excitation energy. At the excitation energy of 7 MeV (red line), the Q_{20} shows a prominent saw-tooth structure. As the excitation energy increases, on the contrary, Q_{20} of the heavy fragments increases, and the saw-tooth structure is washed out. This result shows the following picture about the change of the
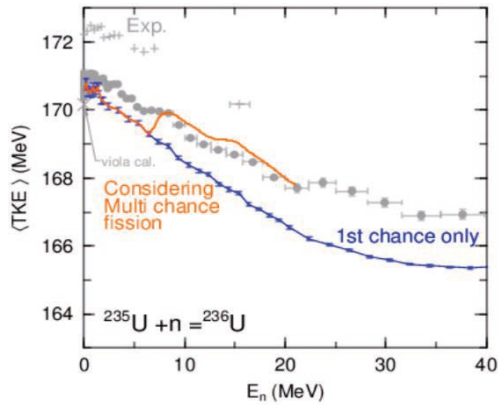
Fig1. Incident neutron energy dependence of TKE of fission fragments in ^{235}U(n,f) reaction. The gray symbols show experimental data [1-4], while the blue line indicates the calculation result of first-chance fission, and the orange line shows the calculation result including multichance fission.
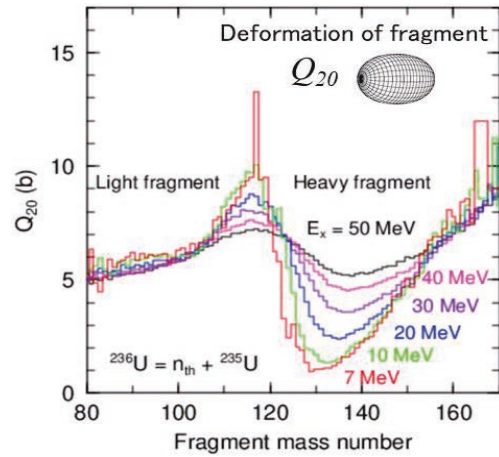

Fig2. The average quadrupole deformation parameter Q_{20} of fission fragments appearing in fission of the ^{235}U + n system.

fragments' shape; At low excitation energies, the complex nucleus splits into a deformed light fragment and a heavy spherical fragment. On the other hand, as the excitation energy increases, the heavy fragments change to elongated shapes. Then, the distance d_{cm} between the centers of mass of the 2 fragments increases. Therefore, the Coulomb repulsion of the nascent fragments, which is the main source of TKE, decreases.

However, the discussion of TKE decrease has been understood in the fission community as the increase of the superlong mode as the excitation energy increases. Left panel of Fig. 3 shows the fragment mass-TKE correlation for ^{236}U at the excitation energy of 10 MeV. The horizontal axis represents the mass number of the fragments, and the vertical axis represents the TKE. The distribution is concentrated in areas surrounded by three ellipses. The red ellipses indicate the location for the standard mode that causes asymmetric mass splitting, and the green ellipse indicates the superlong mode that causes symmetric mass division. In the standard mode of asymmetric splitting, the TKE is large because the d_{cm} is small due to spherical magicity of the heavy fragment, and in the superlong mode (symmetric splitting), the TKE is smaller because the d_{cm} is larger. This situation is schematically shown in the right panel of Fig. 3. As the excitation energy increases, the fraction of superlong mode increases, which causes the TKE to decrease. This is an intuitively reasonable picture to account for the decrease of the TKE of fission fragments discussed so far. In this study, we calculated the incident neutron energy dependence of the average TKE in standard and superlong modes separately and investigated the reason of decrease of TKE as excitation energy increases in more details.

2. Computational method

The Langevin calculation was carried out based on reference [6]. The shape of the complex nucleus during the scission process was expressed by four parameters using the two-center model (TCM) [7]. That is, elongation z_0, deformation of the outer tips of the nuclei δ_1, δ_2 and mass asymmetry $\alpha =$
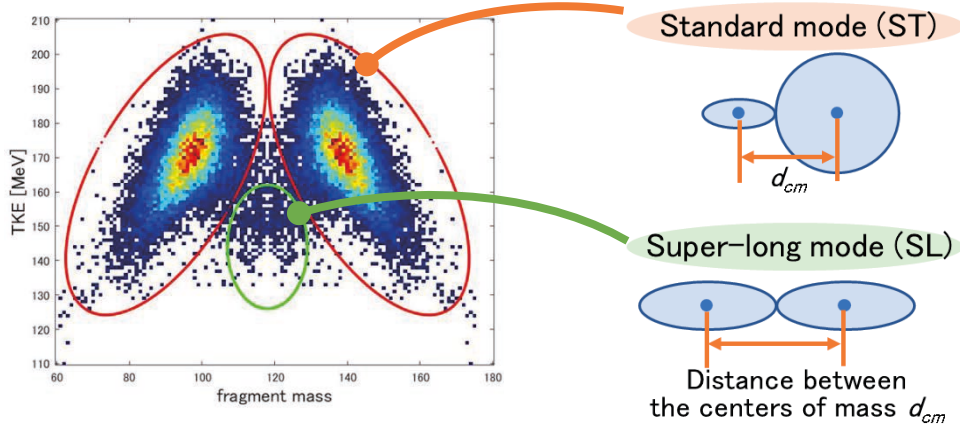
Fig3. Left panel shows mass number-TKE correlation of the fragments when the excitation energy is 10 MeV for ^{236}U. The red ellipses indicate locations of the standard mode, while the green ellipse indicates that of the superlong mode. The right panel shows a qualitative picture of the shapes of the light and heavy fragments for the both modes.

$(A_1 - A_2)/(A_1 + A_2)$. Elongation z_0 corresponds to the distance between the centers of the two oscillators normalized by $R_0 = 1.2 \cdot (A_1 + A_2)^{1/3}$. The Langevin calculation was performed to obtain time evolution of these four parameters, while the neck parameter ε was fixed to 0.275 from our previous studies.

The 4D Langevin equations are expressed as follows. By Eq. (1), parameters of TCM are indicated by using a general coordinates $q_i (i = 1 \dots 4)$, and p_i denote their conjugate momenta. The F in Eq. (2) denotes the free energy $F = V - TS$, where V indicates the nuclear potential, T and S stands for the temperature and entropy of the heat bath consisting of nucleons which interact with the 4 collective coordinates. Shell and pairing corrections to the free energy were applied in terms of the Strutinski and BCS methods [8]. The inertia tensor m_{ij} (i, j = $1 \dots 4$) and the friction tensor γ_{ij} represent the transport coefficients. The symbol $g_{ij} R_j$ represents the random force, where R_j denotes the white noise:

$$\frac{dq_i}{dt} = m_{ij}^{-1} p_j \tag{1}$$

$$\frac{dp_i}{dt} = -\frac{\partial F}{\partial q_i} - \frac{1}{2} \frac{\partial}{\partial q_i} m_{jk}^{-1} p_j p_k - \gamma_{ij} m_{jk}^{-1} p_k + \sqrt{T^{eff}} g_{ij} R_j(t) \tag{2}$$

Here, summation on the repeated indices is implicitly assumed.

3. Result and Discussion

The fragment-mass TKE correlations are shown in Fig. 4. Please notice that we did not consider multichance fission as explained above. As the excitation energy increases, the overall gradation becomes darker, indicating that the total number of fissions has increased. We can also see that the number of the symmetric, superlong, mode region increases rapidly, and it seems to move to the higher TKE side. The latter tendency, however, may be caused due to increasing area of the standard mode, which cannot be eliminated completely. Since the distribution moves for each excitation energy, regions of the standard and superlong modes were visually determined by adjusting ellipses at each excitation energy. Then, average TKE in both modes were obtained separately as well as the average TKE of the whole events,
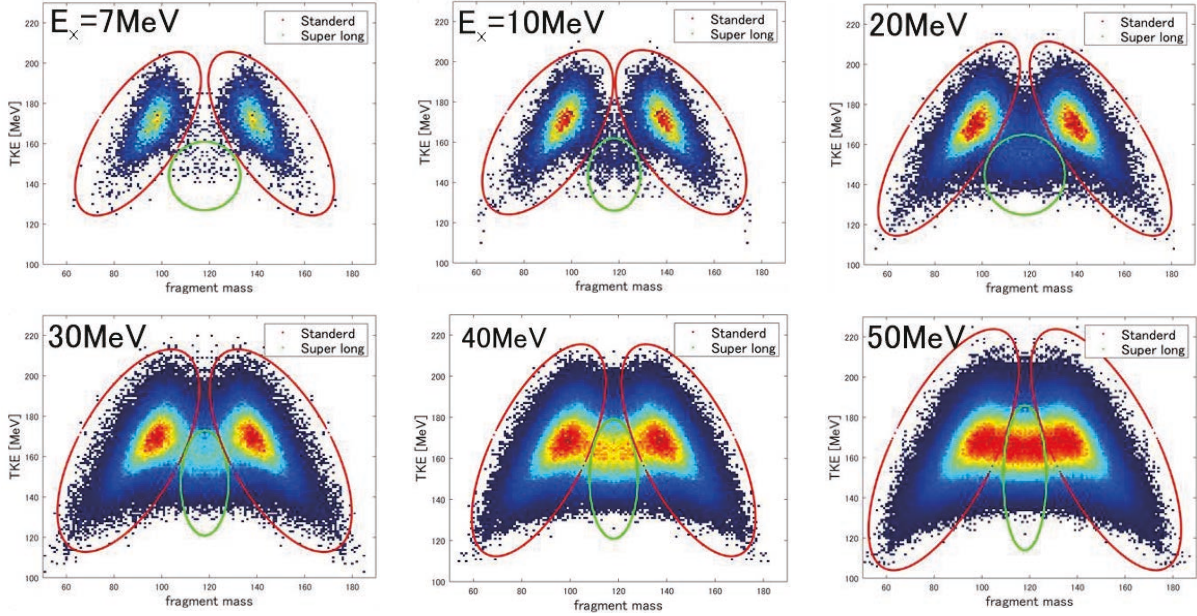
Fig4. The fragment mass-TKE distribution for the first-chance fission of ^{236}U, which is the compound nucleus of ^{235}U + n reaction. The excitation energy is 7, 10, 20, 30, 40, 50MeV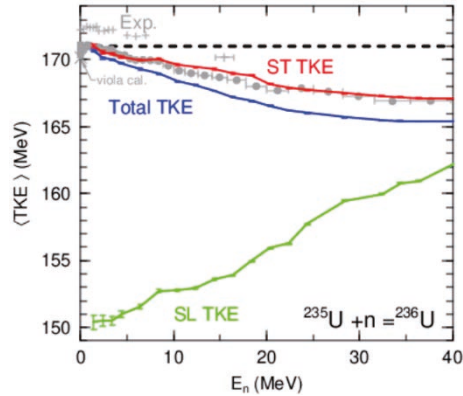 starting from the upper left panel.　The red and green ellipses denote the regions assigned as standard and superlong mode, respectively. Notice that we did not take account of the multichance fission.

which does not depend on the ellipses we assign. In this manner, we are confident to derive the average TKE of the whole events as well as that of the standard mode. However, average TKE of the superlong mode seems to be polluted by the contribution of the standard mode.

　　Figure 5 shows the excitation energy dependence of average TKE of each mode for ^{235}U + n system. As the excitation energy increases, the overall average TKE (blue line, shown as Total TKE) and that of the standard mode (red line) decreases, while that of the superlong mode (green line) increases. The decrease of the overall TKE is larger than that of the standard mode. This is because of increasing contribution by the superlong mode which pulls down the overall TKE. Let us consider in detail how this behavior of the overall average TKE is understood.

Fig 5. Neutron-energy dependence of TKE of standard (ST, red line), superlong (SL, green line) and both (ST+SL, blue line) modes for ^{235}U + n. The gray symbols show the experimental data [1-4]. Notice that we did not take account of the multichance fission.

　　As shown in Eq (3), the overall average TKE is calculated as a sum of contributions from the standard (ST) and superlong (SL) modes. Here, ω_{ST}　and ω_{SL} denotes the fraction of the standard and superlong modes, respectively, in the scission events, while $\omega_{ST} + \omega_{SL} = 1$. When the equation is modified as Eq. (4), we notice that the overall average TKE is obtained as a sum of the average TKE for the pure standard mode ($\langle TKE_{ST}\rangle$, red line in Fig. 6) minus the second term which shows the correction

by the superlong mode:

$$\langle TKE \rangle = \omega_{ST}\langle TKE_{ST} \rangle + \omega_{SL}\langle TKE_{SL} \rangle \tag{3}$$

$$= \langle TKE_{ST} \rangle - \omega_{SL}\{\langle TKE_{ST} \rangle - \langle TKE_{SL} \rangle\} \tag{4}$$

When the entire average TKE decreases, that of the standard mode also decreases. However, decrease of the TKE of the standard mode alone is insufficient to account for that of the total average TKE. The additional amount corresponds to the decrease caused by the second term of Eq. (4), the correction by the superlong mode. The decrease caused by the presence of superlong mode is about a half of that of the first term, namely, standard mode alone. Therefore, we can conclude that decrease of the average TKE of fission fragments in this system as a function of the excitation energy is primarily accounted for by the decrease of the TKE of the standard mode (change of the shape of the heavy fragment from spherical to ellipsoidal form as shown in Fig. 2), and the increase of the fraction of the superlong mode accounts for about a half of the decrease of the entire TKE. Furthermore, it must be pointed out that we do not understand if the increase of the TKE of the superlong mode (green line) is correct or not, since the region assigned as the superlong mode, the green ellipses in Fig. 4, contain inevitably contribution from the (overwhelming) standard mode as explained above.

4. Summary

Reason of the decrease of the average total kinetic energy (TKE) of fission fragments for ^{235}U + n system was investigated in term of the 4-dimensional Langevin model. We have calculated the fragment mass-TKE correlation as a function of the excitation energy, and obtained average TKEs for the standard (ST) and superlong (SL) modes separately as well as that of the entire events including both modes. We noticed that about 2/3 of the decrease of the entire average TKE was accounted for by the decrease of average TKE of the standard mode, and correction by existence of the superlong mode is about a half. We know, as shown in Ref. [5], decrease of the TKE of the standard mode arises as a result of the change of the shape of the heavy fragments which is nearly spherical at low excitation energy, due to magicity of the A=132 shell, to a well deformed ellipses at higher excitation energy where the shell effects are washed out gradually. Therefore, the conclusions obtained in Ref. [5] did not change basically, rather it was strengthened by the present work.

In this work, we assigned the regions of the ST and SL modes by ellipses. However, we cannot assign all the events by this treatment. We should find a better way to assign regions corresponding to these 2 modes, and it will be an issue of the near-future work.

References

1) Duke, Dana Lynn, 'Fission Fragment Mass Distributions and Total Kinetic Energy Release of 235-Uranium and 238-Uranium in Neutron-Induced Fission at Intermediate and Fast Neutron Energies', LA-UR-15-28829, Los Alamos, USA (2015).

2) P.P.D'yachenko, 'Energy and mass distributions of fragments from fission of ^{235}U by monoenergetic neutrons from 0-MeV to 15.5-MeV', J, SNP, 8, 165 (1969).

3) S.Zeynalov et al., 'Investigation of mass-TKE distributions of fission fragments from the U-235(n, f)-reaction in resonances', S,ISINN-13,351 (2006).

4) V.E.Viola, et al., 'Systematics of fission fragment total kinetic energy release', Phys. Rev. C 31, 4, 1550 (1985).

5) Kazuya Shimada, Chikako Ishizuka, Fedir A. Ivanyuk, and Satoshi Chiba, 'Dependence of total

kinetic energy of fission fragments on the excitation energy of fissioning system', Phys. Rev. C 104, 054609 (2021).

6) C.Ishizuka, M.D.Usang, F.A.Ivanyuk, J.A.Maruhn, K.Nishio, and S.Chiba, 'Four-dimensional Langevin approach to low-energy nuclear fission of ^{236}U', Phys. Rev. C 96, 064616 (2017).

7) J. Maruhn and W. Greiner, 'The Asymmetric Two Center Shell Model', Z. Phys. 251, 431 (1972).

8) F.A.Ivanyuk, C.Ishizuka, M.D.Usang and S.Chiba, 'Temperature dependence of shell corrections', Phys. Rev. C 97, 054331(2018).

Acknowledgements

26   Development of activation detector
for ultra-long term DT neutron irradiation

Yoshihide IWANAKA[1*], Ryota EGUCHI[1], Shingo TAMAKI[1], Sachie KUSAKA[1]

Fuminobu SATO[1], and Isao MURATA[1]

[1] Osaka University, 2-1 Yamadaoka, Suita, Osaka 565-0871, Japan

*Email: iwanaka22@qr.see.eng.osaka-u.ac.jp

Commonly, ^{93}Nb(n, 2n) reaction is used for neutron flux measurement in the material integrity test irradiation for a fusion reactor. However, the Nb foil is sometimes not appropriate for recording a long irradiation period of about 1 year, because the half-life of the produced radionuclide is about 10 days. In this study, we developed an activation detector to determine the neutron fluence, even if the irradiation period is extremely long, using nuclides producing very long half-lives. First, we selected nuclides which have reactions with neutron and produce radioisotopes which emit γ-rays, and 33 nuclides were selected as possible γ-ray emitters. Additionally, in order to increase the number of candidate nuclides for various irradiation conditions of neutron source intensity and irradiation time, β-ray emitters were also examined. As a result, 15 nuclides producing β-ray emitters were selected. In the candidates, ^{103}Rh and ^{159}Tb were selected as the nuclides producing γ-ray emitters and ^{63}Cu and ^{159}Tb were found for nuclides producing β-ray emitters for 1 month and 1 year irradiation, respectively.

At present, we are measuring the accurate cross sections of ^{103}Rh(n,2n) and ^{159}Tb(n,2n) reactions at 14 MeV by a short-term irradiation, and long-term irradiation of several months is being carried out with these foils to prove the applicability of these foils as activation detectors in an ultra-long-term DT neutron irradiation.

1.   Introduction

In order to develop materials with high radiation resistance, it is necessary to obtain data of activation and irradiation damage of materials and to evaluate their integrity. Currently, the foil activation method using Nb foil is generally used to obtain the fluence of DT neutron irradiation. However, the half-life of ^{92m}Nb is as short as about 10 days, and the fluence may be underestimated due to decrease in radioactivity after a long-term irradiation. When a Nb foil activation detector is used in a long term irradiation test, it is commonly necessary to change the foil every day and calculate the accumulated neutron fluence. This is really inefficient and complicated.

Therefore, we aim to develop an activation detector that can measure the DT neutron fluence in a long-term irradiation. In order to achieve this goal, we examine suitable nuclides as the activation foil that can

keep the information of neutron fluence within an acceptable error range after 1 month and 1 year DT neutron irradiation. We also carry out test irradiations and the detection system to measure the decay γ-rays.

2. Methods

In order to select suitable nuclides for a long term DT neutron irradiation, nuclides producing β-ray emitters were taken into account, in addition to commonly used nuclides producing γ-ray emitters. This addition would increase the number of candidate nuclides and would also utilize an advantage that β-rays have a shorter range and as a result it can have 100% measurement efficiency.

After selecting the candidate nuclides based on characteristics of the nuclear data, the number of radionuclides produced by DT neutron irradiation and the number of the measured γ-rays from the selected RIs are calculated by MCNPX[1]. Thereafter the most suitable nuclides as the activation foil for a long-term irradiation is determined.

2.1. Nuclides selection criteria

Assuming 1-month and 1-year DT neutron irradiation experiments, nuclides producing γ-ray or β-ray emitters are selected as candidates that satisfy the following criteria.

- The nuclide is solid and stable at room temperature
- The nuclide has a reaction cross section with 14 MeV neutrons
- The half-life of produced radionuclide is between 1 and 1000 years
- Measurable γ and β rays are emitted from produced radionuclides.

2.2. Irradiation and measurement simulation

In this section, procedure of irradiation and measurement simulations is described for the selected candidate nuclides. For the selection, we evaluate fluence estimation errors, i.e., statistical and systematic errors. The statistical errors are calculated using the estimated γ-ray counts predicted by the simulation. The systematic error caused by the decay of radionuclides is evaluated as follows. When the irradiation history is unknown, there is an infinite number of irradiation patterns. Assuming a continuous irradiation with a constant flux, the previous irradiation that the foil remembers (the number of surviving radionuclides) is estimated by theoretical calculations. The relative difference between the total number of produced radionuclides and the number of surviving radionuclides is defined as the systematic error. The sum of these two errors was used as an index for performance evaluation.

2.2.1 Irradiation simulation

The number of produced radionuclides is theoretically estimated by assuming simulation when regular irradiation and cooling are performed in the prescribed irradiation periods of 1 month and 1 year. The calculation process is shown below.

First, the neutron flux ϕ_{MCNP} incident on the foil in the system is calculated by MCNPX. Irradiation

is carried out at OKTAVIAN facility of Osaka University with the following condition:

- The neutron intensity is 5.0×10^9 [n/sec].
- An activation foil is placed in the 0° direction of the beamline at a point 10 cm from the irradiation port.
- The size of the foil is 20×20×1 [mm³].
- Irradiation for 8 hours and cooling for 16 hours on weekdays, and cooling for 24 hours on weekends are repeated for 1 month or 1 year.

The number of radionuclides produced by neutron irradiation for t_1[s], N_1 [1/s], is determined by using the decay constant $\lambda[s^{-1}]$ [2], the number of target nuclide N_0, the activation cross section $\sigma[cm^2]$ [3] for a given neutron energy, and the neutron flux ϕ_{MCNP} [1/cm²/s] as described in Eq. (2-1).

$$N_1 = \frac{N_0 \int \sigma(E)\phi_{MCNP}(E)\, dE}{\lambda}\left(1 - e^{-\lambda t_1}\right) \qquad (2-1)$$

N_1 decays with time and becomes N_1'[1/s]. The number of radionuclides after t_1' [s] from irradiation is obtained by Eq. (2-2).

$$N_1' = N_1 e^{-\lambda t_1'} \qquad (2-2)$$

In the case of repeated irradiations and coolings, the numbers of radioisotope production N_n and N_n' obtained after the n-th irradiation and cooling are obtained from Eqs. (2-3) and (2-4), respectively, by setting n-th irradiation time and cooling time as t_n[s] and t_n'[s], respectively.

$$N_n = \frac{N_0 \sigma \phi_{MCNP}}{\lambda}\left(1 - e^{-\lambda t_n}\right) + N_{n-1}' e^{-\lambda t_n} \qquad (2-3)$$

$$N_n' = N_n e^{-\lambda t_n'} \qquad (2-4)$$

The number of produced radionuclides after the entire irradiation period is calculated by repeating Eqs. (2-3) and (2-4).

2.2.2 Measurement simulation

The estimated number of counts is calculated by numerical simulation assuming the radiation measurement is carried out for 24 hours after the irradiation. As a radiation measurement system, a Ge semiconductor detector is used to measure γ-rays and two CsI(Tl) scintillation detectors are used to measure β-rays as shown in Fig. 1. By sandwiching the activation foil between two CsI crystals (I.S.C. Lab.) and making the crystal thickness thicker than the maximum range of emitted β-rays, it can be assumed that all β-rays are detected and the detection efficiency is 100%. In this study, the maximum range R[cm] of β-rays is evaluated for the maximum energy of β-rays, E_{max}, and density, $\rho[g/cm^3]$ by Eqs. (2-5) or (2-6).

$$R = (0.542 \times E_{max} - 0.133) \times \rho \qquad (0.15\text{MeV} < E_{max} < 0.8\text{MeV}) \quad (2-5)$$

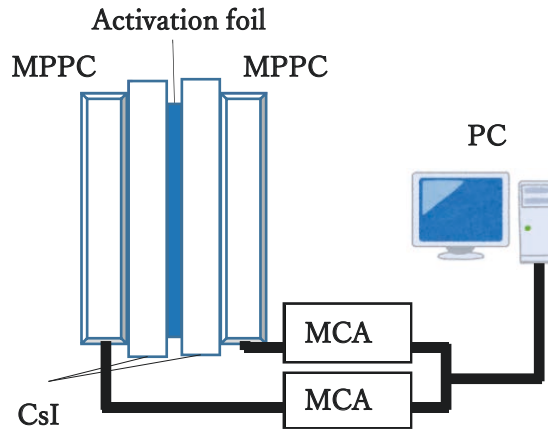$$R = 0.407 \times E^{1.38} \qquad\qquad\qquad (0.8\text{MeV} < E_{max}) \qquad (2-6)$$

Fig.1 β-ray measuring system.

First, the number of radionuclide decays in the activation foil during the measurement time, N_m, is determined by Eq. (2-7), where t_m is the detection time after the n-th irradiation.

$$N_m = N_n(1 - e^{-\lambda t_m}) \qquad (2-7)$$

Therefore, the number of counts, C, is obtained by using the number of decayed isotopes N_m, the radiation detection efficiency of the detector G, the radiation emission ratio of the radioisotope r, and the self-shielding factor P as shown in Eq. (2-8).

$$C = N_m G r P \qquad (2-8)$$

For the β-ray emitters, the β-ray emission ratio r is set to 1, and the self-shielding factor is obtained by PHITS[5]. and calculating the fraction of β-rays incident on the CsI crystal from the activation foil. From Eqs. (2-1) to (2-8), the average neutron flux ϕ_{est} over the total irradiation time incident on the foil obtained by Eq. (2-9) using the number of radionuclides N_n at the end of the n-th irradiation. The neutron fluence incident on the target by the activation detector is estimated by multiplying ϕ_{est} by the total irradiation time t_{tot}.

$$\phi_{est} = \frac{\lambda N_n}{N_0 \sigma (1 - e^{-\lambda t_{tot}})} \qquad (2-9)$$

2.2.3　Error evaluation

Since the decay of radionuclides is an accidental phenomenon and follows a Poisson distribution, the statistical error (relative value) e_r is evaluated by Eq. (2-10) using the total count C, calculated with Eq. (2-8). In this study, we neglect the background count for simplicity.

$$e_r = \frac{1}{\sqrt{C}} \qquad (2-10)$$

Next, we consider the systematic error. The produced radionuclide's survival rate L at a small time dt [s] before t [s] from the end of irradiation is obtained by Eq.(2-11).

$$L = e^{-\lambda t} \qquad (2-11)$$

Therefore, the ratio of surviving radionuclides e_s to the total number of produced radionuclides during the entire irradiation period, t_{tot}, is obtained by Eq.(2-12).

$$e_s = \frac{\int_0^{t_{tot}} L\, dt}{t_{tot}} \qquad (2-12)$$

this is regarded as the systematic error of the nuclide for the irradiation time of t_{tot} with decay constant λ. By selecting nuclides which have smaller sum of these two errors, e_r and e_s, we can finally determine the best nuclide that retains sufficient information of the irradiation-induced activation during the past period of neutron irradiation time 1 month or 1 year.

3. Result

As a result of the nuclides selection, 33 nuclides producing γ-ray emitters and 15 nuclides producing β-ray emitters were selected. In the selected nuclides, the top three nuclides with the smallest errors for nuclides producing γ-ray and β-ray emitters are shown in Tables 1 and 2, respectively.

Table. 1 Selected top three nuclides producing γ-ray emitters as activation detector.

		Isotopic abundance [%]	Half life [year]	Cross section [b]	Systematic error [%]	Random error [%]	Total error [%]
1 year	$^{159}\text{Tb}(n, 2n)^{158}\text{Tb}$	100	180	1.9	0.19	0.31	0.50
	$^{151}\text{Eu}(n, 2n)^{150}\text{Eu}$	48	36	1.8	0.93	0.37	1.30
	$^{109}\text{Ag}(n, 2n)^{108}\text{Ag}$	48	438	0.72	0.079	1.44	1.52
1 month	$^{103}\text{Rh}(n, 2n')^{102m}\text{Rh}$	100	3.7	0.63	0.76	0.15	0.91
	$^{153}\text{Eu}(n, 2n)^{152}\text{Eu}$	52	14	1.9	0.21	0.82	1.03
	$^{159}\text{Tb}(n, 2n)^{158}\text{Tb}$	100	180	1.9	0.016	1.06	1.08

Table. 2 Selected top three nuclides producing β-ray emitters as activation detector.

		Isotopic abundance [%]	Half life [year]	Cross section [b]	Systematic error [%]	Random error [%]	Total error [%]
1 year	$^{159}\text{Tb}(n, 2n)^{158}\text{Tb}$	100	180	1.9	0.19	1.18	1.37
	$^{63}\text{Cu}(n, p)^{63}\text{Ni}$	69.15	101	0.046	0.34	1.33	1.68
	$^{94}\text{Zr}(n, n\alpha)^{90}\text{Sr}$	17.38	28.8	0.00024	1.19	5.21	6.40
1 month	$^{63}\text{Cu}(n, \alpha)^{60}\text{Co}$	69.15	5.27	0.037	0.54	1.17	1.71
	$^{159}\text{Tb}(n, 2n)^{158}\text{Tb}$	100	180	1.9	0.016	4.06	4.08
	$^{63}\text{Cu}(n, p)^{63}\text{Ni}$	69.15	101	0.046	0.028	4.58	4.61

As shown in Tables 1 and 2, ^{159}Tb and ^{103}Rh were selected as the best nuclides producing γ-ray emitters as the activation detector material for 1 year and 1 month irradiation, respectively. ^{159}Tb and ^{63}Cu

were also selected as the best nuclides producing β-ray emitters for 1 year and 1 month irradiation, respectively.

At present, we are conducting short-term irradiation to validate the accurate cross section at around 14 MeV. In addition, long-term irradiation of several months is being carried out. In the future, this method will be applied to the ITER material irradiation tests that are currently being carried out at OKTAVIAN of Osaka University.

4. Conclusion

In this study, we selected suitable nuclides as activation detectors to be used in an ultra-long term irradiation in order to obtain the total fluence for long-term material integrity test of fusion reactor. We added nuclides producing β-ray emitters as candidate in addition to nuclides producing γ-ray emitters to increase the number of candidates. As a result, ^{103}Rh and ^{159}Tb were selected as the nuclides producing γ-ray emitters and ^{63}Cu and ^{159}Tb were found for nuclides producing β-ray emitters for 1 month and 1 year irradiation, respectively.

We are now measuring the accurate cross sections of ^{103}Rh(n,2n) and ^{159}Tb(n,2n) reactions to normalize at 14 MeV by a short-term irradiation. We are also conducting long-term irradiation tests for 1 year to prove the applicability of these foils as activation detectors in an ultra-long term irradiation experiment. In the future, we will apply the obtained results to irradiation tests of ITER materials at OKTAVIAN of Osaka University.

References

[1] X-5 Monte Carlo Team, MCNP - A General Monte Carlo N-Particle Transport Code, Version 5, LA-UR-03-1987; 2005.

[2] R. B. Firestone, et al., Table of isotope 8th ed.:JOHN WILEY & SONS, INC.;1996.

[3] K. Shibata, et al., JENDL-4.0: A New Library for Nuclear Science and Engineering, J. Nucl. Sci. Technol., 48, 1; 2011.

[4] T. Sato, Y. Iwamoto, S. Hashimoto, et al., Features of particle and heavy ion transport code system (PHITS) version 3.02., J. Nucl. Sci. Technol.; 2018.

27 Semi-empirical nuclear fission yield model for astronomical use based on the four-dimensional Langevin approach

Chikako ISHIZUKA[†1], Taiki KONO[1], Kohsuke TSUBAKIHARA[2], and Satoshi CHIBA[1]

[1]Tokyo Institute of Technology, 2-12-1 Ookayama, Meguro-ku, Tokyo 152-8550, Japan
[2]National Institute of Technology, Asahikawa College, Shunkodai 2-2-1-6, Asahikawa-shi, Hokkaido, 071-8142, Japan
[†]Email: ishizuka.c.aa@m.titech.ac.jp

Abstract

Nuclear fission plays an essential role in nuclear reactors and the r-process nucleosynthesis, producing heavy elements like gold and uranium via the fission recycling process. Fission fragments of superheavy nuclei can be the seed nuclei of the r-process. However, there has been considerable ambiguity among theoretical predictions for the fission yields of superheavy nuclei. For a more precise evaluation of the fission contribution to the r-process, we have developed a semi-empirical fission yield model by fitting the results of our four-dimensional Langevin model with four or five Gaussians. Our Langevin model can very well reproduce both fission fragment mass distributions and total kinetic energy. We performed the Langevin calculations nuclei with Z=92- 122 from neutron-deficient side to neutron-rich side. In our semi-empirical model, we provide a fission fragment mass-charge distribution Y(Z, A) with the combination of the five Gaussians Y(A) described above and normalized Gaussian distribution for Y(Z) on each mass(A) evaluated by the abundant experimental data of actinides. The main focus of this manuscript is to show the parameter study of the four or five Gaussians fitted by the Langevin calculations.

1   Introduction

Fission recycling in the r-process is the idea that the fission products of a superheavy nucleus become seed nuclei in the coming r-process. That idea, which was proposed for the first time in 1957 [1], has attracted attention in this field. Significantly, the number of related studies increased as the experimental data became abundant in a couple of decades. However, nuclear fission of a highly neutron-rich superheavy nucleus is very model-dependent and hard to obtain experimental data. That is why we need a more precise model that can better predict the nuclear fission products to understand the r-process. Prediction of nuclear fission products has been challenging even in actinides where we can experimentally access them. For example, fermium and thorium isotopes favour different fission fragment masses. Moreover, quite recently, Nishio et al. found that the fission product mass yield of ^{258}Md shows a pretty other excitation energy dependence than expected. Thus fission fragment mass distributions depend on the proton/neutron number of a fissioning nucleus and its excitation energy.

Our previous study with the three-dimensional Langevin model and semi-empirical fission product yield based on thousands of experimental data [2] found that our fission fragment mass and charge distributions are broader than the well-known Kodama-Takahashi model [3]. It also
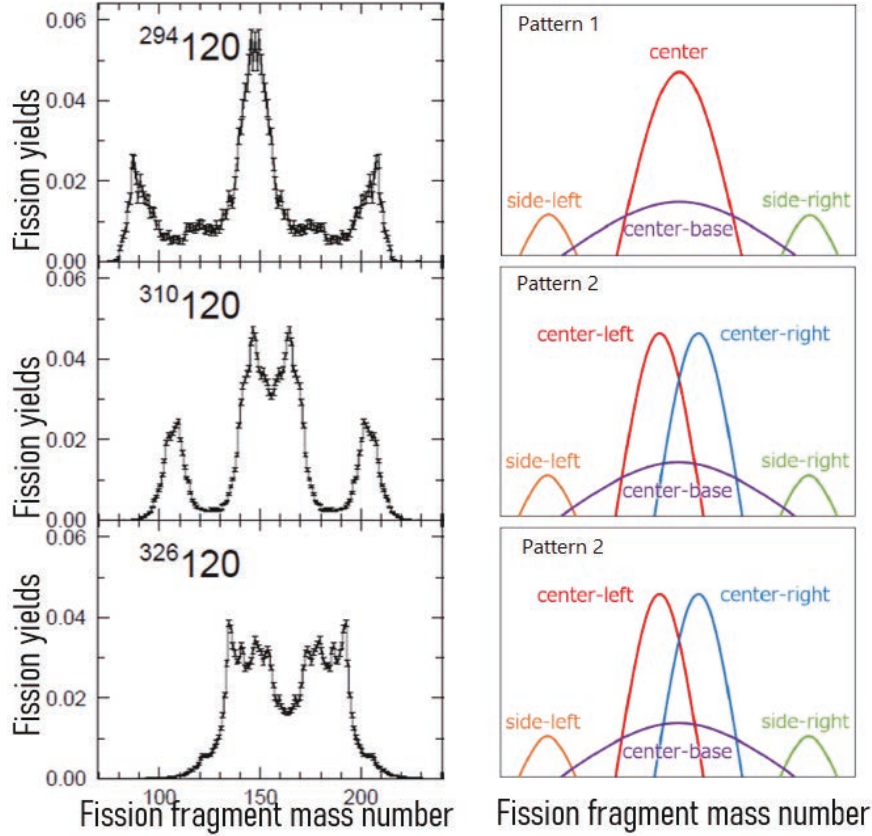
Figure 1: Fission fragment mass yields obtained by the 4D-Langevin model [4] (left panels) and Gaussian fitting patterns (right panels) corresponding to these yields.

suggested that the difference between them appears in the r-process 2nd peak and rare-earth elements in the case of Black Hole Neutron Star (BH-NS) mergers. Based on the previous results [2], we have developed a more precise fission model with the four-dimensional Langevin model [4], which can reproduce fission fragment mass yields and total kinetic energies of more various nuclides than the three-dimensional case. This paper briefly introduces our model and focuses on the systematics in the model parameters.

2 Semi-empirical Nuclear Fission Yield model based on Four-dimensional Langevin Approach

To develop a new yield model, we performed four-dimensional (4D) Langevin calculations [4] for hundreds of nuclei with the proton number $Z = 92\text{-}122$ covering neutron-deficient side to neutron-rich side. In the 4D Langevin model, a fissioning nucleus is expressed by four variables:

- Elongation of a nucleus

- Two independent deformations of left and right parts of a nucleus

- Mass asymmetry of the left and right parts.

For more details of the 4D-Langevin model used here, see our previous work. Then we fitted obtained fission fragment mass yield $Y(A)$ before prompt neutron emission by superposition of

our or five Gaussian functions. We adopted our semi-empirical formula [5] in Equation (1) to provide an independent yield $Y(A, Z)$.

$$
\begin{aligned}
Y(Z, A) \quad &\propto \quad \exp\left[-\frac{E_{LD}(Z, A) + \Phi(E^*)\Delta E_{sh}(Z, A)}{T(Z, A)}\right] \\
&\simeq \quad Y(A)\frac{1}{\sqrt{2\pi}\sigma(A)}\int_{0.5}^{0.5}\exp\left[-\frac{(Z - Z_p(A) + t)^2}{2\sigma(A)^2}\right]dt \times \exp\left[-\frac{\Delta E_{sh}(Z, A)}{E_d(A)}\right] \, , \ (1)
\end{aligned}
$$

where $\sigma(A) \approx 0.5$ and $E_d(A) \approx 5 - 10\text{MeV}$. For the shell correction energy ΔE_{sh}, we adopt the KTUY [6]. Detailed parameter values can be found in our previous work [5].

The Y(A)s obtained from the 4D-Langevin calculations can be categorized into two patterns, pattern (1) or (2). In pattern (1), we can fit Y(A) with four Gaussians as centre-based, centre, side-left, and side-right. In pattern (2), Y(A) shows four peak structures and is fitted with five Gaussians: centre-based, centre-left, centre-right, side-left, and side-right.

Figure 1 shows the sample results of the 4D-Langevin calculations and corresponding fitting pattern using four or five Gaussians. Left panels are fission fragment mass distributions of $^{294,310,326}120$, from top to bottom, respectively. Right panels are Gaussian fitting patterns. Two nuclei in Figure 1, $^{310}120$ and $^{326}120$, can be fitted by five Gaussians, while we need only four Gaussians to fit Y(A) of $^{294}120$ as shown in the top panel. Thus we fitted the Langevin results by Gaussians and made a present model Y(A).

3   Parameter Study of the fitted Gaussian functions

We investigated particular systematics among Gaussian parameters for all the Y(A) of hundreds of nuclei with Z=92-122 obtained by the 4D-Langevin model. This section shows the systematics we found. Figure 2 is the case of Og-isotopes. Og-isotope with $N = 164$ has a single peak $Y(A)$, while Og-isotopes with $N = 168, 172, 176$ have three peaks in $Y(A)$. Og-isotopes with $N = 180$ and 184 show a four-peak structure. Following the pattern (1) and (2) in figure 1, those $Y(A)$s can be fitted by four or five Gaussian functions.

In each panel (1) to (6) of Figure 2, Gaussian parameters a, b, c are plotted as a function of neutron numbers consisting of each Og-isotopes. Here, these parameters provide a Gaussian function as $f(x) = a\exp(-(x - b)^2/2c^2)$. We found a strong linear correlation between each Gaussian parameter and the neutron number of the isotopes.

One may notice the relation between the Gaussian centre, parameter b, of (3) side-left and (5) side-left. In panel (5) (heavy fragment peak), the parameter b is almost constant at A=208, while b in panel (3) (light fragment peak) increases with neutron number. Other features of the parameter systematics are the centre position of (1) the centre-based and (2) the centre. These b-parameters are the same and described in a straightforward formula such as $b = 0.5N + 59$. Interestingly, not only the Gaussian centres but also the amplitude and the width of the Gaussian function show clear correlations to the neutron number of the isotopes. We commonly observed such systematics in all nuclei investigated here. We will report these results in detail in our forthcoming paper.

4   Summary

We performed the four-dimensional Langevin calculations for nuclei with $Z = 92\text{-}122$ from neutron-deficient side to neutron-rich side. Then we fitted fission fragment mass distributions $Y(A)$ with four or five Gaussians. The number of the used Gaussian functions depends on the peak structure of fission mass yields derived from the Langevin calculations. Thus we constructed
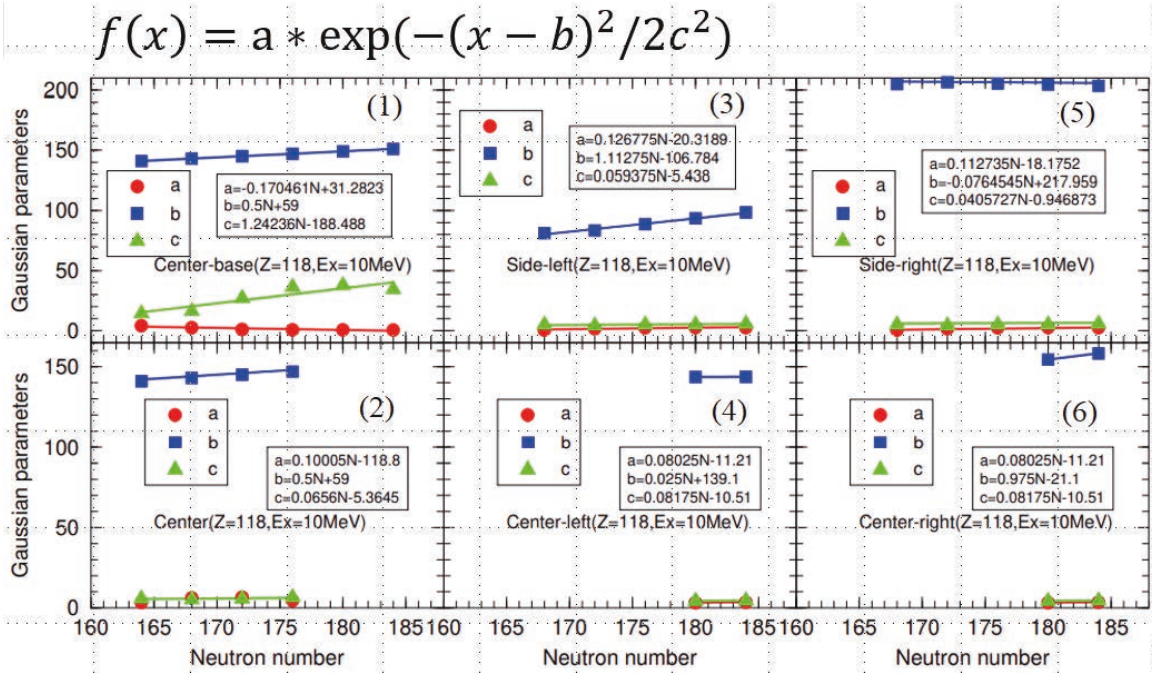
$$f(x) = a * \exp(-(x-b)^2/2c^2)$$

Figure 2: Systematics of Six Gaussian parameters as a function of neutron number in the case of Oganesson isotopes ($Z = 118$) with the excitation energy $E^* = 10$ MeV; (1)center-based, (2)Center, (3)Side-left, (4)Center-left, (5)Side-right, (6)Side-left. Each Gaussian has three paramters a, b, and c.

our $Y(A)$ by the superposition of Gaussians. To develop a semi-empirical independent yield model $Y(Z, A)$, we combined the above $Y(A)$ and the charge distributions $Y(Z)$ evaluated by thousands of experimental fission data of actinides. For our newly developed yield model, we investigated the systematics of each Gaussian parameters. Consequently, we found that each Gaussian parameter had clear systematics with respect to neutron numbers when we fixed the proton number of a fissioning nucleus. We will apply our $Y(Z, A)$ based on the 4D-Langevin model to the r-process calculations during the neutron star mergers and neutron star-black hole mergers shortly.

References

[1] Burbidge, E.M., Burbidge, G.R., Fowler, W.A., and Hoyle, F., Synthesis of the Elements in Stars*, Reviews of Modern Physics, Vol.29, no.4, 1957, pp.547-650.

[2] Ishizuka, C., Tsubakihara, K., Chiba, S., Sekiguchi, Y., and Wanajo, S., Semi-empirical fission model for r-process based on the recent experiments and three-dimensional Langevin approach, Proceedings of The 16th International Symposium on Nuclei in the Cosmos, EPJ Web Conf. vol. 260, no. 3, 2022, 11013.

[3] Kodama, T., Takahashi, K., R-process nucleosynthesis and nuclei far from the region of β-stability, Nucl. Phys. A, vol. 239, 1975, pp.489-510.

[4] Ishizuka, C., Usang, M.D., Ivanyuk, F.A., Maruhn J.A., Nishio, K., Chiba, S., Four-dimensional Langevin approach to low-energy nuclear fission of ^{236}U, Phys. Rev. C, Vol.96, 2017, pp.064616-1-9.

[5] Tsubakihara, K., Okumura, S., Ishizuka, C., Yoshida, T., Minato, F., Chiba, S., Evaluation of fission product yields and associated covariance matrices, J. Nucl. Sci. Tech., Vol.58, 2020, pp.151-165.

[6] Koura, H., Tachibana, T., Uno, M., Yamada, M., Nuclidic Mass Formula on a Spherical Basis with an Improved Even-Odd Term, Prog. Theor. Phys. Vol. 113, 2005, pp.305-325.

Acknowledgments

This is a blank page.

28 Development of a counter telescope for light charged particles emitted from muon capture reaction in Si

Hiroya FUKUDA[1], Shoichiro KAWASE[1#], Yukinobu WATANABE[1], Masaya OISHI[1],
Teppei KAWATA[1], Hiroki NISHIBATA[2], Shintaro GO[*2], Megumi NIIKURA[3],
Daisuke SUZUKI[4], and Seiya MANABE[†1]

[1]Kyushu University, 6-1 Kasuga-koen, Kasuga, Fukuoka, Japan, 816-8580
[2]Kyushu University, 744 Motooka, Nishi, Fukuoka, Fukuoka, Japan, 819-0395
[3]The University of Tokyo, 7-3-1 Hongo, Bunkyo, Tokyo, Japan, 113-8654
[4]RIKEN Nishina Center, 2-1 Hirosawa, Wako, Saitama, Japan, 351-0198
Email: kawase@aees.kyushu-u.ac.jp

Abstract

We are developing a counter telescope to measure the energy spectra of low-energy light charged particles (LCPs), i.e., protons, deuterons, tritons, and alpha particles, emitted from the negative muon capture reaction in a Si nucleus. The telescope is composed of a neutron Transmutation Doped (nTD) Si detector and an n-type Si detector. The nTD-Si detector is suitable for particle identification (PID) using Pulse Shape Analysis (PSA) technique. In order to obtain enough experimental statistics, the nTD-Si detector has to be close to the target in the experiment, which will result in broad angular acceptance of LCPs to the nTD-Si detector. To evaluate the PID performance using PSA for the broad angular acceptance, a detector test was performed to measure the incident angle dependence of the waveform signal from the nTD-Si detector. The PID performance was simulated by a Monte Carlo simulation using the experimental data. The simulated result demonstrated that proton, deuteron, and triton can be well identified even at low energies by using the present PSA technique.

1 Introduction

Soft error is a severe concern for reliability demanding applications, such as autonomous drivings, supercomputers, and public transportations. The soft error occurs by the upset of memory information caused by energy deposition in semiconductor devices, called single event upset (SEU). Recently, the SEU induced by cosmic-ray muons has been increasing attention because the trend of device miniaturization and lower voltage operation degrade the immunity of static RAM (SRAM). Some latest works [1–3] reported that negative muons have higher SEU probability than positive ones because charged particles emitted from the negative muon capture reaction in a Si nucleus result in larger energy deposition in devices than the direct ionization by a muon. In particular, it was pointed out that light charged particles (LCPs) such

---

*Present address: RIKEN Nishina Center, 2-1 Hirosawa, Wako, Saitama, Japan, 351-0198
†Present address: National Institute of Advanced Industrial Science and Technology, 1-1-1, Tsukuba, Ibaraki, Japan, 305-8568

as protons, deuterons, tritons, and alpha particles seriously affect the SEU [1]. However, there are no enough experimental energy spectra of LCPs to accurately estimate the muon SEU rates, especially in the low-energy region.

In this situation, we have planned an experiment to measure the energy spectra of LCPs emitted from the muon capture reaction. In this experiment, the Pulse Shape Analysis [4, 5] (PSA) technique will be adopted for particle identification (PID) of low-energy LCPs instead of the conventional ΔE-E technique. For this purpose, we are developing a counter telescope for PID of LCPs.

In the proposed experiment, the distance between the detector and the target will be placed as close as possible to gain enough counting statistics. Therefore, the angular acceptance of LCPs to the detector becomes large (see Fig. 5), and the detector response may vary with the incident angle. However, there is no report on the PID performance of LCP detection with PSA in the case of such wide angular acceptance. To investigate the incident angle dependence of the waveform signals from the neutron Transmutation Doped (nTD) Si detector, we conducted a detector test. In this article, preliminary results of the detector test and the PID performance simulated by the Monte Carlo simulation based on the experimental data are reported.

2   Experimental method

2.1   Experimental setup

The experiment was performed using the 8 MV tandem accelerator in the Center for Accelerator and Beam Applied Science of Kyushu University. An 11 μm thick ^{27}Al target was irradiated by 24 MeV ^{7}Li ion beam whose intensity was lower than 1 pnA. LCPs produced from the nuclear reaction and scattered ^{7}Li ions were detected by a pair of detector telescopes. Each telescope was composed of three instruments, which are a 7.5 mm in diameter aluminum collimator, a 500 μm thick nTD-Si detector, and a 500 μm thick n-type Si detector. The aluminum collimator was located in front of the nTD-Si detector. The Si detector was installed behind the nTD-Si detector to use as a veto. The nTD-Si detector was operated at a bias voltage of 260 V, which is the best setting for the PID with PSA [6]. The waveform signals from the nTD-Si detector were processed using a charge-sensitive preamplifier. The charge waveform signals were digitized using the digitizer (CAEN V1730SB). In order to measure the incident angle dependence of the waveform signals, the measurements were made for four incident angles (θ) of 0°, 15°, 30°, and 45° by rotating the nTD-Si detector.

2.2   Pulse shape analysis

Figure 1 shows a typical example of the waveform signals. The black line represents the charge waveform signal. The baseline of the charge waveform signal was determined by averaging some samples prior to the rising edge of the signal, and subtracted from each signal. The red line in the figure represents the charge waveform signal processed by the trapezoidal filter [7] with the rise time of 1 μs and the flat top of 1 μs. The energy of LCPs was obtained from the maximum value of the charge waveform signal ($Q_{\max}$), which was calculated by an average of 16 samples on the flat top of the waveform signal processed by the trapezoidal filter. Then the energy calibration was done by

$$E = aQ_{\max} + b, \tag{1}$$

where a and b are the fitting parameters, which were determined by a calibration measurement with standard alpha sources of ^{148}Gd, ^{241}Am, and ^{244}Cm. The energy resolution of the nTD-Si detector was 45 keV in FWHM at the 5763 keV peak of ^{244}Cm.

The blue line in Fig. 1 represents the current waveform signal. The current waveform signal was obtained by the first derivative of the charge waveform signal with a third-order spline interpolation. In this work, PID with PSA was conducted by the two quantities, namely the energy (E) of the LCPs and the maximum value of the current waveform signal ($I_{\max}$).
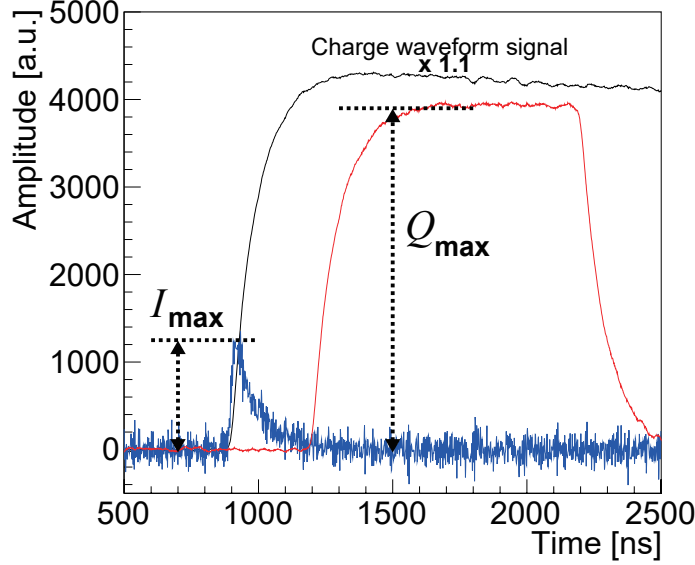

Figure 1: A typical example of waveform signal for alpha particle incidence. The black line is the digitized charge waveform signal. The red line is the charge waveform signal processed by the trapezoidal filter with the rise time of 1 μs and the flat top of 1 μs. The blue line is the current waveform signal obtained by the first derivative of the charge waveform signal.

3 Experimental result and simulation

3.1 Experimental result

A correlation plot of $I_{\max}$ and E at the incident angle of 0° was made. As shown in Fig. 2, the PID was successfully achieved, and hydrogen isotope ions (protons, deuterons, and tritons) and alpha particles were clearly identified above 4 MeV. To investigate the incident angle dependence of the waveform signal from the nTD-Si detector, the $I_{\max}$ for each incident-angle of the hydrogen isotope ions was analyzed. The peak position of the $I_{\max}$ distribution denoted by $\langle I_{\max} \rangle$ was obtained for each energy bin for each incident angle fitted by the Gaussian function. Figure 3 shows the $\langle I_{\max} \rangle$ and the standard deviation of the hydrogen isotope ions for each incident angle at $E = 4$ MeV. It was found that as the incident angle increases, $\langle I_{\max} \rangle$ becomes smaller. To evaluate the observed reduction trend of $\langle I_{\max} \rangle$ for each particle, each $\langle I_{\max} \rangle$ normalized to unity at 0° was fitted by the following quadratic function:

$$r(\theta) = 1 - a_r \theta^2, \tag{2}$$

where a_r is the fitting parameter denoting the strength of the reduction depending on the incident angle. This reduction trend may be caused by a difference in penetration depth depending on the incident angle of charged particles. The detail of the associated physical processes is now under analysis. The parameter a_r depends on the atomic and mass numbers of charged particles and their kinetic energy.
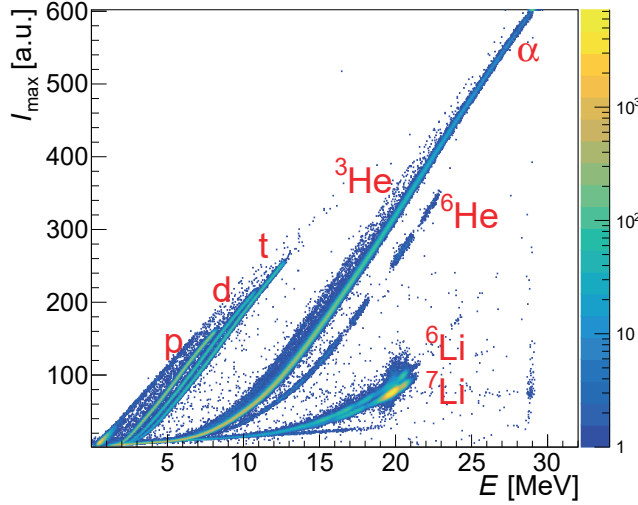
Figure 2: A correlation plot of I_{max} and E at the incident angle of 0°.
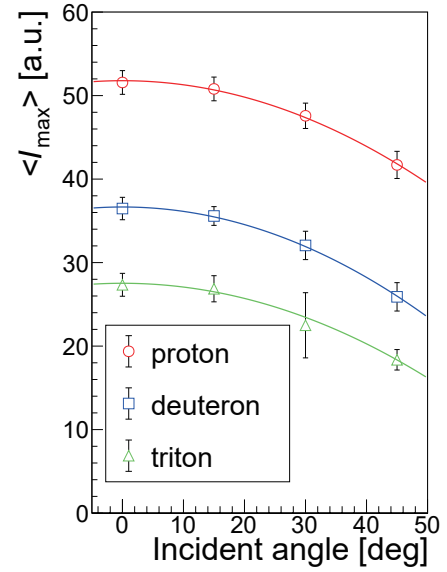

Figure 3: An incident angle reduction of the $r(\theta)$ for protons, deuterons, and tritons at $E = 4$ MeV. The plots and the error bars represent the $\langle I_{max} \rangle$ and $\pm 1\sigma$ derived from the Gaussian fitting, respectively.

3.2   Simulation

We have estimated the PID performance in the proposed experimental setup to measure the energy spectra of LCPs emitted from the muon capture reaction by a simulation based on the results obtained in the present detector test experiment. Figure 4 shows the experimental setup. In this simulation, the distance between the nTD-Si detector and the target was set to 60 mm. The active area of the nTD-Si detector and the size of the target was 20 mm × 20 mm and 50.8 mm in diameter, respectively. A negative muon beam intensity distribution was assumed to be a two-dimensional Gaussian distribution with the standard deviations, $\sigma_x = 15.0$ mm and $\sigma_y = 16.0$ mm.

First, the angular acceptance $(P(\theta))$ of the nTD-Si detector for emitted LCPs was derived using a Monte Carlo simulation. The result is shown in Fig. 5. Then, the I_{max} distribution for each LCP was calculated by a Monte Carlo simulation based on the measured I_{max} distribution at the incident angle of 0° (see Fig. 2), the angle-dependent reduction factor given by Eq. (2), and $P(\theta)$. Figure 6 shows the simulated I_{max} distribution at $E = 4$ MeV (the red line) together with the measured I_{max} distribution at the incident angle of 0° (the blue line). Here, the relative yields of detected protons, deuterons, and tritons were determined from a PHITS simulation of the muon capture reactions in a Si nucleus which was done in Ref. [8].

As shown in Fig. 6, each peak position in the simulated I_{max} distribution is shifted slightly to lower I_{max} and the spreading width increases slightly compared to the measured I_{max} distribution at 0°. The slight shift of each peak position is caused by the reduction of I_{max} corresponding to the weighted average of Eq. (2) with $P(\theta)$. However, the PID of protons, deuterons, and tritons is found to be still clear. This simulation result demonstrates that the PID will be achievable in the proposed nTD-Si detector setup with the broad angular acceptance even at low emission energies. It should be noted that similar results were obtained at other emission energies above 4 MeV.
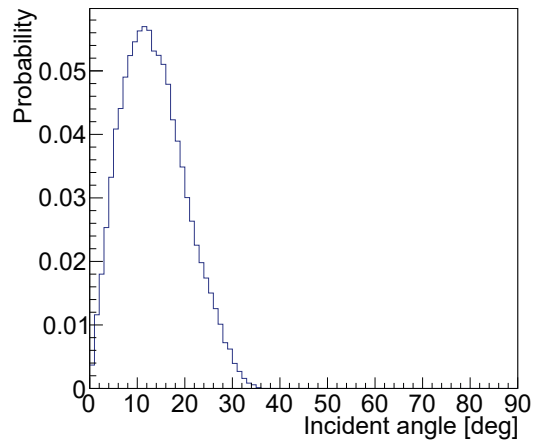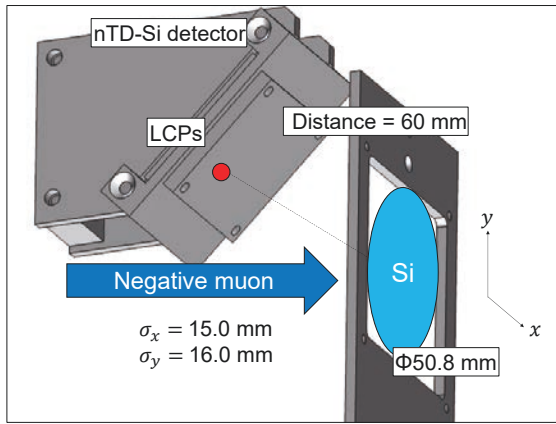
Figure 4: An experimental setup to measure the energy spectra of LCPs emitted from the muon capture reaction.

Figure 5: The simulation result of an angular acceptance of LCPs to the nTD-Si detector.
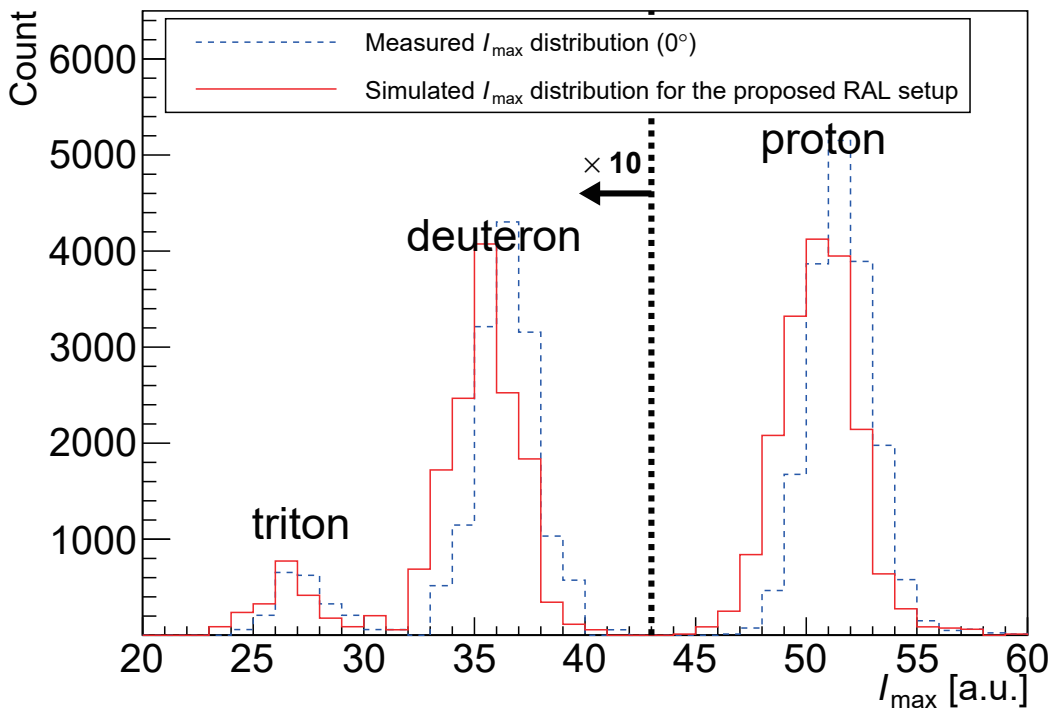

Figure 6: The simulated $I_{\max}$ distribution for proton, deuteron, and triton at $E = 4$ MeV (the red line) and the measured $I_{\max}$ distribution at the incident angle of 0° (the blue line).

4   Summary and future plan

A counter telescope is under development for measurement of the energy spectra of low-energy light charged particles (LCPs) emitted from the negative muon capture reaction in a Si

nucleus. The counter telescope consists of a nTD Si detector which is suitable for PID using PSA technique. In order to investigate the incident-angle dependence of the waveform signals from the nTD-Si detector, we conducted a detector test at Kyushu University. The results show that the larger the incident angle, the smaller the $I_{\max}$. Moreover, the reduction trend of $I_{\max}$ depends on the atomic and mass numbers of charged particles and their kinetic energy. Based on the results of the detector test, the PID performance with PSA for the finite angular acceptance assumed in the proposed experiment of the muon capture reaction was simulated using a Monte Carlo simulation. The result indicates that the PID for protons, deuterons, and tritons by PSA will be clearly achieved in the experimental setup with the broad angular acceptance even at low emission energies.

In the future, we will complete the counter telescope development and measure the energy spectra of LCPs emitted from the muon capture reaction. Further work will be devoted to understanding of the observed incident angle dependence of $I_{\max}$ on the basis of physical processes in the nTD-Si detector.

Acknowledgment

References

[1] S. Manabe et al., Negative and Positive Muon-Induced Single Event Upsets in 65-nm UTBB SOI SRAMs, IEEE Trans. Nucl. Sci., 65:8, 1742-1749 (2018).

[2] W. Liao et al., Measurement and Mechanism Investigation of Negative and Positive Muon-Induced Upsets in 65-nm Bulk SRAMs, IEEE Trans. Nucl. Sci., 65:8, 1734-1741 (2018).

[3] T. Kato et al., Muon-Induced Single-Event Upsets in 20-nm SRAMs: Comparative Characterization With Neutrons and Alpha Particles, IEEE Trans. Nucl. Sci., 68:7, 1436-1444 (2021).

[4] J. A. Dueñas et al., Identification of light particles by means of pulse shape analysis with silicon detector at low energy, Nucl. Inst. Methods Phys. Res., Sect. A, 676, 70-73 (2012).

[5] K. Mahata et al., Particle identification using digital pulse shape discrimination in a nTD silicon detector with a 1 GHz sampling digitizer, Nucl. Inst. Methods Phys. Res., Sect. A, 894, 20-24 (2018).

[6] T. Murota, Development of a charged particle measurement system capable of identifying particles by waveform analysis using a nTD-Si detector, Master dissertation, Kyushu University (2021) (in Japanese).

[7] V. T. Jordanov et al., Digital techniques for real-time pulse shaping in radiation measurements, Nucl. Inst. Methods Phys. Res., Sect. A, 353, 261-264 (1994).

[8] S. Manabe, Study of Muon-Induced Single Event Upsets in SRAMs and Its Fundamental Physical Process, Doctoral dissertation, Kyushu University (2021).

29 Study on JQMD and INCL models for α particle incident neutron production

Kenta SUGIHARA[†1,2], Nobuhiro SHIGYO[1,2], Eunji LEE[*2], Toshiya SANAMI[1,3,4], and Kanenobu TANAKA[1]

[1]RIKEN Nishina Center, RIKEN, 2-1 Hirosawa, Wako, Saitama 351-0198, Japan
[2]Department of Applied Quantum Physics and Nuclear Engineering, Kyushu University, Motooka, Nishi-ku, Fukuoka 819-0395, Japan
[3]High Energy Accelerator Research Organization (KEK), Oho, Tsukuba, Ibaraki 305-0801, Japan
[4]The Graduate University for Advanced Studies (SOKENDAI), Hayama, Kanagawa 240-0193, Japan
[†]Email: kenta.sugihara@riken.jp

Abstract

An experiment of neutron production thick target yields from 7.2 MeV/u α incidence on ^{209}Bi was performed. The measured data was compared with both Liége IntraNuclear Cascade (INCL) and JAERI Quantum Molecular Dynamics (JQMD) models. The comparison suggested that INCL agreed with the measured data better than JQMD. We investigated the reason that the prediction ability of both models came from. As a result of the study, the prediction ability of the INCL model seemed to be originated from the process of "Local E procedure". For the JQMD calculation, the modification of the mean-field approximation could be a key to improve the prediction capacity.

1 Introduction

Targeted alpha therapy using short lived α-emitters (e.g. ^{225}Ac, ^{223}Ra and ^{227}Th)[1, 2, 3, 4] has recently been performed. Astatine-211 is regarded as a promising isotope for the therapy. In RIKEN, a new beam line for generating Astatine-211 is being constructed. Astatine-211 is produced via the ^{209}Bi$(\alpha\ 2n)^{211}$At reaction at the beam line. The energy of incident α beam is 7.2 MeV/u in order to avoid producing ^{210}Po, a toxic nucleus[5]. The α beam intensity is 100 pμA, which is the highest in the world. For the precise radiation shielding of the new beam line, the measured data for neutron yields are required. Thus, the neutron production thick target yields (TTY) for the reaction of α beam incident on ^{209}Bi was measured[6]. The measured data was compared with both the Liége IntraNuclear Cascade[7] (INCL) and the JAERI Quantum Molecular Dynamics[8] (JQMD) models followed by the Generalized Evaporation Model[9] implemented in Particle and Heavy Ion Transport code System[10] (PHITS). Through the comparison, it is found that INCL reproduces the measured neutron production TTY better than JQMD. The purpose of this study is to explore the reasons of the descrepancy for the two models' prediction ability and the possibilities for improvement of the nuclear reaction models by focusing on the reaction of 7.2 MeV/u α beam incident on ^{209}Bi.

---

[*]Present address: Department of Nuclear Engineering, North Carolina State University, 121 Peele Hall, Campus Box 7103, Raleigh, NC, 27695 U.S.A.

2 Comparison between experimental data and calculation

Comparison of the measured neutron yields and calculation results by INCL and JQMD for the reaction of 7.2 MeV/u α beam incident on ^{209}Bi is shown in Figure 1. This figure shows that INCL agrees with experimental data better than JQMD.

Figure 2 shows the ratios of the calculation results to experimental data (C/E) for each angle above 4 MeV. For 0°, INCL and JQMD underestimate the measured result by approximately 20 % and 80 %, respectively. For 45°, underestimation by approximately 30 % and 70 % are observed for INCL and JQMD, respectively. For 90°, INCL / Exp. and JQMD / Exp. are roughly to be 1.2 and 1.0, respectively.

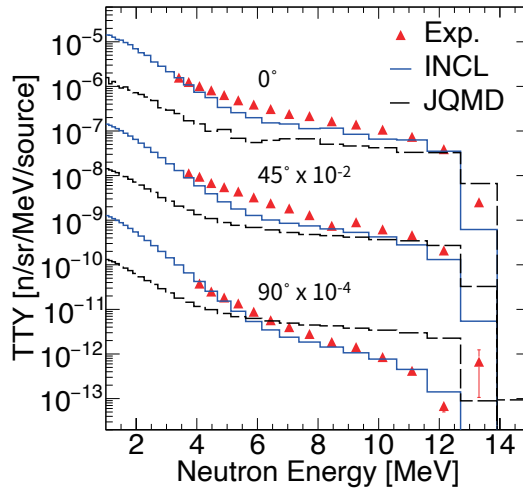Studies for each nuclear reaction model are carried out in following sections.

Figure 1: Comparison of the measured data and calculation results by INCL and JQMD. Triangle, blue solid line, and black dotted line represent the experimental data, INCL results, and JQMD one, respectively.
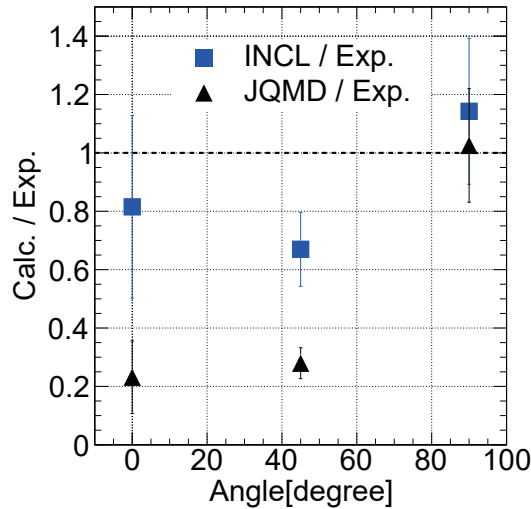

Figure 2: Ratios of the calculation results to experimental data (C/E) for each angle above 4 MeV. Blue rectangular and black triangle represent the INCL and JQMD result, respectively.

3   Liége IntraNuclear Cascade

According to Figures 1 and 2, INCL reproduces the measured neutron production TTY better than JQMD. In this section, the study for the INCL model is given.

Because the incident energy of this reaction is below 10 MeV/u, the nucleons in the beam particle have collisions with the nucleons near the surface of the target nucleus. In the INCL calculation, a target nucleus is prepared by the square-well potential, the depth of which is 45 MeV. Near the surface of the nucleus, the depth of the square-well potential is greater than that of the Woods-Saxon (WS) potential. This means that nucleons with higher energies than the WS potential can stay in the square-well potential. In other words, the overestimation of the energies of the nucleons near the target surface is possible. This causes the underestimation of the nucleon-nucleon (NN) reaction cross section.

The modification of the nucleon energies of the target nucleus is implemented in recent versions of INCL. When the NN reaction is occurred, the nucleons' energies of the target nucleus are recalculated under the approximation of the phenomenological potential. This process is called "Local E procedure (LocE)".

The influence of LocE was examined as shown in Figure 3. Above 6 MeV, neutron production TTY of INCL with LocE is apparently greater than that of INCL without LocE. The TTYs are tabulated at the energy bin from 9.67 MeV to 10.6 MeV in Table 1. For $0°$, the result of INCL with LocE becomes about 4 times larger than that of INCL without LocE. For $45°$ and $90°$, the increase by approximately one order of magnitude for INCL with LocE from INCL without LocE is observed. It is clearly demonstrated that LocE benefits INCL to improve the prediction ability for the reaction of 7.2 MeV/u α beam incident on ^{209}Bi.
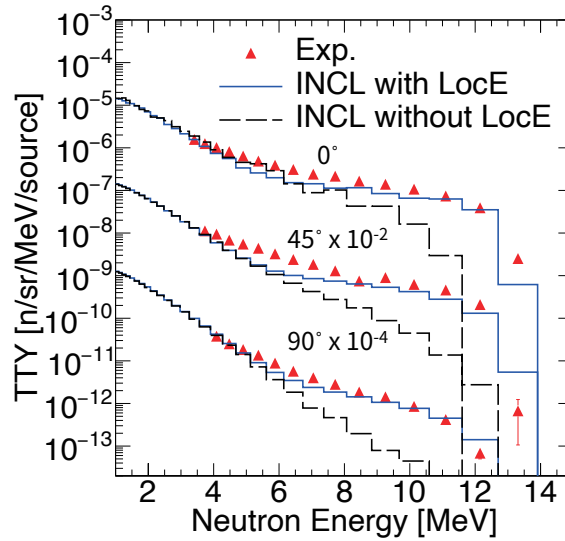

Figure 3: Comparison of the measured neutron production TTY and calculation results by INCL with LocE and INCL without LocE. Triangle, blue solid line, and black dotted line represents the experimental data, INCL with LocE results, and INCL without LocE ones, respectively.

Table 1: Comparison of the neutron yields by INCL with and without LocE in Figure 3.

	$0°$	$45°$	$90°$
INCL with LocE [n/sr/MeV/source]	6.57×10^{-8}	4.22×10^{-8}	7.69×10^{-9}
INCL without LocE [n/sr/MeV/source]	1.62×10^{-8}	4.47×10^{-9}	4.46×10^{-10}

4 JAERI Quantum Molecular Dynamics

According to Figures 1 and 2, JQMD agrees with the measured neutron yields less than INCL. In this section, the study for the JQMD model is introduced.

In the JQMD calculation, nuclei are described based on the Fermi gas model. In the model, the depth of the nuclear force potential (V_{skyrme}) and the Fermi energy (E_F) should be the same. We checked those values for α and ^{209}Bi calculated in JQMD as shown in Table 2. For the ^{209}Bi target, V_{skyrme} equals to E_F. On the other hand, the condition is not satisfied for the α nucleus because the mean-field approximation is not suitable. It is suggested that nucleons with lower energies than E_F for the α nucleus is only bound below V_{skyrme}.

Table 2: Depth of the nuclear force potential and the Fermi energy for α and ^{209}Bi calculated in JQMD.

	V_{skyrme} [MeV]	E_F [MeV]
α	7.8	10
^{209}Bi	31	31

Therefore, the energy distribution for the nucleons of the α and ^{209}Bi nuclei prepared in JQMD is retrieved as given in Figure 4. In the JQMD calculation, the density distribution of nucleons is determined by overlap of nucleons. In other words, each nucleon has each density. Thus, every nucleon has different E_F. In Figure 4, maximum and minimum E_F is depicted as denoted by two red circles. When it comes to the Fermi gas model, the average nucleons' energy should be $0.6 \times E_F$. As shown in the Figure 4, the pink and blue lines are almost same for the ^{209}Bi nucleus. On the other hand, the requirement is not met for α. This means that the initial condition for the nucleons of α is not described properly.

It is concluded that one of the reasons that JQMD cannot reproduce the measured neutron yields for the reaction of 7.2 MeV/u α beam incident on ^{209}Bi is attributed to the fact that the description of the initial condition is inadequate.
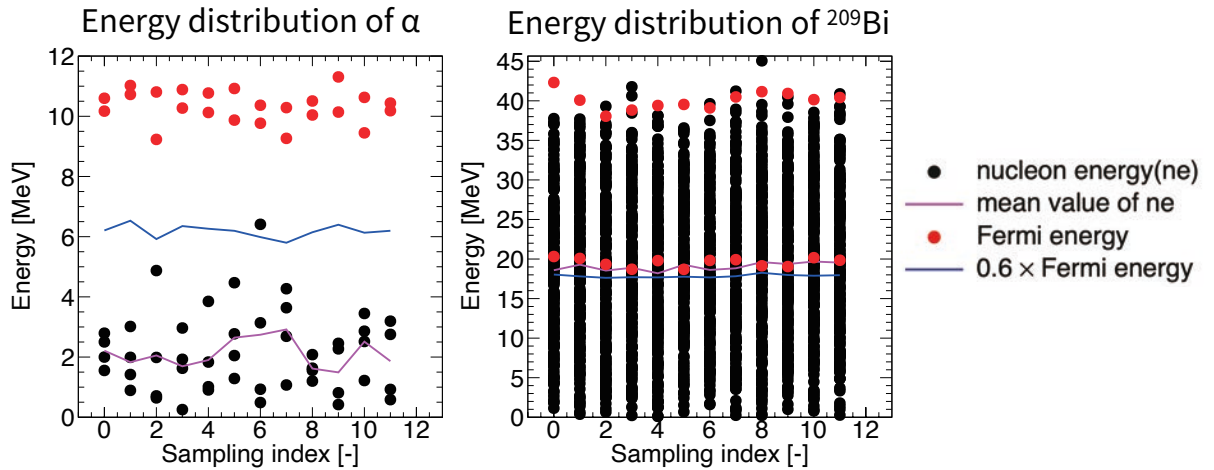

Figure 4: Energy distribution for the nucleons of the α and ^{209}Bi nucleus. Horizontal and vertical axis represents the index that succeeded in creating the initial state of the nucleus and the energy [MeV], respectively. Black and red circle is nucleons' energy and the E_F, respectively. Pink and blue line means the average energy of nucleons derived from the theory and the average nucleons' energy in JQMD, respectively.

5   Conclusion

The measured neutron production TTY for the reaction of 7.2 MeV/u α beam incident on ^{209}Bi was compared with the JQMD and INCL calculations. The comparison shows that INCL reproduces the measured data better than JQMD. The reason was discussed.

For the INCL model, the nucleons energy is recalculated under the approximation of the phenomenological potential. Due to the process, the NN reaction cross section is expressed properly. Due to the comparison between INCL with and without LocE, it is concluded that LocE is greatly influenced to the prediction ability of INCL.

For the JQMD model, it is found that the initial energy condition for α is not described accurately. It is suggested that the modification of nucleons' energies could be one of the idea to improve the prediction ability of the JQMD.

References

[1] Dekempeneer, Y., *et al.*, Targeted alpha therapy using short-lived alpha-particles and the promise of nanobodies as targeting vehicle, Expert Opin. on Biol. Thera. 16 (2016), pp. 1035-1047.

[2] Fujiki, K., *et al.*, ^{211}At-labeld immunoconjugate via a one-pot three-component double click strategy: practical access to α-emission cancer radiotherapeutics, Chem. Sci. 10 (2019), pp. 1936-1944.

[3] Captain, I., *et al.*, Engineered Recongnition of Tetravalent Zirconium and Thorium by Chelator-Protein Systems: Toward Flexible Radiotherapy and Imaging Platforms, Inorg. Chem. 55 (2016), pp. 11930-11936.

[4] Thiele, N. A., *et al.*, An Eighteen-Membered Macrocyclic Ligand for Actinium-225 Targeted Alpha Therapy, Angew. Chem. Int. Ed., 56 (2017), pp. 14712-14717.

[5] Hermanne, A., *et al.*, Experimental study of the cross-sections of α-particle induced reactions on ^{209}Bi, Appl. Radiat. Isotope 63 (2005), pp. 1-5.

[6] Sugihara, K., *et al.*, Measurement of thick target neutron yields from 7 MeV/u α incidence on ^{209}Bi, Nucl. Instrum. Meth. B 470 (2020), pp. 15-20.

[7] Boudard, A., *et al.*, New potentialities of the Liège intranuclear cascade model for reactions induced by nucleons and light charged particles, Phys. Rev. C 87, (2013), 014606.

[8] Niita, K., *et al.*, Analysis of the (N, xN') reactions by quantum molecular dynamics plus statistical decay model, Phys. Rev. C 52, 2620 (1995), pp. 2620-2635.

[9] Furihata, S., Statistical analysis of light fragment production from medium energy proton-induced reactions, Nucl. Instrum. Meth. B 171 (2000), pp. 251-258.

[10] Sato T., *et al.* Features of Particle and Heavy Ion Transport code System (PHITS) version 3.02. J. Nucl. Sci. Technol. 55 (2018), pp. 684-690.

This is a blank page.

30　Theoretical Evaluation of Neutron Thermal Scattering Laws of Heavy Water for JENDL-5

Akira ICHIHARA[1], Yutaka ABE[2]

[1]Nuclear Data Center, Japan Atomic Energy Agency, Tokai-mura, Naka-gun, Ibaraki-ken, 319-1195, Japan

[2]Department of Nuclear Engineering, Kyoto University, Kyotodaigaku-Katsura, Nishikyo-ku, Kyoto,

615-8540, Japan

e-mail: ichihara.akira@jaea.go.jp

Neutron thermal scattering law data were computed for the heavy water molecule toward the fifth version of the Japanese Evaluated Nuclear Data Library, JENDL-5. The scattering laws for deuterium and oxygen atoms were evaluated using the molecular dynamics simulation. The simulations have been performed in the temperature range from 283.6 K to 600 K, and the scattering law data were evaluated in the neutron incident energies between 0.01 meV to 10 eV. We confirmed that experimental cross sections at room temperature were well reproduced with the scattering laws. In the neutron energy above 1 meV, the total cross sections were almost consistent with the ENDF/B-VIII.0 evaluations.

1. Introduction

Heavy water is being used as a moderator in fission reactors. Therefore, reliable information of thermal neutron scattering by heavy water is fundamental to the analysis of reactor cores and the verification of nuclear criticality safety. In this study we attempted to evaluate thermal scattering law (TSL) data of heavy water theoretically, where the thermal neutron is characterized as a neutron with kinetic energy around 25 meV. In recent years, TSLs for light and heavy water have been evaluated using the molecular dynamics (MD) simulations [1,2]. To obtain TSLs, we also employed MD simulations [3]. From TSLs, the angle-energy double-differential cross section for neutron scattering can be derived. We checked the validity of the obtained TSLs by comparing with the experimental cross sections and the ENDF/B-VIII.0 [4] evaluations.

In this report, theoretical models of TSL and simulation conditions of MD are mentioned. Some results of the MD simulations which serve as the input of the TSL evaluation are shown. The cross sections derived from TSLs are compared with the measured data at 20ºC and the ENDF/B-VIII.0 evaluations (the ENDF/B-VIII.0 evaluations have been adopted in JEFF-3.3 [5]).

2. Theoretical Models

The angle-energy double-differential cross section for neutron scattering by a heavy water molecule is given by the sum of double-differential cross sections for two deuterium (D) and one oxygen (O) atoms. The atomic cross section is represented with TSL (it is also known as the scattering function) multiplied by a normalization factor (bound scattering cross section divided by 4π) and the factor $\sqrt{E'/E}$, where E is the neutron incident energy and E' is the neutron emission energy. [6,7]

The neutron scattering by D consists of incoherent and coherent scattering components, while the neutron scattering by O is entirely coherent. In this study, TSL for incoherent scattering has been derived from the self-intermediate scattering function (SISF) represented with the Gaussian approximation form [1,6]. SISF of each atom was evaluated with the atomic frequency distribution function obtained from the MD simulation. On the other hand, in the coherent scattering, the Sköld approximation was applied, as the same with the ENDF/B-VIII.0 evaluation by Damián et al. [2,8] The coherent TSL was evaluated with the incoherent TSL altered by introducing the effective target mass, and the atomic structure factor obtained from the MD simulation. The coherent TSL was given by the product of the modified incoherent TSL and the structure factor.

3. MD Simulation

The MD simulations have been performed with the GROMACS code [9,10] on the software Winmostar [11].

In GROMACS the TIP4P/2005f [12] water model was applied. The Newton's equations of motion were integrated by the leap-frog algorithm with the time step of 0.1 fs. The Nosé-Hoover thermostat was employed with the time constant of 1 ps for temperature coupling. The Parrinello-Rahman barostat was applied with the time constant of 1 ps and the compressibility of 4.5×10^{-5} bar^{-1}, for pressure coupling. We carried out the MD simulations for 14 temperatures. The temperature and the reference pressure were (283.6 K, 1 bar), (293.6 K, 1 bar), (325 K, 1 bar), (350 K, 1 bar), (375 K, 2 bar), (400 K, 10 bar), (425 K, 50 bar), (450 K, 50 bar), (475 K, 50 bar), (500 K, 90 bar), (525 K, 90 bar), (550 K, 90 bar), (575 K, 100 bar), and (600 K, 150 bar), respectively. For the temperature higher than 350 K, the pressure was set to be larger than the saturated vapor pressure.

To obtain the frequency distribution functions, 343 molecules were employed in the simulation and the Newton's equations of motion were integrated up to 421 ps. The trajectory data were recorded at each 0.2 fs time step, and the frequency distribution functions were evaluated using the recorded velocity vectors. Also, to obtain the structure factors, 2197 molecules were employed and the Newton's equations of motion were integrated up to 10 ps. The trajectory data were recorded at each 0.5 fs time step, and the structure factors were evaluated with the recorded position vectors.
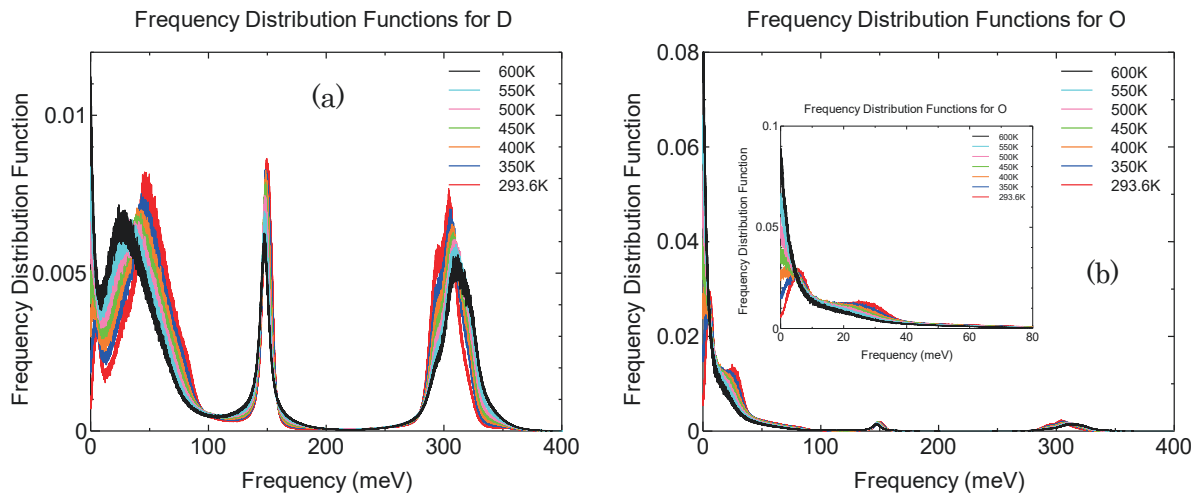
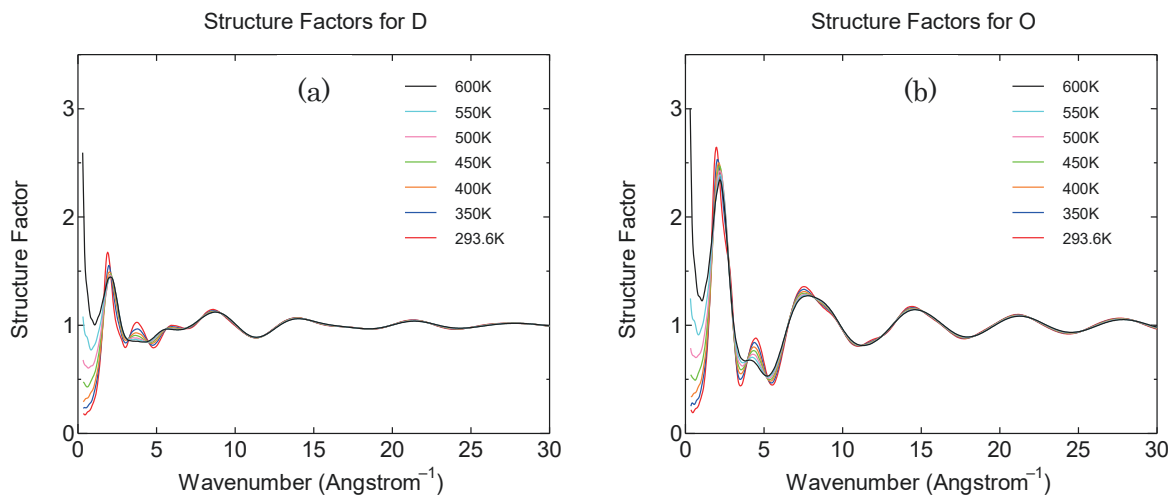Fig.1. Frequency distribution functions for D (a) and O (b).

Fig.2. Structure factors for D (a) and O (b).

4. Results and Discussion

Figure 1 shows the frequency distribution functions for D (a) and O (b). It is seen that the distribution functions change gradually as the temperature increases, for both atoms. In the low frequency region below 5 meV, the distribution function increases as the temperature increases. The peeks appearing at frequencies above 100 meV correspond to the vibrational motion.

Figure 2 indicates the structure factors for D (a) and O (b). In Fig.2 the structure factor increases as the temperature increases in the wavenumber region below 2 Å^{-1}. The temperature dependence is significant only for the wavenumber less than 5 Å^{-1}.
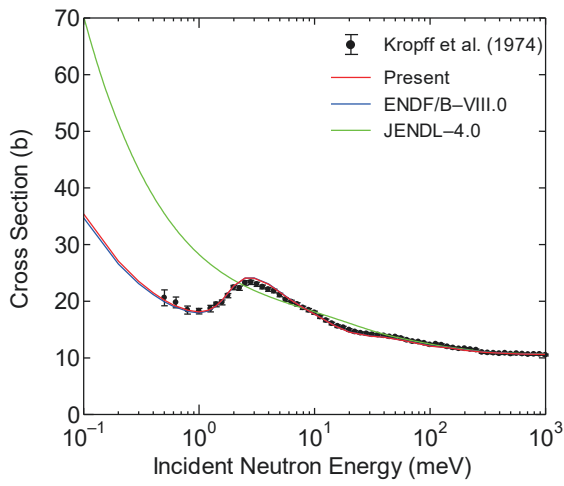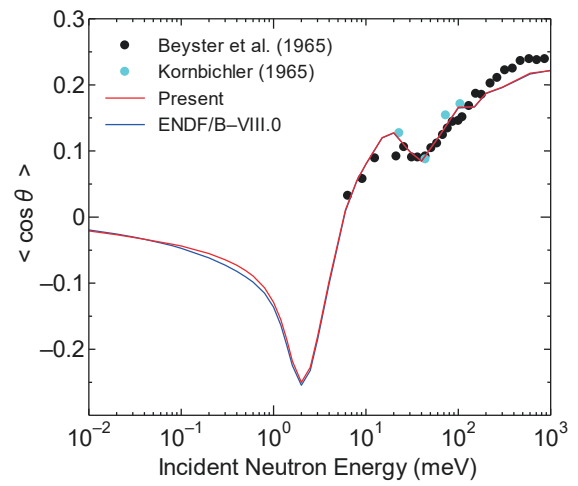
Fig.3. Total cross section at room temperature.

Fig.4. Average cosine of scattering angle at room temperature.
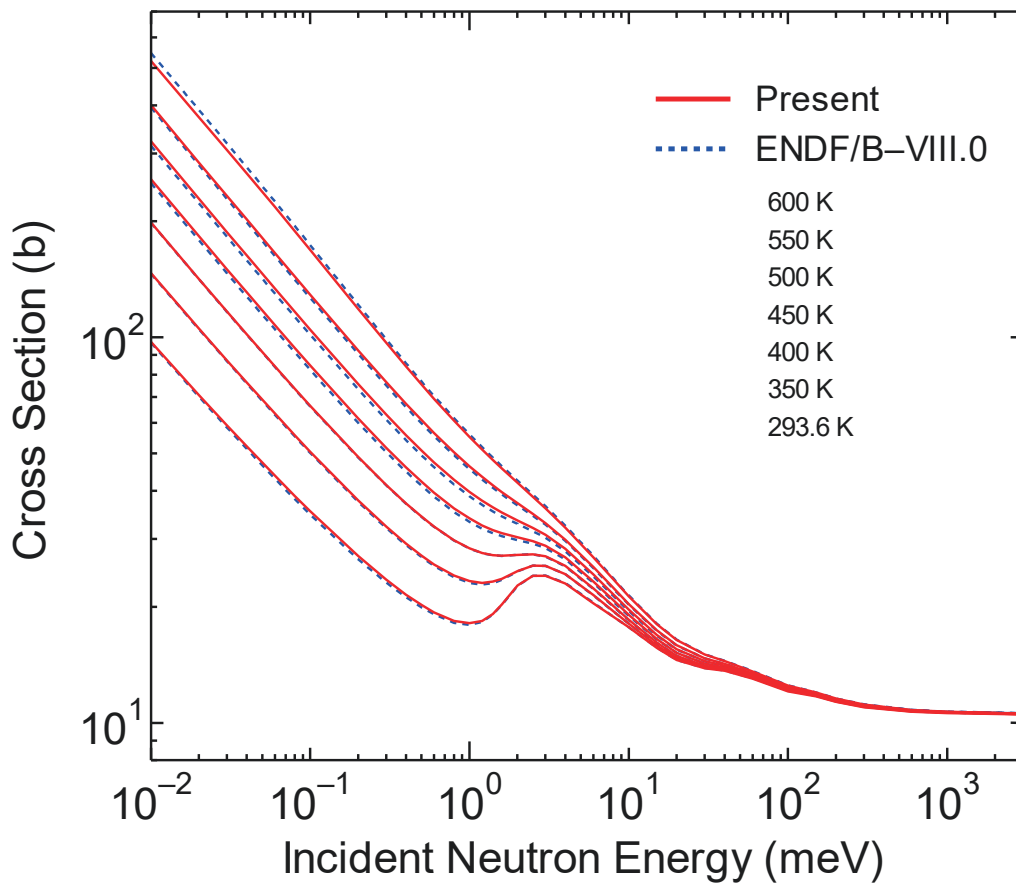

Fig.5. Total cross sections for D_2O from 293.6 K to 600 K. The cross section for 293.6 K appears at the bottom of the figure, and the cross section increases with the increase of temperature.

Figure 3 shows the total cross section for D_2O at room temperature, where Kropff et al. measured the cross sections at 20ºC [13]. In Fig.3 the evaluated cross sections for ENDF/B-VIII.0 and JENDL-4.0 [14] are also indicated. The present result almost overlaps the ENDF/B-VIII.0 evaluation. Both the ENDF/B-VIII.0 and the present evaluations are in good agreement with the experimental data. The bump appearing around 3 meV has been reproduced by considering the coherent scattering. In JENDL-4.0, the ENDF/B-VI.8 evaluation [2,15] based on the incoherent approximation, was adopted. The JENDL-4.0 evaluation overestimates the cross section for the neutron energy below 2 meV.

Figure 4 shows the average cosine of the neutron scattering angle at room temperature. The experimental data [16,17] were obtained from Fig. 17 of [2] using WebPlotDigitizer [18]. Both the ENDF/B-VIII.0 and the present curves have a similar energy dependence, which accord with the experimental data.

Finally, Fig. 5 shows the total cross sections in the temperature range from 293.6 K to 600 K. For the neutron energy smaller than 1 meV, the cross section increases as the temperature increases. The temperature dependence becomes small with the increase of the neutron energy. For the neutron energy larger than 10 meV, the difference is less than 20 % between 293.6 K and 600 K. At the neutron energy above 1 eV, the cross section converges to the sum of the free atom cross sections of 10.5 b [19]. It is seen that the present results are almost consistent with the ENDF/B-VIII.0 evaluations.

5. Summary

TSLs were calculated for heavy water using the MD simulation. The Sköld approximation was applied to consider the coherent scattering. We derived the cross sections from the obtained TSLs, and compared them with the experimental data and the ENDF/B-VIII.0 and JENDL-4.0 evaluations. We confirmed that the measured cross sections at room temperature were well reproduced by the present calculation. The total cross sections were almost consistent with the ENDF/B-VIII.0 evaluations. We published the present TSLs in the ENDF-6 format file in JENDL-5.

Acknowledgement

References

[1] Abe, Y. et al., Evaluation of the neutron scattering cross-section for light water by molecular dynamics, Nucl. Instrum. Methods. Phys. Res. A, vol. 735, 2014, pp. 568-573.

[2] Damián, J.I.M. et al., CAB models for water: a new evaluation of the thermal neutron scattering laws for light and heavy water in ENDF-6 format, Ann. Nucl. Energy, vol. 65, 2014, pp. 280-289.

[3] Ichihara, A., Survey of Computational Methods of Cross Sections for Thermal Neutron Scattering by

Liquids, JAEA-Review 2019-046, 2020, 36 p.

[4] Brown, D.A. et al., ENDF/B-VIII.0: the 8th major release of the nuclear reaction data library with CIELO-project cross sections, new standards and thermal scattering data, Nucl. Data Sheets, vol. 148, 2018, pp. 1-142.

[5] OECD Nuclear Energy Agency Data Bank, JEFF-3.3, https://www.oecd-nea.org/dbdata/jeff/jeff33 (accessed 2022-01-06).

[6] Rahman, A. et al., Theory of slow neutron scattering by liquids. I, Phys. Rev., vol. 126, no. 3, 1962, pp. 986-996.

[7] Squires, G.L., Introduction to the Theory of Thermal Neutron Scattering, Cambridge University Press, 2012, 260 p.

[8] Sköld, K., Small energy transfer scattering of cold neutrons from liquid argon, Phys. Rev. Lett., vol. 19, no. 18, 1967, pp. 1023-1025.

[9] Van Der Spoel, D. et al., GROMACS: fast, flexible, and free, J. Comput. Chem., vol. 26, 2005, pp. 1701-1718.

[10] Abraham, M.J., Van Der Spoel, D., Lindahl, E., Hess, B., and the GROMACS development team, GROMACS User Manual version 2016.5, www.gromacs.org (accessed 2022-01-06).

[11] Winmostar V9.3.4, X-ability Co. Ltd., Tokyo, Japan, 2019.

[12] González, M.A., Abascal, J.L.F., A flexible model for water based on TIP4P/2005, J. Chem. Phys., vol. 135, 2011, 224516-1-8.

[13] Kropff, F. et al., http://www-nds.iaea.org/EXFOR/30283.002 (accessed 2022-01-06).

[14] Shibata, K. et al., JENDL-4.0: a new library for nuclear science and engineering, J. Nucl. Sci. Technol., vol. 48, no. 1, 2011, pp. 1-30.

[15] Koppel, J.U., Houston, D.H., Reference Manual for ENDF Thermal Neutron Scattering Data, GA-8774, General Atomics Technical Report, 1968, 174 p.

[16] Beyster, J. et al., Integral Neutron Thermalization – Annual Summary Report, GA-6824, General Atomics Technical Report, 1965.

[17] Kornbichler, S., Determination of the diffusion constants D(E,T) and D(T) of thermal neutrons in H_2O, phenylene, $ZrH_{1.92}$, and D_2O by measurement of scattering angular distributions. II. Zirconium hydride and heavy water, Nukleonik, vol. 7, 1965, pp. 281-286.

[18] Rohatgi, A., WebPlotDigitizer version 4.5, https://automeris.io/WebPlotDigitizer, California, USA, 2021, (accessed 2022-01-06).

[19] Mughabghab, S.F., Atlas of Neutron Resonances, sixth edition, Volume 1, Elsevier, 2018, 822 p.

31 Study of thermal scattering law of hydrogen in water with analysis of TCA critical experiments

Toru YAMAMOTO[a]

1-16-22, Higashi-asahina, Kanazawa-ku, Yokohama, 236-0033, Japan
∗Email: yamamototoru12345@gmail.com

From a number of the critical experiments performed at the Tank-type Critical Assembly (TCA), a series of experiments was selected to validate the thermal scattering law of hydrogen in water $S(\alpha, \beta)$ and analyzed by the continuous-energy Monte Carlo code MVP3 with JENDL-4.0. In the experiments, the critical water levels were measured changing the number of water holes in the center of the core. As a result, the calculated k_{eff} values systematically decreased along with the critical water levels. When the same analysis was performed with the free-gas-model scattering cross-section of hydrogen in place of $S(\alpha, \beta)$, the k_{eff} values increased with the critical water levels. From this fact, a slightly smaller $S(\alpha, \beta)$ was expected to cancel the decreasing trend of the k_{eff} values. Using the perturbation function of MVP3, the reactivity changes for the perturbation in the atomic number densities of hydrogen were calculated. They corresponded to the reactivity changes for the perturbation in the neutron-flux-weight total cross-sections ($\langle\Phi\sigma\rangle$). Decreasing $\langle\Phi\sigma\rangle$ of hydrogen by about 2% almost cancel the trend. The main part of the total reaction rate of hydrogen in water is the thermal scattering. The modification of $\langle\Phi\sigma\rangle$ would be obtained by modifying $S(\alpha, \beta)$ in 10^{-2} to 10^{-1} eV.

1. Introduction

For the thermal scattering law of hydrogen in water ($S(\alpha, \beta)$), JENDL-4.0 [1] has adopted the data of ENDF/B-IV.8 [2]. In the new compilation of JENDL-5, the revision of $S(\alpha, \beta)$ has been studied [3]. To validate the revised $S(\alpha, \beta)$, appropriate integral experiments are needed. The object of this study is to select the critical experiments performed at the Tank-type Critical Assembly (TCA) of the Japan Atomic Energy Agency, analyze the experiments with MVP3 [4] with the JENDL-4.0 library, and obtain information to be used for the revision of $S(\alpha, \beta)$.

2. TCA Experiments on Water Holes and Analysis

2.1. Critical Experiments on Water Holes

---

[a] Former affiliation: Regulatory Standard and Research Department, Secretariat of Nuclear Regulation Authority (S/NRA/R), Tokyo, Japan.

Among a large number of critical experiments on the light-water-moderated lattice cores implemented at TCA, there is a data set on the 19-by-19 square lattice cores with a fuel rod pitch of 1.956 cm composed of 2.6 wt% UO_2 fuel rods [5]. A set of the experimental cores consisted of a core without a water hole, and nine cores that had one water hole, and 3, 4, 5, 8, 9, 13, 20, and 21 water holes. For the cores with water holes, the fuel rods in the core central region were withdrawn and remained as water holes. Figure 1 illustrates the locations of the water holes in the core central 5-by-5 cell regions. The critical water levels were measured for these ten cores.
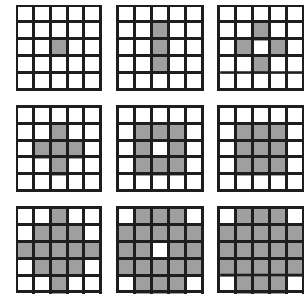

Figure 1. Water hole locations in the core central 5-by-5 cell regions [5].

2.2. Analysis with MVP3

The inside of the core tank and the base concrete under the core tank were modeled in the Monte Carlo calculations with MVP3. The materials in the core tank included the fuel rods, the moderator and reflector of water, the upper and lower grid plates, the fuel support, and the stainless beam. The dry lattice over the critical water level and the top fuel plugs over the upper grid plate were also modeled. Figure 2 illustrates the horizontal and vertical cross-sections of the main part of the core with 21 water holes in the calculation model, as an example.
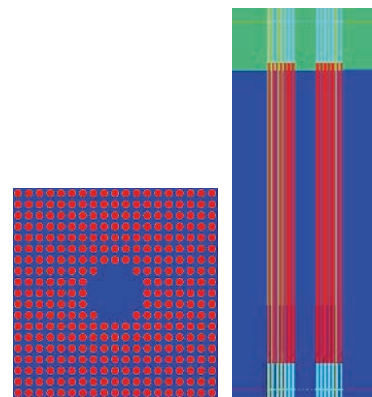

Figure 2. Illustrations of the horizontal (left) and vertical (right) cross-sections of the main part of the core with 21 water holes in the calculation model.

The atomic number densities were calculated following the specifications of the fuel rods and structure materials [5]. In this calculation, the abundance of ^{234}U in the UO_2 fuel and the impurities in the Aluminum alloy were taken into account [6]. The density of water in the core was calculated based on the formulation of air-saturated water as a function of temperature in Reference [7].

The Monte Carlo calculations coupled with JENDL-4.0 [1] were performed with 40 million histories (100 inactive and 4,000 active batches with 10,000 histories per batch). Under these calculation conditions, the statistical uncertainties (1 σ) in the k_{eff} values ranged from 0.00011 to 0.00013.

Table 1 shows the calculation cases and the calculated k_{eff} values. The total uncertainties which were obtained considering the statistical

Table 1. The calculated cases and the calculated k_{eff} values.

Number of water holes of the core [5]	Critical water level (cm) [5]	Core temperature (℃) [5]	Calculated k_{eff} with JENDL-4.0
0	60.60	15.9	1.00018
1	60.43	15.9	1.00012
3	61.00	16.0	1.00004
4	60.80	16.2	0.99981
5	62.65	16.1	0.99991
8	65.00	16.2	0.99966
9	70.00	16.2	0.99943
13	78.03	16.3	0.99904
20	103.03	16.6	0.99864
21	140.64	16.5	0.99806

uncertainties in the Monte Carlo calculations and the uncertainties in the measurements were 0.00015 Δk_{eff}. The calculated k_{eff} values ranged from 0.99806 to 1.00018 and were similar to those of the precedent studies. [8-10].

Figure 3 illustrates the calculated k_{eff} values against the critical water levels. The error bars show the total uncertainties. A

Figure 3. The calculated k_{eff} values against the critical water levels.

decreasing trend in the k_{eff} values was observed with the critical water levels. The difference in the k_{eff} values between the lowest and highest critical water levels was 0.00212 Δk_{eff}, and considerably larger than the total uncertainties. Even though there may be some other alternative interpretations of the trend, this study focused on the uncertainties in the neutron cross-sections of the relevant main nuclides: hydrogen (^{1}H), oxygen (^{16}O), and uranium (^{235}U and ^{238}U).

3. Cross-Section of Hydrogen
3.1. k_{eff} Values with Free-gas-model Cross-section

To obtain reference information relating to the scattering cross-section of hydrogen in the thermal neutron energy region, the calculations were performed by replacing $S(\alpha, \beta)$ with the free-gas-model cross-section in JENDL-4.0 for the core without a water hole, and the cores with 13, and 21 water holes. The calculated k_{eff} values are illustrated compared with those with $S(\alpha, \beta)$ in Figure 4. The k_{eff} values with the free-gas-model
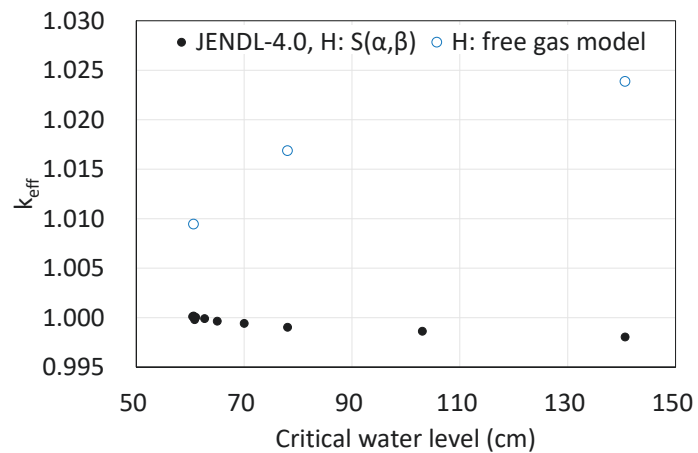

Figure 4. The calculated k_{eff} values against the critical water levels with $S(\alpha, \beta)$ and the free-gas-model cross-section.

cross-section were larger than those with $S(\alpha, \beta)$ and showed an increasing trend with the critical water levels. Figure 5 shows the neutron-energy-dependent total macroscopic cross-sections of the water in the fuel cells. They are the calculation results of MVP3 for the core without a water hole. The figure indirectly shows the difference between $S(\alpha, \beta)$ and the free-gas-model cross-section of hydrogen since a main part of the total cross-section is the scattering cross-section of hydrogen. The smaller

scattering cross-section of the free-gas-model cross-section in the thermal energy region reduces the neutron up-scattering and causes a softer thermal neutron spectrum, which increases fission reaction in the fuel. This effect is large in the cores with 13 and 21 water holes which have softer neutron energy spectra than that of the core without a water hole. This indicated that a slightly smaller S(α, β) than that in JENDL-4.0 would reduce the decreasing trend in the k_{eff} values.
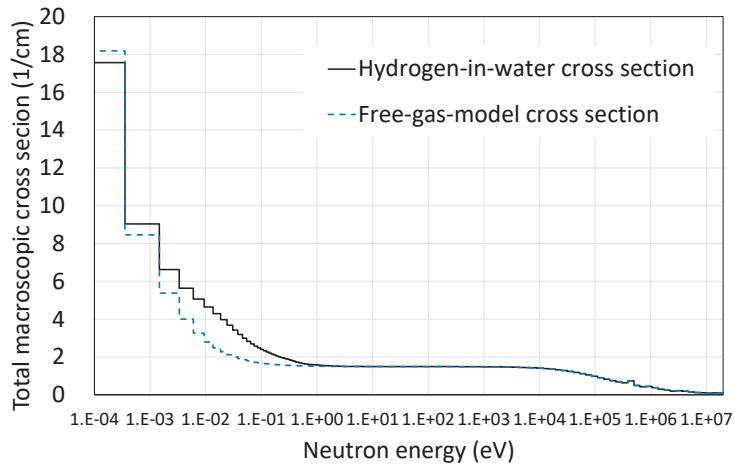

Figure 5. Total macroscopic cross-sections of the water in the fuel cells with S(α, β) and the free-gas-model cross-section.

3.2. Perturbation Calculation of Hydrogen Number Density

In this study, the number density of hydrogen was modified in place of S(α, β). A neutron reaction rate of a nuclide in a unit volume of a specific region is expressed by the product of the neutron-flux-weight total cross-section and the atomic number density of the nuclide. The neutron-flux-weight total cross-section is defined by,

$$< \Phi\sigma > = \int_V \int_0^{E_{max}} \Phi(x,y,z,E)\sigma(x,y,z,E)dEdxdydz \Big/ \int_V \int_0^{E_{max}} dEdxdydz$$

here, $\int_V dxdydz$ is a volume integral over the specific region, and $\int_0^{E_{max}} dE$ is an energy integral from 0 to Emax. When a core calculation is performed with the deviated atomic number density from the nominal value, the results of the core calculation can be also regarded as those obtained with the deviated neutron-flux-weight total cross-section from the nominal value in the condition of the nominal atomic number density. The differences in the k_{eff} values caused by the deviated number density of hydrogen were obtained by using the perturbation function of MVP3. The calculations with the atomic number densities increased by 5% from the nominal values were performed as a reference calculation. The differences in the k_{eff} values are listed in Table 1 for the core without a water hole and that with 21 water holes, as examples. As a result of the survey using the reference data, decreasing the hydrogen number density by 1.8% almost made the k_{eff} values constant with the critical water levels as shown in Figure 6. The uncertainties in k_{eff} values for the 1.8%-smaller hydrogen number densities included the uncertainties in the perturbation calculations of the number density.

The total reaction rates of hydrogen calculated by MVP3 are illustrated in Figure 7 for the reflector, fuel cells, and water holes in the core without a water hole and the core with 21 water holes. The total reaction rates of hydrogen have peaks in the neutron energy 10^{-2} to 10^{-1} eV where the main reaction is scattering and the scattering cross-section is expressed by S(α, β). The modification of the neutron-flux-weight total cross-section of hydrogen would be obtained by

modifying $S(\alpha, \beta)$ in 10^{-2} to 10^{-1} eV.

4. Cross-sections of ^{16}O, ^{235}U, and ^{238}U

To examine the effect of the cross-sections of ^{16}O, ^{235}U, and ^{238}U, the calculations with the atomic number densities increased by 5% from the nominal values were performed in the same way for hydrogen. The calculation results are listed in Table 2. The differences in the effects of the deviation in the number densities on the core reactivity between the core without a water hole and that with 21 water holes are small, while those of hydrogen are considerably large. For the core with 21 water holes, the absolute value of the reactivity of ^{16}O decreased and those of ^{235}U and ^{238}U increased compared with those for the core without a water hole. It is attributed to the difference in the neutron energy spectra which are softer in the core with 21 water holes than that in
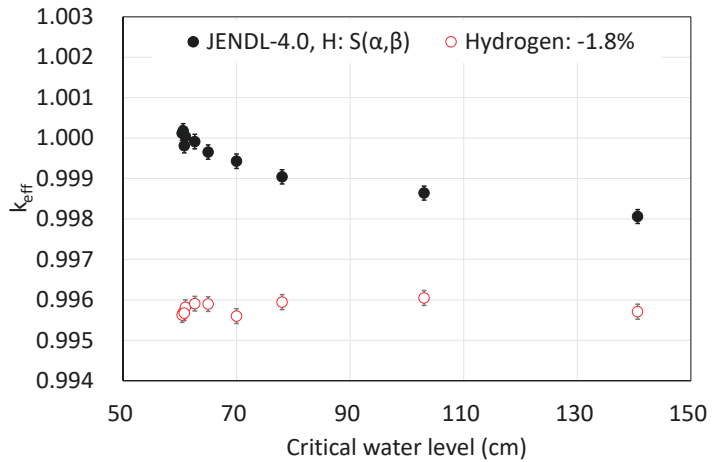

Figure 6. Calculated k_{eff} values against the critical water levels with the nominal and 1.8%-smaller hydrogen number densities.
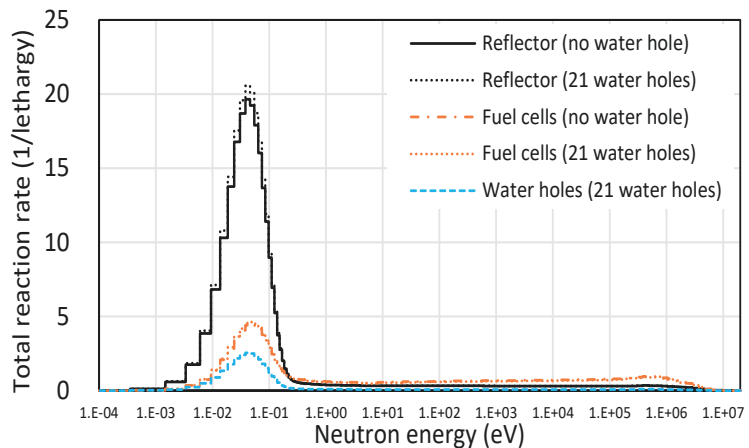

Figure 7. Total reaction rates of hydrogen in the three water regions for the core without a water hole and the core with 21 water holes.

Table 2. The differences in the k_{eff} values (Δk_{eff},) with the atomic number densities larger by 5% than the nominal values for the core without a water hole and that with 21 water holes.

Number of water holes	Δk_{eff} for +5% atomic number density of ^{1}H	Δk_{eff} for +5% atomic number density of ^{16}O	Δk_{eff} for +5% atomic number density of ^{235}U	Δk_{eff} for +5% atomic number density of ^{238}U
0	0.01250	0.00158	0.01023	−0.00539
21	0.00654	0.00118	0.01060	−0.00562

the core without a water hole. The correction of the decreasing trend was attempted with the neutron-flux-weight total cross-sections of ^{16}O, ^{235}U, and ^{238}U. It indicated that the necessary decrease of the neutron-flux-weight total cross-section of ^{16}O for canceling the decreasing trend in the k_{eff} values is about 27%, which seems to be too large. The relation of the cross-sections of ^{235}U and ^{238}U to the

trend seemed to be small since the necessary amount of modifying the neutron-flux-weight total cross-section is too large.

5. Conclusions

The analysis of the critical experiments on the water holes was performed using MVP3 coupled with JENDL-4.0. The results of k_{eff} values ranged from 0.99818 to 1.0005 and showed a decreasing trend with the critical water levels. Assuming that the trend was relating to the uncertainties in the cross-sections filed in JENDL-4.0, the investigations of modifying the neutron-flux-weight total cross-sections were carried out by changing the atomic number densities of hydrogen, ^{16}O, ^{235}U, and ^{238}U with the perturbation function of MVP3. The results of the perturbation analysis of the hydrogen number density indicated that the neutron-flux-weight total cross-sections of hydrogen should be smaller about 2% than that in JENDL-4.0. The modification of the cross-section would be obtained by modifying S(α, β) in 10^{-2} to 10^{-1} eV. The relation of the cross-sections of ^{16}O, ^{235}U, and ^{238}U to the trend seemed to be small.

It was demonstrated that the experimental data set investigated in this study is appropriate to validate S(α, β).

References

1) Shibata K, Iwamoto O, Nakagawa T, et al. JENDL-4.0: a new library for nuclear science and engineering. J Nucl Sci Technol. 2011 Jan;48:1-30.

2) CSEWG-Collaboration. Evaluated nuclear data file ENDF/B-VI.8. www.nndc.bnl.gov/endf (accessed 2021-08-15).

3) Iwamoto O, Yokoyama K. Status of the JENDL project. OECD/NEA, 31st WPEC meeting, 27-28 June 2019.

4) Nagaya Y, Okumura K, Sakurai T, et al. MVP/GMVP version 3: general purpose Monte Carlo codes for neutron and photon transport calculations based on continuous energy and multigroup methods. JAEA-Data/Code 2016-018, 2017, 421p.

5) Cao X, Suzaki T, Kugo T, et al. Effects of volume fraction and non-uniform arrangement of water moderator on reactivity. JAERI-Tech 2003-069, 2003, 36p.

6) Miyoshi Y, Arakawa T, Yamamoto T, et al. Critical arrays of low-enriched UO$_2$ fuel rods with water-to-fuel volume ratios ranging from 1.5 to 3.0. OECD/NEA Nuclear Science, International Handbook of Evaluated Criticality Safety Benchmark Experiments, NEA/NSC/DOC (95) 03/IV, LEU-COMP-THERM-006, Jun 2019.

7) Jones FE, Harris GL. ITS-90 density of water formulation for volumetric standards calibration. J Res Natl Stand Technol. 1992 May-Jun;97:335-340.

8) Chiba G, Okumura K, Sugino K, et al. JENDL-4.0 benchmarking for fission reactor applications. J Nucl Sci Technol. 2011 Feb;48:172-187.

9) Compilation of the data book on light water reactor benchmark to develop the next version of JENDL - utilization of criticality data in ICSBEP and IRPhEP open databases -. JAEA-Data/Code 2017-006, 2017, 152p. (in Japanese).

10) Yamamoto T. Critical analysis of light-water moderation UO$_2$ and uranium-plutonium mixed oxide lattices by continuous-energy Monte Carlo calculation. J Nucl Sci Technol. 2021 Jul;58:845-855.

32 Formulation of a shell-cluster overlap integral with the Gaussian expansion method

Riu NAKAMOTO[1], Makoto ITO [†1], Eiju UEDA[1], and Noritaka SHIMIZU[2]

[1]Department of Pure and Applied Physics, Kansai University, Yamatecho, 3-3-35, Suita 564-8680, Japan
[2]Center for Nuclear Study, The University of Tokyo, 7-3-1 Hongo, Bunkyo-ku, Tokyo 113-0033, Japan
[†]Email: itomk@kansai-u.ac.jp

We show the theoretical framework to evaluate the overlap integral of the shell-model and cluster-model wave functions. The framework is applied to the system of the core plus two neutrons (n), and the magnitude of the overlap of the shell model configuration (core $+ n + n$) and the di-neutron cluster one (core $+2n$) are calculated. In this calculation, we have confirmed that the magnitude of the overlap integral is prominently enhanced when two neutrons occupy the shell model orbits having the lower orbital angular momenta, such as the s and p wave orbits. The shell-cluster overlap is also evaluated for the systems with the jj-closed cores plus two neutrons, and the enhancement due to the occupation of the s or p orbit appears in the systematic calculation. The feature of the shell-cluster overlap is also discussed in the core + four nucleons systems, which corresponds to the evaluation of the formation amplitude of the α cluster around the core nucleus.

1 Introduction

Nuclear shell model based on a mean field picture is a standard model to explain ground and low-lying states in nuclear systems [1, 2, 3]. In the ground state of a nucleus, all nucleons perform the independent particle motion in the self-consistent mean field by occupying the single particle orbits [1]. There appear energy gaps in a sequence of the single particle orbits, and such the level structure is called the shell structure [1, 2, 3]. The nuclear shell model, which considers the single particle configurations based on the shell structure, is quite successful in explaining the properties of the low-lying states over a wide mass region except for a few examples.

On the contrary, in the lighter mass systems, there appears the clustering phenomena, in which one nucleus is decomposed into the several subunits called clusters. An typical and well known example of such the cluster is the [4]He nucleus called α cluster [4, 5, 6], The α cluster is a quartet of two proton plus two neutrons. In the ground state, the α cluster and the residual nucleus are merged, which leads to the formation of the one-body mean field structure, but the α clustering is prominently enhanced in the excited states [4, 5, 6]. Moreover, in recent studies, di-neutron correlations are extensively investigated in the lighter mass region [7, 8, 9, 10]. A pair of neutrons does not form the bound state in a free space but the spatial localization of the di-neutron around the nuclear surface has been confirmed experimentally [7, 8], which is compared with the theoretical calculations based on the three-body models [9, 10].

The independent particle configuration in the self-consistent mean field seems to be inconsistent to the cluster configuration involving a spatial localization of the several nucleons but they

are non-orthogonal, and hence the amplitude of the cluster formation is non-zero even if the pure shell model structure is realized, in which the individual nucleons completely perform the independent particle motions. The relation of the shell model and the α-cluster model configurations is deeply discussed in the lighter mass region, where the effect of the spin-orbit interaction is not so strong [4, 5, 6, 11]. However, the relation of the shell-cluster configurations still remains unclear in the heavy mass region, in which the spin-orbit interaction must be prominent due to the occupation of the shell model orbits with the higher orbital angular momentum [1].

The evaluation of the non-orthogonal amplitude of the shell and cluster models is important to characterize the relation of these two models, which seem to describe the different particle motions intuitively. The non-orthogonal amplitude can be directly calculated by the overlap integral of the wave functions in the shell and cluster models, which are defined by the multi-dimensional integration with the coordinate rearrangements [12, 13]. It is interesting and instructive to explore the systematic feature of the shell-cluster overlap integral in the systems of core plus valence nucleons, which can be obtained by varying the the shell model orbits, the core mass number, the spatial size of the cluster, and so on.

Recently, we have formulated a new method to calculate the overlap integral of the wave functions in the shell and cluster models by combining the Gaussian expansion method, which is a powerful tool for the variational treatments of the few-body problems [12, 13, 14], and the Fourier transformation [15]. The new framework has been applied to the core + two neutrons systems, and we have investigated the basic feature in the overlap integrals of the naive shell model configuration and the di-neutron cluster one. Furthermore, the calculation of the configuration interaction (CI) is also performed [2, 3, 16], and the CI effect on the shell-cluster overlap integral is systematically investigated. Although we have focused on the discussion about the core + two neutrons system in the present report, the new framework can also be extended to the core + four nucleons, corresponding to the core plus α cluster systems, in a straight forward manner. In this report, we will present the essential aspects of our calculation, and all of the results shown in this report are compressed from Ref. [15].

2 Theoretical framework

The shell model wave function Ψ_s for two neutrons around the heavy core is constructed from the direct product of the single particle orbits, which is written in a symbolic form,

$$\Psi_s = N\mathcal{A}\left\{\phi_a(\mathbf{r}_1)\phi_b(\mathbf{r}_2)\right\} \quad . \tag{1}$$

Here $\phi_a(\mathbf{r}_i)$ shows the single particle wave function for the i-th valence neutron. The subscripts a and b in ϕ are the abbreviation of a set of the i-th single particle orbit, such as $a \equiv (n, l, j, j_z)$ with the radial node n, the orbital spin l, the total spin j and its third component j_z. The vector $\mathbf{r}_i$ contains a set of the coordinates for the single particle orbit: the position vector and the spin coordinates. Both of the single particle orbits are orthogonal to the orbits contained in the core nucleus, which is not considered explicitly in the present calculation. The core part in the total wave function does not explicitly contribute to the final amplitude of the overlap integral [15]. In Eq. (1), $\mathcal{A}$ and N mean the anti-symmetrization operator for all nucleons and the respective normalization constant, respectively.

The wave function of the di-neutron ($2n$) cluster model is

$$\Psi_c = N\mathcal{A}\left\{\chi_{LM}(\mathbf{R})\varphi(\rho, \zeta)\right\} \quad . \tag{2}$$

where N, $\mathcal{A}$ are the same symbols as those in Eq. (1): the normalization constant and the anti-symmetrizer, respectively. $\chi_{LM}(\mathbf{R})$ denotes the wave function for the core – $2n$ relative

motion with the orbital spin L and its third component M, which is a function of the core – $2n$ relative coordinate, $\mathbf{R}$. Here we assume the $L = M = 0$ state for simplicity.

In Eq. (2), $\varphi(\rho, \zeta)$ shows the internal wave function of the $2n$ cluster with the spin-less neutron pair ($S = 0$). The coordinate ρ denotes the $n - n$ relative coordinate, while ζ represents the spin coordinate. Here the spatial part in $\varphi(\rho, \zeta)$ is set to the simple Gaussian function corresponding to the $(0s)^2$ configuration in the harmonic oscillator potential with the width parameter ν.

We calculate the shell-cluster overlap, $\langle \Psi_s | \Psi_c \rangle$, by combing the Gaussian expansions [12, 13, 14] for the radial wave functions, which appear in Eqs. (1) and (2), and the Fourier transformation. The final expression of overlap becomes quite simple, and the schematic expression for the core + two neutrons system is given by

$$
\begin{aligned}
\langle \Psi_s | \Psi_c \rangle &= \langle \Psi_s(\boldsymbol{n}, \boldsymbol{l}, \boldsymbol{j}, \boldsymbol{j_z}, \boldsymbol{\tau}) | \Psi_c^\nu(LMSS_zTT_z) \rangle \\
&= F(LSS_zTT_z, \boldsymbol{l}, \boldsymbol{j}, \boldsymbol{j_z}, \boldsymbol{\tau}) \cdot G^\nu(L, \boldsymbol{n}, \boldsymbol{l}, \boldsymbol{j}) \\
&\times \delta(M + S_z, \sum_{i=1}^2 j_{zi}) \ ,
\end{aligned} \tag{3}
$$

where the bold symbols denote sets of quantum numbers of two nucleons, such as $\boldsymbol{n} = (n_1, n_2)$, $\boldsymbol{l} = (l_1, l_2)$ and so on. The $2n$-cluster model wave function Ψ_c depends on the internal width parameters of the $2n$ cluster, ν, which is specified by the superscript in the first and second lines of Eq. (3). Kronecker delta in the last line guarantees the conservation of the z-component of angular momentum.

In the second line of Eq. (3), the basic structure of the overlap integration is shown; specifically, the overlap integral is given by the direct product of the kinematic part F and the dynamical part G. F is determined by the angular momentum algebra independent of the details of the radial wave functions, while G is calculated from the radial wave functions in the shell model wave funciton ($\phi(\mathbf{r})$ in Eq. (1)) and the cluster model one ($\chi_{LM}(\mathbf{R})$ in Eq. (2)).

The separable expression in Eq. (3) is useful to interpret the computational results on the overlap integrals in terms of the matching between the angular momentum scheme and the radial wave functions. This is an advantage arising from the Fourier transformation. The final expression becomes the complicated expression if we employ the standard technique of the coordinate rearrangement using the transformation of $(\boldsymbol{r_1}, \boldsymbol{r_2}) \leftrightarrow (\boldsymbol{R}, \boldsymbol{\rho})$ [12, 13]. The explicit expression of the overlap integral in Eq. (3) for the case of the spin-singlet ($S = S_z = 0$), isospin-triplet ($T = |T_z| = 1$) pair of the two nucleons is given in Ref. [15].

3 Results

We have calculated the overlap integral of the shell model configuration (core + n + n) and the di-neutron cluster configuration (core + $2n$) in the various systems with the jj-closed cores, such as ^{16}O, ^{28}Si, ^{32}S, ^{40}Ca, ^{64}Ge and ^{76}Sr. In Fig. 1, we show the results of the systematic calculations of the shell-cluster overlap integrals. In this calculation, the harmonic oscillator (HO) wave function is applied to all of the radial wave functions The internal width parameter of the $2n$ cluster (ν) is fixed so as to reproduce the root-mean-squared radius of a deuteron (~ 2.1 fm). The width parameters of the single particle wave function in the shell model and the relative wave function in the cluster model is determined from the relation of $\hbar\omega = 41 A_C^{-1/3}$ with the core mass number A_C.
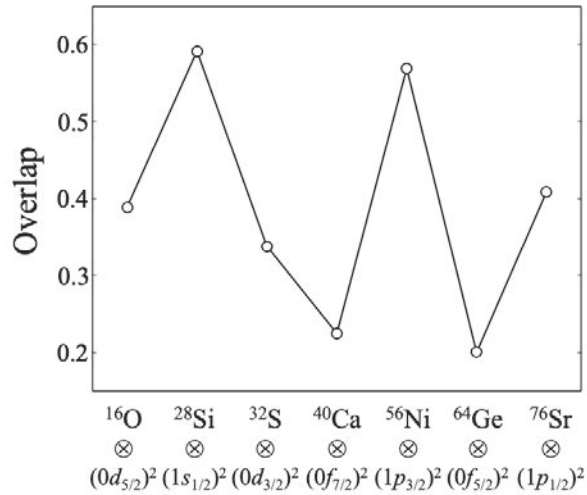
Figure 1: Systematic calculations of shell-cluster overlap. In the abscissa, the combination of the core and the shell configuration of two neutrons is shown, while the ordinate shows the magnitude of the shell-cluster overlap integral $\langle \Psi_s | \Psi_c \rangle$.

In the calculation shown in Fig. 1, the lowest shell model configuration around the core nucleus is assumed for the valence two neutrons, which couples to the spin zero pair, such as $j_1 \otimes j_2 = J = 0$. In Fig. 1, the prominent enhancements can be seen at the core of ^{28}Si, ^{56}Ni and ^{76}Sr, which corresponds to the two neutrons configurations of $(1s_{1/2})^2$, $(1p_{3/2})^2$ and $(1p_{1/2})^2$, respectively. This result means that the shell-cluster overlap is increased if the two neutrons occupy the shell model orbit having the lower orbital spins, such as $l = 0$ and 1. On the other hand, the overlap is suppressed when two neutrons occupy the higher orbital spin states, $l \geq 3$.

The result in Fig. 1 is obtained by assuming the naive shell model configurations for the valence two neutrons, which is the occupation of the lowest orbit around the core. In the realistic nuclei, however, there must be the effect of the configuration interaction (CI), and we have checked the CI effect on the systematics in the overlap integral. In order to see the CI effect on the shell-cluster overlap, we have performed the CI calculation employing the computational code of KSHELL [16]. Here we use the interactions of SDPF-M for the ^{16}O, ^{28}Si and ^{32}S cores [19], GXPF1A for ^{56}Ni and ^{64}Ge [20] and JUN45 for ^{76}Sr [21].

From the comparison of the calculation with and without CI, we have found that the CI effect is not strong. Specifically, the feature of the enhancement (suppression) at $1s$ and $1p$ ($0f$ and $0g$) orbits, which appears in Fig. 1, is not changed so much even if the CI effect is taken into account. Roughly speaking, the CI effect enhances the magnitude of the overlap but its amount is almost constant over all of the core systems [15]. Thus, the peak structure without CI survives after switching on the CI effect, and we can trace the original peak structure, which appears in the naive shell model configuration, from the CI solutions.

We should be careful for the calculation of the ^{76}Sr core because it is the strongly deformed nucleus having the prolate shape, which can be described by the large scale CI calculation, which requires the active model space of the $1p0f$ and $0g1d$ shells built on the ^{56}Ni core [18]. Analysis in Ref. [18] has pointed out that the quasi-SU(3) coupling of $0g_{9/2}$ and $1d_{5/2}$ orbits plays an important role in reproducing the large collectivity in ^{76}Sr. Therefore, the deformation effect in ^{76}Sr should be taken into account in the realistic calculation of the shell-cluster overlap integrals.

It is very interesting to study the overlap integral in the systems of the core plus four nucleons.

It is possible to extend our formulation to the core $+$ $4N$ systems, which correspond to the α cluster systems, in a straight forward manner. We have done the similar calculations of the shell-cluster overlap of the four nucleon systems with the jj-closed cores from ^{16}O to ^{56}Ni. In this calculation, we have assumed the naive shell model configurations around the individual cores. The enhancements of the overlap at the lower orbital spins, such as $l = 0, 1$, are confirmed. This is the similar to the result of the core $+$ two neutrons systems shown in Fig. 1. Since, in this calculation, we do not consider the CI effect for the shell model states of the four nucleons, the inclusion of the CI effect is important in future studies.

4 Summary

In summary, we have formulated the computational technique to calculate the shell-cluster overlap integral [15]. The formulation is achieved by combing the Gaussian expansion method of the radial wave function [12, 13, 14] and the Fourier transformation. Although we do not show the final expression of the shell-cluster overlap, it becomes quite simple from, which is given by the direct product of the kinetic part and the dynamical part. The former and latter parts are determined by the angular momentum algebra and the radial wave functions, respectively.

Our formula has been applied to the systems of the core plus valence two neutrons, and the shell-cluster overlap is evaluated in the systems with the jj-closed cores. In the systematic calculations, we have found the enhancement in the overlap when two neutrons occupy the shell model orbits having the lower orbital angular momentum, such as the s and p wave orbits.

We have also considered the effect of the configuration interaction (CI) in the calculation of the overlap integrals by employing the computational code of KSHELL [16]. The CI effect, which gives rise to the mixture of the component of the higher orbital spin, increases the magnitude of the overlap integral but its amount is almost constant, and hence the original peak structure appearing at the s and p orbits survived after the CI effect is switched on.

It is important to apply our calculation to the core $+$ four nucleon systems, corresponding to the α cluster systems. In the present report, the simple analysis without the CI effect has been done, and we have confirmed the enhancements of the overlap by the occupation of the s and p orbits in the shell model configuration for the four nucleons. The more sophisticated analysis with CI for the four nucleons is now under progress.

Acknowledgment

References

[1] P. Ring and P. Schuck, 2004 Nuclear Many-Body Problem 1st edn (Berlin: Springer).

[2] E. Caurier *et al.*, The shell model as a unified view of nuclear structure, Rev. Mod. Phys. **77**, 427 (2005).

[3] T. Otsuka, A. Gade, O. Sorlin, T. Suzuki and Y. Utsuno, Evolution of shell structure in exotic nuclei, Rev. Mod. Phys. **92**, 015002 (2020).

[4] K. Ikeda *et al.*, Comprehensive Study of Structure of Light Nuclei, Prog. Theor. Phys. Suppl. **68**, 1 (1980).

[5] H. Horiuchi, Recent Developments in Nuclear Cluster Physics, Suppl. Prog. Theor. Phys. **192**, 1 (2012).

[6] H. Horiuchi et al., Kernels of GCM, RGM and OCM and Their Calculational Methods, Prog. Theor. Phys. Suppl. **62**, 90 (1977).

[7] K. J. Cook, *et al.*, Halo Structure of the Neutron-Dripline Nucleus ^{19}B, Phys. Rev. Lett. **124**, 212503 (2020).

[8] Y. Kubota *et al.*, Surface Localization of the Dineutron in ^{11}Li, Phys. Rev. Lett. **125**, 252501 (2020).

[9] K. Hagino and H. Sagawa, Pairing correlations in nuclei on the neutron-drip line, Phys. Rev. C **72**, 044321 (2005).

[10] Y. Kikuchi, K. Ogata, Y. Kubota, M. Sasano, and T. Uesaka, Determination of a dineutron correlation in Borromean nuclei via a quasi-free knockout (p, pn) reaction, Prog. Theor. Exp. Phys. **2016**, 103D03 (2016).

[11] T. Yamada, Y. Funaki, H. Horiuchi, K. Ikeda, and A. Tohsaki, Monopole Excitation to Cluster States, Prog. Theor. Phys. **120**, 1139 (2008).

[12] E. Hiyama, Y. Kino, M. Kamimura, Gaussian Expansion Method for Few-Body Systems, Prog. Part. Nucl. Phys. **51**, 223 (2003).

[13] S. Aoyama, S. Mukai, K. Katō and K. Ikeda, Binding Mechanism of a Neutron-Rich Nucleus ^{6}He and Its Excited States, Prog. Theor. Phys. **93**, 99 (1995).

[14] H. Masui, K Katō, N. Michel, and M. Ploszajczak, Precise comparison of the Gaussian expansion method and the Gamow shell model, Phys. Rev. C**89**, 044317 (2014).

[15] R. Nakamoto, M. Ito, E. Ueda, and N. Shimizu, Formulation of a shell-cluster overlap integral with the Gaussian expansion method, Prog. Theor. Exp. Phys. **2021**, 113D01 (2021).

[16] N. Shimizu, T. Mizusaki, Y. Utsuno and Y. Tsunoda, Thick-restart block Lanczos method for large-scale shell-model calculations, Comp. Phys. Comm. **244**, 372-384 (2019).

[17] H. Friedrich, Microscopic nucleus-nucleus potentials, Phys. Rep. **74**, 209 (1981).

[18] K. Kaneko, N. Shimizu, T. Mizusaki and Y. Sun, Triple enhancement of quasi-SU(3) quadrupole collectivity in Strontium-Zirconium $N \approx Z$ isotopes, Phys. Lett. B **817**, 136286 (2021).

[19] Y. Utsuno, T. Otsuka, T. Mizusaki and M. Honma, Varying shell gap and deformation in $N \sim 20$ unstable nuclei studied by the Monte Carlo shell model, Phys. Rev. C **60**, 054315 (1999).

[20] M. Honma, T. Otsuka, B. A. Brown and T. Mizusaki, Shell-model description of neutron-rich pf-shell nuclei with a new effective interaction GXPF1, Eur. Phys. Jour. A **25**, Suppl. **1**, 499 (2005).

[21] M. Honma, T. Otsuka, T. Mizuaki and M. H.-Jensen, New effective interaction for f_5pg_9-shell nuclei, Phys. Rev. C **80**, 064323 (2009).

This is a blank page.

33　Design of Real-time Absolute Epi-thermal Neutron Flux Intensity Monitor with LiCaF Scintillator

Daisuke HATANO, Shingo TAMAKI, Sachie KUSAKA, Fuminobu SATO, Isao MURATA

Division of Sustainable Energy and Environmental Engineering, Graduate School of Engineering, Osaka University, Suita, Osaka, 565-0871 Japan

Email: hatano@qr.see.eng.osaka-u.ac.jp

In recent years, BNCT, a new radiation therapy for cancers, has attracted attention of many researchers due to selective treatment ability of cancer cells. In BNCT procedure, ^{10}B and low-energy neutron cause a (n, α) reaction to kill only the cancer cells by produced charged particles, and epi-thermal neutrons are used for treatment of deep-seated cancers. Because the number of irradiated epithermal neutrons determines the therapeutic effect, it is crucial to measure the absolute epi-thermal neutron intensity. For that purpose, we are developing a novel monitor to measure the absolute epithermal neutron flux intensity on the human body surface in real time.

In this study, we designed a monitor with a flat detection efficiency for epithermal neutrons between 0.5 eV and 10 keV. We employed a LiCaF scintillator as a neutron detection device due to its high sensitivity to neutron via ^{6}Li(n,α)^{3}H reaction, which was covered by a neutron absorber to make a flat efficiency. As a result, the detection efficiency of the monitor showed a flat feature, irrespective of the thickness of the absorbers.

1.　Introduction

In recent years, BNCT, a new radiation therapy for cancers, has attracted attention of many researchers due to selective killing of cancer cells. In BNCT protocol, boron compounds that can accumulate only in cancer cells are administered into a human body. After that, low-energy neutrons are irradiated to cause a nuclear reaction of ^{10}B(n, α)^{7}Li to kill cancer cells [1]. Thermal neutrons are used for surface cancers, while epithermal neutrons are employed to treat deep-seated cancers [2]. For the deep-seated cancers the therapeutic effect is determined by the number of irradiated epithermal neutrons. Therefore, it is necessary to measure the absolute number of epithermal neutrons irradiated on the human body surface in real time.

To solve this problem, we are developing a novel monitor to measure the absolute epithermal neutron flux intensity on the human body surface in real time. For measuring neutrons in real time, we employed a LiCaF scintillator due to its high sensitivity to neutron via ^{6}Li(n, α)^{3}H reaction. By covering the LiCaF scintillator with neutron absorbers, a flat detection efficiency is expected to realize. In this study, we investigate suitable design of the absorbers to have a flat detection efficiency.

2. Design of one-thickness absorbers

2.1. Neutron detection device

LiCaF measures the number of neutrons by detecting light emitted from the substance excited by the ^{6}Li(n, α)^{3}H reaction. Figure 1 shows the reaction cross section of ^{6}Li(n, α)^{3}H [3]. The reaction cross section decreases linearly in the epithermal neutron region (0.5 eV-10 keV), thus the detection efficiency has the same dependence.
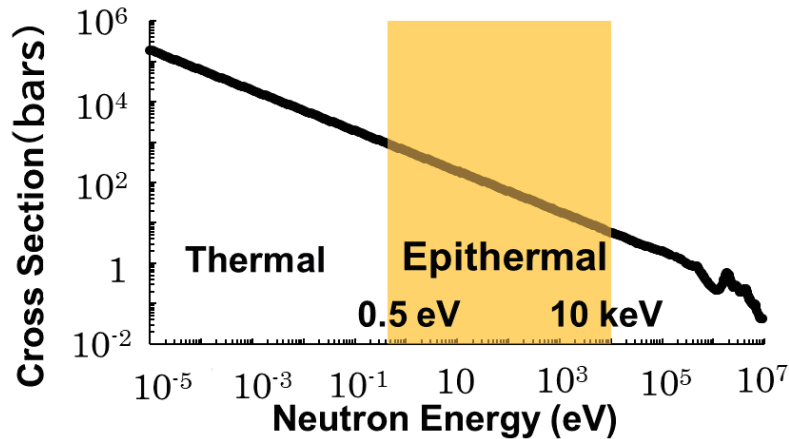
Fig. 1 Reaction cross section of ^{6}Li(n, α)^{3}H reaction [3]

The relationship between the detection signal count C, the incident neutron flux ϕ_n(E), and the detection efficiency ε(E) defined by the reaction cross section σ(E), is expressed by the following equation (1).

$$C = \int \varepsilon(E)\phi_n(E)\, dE \tag{1}$$

Due to the energy dependence of the detection efficiency ε, the number of neutrons cannot be measured directly from the measured value C. Therefore, it is necessary to make the energy dependent sensitivity flat to measure the neutron flux intensity directly. With an energy-independent constant detection efficiency $\bar{\varepsilon}$, the neutron flux can be derived by $C/\bar{\varepsilon}$.

2.2. Design calculation method

At first, we designed a simple monitor with a single layer absorber. As described in the previous section, this monitor was required to have a flat sensitivity to epithermal neutrons between 0.5 eV and 10 keV. A $2 \times 2 \times 2$ mm^3 cubic LiCaF was employed for a detection element, and filtering absorber was designed using Monte-Carlo simulation. ^{10}B enriched boron (^{10}B 90.4 %) was employed for the absorber material, because ^{10}B strongly absorbs low energy neutrons and can change the detection efficiency dramatically. The design calculations were carried out with the PHITS code which simulates particle transportation [4]. In the simulation by PHITS, a parallel beam is irradiated to LiCaF from a plane neutron source with the same area

as LiCaF, and the energy deposition to LiCaF was calculated to determine the number of measured neutrons by the deposited energy to LiCaF via ^{6}Li(n,α)^{3}H reaction using t-deposit tally. The relationship between the total energy deposition in LiCaF by charged particles of α and ^{3}T, E (MeV), and the number of neutrons LiCaF detects, n, is shown by the following equation (2), using the energy release in one 6Li(n, α)t reaction (4.78 MeV).

$$n = \frac{E}{4.78} \tag{2}$$

The detection efficiency was calculated from the ratio of the number of neutrons detected by LiCaF, n, and the number of incident neutrons. Finally we calculated detection efficiency changing the design of absorbers around LiCaF such as absorber thickness to investigate suitable absorber design from the ratio of the maximum and minimum values of the detection efficiency curve for epithermal neutrons between 0.5 eV and 10 keV.

2.3. Result

Figure 2 shows calculated detection efficiency of LiCaF with boron absorber for each boron thickness. The dark region indicates the epithermal neutron region. As a result, 10 mm thickness of boron made the flat detection efficiency between 1 keV and 10 keV, however, the detection efficiency was not flat from 0.5 eV to 1 keV, so further improvement was required for developing the monitor.
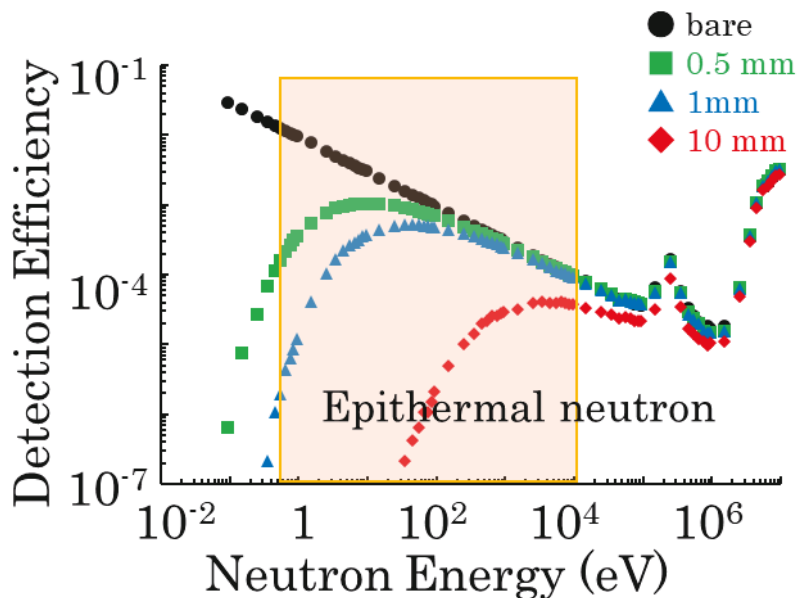

Fig. 2 Detection efficiency of LiCaF with boron absorbers.

3. Design of various-thickness absorbers

3.1. Monitor design procedure

We have designed various-thickness boron filters to make the flat detection efficiency between 0.5 eV and 10 keV. Figure 3 shows the basic design of boron absorber. By combining several different thickness boron filters, which were thinner than 10 mm, the detection efficiency between 0.5 eV and 1 keV was increased to make the detection efficiency flat. Figure 4 shows examples of the detection efficiency with various-thickness absorbers. As shown in Figure 4, the detection efficiency of two-thickness boron absorbers improves the detection efficiency from 10 eV to 10 keV, and three-thickness boron absorbers indicates that the efficiency can be more improved within the whole epithermal neutron region (0.5 eV – 10 keV). We in this way investigated the optimal design of the absorber.

In the design procedure, the detailed size was determined by the following order: The first thickest boron thickness t1 and length t2, medium boron thickness t3 and length t4, and thin boron thickness t5 to finally make the detection efficiency flat.
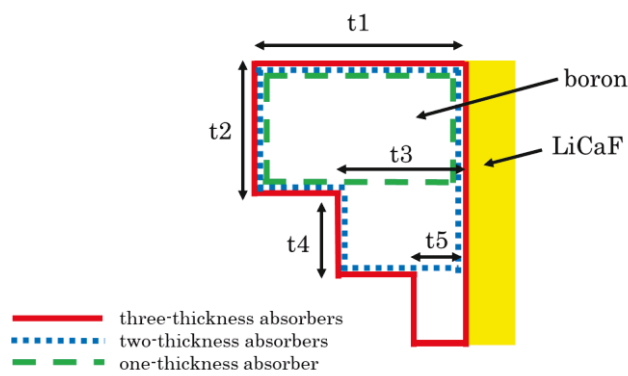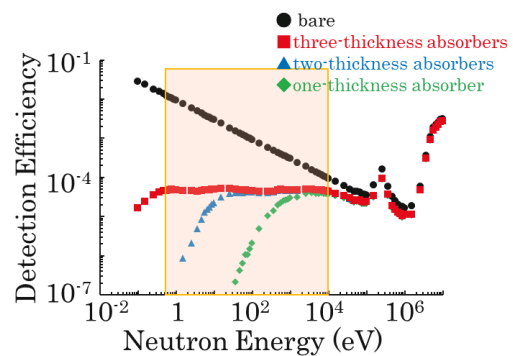

Fig. 3 Basic design of the boron absorber.

Fig. 4 Detection efficiency with various-thickness absorbers.

3.2. Result

Figure 5 shows the design result of the boron absorber and Figure 6 shows the detection efficiency of LiCaF with the designed boron absorber. Although the ratio of maximum and minimum detection efficiency of the epithermal neutron region of bare LiCaF between 0.5eV and 10 keV, L_1 was 130, that of LiCaF with boron absorber L_2 was greatly improved to be 1.23. As a result, the sensitivity of the monitor was successfully made flat between 0.5 eV and 10 keV within about 20%.
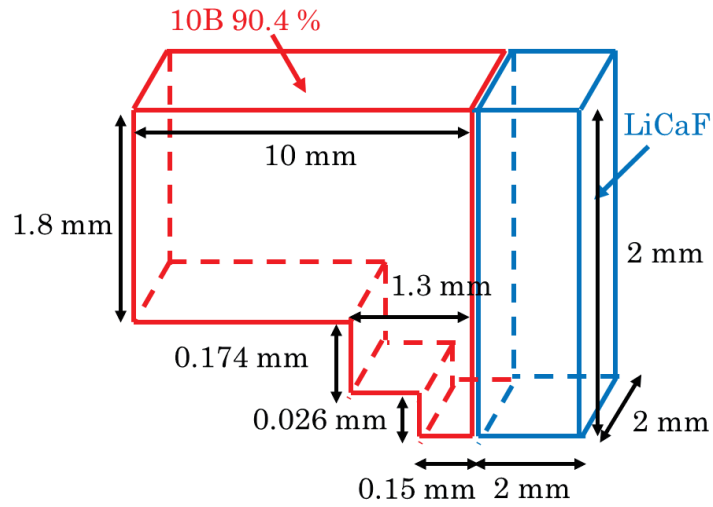
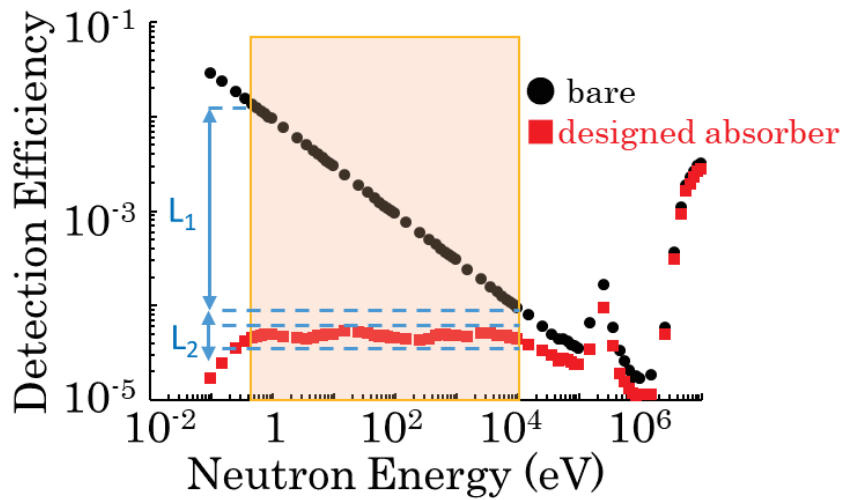Fig. 5 Design drawing of the boron absorber.

Fig. 6 Detection efficiency of LiCaF with the boron absorber.

4. Conclusion

In this study, we designed an epithermal neutron monitor with LiCaF scintillator and boron filters to measure the absolute epithermal neutron flux intensity on the human body surface in real time. As a result, the monitor was successfully designed having a flat detection efficiency, that is, practically 1.23 of ratio of maximum and minimum detection efficiency within the epithermal neutron region between 0.5 eV and 10 keV. However, designed monitor still have some problems. The first is that the boron absorber length is too

small to create. The second is that it is also sensitive to fast neutrons, though we first focus on low energy p-Li neutrons. In future, we will solve these problems, develop the designed monitor and carry out experiments to confirm the performance to estimate the epi-thermal neutron flux in real time.

References

[1] Miyatake S., Kawabata S., Hiramatsu R., Kuroiwa T., Suzuki M., Kondo N., and Ono K., Boron Neutron Capture Therapy for Malignant Brain Tumors, Neurol. Med. Chir. (Tokyo) 56, 2016, pp.361–371.

[2] Kumada H., Naito F., Hasegawa K., Kobayashi H., Kurihara T., Takada K., et al, Development of LINAC-based neutron source for boron neutron capture therapy in University of Tsukuba, Plasma Fusion Res, 2018.

[3] Shibata K., Iwamoto O., Nakagawa T., Iwamoto N., Ichihara A., Kunieda S., Chiba S., Furutaka K., Otuka N., Ohsawa T., Murata T., Matsunobu H., Zukeran A., Kamada S., and Katakura J., JENDL-4.0: A New Library for Nuclear Science and Engineering, *J. Nucl. Sci. Technol.* 48(1), 2011, pp.1-30.

[4] Sato T., Niita K., Matsuda N., Hashimoto S., Iwamoto Y., Noda S., Ogawa T., Iwase H., Nakashima H., Fukahori T., Okumura K., Kai T., Chiba S., Furuta T. and Sihver L., Particle and Heavy Ion Transport Code System PHITS, Version 2.52, J.Nucl. Sci. Technol. 50:9, 2013, pp.913-923.

34 Measurement of ^{nat}In (γ, xn) reaction cross sections with the 63 MeV bremsstrahlung

Ayano MAKINAGA[1,2] *, Muhammad ZAMAN[3], Muhammad SHAHID[3], Haladhara NAIK[3,4],

Man-woo LEE[5], Guinyun KIM[3], Moo-Hyun CHO[6]

[1]JEIN institute of Fundamental Science, NPO Einstein

5-14 Yoshida-honmachi, Sakyo-ku, Kyoto, 606-8317, Japan

[2]Faculty of Science, Hokkaido Univeristy

Kita-15, Nishi-7, Sapporo, 060-0810, Japan

[3]Department of Physics, Kyungpook National University

80 Daehak-ro, Buk-gu, Daegu 702-701, Korea

[4]Radiochemistry Division, Bhabha Atomic Energy Research Centre

Trombay, Mumbai 400085, India

[5]Research Center, Dongnam Institute of Radiological & Medical Science

40 Jwadong-gil, Jangan-eup, Gijang-gun, Busan 619-953, Korea

[6]Division of Advanced Nuclear Engineering, Pohang University of Science and Technology

77 Cheongam-ro, Hyogok-dong, Nam-gu, Pohang 790-784, Korea

*Email: ayanomakinaga@gmail.com

Precise nuclear data information is important to evaluate the production method, cross -sections and impurities in medical radioisotopes. In this study, the ^{nat}In (γ, nx) ^{110,111}In reaction cross sections were measured with the bremsstrahlung end-point energy of 63 MeV. The experiments were performed by using the 100 MeV electron linac facility of the Pohang Accelerator Laboratory (PAL) at Pohang, Korea. Energy averaged cross sections for ^{nat}In (γ, nx) ^{110,111}In reactions were compared with the theoretically calculated values based on TALYS 1.6 code.

1. Introduction

During the past half century, precise measurements and evaluations of photonuclear reaction cross sections, mainly for stable isotopes, have been carried out using the facilities around the world. The precise measurement of photonuclear reactions is closely linked to human life, not only in basic science but also in nuclear power, medical applications, and the space industry. Based on these results, the IAEA Evaluated Photonuclear Data Library was updated to provide precise information on photonuclear reaction cross sections mainly in the GDR region (IAEA/PD-2019) [1]. At the same time, the JENDL photonuclear data library [2] has been updated to provide more complete data. There are still remaining problems in photonuclear reactions, both in measurement and evaluation. Some of them are the measurement of isotopes with low natural abundance, double differential cross sections, multiple particle

emissions, and the higher energy side of GDR in competition with the quasi-deuteron decay process. These topics will become more important from the viewpoint of radiation protection in facilities, and also in the space industry.

We report here on the measurement of the photonuclear reaction cross section of indium using the activation method with the bremsstrahlung end-point energy of 63 MeV. Indium isotopes are important for the development of medical radioisotopes. For example, ^{111}In is used for cerebrospinal fluid imaging, bone marrow scintigraphy and so on. On the other hand, it is known that ^{114m}In is suitable for imaging because it emits γ – ray with 190 keV ($T_{1/2}$: 49.51 days), and at the same time, it can be used for internal beta ray therapy because of its beta decay property. Methods using radioactive nuclei for both diagnosis and treatment are called "theranostics". The radionuclide ^{111}In can be usually produced by irradiating ^{111}Cd or ^{112}Cd isotopes with protons or deuterons. On the other hand, ^{114m}In production method has four possible ways, such as ^{113}In (n, γ)^{114m}In, ^{115}In (γ, n)^{114m}In, ^{114}Cd (p, n)^{114m}In and ^{113}Cd (d, n)^{114m}In reactions. Although ^{114m}In is a useful nuclear medicine, it is reported as an "emerging isotope" in the IAEA publication because of its difficulties in establishing a stable supply system [3, 4, 5, 6]. In this study, an experiment on the ^{nat}In (γ, xn) reaction was performed to investigate the photo nuclear reaction cross sections in a wide range of energies, including the GDR region.

2. Experiment

The photo activation experiment was performed using the 100 MeV electron linear accelerator of Pohang Accelerator Laboratory (PAL) at Pohang, Korea. The photon beam was generated by irradiating a 0.1 mm thick tungsten with a 63 MeV electron beam. The electron beam current was 37 mA and the end-point energy of the generated bremsstrahlung photon beams was 63 MeV. As a photon flux monitor, we used ^{197}Au (γ, n) ^{196}Au reaction. The natural indium samples were irradiated for 30 minutes together with a natural gold flux monitor. The sizes of natural indium and gold samples were 1 cm x 1 cm x 0.1 mm each with weights of 0.0832 g and 0.1905 g, respectively.

After the irradiation, the number of γ-rays emitted from the radioactive samples were counted in off-line situation using a HPGe detector. The detector's full energy photopeak efficiency was measured as a function of photon energy using ^{133}Ba and ^{153}Eu standard sources (See, Figure 1). In Figure 1, solid lines show the detection efficiency of HPGe detector using the least – squares method expressed as the natural logarithm of the polynomial function. Figure 2 shows the γ-ray spectrum of the indium isotopes obtained from the ^{nat}In (γ, xn) reactions. Experimental details are shown somewhere else [7, 8].
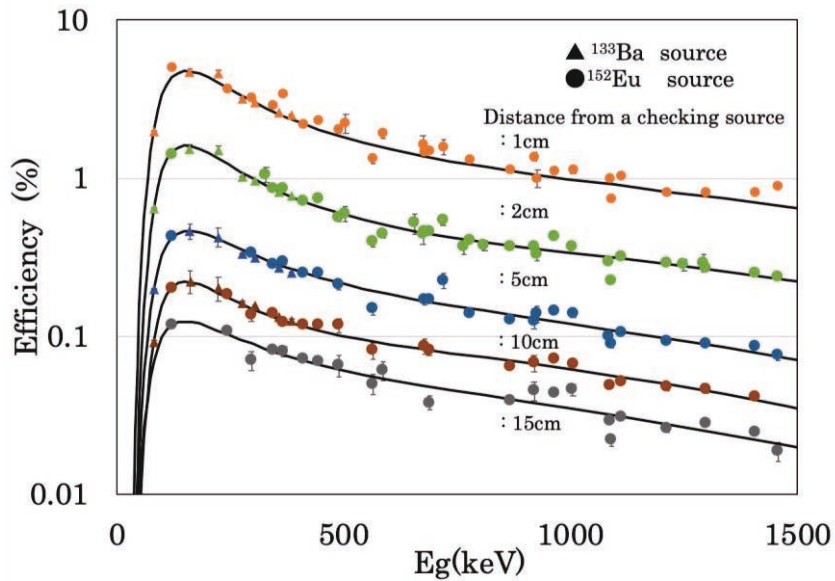
Figure 1. The detection efficiency of HPGe detector using γ-ray standard sources of ^{133}Ba and ^{152}Eu

3. Data analysis and the result

The ^{nat}In sample, which has been activated by the bremsstrahlung, was removed from the irradiation site after cooling time of about 30 minutes, and measured its γ-rays by an HPGe detector. One of the observed γ - ray spectrum is shown in Figure 2. Neutron multiple emission threshold energies in Reference [9] are also shown in Table 1. Following is the classical photo activation analysis formula.

$$N_{obs}\left(\frac{RT}{LT}\right) = \frac{n\sigma_R\phi I_\gamma\varepsilon(1-e^{-\lambda t})e^{-\lambda T}(1-e^{-\lambda RT})}{\lambda} \tag{1}$$

where N_{obs} is the detected photo-peak counts of the γ-ray of interest, n is the number of atoms (/cm^2), ϕ is the number of incident photons, t is an irradiation time, T is the cooling time. RT and LT are the real time and live time, respectively. Number of incident photons was determined from the ^{197}Au (γ, n)^{196}Au reaction using Eq. (2). Here, we used the detected photo-peck the counts of 355.7 keV γ - ray of ^{196}Au from the present measurement, whereas the ^{197}Au (γ, n)^{196}Au reaction cross section σ_R from TALYS1.6. Energy distribution of the incident photon was defined as the Schiff formula.

$$\phi = \frac{N_{obs}(\frac{RT}{LT})\lambda}{n\sigma_R I_\gamma\varepsilon(1-e^{-\lambda t})e^{-\lambda T}(1-E^{-\lambda RT})} \tag{2}$$

Since, the photon beam has broad energy distributions, the estimated cross section is the flux weighted average value and can be given in Eq. (3), which is the modified form of Eq. (1).

$$\langle\sigma_{exp}\rangle = \frac{N_{obs}(\frac{RT}{LT})\lambda}{n\phi I_\gamma\varepsilon(1-e^{-\lambda t})e^{-\lambda T}(1-e^{-\lambda RT})} \tag{3}$$
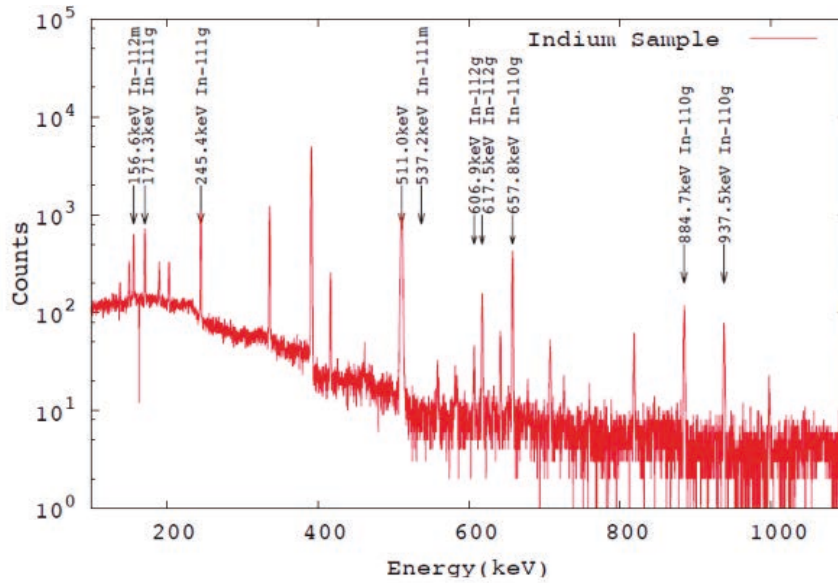
Figure 2. One of the γ -ray spectrum of the isotopes of indium obtained from the ^{nat}In (γ, xn) reaction and measured by HPGe detector.

Table 1. Photo neutron separation energies for indium isotopes [9]

	S_n (MeV)	S_{2n} (MeV)	S_{3n} (MeV)	S_{4n} (MeV)	S_{5n} (MeV)	S_{6n} (MeV)	S_{7n} (MeV)	S_{8n} (MeV)
^{115}In (95.7%)	9.04	16.31	25.76	33.43	43.43	51.49	61.94	70.57
^{113}In (4.3%)	9.45	17.12	27.11	35.17	45.62	54.25	65.28	74.85

In order to compare the experimentally determined flux weighted average cross sections with the theoretical values, we estimated the theoretical values using the cross sections using the TALYS 1.6 code [9] and energy distribution of the bremsstrahlung calculated by the Schiff formula as follows.

$$\langle \sigma_{cal} \rangle = \frac{\int_{E_{th}}^{E_{max}} \sigma(E)\phi(E)dE}{\int_{E_{th}}^{E_{max}} \phi(E)dE} \tag{4}$$

Figure 3 shows the preliminary result of the flux weighted average cross sections for ^{nat}In (γ, xn) reactions. In this study, we measured only the ^{nat}In (γ, xn)^{111}In and ^{nat}In (γ, xn) ^{110}In reaction cross-sections as test studies. The experimental and theoretical values were found to be in good agreement. Since the experimental spectra contain more γ -ray information, we would like to analyze all the data in detail in the future.

4. summary

The ^{nat}In (γ, nx) ^{110,111}In reaction cross sections were measured with the bremsstrahlung end-point energy of 63 MeV from the 100 MeV electron linac facility of the Pohang Accelerator Laboratory (PAL) in Korea. Flux weighted averaged cross sections for ^{nat}In (γ, xn) ^{110,111}In reactions were obtained as a trial basis and compared with the theoretically calculated values based on TALYS 1.6 code. We confirmed that both results showed good agreements and will continue to analyze them in detail.
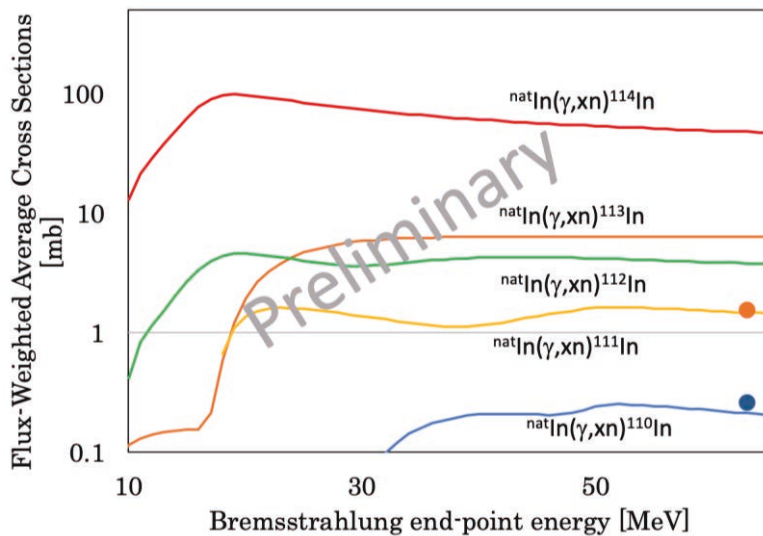
Figure 3. Flux weighted average cross sections for the ^{nat}In (γ, xn) ^{110,111}In reactions. The colored lines are the results of calculations using TALYS1.6 code, and the colored dots are the results of present experiments.

Acknowledgements

We thank the staff in Hokkaido University Nuclear Data Center for their warm – hearted discussion about nuclear data. A. M also thanks to Dr. N. Otsuka in IAEA for his advice about photo nuclear reaction. This presentation was partly reported in the Atomic Energy Society Japan 2018 Spring meeting.

References

1) Kawano, T. et al., IAEA Photonuclear Data Library 2019, Nucl. Data Sheets 163, 2020, p.109.
2) Iwamoto, N. et al., Photonuclear Data File, JAEA-Conf 2016-004, 2016, p.53.
3) Capote, R. et al., Consultants' Meeting on Improvements in charged – particle monitor reactions and nuclear data for medical isotope production, IAEA Headquarters Vienna Austria, 21-24 June 2011, IAEA report INDC(NDS)-591, 2011.
4) Nichols, A. L. et al., Technical Meeting on Intermediate-term Nuclear Data Needs for Medical Applications: Cross Sections and Decay Data. IAEA Headquarters Vienna, Austria, 22-26 August 2011, IAEA report INDC(NDS)-0596, 2011.
5) Nichols. A. L. et al., Summary report from the 1st Research Coordination Meeting, IAEA Headquarters Vienna, Austria, 3-7 December 2012, IAEA report INDC(NDS)-0630, 2013.
6) Tarkanvi, Y. et al., Investigation of activation cross sections of proton induced reactions on indium up to 70 MeV for practical applications, Nucl. Instrum. Methods B 351, 2015, pp.6-15.
7) Shakilur, R. Md. et al., Measurement of isomeric yield ratios in ^{nat}In and ^{nat}Sn with 50, 60, and 70 MeV bremsstrahlung photons, Nucl. Instrum. Methods B 268, 2010, pp. 13-19.
8) Makinaga, A. et al., Activation experiment for In-nat(g,xn) reactions using bremsstrahlung at Pohang Accelerator Laboratory, Atomic Energy Society Japan 2018 Spring meeting [in Japanese].
9) Center for Photonuclear Experiments Data (CDFE), Calculator and Graph Engine for Atomic Nuclei Parameters and Nuclear Reactions and Radioactive Decays Features, http://cdfe.sinp.msu.ru/services/calc_thr/calc_thr.html (accessed 2022-02-02).

10) Koning, A. J. et al., Modern Nuclear Data Evaluation with The TALYS Code System, Nucl. Data Sheets 113, 2012, p. 2841.

35　Shielding design for 3 GeV next-generation synchrotron radiation facility

Hiroki MATSUDA[1*], Masayuki HAGIWARA[1], Akihiro TAKEUCHI[1], Toshiro ITOGA[2],
Hiroyuki KONISHI[1]

[1]QST, [2]JASRI

6-6-11-901, Aramaki aza aoba, Aoba-ku, Sendai-shi, Miyagi-ken, 980-8579, Japan

1-1-1, Kouto, Sayo-cho, Sayo-gun, Hyogo-ken, 679-5198, Japan

[*]Email: matsuda.hiroki@qst.go.jp

A compact 3 GeV next-generation synchrotron radiation facility is currently being constructed at Aobayama New campus of Tohoku University in Miyagi prefecture, in which intense synchrotron radiations of both soft and hard x-rays are to be available. In this facility, the radiation-controlled area in the experimental hall is limited to the optical and experimental hatches so that even non-radiation workers can use synchrotron radiations. An area outside of the optical hatch is set to a non-controlled area. For that purpose, gas bremsstrahlung radiation that is generated by interacting electrons with residual gas in the beam pipe must be shielded. A shielding design for optical hatch by using PHITS code is presented in this paper.

1. Introduction

A compact 3 GeV next-generation synchrotron radiation facility is currently being constructed at Aobayama New campus of Tohoku University in Miyagi prefecture, in which intense synchrotron radiations of both soft and hard x-rays from a 3 GeV electron storage ring are supplied for users from FY2024 [1]. This facility is the first-ever synchrotron radiation facility in the Tohoku district in Japan.

The accelerator parameters are summarized in Table 1.

Table 1 Parameters of 3 GeV next-generation synchrotron radiation facility

Accelerator energy	3 GeV
Ring current	400 mA (at normal operation)
Number of cells	16
Ring length	349 m
Emittance	1.14 nmrad
Maximum number of beamlines	28
Maximum annual operation	6000 hours (goal)

2. Calculation procedure

All calculations were performed by the particle transporting code PHITS with version 3.24 [2]. The geometry was based on a CAD file containing beamline details. The following beamline components

were considered for the PHITS calculation; scattering mirrors made of silicon, mirror chambers made of stainless, gamma stopper made of lead, guillotine made of lead, and shielding walls made of lead sandwiched by irons. Parameters of residual gas composition and pressure in the 3 GeV electron storage ring were quoted from the technical design report [3]. 3 GeV electrons were transported in the residual gas region, generating photons, namely, gas bremsstrahlung. Only photons were tallied at the end of the straight part of the 3 GeV electron storage ring, and those photons were transported into the optical hatches. Effective doses in and outside of the hatch were evaluated. Synchrotron radiation is created by an insertion device and simultaneously transported into the hatch, but most of the synchrotron radiations do not have enough energies to leak from the iron vacuum pipe. A schematic view of the storage ring and an optical hatch is shown in Figure 1.

An effective dose below 1.3 mSv/3month in a non-controlled area is required in Japanese law and regulation. When 500 operation hours for three months are assumed, the effective dose rate of 1.3 mSv/3month corresponds to 2.5 uSv/h. Taking a safety factor as two into account, the shields were designed to achieve the effective dose at the non-controlled area below 1.25 uSv/h in the calculation.
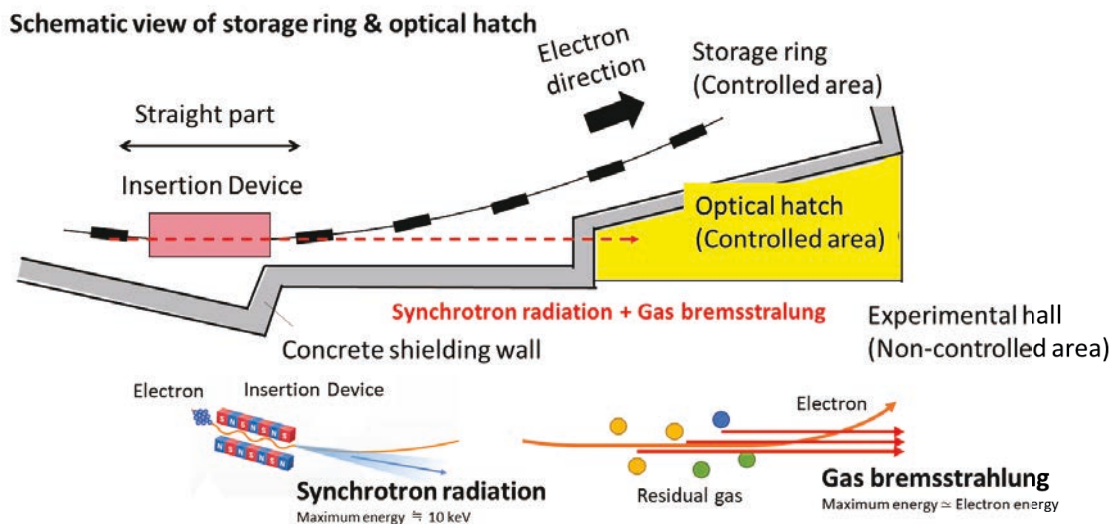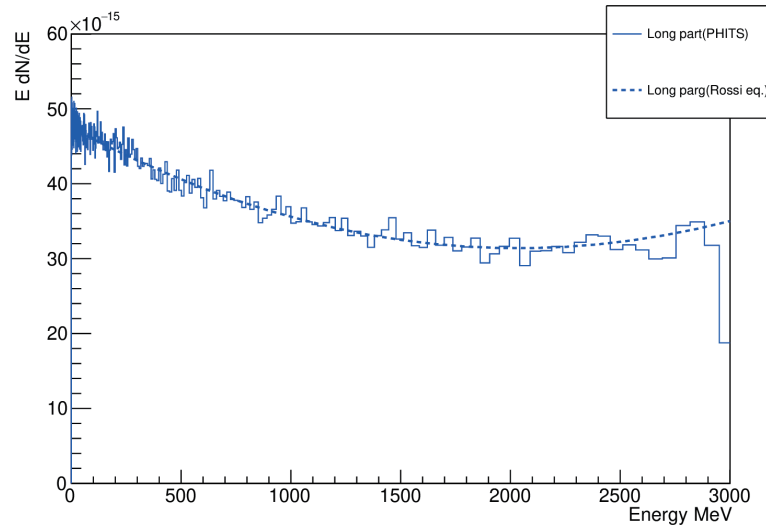

**Figure 1 A schematic view of the storage ring and the optical hatch**

3. Result

A spectrum comparison of PHITS with theoretical calculation [4] is shown in Figure 2, which clearly showed good agreement.

Figure 2 Comparison of gas bremsstrahlung spectrum of PHITS with theoretical calculation as a function of photon energy. PHITS: line, Theory: dashed line.

The effective dose distributions at a QST beamline, BL06U, with the top view are shown in Figure 3. On the downstream of the optical hatch, photons mainly contribute to the effective dose. On the other hand, on the sidewall, neutrons are dominated. Nonetheless, serious radiation leakage was not found from the optical hatch. Here the cross-sections of photo-nuclear reactions, which describe neutron emission from an evaporation or de-excitation process in giant dipole resonance of atomic nuclei, are taken from the nuclear data library (JENDL-PD/2004 [5]).
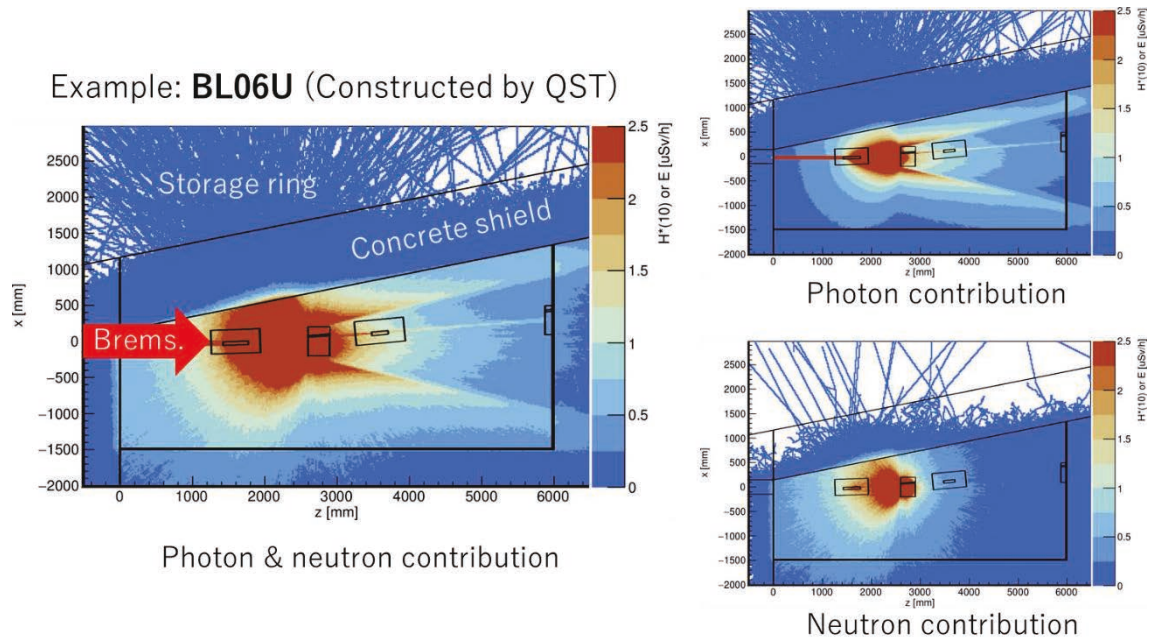

Figure 3 The effective dose distributions with a top view at BL06U

The effective dose rates calculated by PHITS were compared with those calculated by empirical formulas outside the optical hatch. The empirical values shown in Fig.4 were a summation of contributions of direct photons [6], scattered photons from a mirror [7], scattered photons from a gamma

stopper [8], and scattered neutrons from the mirror and the gamma stopper [8]. As shown in Figure 4, consistent results were obtained, considering the self-shielding effects.
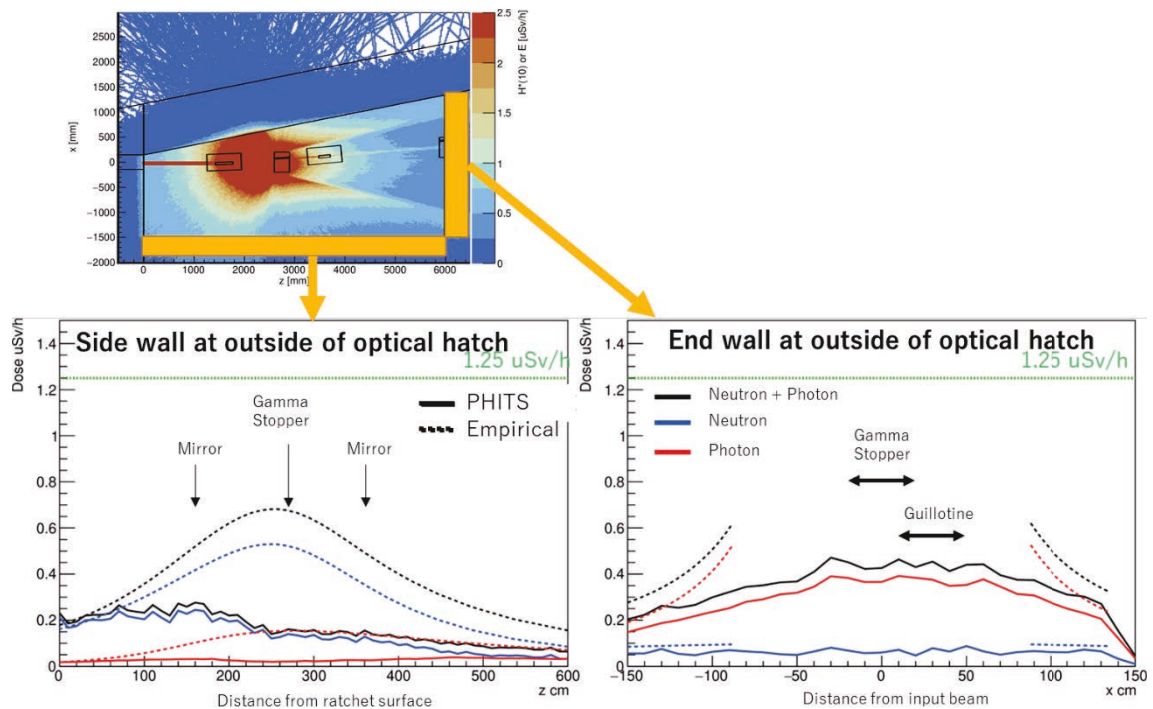
Figure 4 Comparison of the calculation with the empirical value

4. Summary

A compact 3 GeV next-generation synchrotron radiation facility is currently being constructed at Aobayama New campus of Tohoku University in Miyagi prefecture. From FY2024, synchrotron radiations will be supplied for ten beamlines at first. An experimental hall is designed to be a non-controlled area to utilize the facility more easily because a registration process for radiation work is not required.

The shielding design of the optical hatch at BL06U for gas bremsstrahlung was performed with PHITS version 3.24. In the calculation, the cross section of photo-nuclear reactions, which describe neutrons emitted from an evaporation or de-excitation process in giant dipole resonance of atomic nuclei, were taken from the nuclear data library (JENDL-PD/2004). As a result, no severe leakage outside the optical hatch was found. Comparison of the effective dose rates calculated by PHITS with the empirical formulas was also performed; consistent results were observed, considering the self-shielding effect.

Other simulation studies of shielding for an electron beam, x-rays, and gas bremsstrahlung will be performed in future work.

References

1. QST, Institute for Advanced Synchrotron Light Source, https://www.qst.go.jp/site/3gev-eng/ (accessed 2021-12-28).
2. Sato, T. et al., Features of Particle and Heavy Ion Transport code System (PHITS) version 3.02, J. Nucl. Sci. Technol. 55(5-6), 2018, pp.684-690.
3. QST, Accelerator design report for 3-GeV Next-Generation Synchrotron Radiation Facility,

https://www.qst.go.jp/uploaded/attachment/18596.pdf (accessed 2021-12-28).

4. Rossi, B.B., High-energy particles, Prentice-Hall, 1952.

5. N. Kishida et al., JENDL Photonuclear Data File, Proceedings of International Conference on Nuclear Data for Science and Technology, Santa Fe, New Mexico, USA, Sep. 26 - Oct. 1, 2004, Vol. 1, p.199 (2004).

6. Ban, S. et al., Estimation of Absorbed Dose Due to Gas Bremsstrahlung from Electron Storage Rings, Health Phys. 57(3), 1989, pp.407-412.

7. Liu, J.C., et al., Generic radiation safety design for SSRL synchrotron radiation beamlines, Radiat. Meas. 41(SUPPL.2), 2007, pp.S156-S162.

8. Liu, J.C., et al., Gas Bremsstrahlung and Associated Photon-Neutron Shielding Calculations for Electron Storage Rings, Health Phys. 68(2), 1995, pp.205-213.

This is a blank page.

36　Design and Construction of Epi-thermal Neutron Field with an Am-Be Source for Basic Researches for BNCT

Takahiro HIRAYAMA*, Yu FUJIWARA, Shingo TAMAKI, Sachie KUSAKA, Fuminobu SATO, Isao MURATA

Graduate School of Engineering, Osaka University, Yamadaoka 2-1, Suita, Osaka, Japan

*E-mail:hirayama@qr.see.eng.osaka-u.ac.jp

Recently, Boron Neutron Capture Therapy (BNCT) has been attracting more and more attention as a new type of radiation therapy. In BNCT, it is important to measure and evaluate the neutron field of accelerator-based neutron sources, and it is required to establish a method to characterize the neutron field using a low-energy neutron spectrometer. To solve this problem, we have been developing a new low-energy neutron spectrometer. This device measures the position distribution of the neutron-nuclear reaction as the penetration depth distribution of the incident neutron, and estimates the neutron energy spectrum. Currently, we are preparing the experimental setup for the verification of this spectrometer. In this study, we designed the epi-thermal neutron field with an AmBe neutron source by optimizing the moderator materials and their configuration by numerical simulations.

1. Introduction

Boron Neutron Capture Therapy (BNCT) has been attracting attention as a new cancer treatment method because it can selectively kill tumor cells without damaging normal cells, and patients can receive a therapeutic effect with less physical burden. In the past study, only nuclear reactors have been used as a neutron source for BNCT. However, there are few facilities that can treat patients using nuclear reactors worldwide as well as in Japan, and it is difficult to popularize reactor based BNCT as a cancer treatment option. To solve this problem, the Accelerator Based Neutron Source (ABNS) is under development. The accelerator is relatively less regulated than nuclear reactors, and currently one BNCT system with ABNS is approved by Japanese government. Therefore, it is expected to promote usage of ABNS as a neutron source for BNCT. However, the characteristics of the neutron field of ABNS, such as the neutron spectrum and the neutron intensity, depend on the type and parameters of the accelerator. Therefore, it becomes more important to evaluate the characteristics of the neutron field obtained from the accelerator in order to assess the treatment effect and to determine the treatment time. This is the reason why it is necessary to develop a neutron spectrometer having sensitivity to low energy neutrons for the developed ABNS for BNCT. To solve this problem, we are developing a neutron spectrometer based on a position sensitive ^{3}He proportional counter. [1]. This detector measures the position distribution of the neutron-nuclear reaction as the penetration depth of the neutron when the neutron enters the detector in parallel to the detector axis. The energy spectrum can

be estimated with the measured detection depth distribution. The spectrometer was already developed [2], however, the performance has not yet been validated. Therefore, it is necessary to experimentally verify the performance of this detector. Because it is essential to have an epi-thermal neutron field with a known energy spectrum to perform the verification experiment, we try to produce an optimal epi-thermal neutron field. In this study, we design a new epi-thermal neutron field by using an Am-Be neutron source.

2. Design of epi-thermal neutron field [3]

2.1 Design Goals

We employed the following two design goals for the epi-thermal neutron field.

（1）**Epi-thermal neutron flux：$\phi_{epi-thermal} \geq 1$** [n/cm²/sec]

The epi-thermal neutron field is designed to evaluate the performance of the present spectrometer. By this performance for one-day irradiation experiment, an enough number of counts could be obtained to evaluate the performance with acceptably high statistical accuracy.

（2）**Mixing ratio of fast neutrons in an epi-thermal neutron field：$\eta = \frac{\Phi_{epi-thermal}}{\Phi_{fast}} \geq 10$**

The η value is the parameter that indicates the ratio of epi-thermal neutron flux to fast neutron flux. In this design, η value is required to be more than 10, that means the epi-thermal neutron flux is one order of magnitude higher than the fast neutron flux. Meanwhile, thermal neutrons are easily removed with a cadmium sheet set in front of the column.

2.2 Design Procedure

In this study, we designed the epi-thermal neutron field by using the Monte Carlo N-Particle Transport code (MCNP-5) [4] in the following four steps: (1) Selection of moderator material, (2) Selection of reflector, (3) Removal of fast neutrons, and (4) Improvement of η value. In each step, we determined the optimal material and thickness by searching for the optimal results of the epi-thermal neutron flux and η value.

2.3 Design Detail

Step 1: Selection of moderator

At first, we determined the appropriate material of the main moderator and its thickness so as to efficiently convert fast neutrons into epi-thermal neutrons. The candidates for the moderators were PE, CF_2, D_2O, C, MgF_2, AlF_3, CaF_2. The calculation model is shown in Fig.1. Under the calculation condition shown in Fig.1, we calculated the epi-thermal neutron flux, fast neutron flux, and η value for various thicknesses (from 10 to 50 cm.) of the moderator. In this step, the epi-thermal neutron flux was required to be tentatively at least higher than the fast neutron flux, in other words, η > 1. The results are shown in Figs. 2 to 3, and it was found that magnesium fluoride and
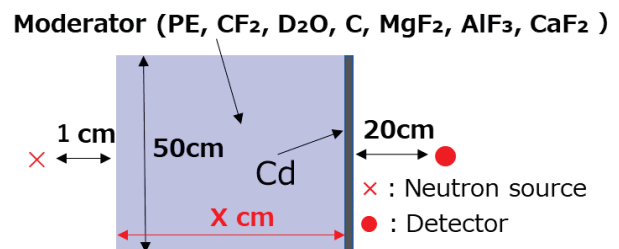

Figure 1 Calculation model (Step1)

aluminum fluoride were selected as the final candidates. Heavy water was not selected as the candidate since it is not suitable for this design. This is because it is liquid in room temperature and difficult to keep a rectangular shape. Magnesium fluoride was determined to be also not suitable, because it is technically difficult to produce a 50 cm × 50 cm × 40 cm solid shape. For these reasons, aluminum fluoride was adopted as the moderator in this design. The thickness of aluminum fluoride was decided to be 40 cm because the η value exceeded 1 and the epi-thermal neutron flux was maximum for $\eta > 1$.
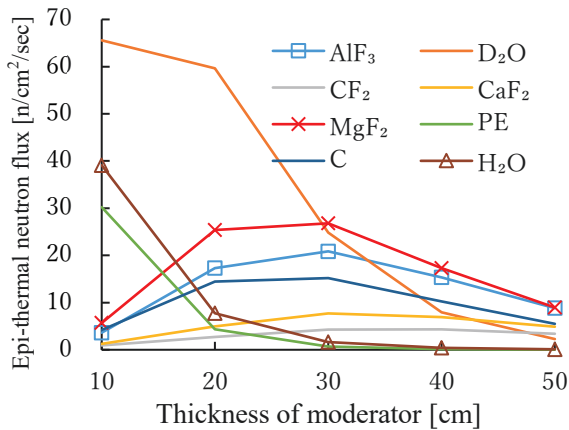
Figure 2 Epi-thermal neutron flux
for each moderator thickness.
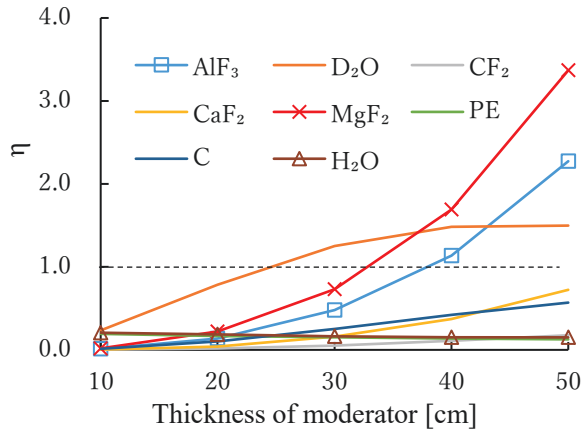
Figure 3 η for each moderator thickness.

Step 2: Selection of reflector

Secondary, we designed surrounding materials at the side of the moderator as a reflector material to prevent neutrons from leaking out from the moderator and to increase the epi-thermal neutron flux. Candidates for reflector materials are shown in Table 1. We calculated the epi-thermal neutron flux and η value for each candidate. As a result, Fig. 4 shows no difference in the epi-thermal neutron flux. Finally, we adopted candidate (A) due to the largest η value having the lightest weight among higher η of (A), (B) and (C).

Table 1 Candidate of reflector.

	Inside	Thickness [cm]	Outside	Thickness [cm]
(A)	C	10	Pb	5
(B)	Pb	5	C	10
(C)	Pb	10	C	5
(D)	C	5	Pb	10
(E)	Pb	7.5	C	7.5
(F)	C	7.5	Pb	7.5

Step 3 Removal of fast neutrons

Because Am-Be source emits high energy neutrons of 4 MeV on average, many fast neutrons above 1 MeV are still included in the neutron field. As shown later, in Fig. 13, the spectra of STEP1 and STEP2 show that many neutrons with energies higher than 1 MeV still remain. Therefore, we tried to remove them with an iron filter, because it has a large reaction cross section in the high-energy region above 1 MeV. The thickness of the iron
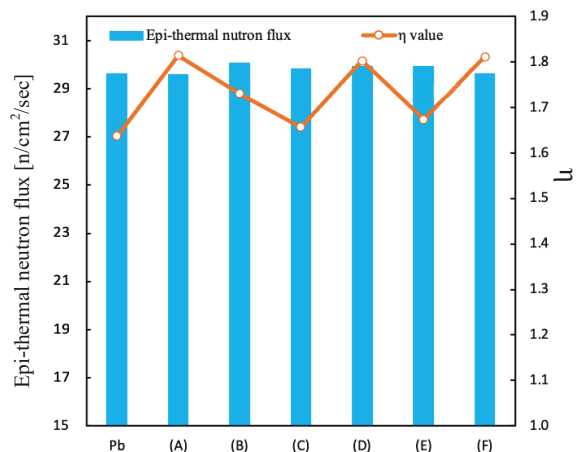

Figure 4 Epi-thermal neutron flux and η
for various reflectors.
(Left axis: Neutron flux, Right axis: η)

was varied from 5 to 30 cm, and the neutron flux was calculated to evaluate η values. The results are shown in Figs. 5 and 6. As a result, it was found that the neutron flux above 1 MeV was decreased to be less than 1 % of the epi-thermal neutron flux when the iron thickness was 20 cm or more as in Fig. 6. On the other hand, as shown in Fig. 5 η value is 9.6 and still not enough to achieve the design target η ≥ 10, due to the large fast neutron flux around 10 keV (see Fig. 13 to be detailed later).
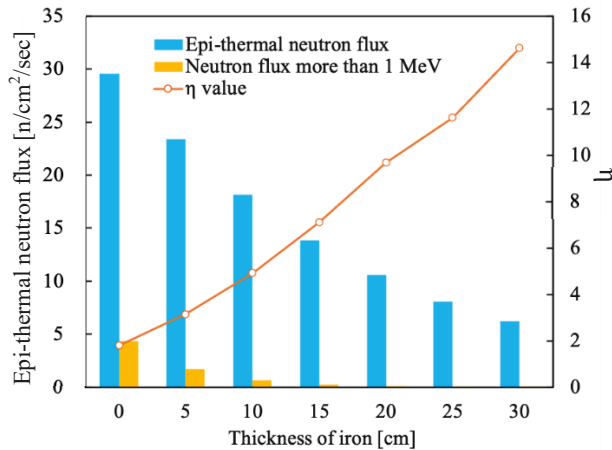
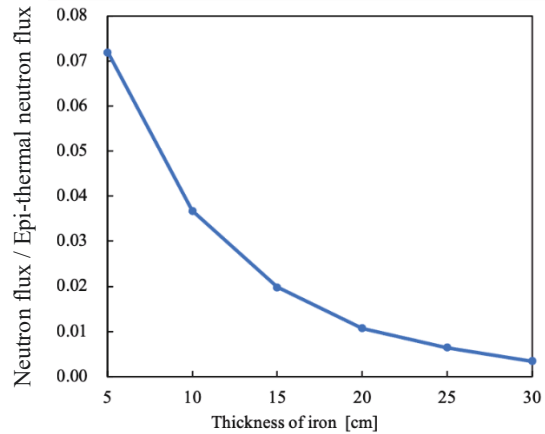Figure 5 Epi-thermal neutron flux and η for thickness of Fe filter. (Left axis: Neutron flux, Right axis: η)

Figure 6 Neutron flux (>1 MeV) over epithermal neutron flux for each thickness of Fe filter.

Step 4 Improvement of η value

To increase the η value, we tried to remove the fast neutron flux around 10 keV by using titanium, which has a large reaction cross section due to strong resonances around 10 keV. Titanium was placed on the rear surface of the AlF_3 moderator, and the epi-thermal neutron flux and η value were calculated by varying the thickness of titanium from 0 to 8 cm. The calculation result shown in Fig. 7 indicates that the epi-thermal neutron flux decreases as the titanium thickness increases, while the η-value reaches η = 39 at 7 cm thickness of titanium. Finally, the design result of the optimized epi-thermal neutron field is shown in Fig. 8. In the designed epi-thermal neutron field, the epi-thermal neutron flux is 7.34 n/cm²/sec and the η value is 23.9, which meets the design goals. (The neutron intensity of the Am-Be source is $4×10^6$ [n/sec].)
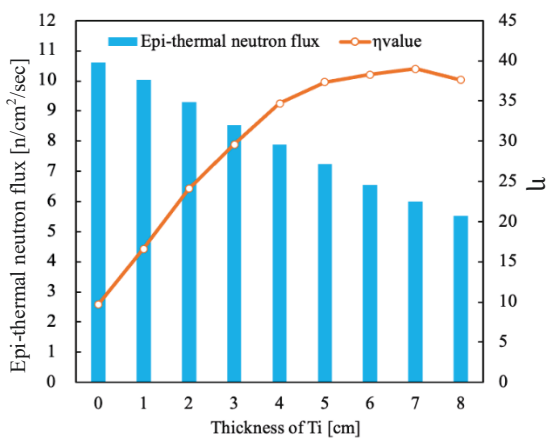

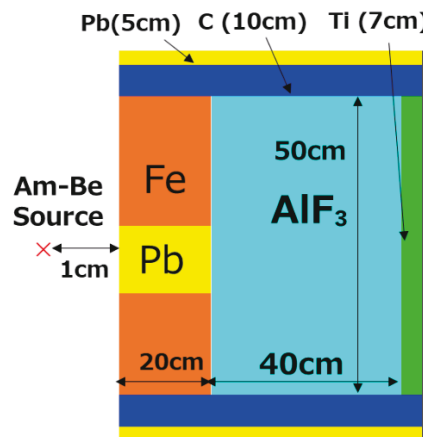Figure7 Epi-thermal neutron flux and η for Ti thickness. (Left axis: Neutron flux, Right axis: η)

Figure 8 Final design result (ideal case).

3. Construction of real epi-thermal neutron field

Because the epi-thermal neutron field designed in chapter 2 was an "ideal" design, there were two major problems left to construct the actual epi-thermal neutron field. The first problem is a technical difficulty for producing a large solid aluminum fluoride (50 cm × 50 cm × 40 cm). Second is very high cost of titanium plate with a size of 50 cm × 50 cm × 7 cm. Therefore, we aimed at achievable design by employing a cylindrical aluminum fluoride of 20 cm in diameter and 42 cm in length, which is the maximum size we could produce now, a titanium plate of 30 cm × 30 cm × 4 cm. Additional moderator instead of AlF_3 outside the cylindrical aluminum fluoride and substitute materials for titanium to fill the space outside the titanium plate were investigated as shown in the following sections.

3.1 Investigation of combined moderator

At first, suitable material for the second moderator (50 cm × 50 cm × 43 cm) outside the cylindrical AlF_3 was investigated. The candidates for the second moderator were polyethylene, carbon, water and granular Teflon, and the epi-thermal neutron flux and η value were calculated for each candidate. The calculation results shown in Fig. 9 indicates that the granular Teflon had the highest epi-thermal neutron flux and η value.

3.2 Investigation of titanium substitute material

In the next step, the titanium substitute material was investigated. The candidates for the titanium substitute material were aluminum, carbon, lead, polyethylene, iron, copper, and nickel. The epi-thermal neutron flux and η value were calculated for each type of titanium substitute material. As a result, carbon was found to be the best material due to the highest epi-thermal neutron flux and the highest η value as shown in Fig. 10.
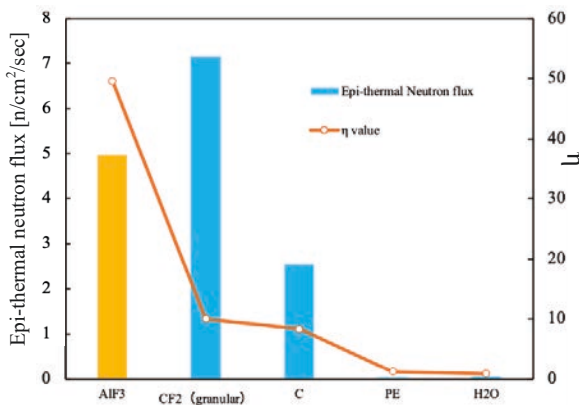

Figure 9 Neutron flux and η for the second moderator. Yellow bar is the reference of AlF_3. (Left axis: Neutron flux, Right axis: η)
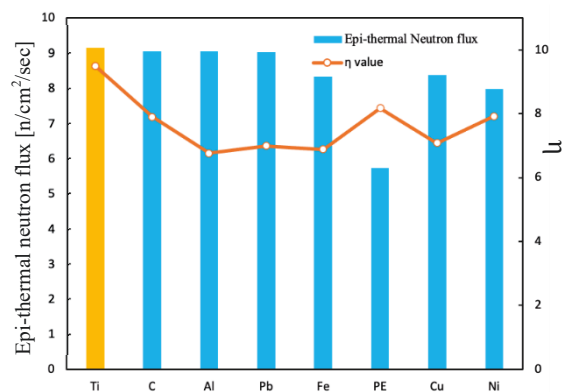
Figure 10 Neutron flux and η for the titanium substitute. Yellow bar is the reference of AlF_3. (Left axis: Neutron flux, Right axis: η)

3.3 Improvement of η value

The system obtained by the above realistic design resulted in η value of 7.98, which was lower than the design target (η≥10). We thus replaced some of the granular Teflon to solid Teflon to improve the η-value. The thickness of the solid Teflon was varied between 0 cm and 10 cm, and the η value and the epi-thermal neutron flux were calculated. The results are shown in Fig. 11. As a result, the η value successfully exceeded 10 when the thickness of the solid Teflon was longer than 5 cm. Therefore, mixture of 5 cm thick Teflon and granular Teflon was employed as the
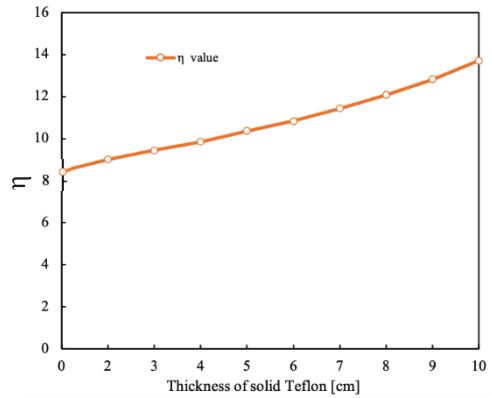

Figure 11 The η for each solid Teflon thickness

second moderator. The final designed experimental system is shown in Fig. 12. The spectra of each step and final construction system are shown in Fig. 13. The performance of the present epi-thermal neutron irradiation system shows epi-thermal neutron flux of 13.7 [n/cm²/sec] and η value of 10.4, which meet the design goal.

4. Conclusion

In this study, we designed an epi-thermal neutron field to conduct a validation experiment of the low energy neutron spectrometer under development by the authors' group. The design goals are epi-thermal neutron flux higher than 1 n/cm²/sec and the η value higher than 10. As a result of design, the designed epi-thermal neutron field has performance, i.e., epi-thermal neutron flux of 13.7 [n/cm²/sec] and η value of 10.4. In the future, we plan to evaluate the performance of the produced epi-thermal neutron field experimentally and carry out the validation experiment for the low energy neutron spectrometer.
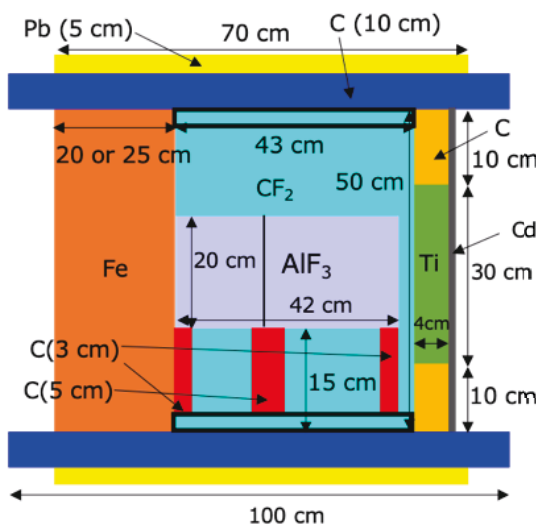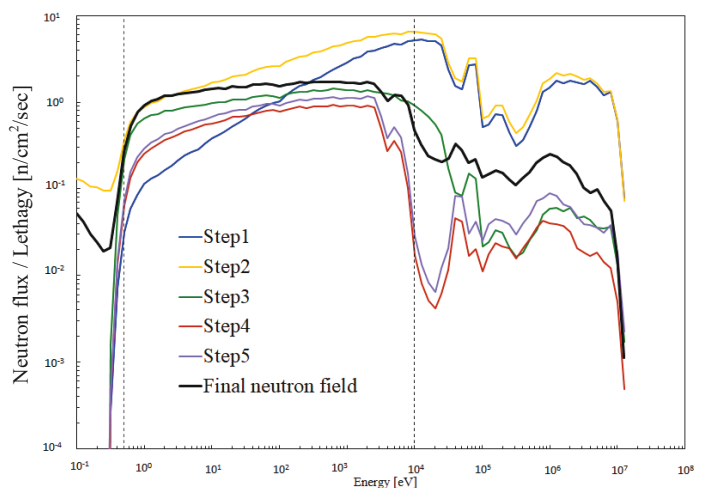

Figure 12 Finally designed system.

Figure 13 Neutron spectra in 5 steps and finally designed neutron field.

References

[1] I, Murata, H. Miyamaru, "Low-energy neutron spectrometer using position sensitive proportional counter —Feasibility study based on numerical analysis" Nuclear Instruments and methods in Physics Research A 589,445-454(2008).

[2] I. Murata, T. Obata, "Boron Neutron Capture Therapy (BNCT) - Low-Energy Neutron Spectrometer for Neutron Field Characterization –", *Plasma and Fusion Res.*, 9, 4401107 (2014).

[3] Yuta Osawa, Shoichi Imoto, Sachie Kusaka, Fuminobu Sato, Masahiro Tanoshita, Isao Murata, "Development of An Epi-thermal Neutron Field for Fundamental Researches for BNCT with A DT Neutron Source", *EPJ Web of Conferences* **153**, 04008, 9p (2017).

[4] X-5 Monte Carlo Team: MCNP-A General Monte Carlo N-Particle Transport Code(2003) Nparticle transport code, version 5(2003).

This is a blank page.

37 Visualization of nuclear data used in PHITS and utilization of a tool to convert EXFOR to PHITS-readable format

Naoya FURUTACHI

Research Organization for Information Science and Technology, Shirakata 2-4, Tokai, Ibaraki 319-1106, Japan

Abstract

Nuclear data with A Compact Evaluated nuclear data file (ACE) format is used in Monte Carlo particle transport codes such as PHITS to simulate nuclear reactions. Since it is not so simple to extract cross sections embedded in ACE, PHITS has only a limited feature to display them directly. In this work, an effective process to extract cross sections, including double-differential ones, of ACE loaded in PHITS was studied. It was confirmed that the cross sections obtained by a PHITS-simulation with a thin-target and those extracted from the ACE by the present process perfectly agree.

There is an alternative way to use nuclear data in PHITS. By using the PHITS "[Frag Data]" feature, user-defined nuclear data can be incorporated in a PHITS-simulation. In near future, a tool to convert a file of EXFOR library, which is the most comprehensive compilation of experimental nuclear reaction data, to a "[Frag Data]" file will be released by the PHITS developer team. In this work, usage of this tool was also studied.

1 Introduction

Nuclear data are used to simulate nuclear reactions in A general-purpose Monte Carlo Particle and Heavy-Ion Transport code System (PHITS) [1], which is used in various application fields. I worked on following two subjects that are related to the nuclear data used in PHITS.

1.1 Visualization of nuclear data in ACE format loaded in PHITS

Monte Carlo particle transport codes such as PHITS uses A Compact Evaluated nuclear data file (ACE) format data to simulate nuclear reactions. Recently, the feature to use ACE in PHITS and the evaluated nuclear data libraries presented by ACE have been extended. In the latest version of PHITS (3.26 after), the transportation of deuteron and alpha particle using ACE have been enabled. Ahead of this progress, the JENDL/DEU-2020 has been published [2], and now the ACE files of JENDL/DEU-2020 are available. As for the high-energy nuclear data for the neutron and proton, ACE files of JENDL-4.0/HE[3] have been extended by ACE-J40HE [4]. More general topic about ACE is the publication of the domestic nuclear data processing code FRENDY [5]. FRENDY will make ACE files more familiar to general users.

With increasing ways of using ACE files, it is desired that users are more aware of the contents and the validity of newly presented data. However, the feature to display the cross section data of ACE loaded in PHITS is limited. While the integrated cross sections of total, non-elastic, and elastic can be directly obtained by icntl = 1 feature, differential cross sections

and explicit reaction channel cross sections can not. If users want to obtain differential cross sections, it is necessary to execute particle-transport simulations with thin-targets and proper tally settings.

In this work, an effective process to extract differential cross sections from ACE loaded in PHITS was studied. While the differential cross section values are not directly written in ACE format, I found that it is rather easy to construct differential cross sections by using the PHITS subroutine to sample the energy and angle of the secondary particle. I compared the obtained differential cross sections with those obtained by executing the particle-transport simulations with thin-targets, and confirmed that they agree.

1.2　A trial of a tool to convert EXFOR to the PHITS "Frag Data" format

PHITS can use user-defined cross section data by specifying a data file in "[Frag Data]" section. This is alternative way to utilize nuclear data in PHITS. While it is not realistic for general users to prepare their own evaluated nuclear data files, It is expected that there is a demand for incorporating latest experimental data in a PHITS simulation. While "[Frag Data]" feature is suitable for such a demand, preparing a file for "[Frag Data]" feature using the experimental nuclear reaction data is not so easy for general users.

The PHITS developer team plans to release a tool to convert a file of EXFOR library [7], which is the most comprehensive compilation of experimental nuclear reaction data, to a file that can be used for "[Frag Data]" feature. By using this tool, it will be easier to incorporate experimental nuclear reaction data in PHITS simulations. In this work, usage of the pre-release version of the tool was studied. Expected difficulty to utilize such a tool and its solution are discussed.

2　Technical details

Here the terms in the instructions for ACE format written in MCNP manual [6] are used. In this work, differential cross section data are extracted from ACE loaded in PHITS by the following procedure. All of ACE data and pointers to specify the data are stored in XSS array and JXS array in the PHITS program, respectively, after some processes for reading ACE files. The integrated cross section values of total, absorption, and elastic are easily extracted by specifying corresponding positions in ESZ Data Block of XSS array with JXS array. Unlike the integrated cross sections, the differential cross section values are not directly written in a ACE file. To deduce the double-differential cross section values, data in AND and DLW Blocks are used, in which the angular distribution and the energy distribution are given, respectively. In DLW Block, the contents of data arrays are different depending on the LAW, and it is necessary to calculate the emitted particle energy using the values in the data array according to the LAW. Since it is difficult to implement the calculation processes for all of needed LAWs, the subroutine of PHITS to sample the angle and energy of the emitted particle is utilized in this work. Due to the random sampling process, data on specific angle and energy points can not be obtained, but counts on the energy and angle bins are obtained. The counts are converted to the probability distributions as functions of the angle and energy for every reaction MT, then the partial cross section values of each MT extracted from SIG Block are multiplied to them. In a high-energy file case, the data are given in MT=5. In this case, the neutron multiplicity is also must be multiplied to deduce the neutron-production double-differential cross section. As for photon-production cross sections, data in ANDP, DLWP, and SIGP Blocks are used. The photon-production differential cross sections are obtained by a similar process explained above.

To use the tool to convert a EXFOR file to a "[Frag Data]" file, it is necessary to prepare

"original EXFOR" format files by users themselves. In the present trial, the EXFOR file for ^{27}Al+p neutron production double-differential cross section (accession number T0203; REAC-TION 13-AL-27(P,X)0-NN-1,,DA/DE) data that was taken from IAEA NDS web system[8] was used. The tool read the incident particle, target, and product particle or nuclei from the RE-ACTION field of a EXFOR file adding to the cross section data, and generate corresponding "[Frag Data]" file. In this work, an advanced feature that is not implemented in the original tool is also proposed. Because experimental data are often incomplete, a feature to compensate lacked data will be useful. For this purpose, a smoothing feature with evaluated nuclear data was implemented to the original tool as a trial. The smoothing process is carried out by using splines. The feature is tested using the EXFOR files of excitation function data for the ^{16}O+p reaction (accession number E2449, E2568, and C0507; REACTION 8-O-16(P,X)7-N-13,,SIG and 8-O-16(P,X)4-Be-10,,SIG). As for evaluated nuclear data, the production cross section data files of TENDL [9] were used.

3   Results

The present process to extract cross sections embedded in ACE was tested using ^{56}Fe+n ACE files of JENDL-4.0[10] and JNEDL-4.0/HE. The incident neutron energies of 15 MeV and 100 MeV are chosen for JENDL-4.0 and JENDL-4.0/HE files, respectively. In the left panel of Fig. 1, the differential cross sections with respect to the outgoing neutron energy extracted from the ACE are shown. The cross sections are obtained for every reaction MT, and the inelastic total shown by a solid line is obtained by summing them all. In the right panel, the double-differential cross sections at 15, 30, 45, and 60 deg are shown. The present results are compared with those obtained by simulating neutron impinged on thin ^{56}Fe target (PHITS-simulation) shown by circles. It was confirmed that both results agree. Figure 2 shows the differential-cross section of product photon. While the results are obtained for every photon production MT, only the total is shown by a solid line. The present result agrees with the PHITS-simulation result shown by circles. A high-energy file case is also tested, and the results are shown in Fig. 3. It was confirmed that the present results and the PHITS-simulation results agree even in a high-energy file case.
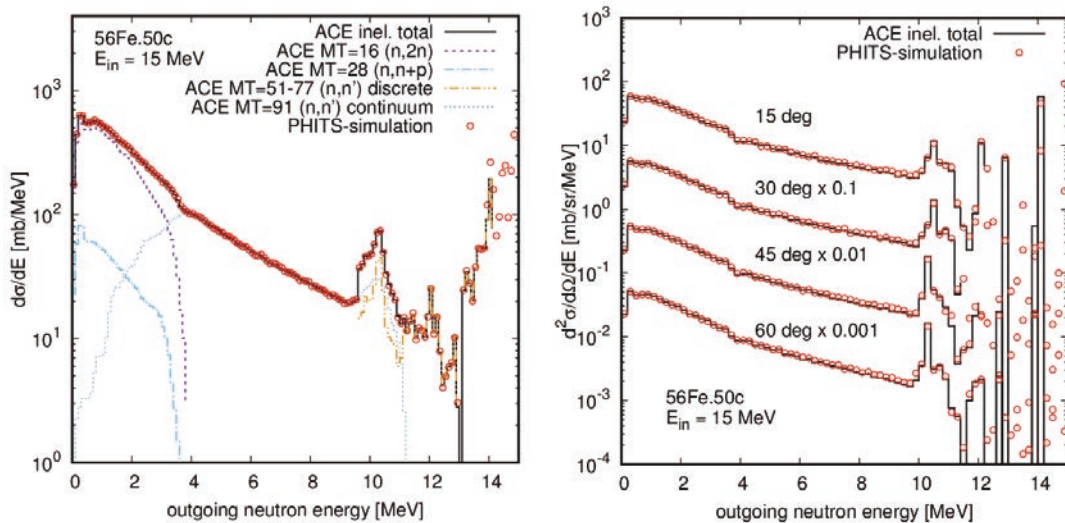

Figure 1: Differential cross sections with respect to outgoing neutron energy (left panel) and double-differential cross sections at 15, 30, 45, and 60 deg (right panel). Results are obtained using ^{56}Fe+n ACE file of JENDL-4.0 at incident neutron energy of 15 MeV.
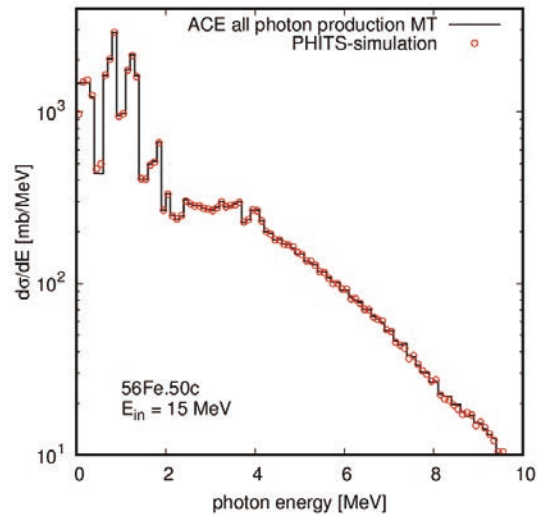
Figure 2: Photon-production differential cross sections. Results are obtained using ^{56}Fe+n ACE file of JENDL-4.0 at incident neutron energy of 15 MeV.
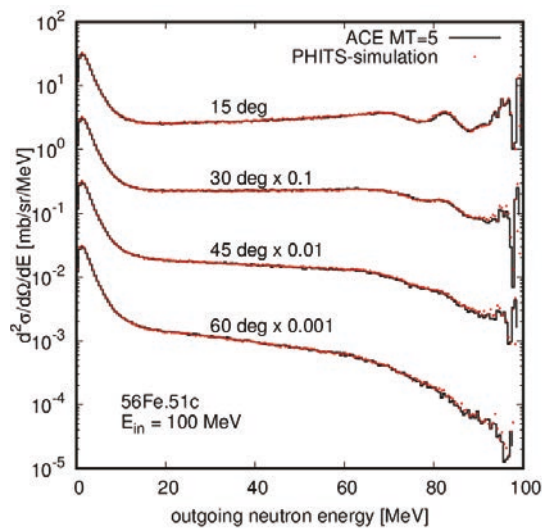

Figure 3: Neutron-production double-differential cross sections at 15, 30, 45, and 60 deg. Results are obtained using ^{56}Fe+n ACE file of JENDL-4.0/HE at incident neutron energy of 100 MeV.

The tool to convert a EXFOR file to a "[Frag Data]" file was tested using the original EXFOR file for the neutron-production ^{27}Al+p double-differential data. The particle-transport simulation incorporating the generated "[Frag Data]" file with a thin-target of ^{27}Al was executed. Figure 4 compares the present results and the original experimental data points, which are shown by lines and symbols, respectively. It was confirmed that the tool and "[Frag Data]" feature worked fine from the perfect agreement between the PHITS-simulation results and the experimental data. It is also obvious that neutrons up to $\sim$ 30 MeV, where experimental data are absent, are not produced. The PHITS-simulation results without "[Frag Data]" file shown by dotted lines indicate that there should be evaporated neutron spectrum in that energy region, naturally. That is a difficult point to incorporate experimental data in a simulation. To study how to mitigate this problem, a smoothing feature with evaluated nuclear data was tried. The feature was tested using the excitation function data of ^{16}O+p reaction. In Fig.

5, the excitation functions smoothed using the experimental data (squares) and the evaluated nuclear data (crosses) are shown by solid lines. With an appropriate weight setting on the data, the smoothed lines come close to the experimental data with priority and toward the evaluated nuclear data if there is no experimental data. It was confirmed that the "[Frag Data]" file generated using the smoothed lines was successfully incorporated to the PHITS-simulation. Naturally, ^{13}N and ^{10}Be are produced with any incident energies up to 200 MeV in that simulation. Such a feature will make it easier to utilize the conversion tool.

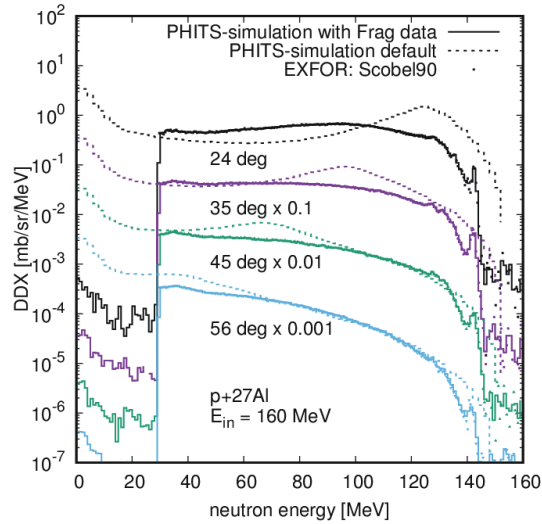Figure 4: Neutron-production double-differential cross sections of ^{27}Al+p reaction at incident proton energy of 100 MeV. Results of PHITS-simulation with and without "[Frag Data]" file, and experimental data points are shown by solid lines, dotted lines, and symbols, respectively.
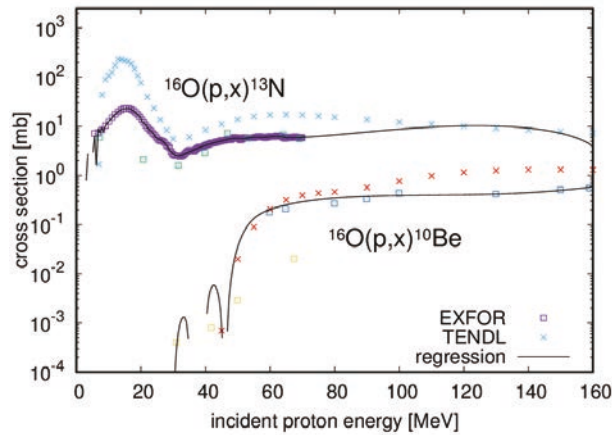

Figure 5: Excitation functions of ^{16}O(p,x)^{13}N and ^{16}O(p,x)^{10}Be reactions. Smoothed result, experimental data, and evaluated nuclear data are shown by solid lines, squares, and crosses, respectively.

4 Summary

In the first subject of the present work, a process to display cross sections of ACE loaded in PHITS was studied. The double-differential cross sections were successfully extracted from the

ACE files of JENDL-4.0 and JENDL-4.0/HE by utilizing the PHITS subroutine to sample the angle and energy of the emitted particle. In the second subject, usage of the tool to convert a EXFOR file to a "[Frag Data]" file was studied. It was confirmed that the "[Frag Data]" feature with a file generated by the tool worked fine. Expected difficulty to utilize the tool was discussed and one of solution was proposed.

References

[1] Sato, T., et al., Features of Particle and Heavy Ion Transport code System (PHITS) version 3.02, J. Nucl. Sci. Technol. 55, 2018, pp. 684-690.

[2] Nakayama, S., et al., JENDL/DEU-2020: deuteron nuclear data library for design studies of accelerator-based neutron sources, J. Nucl. Sci. Technol., vol.58, no.7, 2021, pp. 805-821.

[3] Kunieda, S., et al., Overview of JENDL-4.0/HE and benchmark calculation, JAEA-Conf 2016-004, 2016, pp. 41-46.

[4] Download of cross-section library for MCNP/PHITS, https://rpg.jaea.go.jp/main/en/ACE-J40HE/index.html (accessed 2021-11-10).

[5] Tada, K., Development and verification of a new nuclear data processing system FRENDY, J. Nucl. Sci. Technol., vol.54, 2017, pp.806-817.

[6] X-5 Monte Carlo Team, MCNP – A General Monte Carlo N-Particle Transport Code, Version 5, 2003, LA-UR-03-1987.

[7] Otuka, N., et al., Towards a More Complete and Accurate Experimental Nuclear Reaction Data Library (EXFOR): International Collaboration Between Nuclear Reaction Data Centres (NRDC), Nucl. Data Sheets, vol.120, 2014, pp. 272-276.

[8] Experimental Nuclear Reaction Data (EXFOR), https://www-nds.iaea.org/exfor/ (accessed 2021-11-05).

[9] TALYS-based evaluated nuclear data library, https://tendl.web.psi.ch/tendl_2019/tendl2019.html (accessed 2021-11-05).

[10] Shibata, K., et al., JENDL-4.0: A New Library for Nuclear Science and Engineering, J. Nucl. Sci. Technol., vol.48, no.1, 2011, pp. 1-30.

Acknowledgments